



**University of
Nottingham**
UK | CHINA | MALAYSIA

Quantum Circuits as Minimal Models of Many-Body Dynamics

Thesis submitted to the University of Nottingham for the degree of
Doctor of Philosophy, July 2024.

Alessandro Foligno

20399624

Supervised by

**Bruno Bertini
Juan P. Garrahan**

Signature _____

Date ____ / ____ / ____

Contents

Chapter 1	Introduction	3
1.1	Motivation	3
1.2	From ground state to many-body dynamics	6
1.3	Quantum circuits	9
1.3.1	Entanglement growth for a subsystem: Membrane vs Quasiparticle picture	15
1.4	Dual Unitary circuits	17
Chapter 2	Growth of entanglement of generic states un- der dual-unitary dynamics	20
2.1	Summary	20
Chapter 3	Temporal entanglement	38
3.1	Summary	38
Chapter 4	Quantum information spreading in general- ized dual unitary	76
4.1	Summary	76
Chapter 5	Non-equilibrium dynamics of charged dual- unitary circuits	88
5.1	Summary	88
Chapter 6	Entanglement of disjoint intervals in dual unitary circuits: exact results	121
6.1	Summary	121
Chapter 7	Conclusions	134
7.1	Acknowledgements	135
	Bibliography	136

Chapter 1

Introduction

1.1 Motivation

Physical systems of all kinds and scales display a tendency to thermalize, from few atoms [1], to black holes [2, 3]. While an axiomatic study of thermodynamics started centuries ago, it was not until the advent of quantum mechanics that it became a built-in feature of the underlying theory and shown to emerge even at sizes well below the thermodynamic limit and in non-equilibrium situations [4].

Given the non-deterministic nature of quantum mechanics, thermal ensembles can be considered as *intrinsic* random objects; this has given new perspectives to centuries-old information paradoxes such as Maxwell's demon [5]. A random ensemble, in this case, is defined as a set of possible states for the system with corresponding probabilities: a measurement can specify in which of these states the system is. Classically, the statistical nature of the ensemble is due to the lack of information on the state of the system; in this case the second law of thermodynamics does not allow to gain information on the system without some external work. In quantum mechanics, statistical ensembles are the most complete description of physical objects and no more information can be obtained on the system

without altering its state; this intrinsic uncertainty was formalized by Bell's inequality which has been experimentally verified [6, 7].

Thus quantum mechanics, in the formalism of density matrices, provides a natural framework to study thermalization: a pure state defined on both some system S and environment E

$$|\Psi(t)\rangle_{E,S} = U(t) |\Psi(0)\rangle_{E,S} \quad (1.1)$$

can be studied locally in S by tracing out the environment E and defining a *reduced density matrix*

$$\rho_S(t) = \text{tr}_E \left[|\Psi(t)\rangle\langle\Psi(t)|_{E,S} \right], \quad (1.2)$$

which allows one to compute the expectation value of any observable localized in S . Since the reduced density matrix ρ_S is positive¹, it can be diagonalized with positive eigenvalues

$$\rho_S = \sum_i p_i |\psi_i\rangle\langle\psi_i| \quad \sum_i p_i = 1. \quad (1.3)$$

Crucially, these eigenvalues p_i sum to 1 and so ρ_S can be interpreted as a classical ensemble where each state $|\psi_i\rangle$ has an associated probability p_i . At late times, the reduced density matrix (1.2) will relax to a constant ensemble. The Shannon entropy of the corresponding distribution of $\{p_i\}$

$$S[\{p_i\}] = - \sum_i p_i \log(p_i) \quad (1.4)$$

measures how "ergodic" the final distribution of p_i is and corresponds to the microscopic thermodynamical definition of entropy for a thermal distribution of probabilities. However, the state in (1.2) is defined at all times, well before it relaxes to some constant ensemble: the Shannon entropy of the time dependent eigenvalues $p_i(t)$ can then be studied as a dynamical quantity, which quantifies the ongoing thermalization process of the sub-

¹this is because the partial trace is a completely positive, trace-preserving map

system out of equilibrium. This quantity is called *entanglement entropy* and is the most widely used measure to quantify the quantum correlations in the system: in a basis independent fashion, it can be expressed as the Von Neumann entropy of ρ_S , namely

$$S[\rho_S] = -\text{tr} [\rho_S \log(\rho_S)]; \quad (1.5)$$

where it is understood that the function $x \log(x)$ is extended by continuity in 0 and is thus well defined and bounded in $[0, 1]$.

Together with the entanglement entropy of the state, it is convenient to define a family of entanglement measures, called Rényi entropies or α -entropies. They are dependent on a parameter α and defined as

$$S^{(\alpha)}[\rho_S] = \frac{1}{1-\alpha} \log\left(\text{tr} [\rho_S^\alpha]\right); \quad (1.6)$$

the reason for introducing this family of entropies is two-fold: on the one hand, they are a valuable tool to analytically find expression for the Von Neumann entropy via the so-called *replica trick* [8]; on the other hand, they have some useful properties on their own. For example, they obey the following inequalities [9]

$$\frac{m-1}{m} \frac{n}{n-1} S^{(m)} \leq S^{(n)} \leq S^{(m)} \quad n > m, \quad (1.7)$$

which shows, for example, that the scaling law in the subsystem size of all Rényi entropies with index $n > 1$ is the same [10, 11, 12].

The thermodynamic interpretation of the entanglement entropy as a state function is attained at long times when the system converges to some static ensemble, after a thermodynamic limit. Formally one needs to take the following order limits in order to define thermal relaxation [13, 14, 15]:

$$\lim_{t \rightarrow \infty} \lim_{L \rightarrow \infty} \rho_S(t) = \rho_{stat}, \quad (1.8)$$

where S is a subsystem with a size kept constant, while L is the size of the whole system (subsystem + environment E) which is instead taken to be infinitely large. It is crucial take the long time limit *after the thermodynamic limit*; this is because a long time limit on any finite-sized quantum system is not well defined, as the system would be quasi-periodic in time due to the unitary evolution [16]. The state is expected to relax to the Generalized Gibbs Ensemble (GGE) [17, 18, 19, 13, 20, 21, 22, 23], which is built using local and *quasi*-local charges of the system:

$$\rho^{GGE} \propto \exp\left(-\sum_i \beta_i Q_i\right). \quad (1.9)$$

More precisely, for a many-body system, a local charge is an operator which can be written as sum of other operators which have a finite support (for a spin system, finite support means the operator is the identity everywhere but on a finite number of sites)

$$Q = \sum_x q_x, \quad \text{supp}(q_x) < +\infty, \quad (1.10)$$

while a quasi-local one is an operator that can be approximated up to exponentially small correction with a local operator. Quasi-local charges were discovered in the context of the XXZ spin chain [24] and proved crucial for an accurate representation of the steady state [25].

1.2 From ground state to many-body dynamics

A crucial ingredient for a system to thermalize, is to have enough degrees of freedom, in order for ergodicity to emerge; in principle one would have to have infinitely many degrees of freedom, in order to take the thermodynamic limit $L \rightarrow \infty$ as in Eq. (1.8). This is the main obstacle to obtain

a precise description of the dynamics and makes it an exceedingly hard problem already at the classical level. In classical physics, it is well known that the three-body problem is not exactly solvable, while the two body one is only solvable because it can be reduced to a one-body problem using momentum conservation. It is then clear that having infinitely many degrees of freedom makes dynamics extremely difficult to obtain. At the quantum level, there are exponentially more degrees of freedom, thus even numerical approach to the problem are generally unfeasible with classical computers; this is one of the aspects of quantum advantage.

Only some special classes of problems can be reasonably dealt with a classical computer: an example is the characterization of the ground state of a local, one dimensional Hamiltonian. The underlying reason for this is that gapped Hamiltonians have a ground state with a low entropy [26, 27, 28]; in particular, the entropy is said to follow an *area law*, meaning it scales with the size of its boundary with the rest of the system. For one dimensional system, this means that the entropy saturates, as boundaries between intervals are just points.

More rigorously, a favourable (i.e. logarithmic or constant) scaling of the Rényi entropies $S^{(\alpha)}$ with $\alpha < 1$ implies that algorithms that use Matrix Product states (MPSs) to find the ground states, i.e. Density Matrix Renormalization Group (DMRG) algorithms [29, 30] have a polynomial scaling in the error tolerance requested. This implies that even some gapless systems that can violate the area law requirement, can be efficiently simulated as long as the Rényi entropies scale logarithmically in the system size. In particular, for Conformal Field Theories, a general result [31] shows that the entanglement entropy of a subsystem of size l , assuming the system is in the ground state, has Renyi entropy which grow logarithmically in the system size:

$$S^{(n)} = \frac{n+1}{n} \frac{c}{6} \log\left(\frac{l}{a}\right), \quad (1.11)$$

where c is the central charge of the theory and a is a cut-off length. Moving away from the ground state to the study of the dynamics from generic initial conditions, entanglement generically experiences a linear phase of growth, making simulability with MPSs only feasible at very short times and exponentially hard in general. Despite this, algorithms using an MPS decomposition (such as Time Evolving Block Decimation - TEBD) of the state at short times are still the most powerful tools at our disposal to investigate short times dynamics numerically; TEBD will be briefly presented in Section 1.3.

As for analytical toy models of many-body dynamics, very few examples are known and most require that the dynamics is non-interacting (i.e. the Hamiltonian is a quadratic form). A class of systems which is amenable to some analytic treatment (although with some limitations) is the one of integrable systems.

Integrable systems have a number of local conserved charges that scales with the size of the system. However, while for free systems it is rather straightforward to diagonalize the Hamiltonian and find the energy spectrum, in the case of interacting integrable systems one has to solve a system of non-linear equations whose number is extensive in the system size. Even if this task can be done numerically for moderate sizes [32], exact results are much harder to obtain. The Bethe equations can be solved in the thermodynamic limit under certain assumptions (namely the "string hypothesis" which assumes that solutions to the Bethe Equations form "string patterns" at finite densities [33]) in order to obtain the so called "thermodynamic Bethe Ansatz", which allows to access the thermodynamics of the system, rather than the dynamics. Moreover, while integrability provides a useful example of many-body dynamics, the fact that the underlying Hamiltonian has many conserved charges suggests it may belong to a different universality class from a chaotic dynamics without many conservation laws. An example of chaotic system which can be analytically studied is the SYK model [34] [35]; in order to work out the dynamics, here it is introduced an

average over the interaction terms and, in high enough dimensions, a mean field approach allows for exact results.

1.3 Quantum circuits

On the one hand, as stressed in the previous section, accessing many body dynamics is an extremely difficult task; on the other, finite size numerics and partial analytical results in recent years, suggest that out of equilibrium quantum matter can present very exotic phenomena, placing its understanding among the key questions of modern theoretical physics [36, 37, 38, 39, 40].

This highlights the need for simple, treatable toy models that can offer analytical insights and model different universality classes [41].

In recent years quantum circuits have gained popularity as a possible candidate to achieve this task: they can be used to describe fully chaotic [42, 43, 44] but also charge conserving dynamics [45, 46, 47, 48, 41]. The underlying idea of a quantum circuit is to evolve a spin chain with a discrete time evolution, implemented with local gates. Such systems can be thought as obeying a stronger version of the Lieb-Robinson bound [49, 50] where one has a hard cut-off for the tails outside the light-cone instead of an exponential suppression.

The setting of circuits arises very naturally in numerical simulations of d -local Hamiltonians. A popular approach for this is the one followed by TEBD algorithms [51]; the starting point is that a generic Hamiltonian with two site interaction (renormalizing the sites one can always make the range of the interaction fall into this category) can be broken down in two

parts:

$$H = \sum_i V_{i,i+1} = H^e + H^o \quad (1.12)$$

$$H^e = \sum_i V_{2i,2i+1} \quad H^o = \sum_i V_{2i-1,2i}, \quad (1.13)$$

where, crucially, each term within H^e commutes with itself (and the same goes for H^o), so that they are easily exponentiated

$$e^{iH^e t} = \prod_j e^{iV_{2j,2j+1}t} \quad e^{iH^o t} = \prod_j e^{iV_{2j-1,2j}t}. \quad (1.14)$$

Choosing a control parameter N for the approximation, the time evolution up to time t can be written as

$$e^{iHt} = \left(e^{iH \frac{t}{N}} \right)^N = \left(e^{i(H^e+H^o) \frac{t}{N}} \right)^N \approx \left(e^{iH^e \frac{t}{N}} e^{iH^o \frac{t}{N}} \right)^N. \quad (1.15)$$

The crucial insight here is that, for N large enough, Hausdorff formula yields

$$e^{i(H^e+H^o) \frac{t}{N}} \approx e^{iH^e \frac{t}{N}} e^{iH^o \frac{t}{N}} e^{i[H^e, H^o] \frac{t^2}{2N^2}} \approx e^{iH^e \frac{t}{N}} e^{iH^o \frac{t}{N}} (1 + O(1/N^2)). \quad (1.16)$$

This means that the final error in the approximation scales as $O(1/N)$ showing that for N large enough one can obtain an exact evolution. The approximate formula in (1.15) is a quantum circuit: representing a gate acting on sites $j, j+1$ as

$$e^{V_{j,j+1} \frac{t}{N}} = \begin{array}{c} | \\ | \\ \text{---} \\ | \\ | \\ | \end{array} \quad , \quad (1.17)$$

$j \qquad \qquad j+1$

Eq. (1.15) can be represented as

(1.18)

where we have $2N$ layers of gates which is also called the *depth* of the circuit. These gates are very close to the identity matrix for large values of N . The idea of quantum circuit is to instead lift this constraint and choose *generic* matrices for time evolution. This setup is rather similar to experiments with superconducting junctions, see e.g. [52, 53, 54]; here the discrete dynamics of qubits is obtained through the application of unitary operations (gates), measurements, and feedback.

Moving the gates away from the identity opens up for some new classes of solvable dynamics, which can offer insight and intuition for the typical behaviour of gates, while preserving locality and unitarity in the evolution (although one can generalize this to include monitoring and measurements, which break unitarity [48, 54, 55]). There are two main strategies employed in order to obtain analytically treatable circuits, which can also be used in conjunction.

The first one is to introduce some average over the gates, considering them as noisy, and assuming that typical realization of the circuit behave similarly to the averaged one. The gates are taken from a certain ensemble, usually the one for which each gate evolving a circuit as in the diagram (1.15) is extracted randomly from the unitary group $U(d^2)$ with a probability density equal to the Haar measure, where d is the local Hilbert space

dimension on each site [42, 56, 43, 57, 44, 47]. The second approach is to require additional constraints on the gate, apart from unitarity, which in turn enables for crucial simplifications in the diagrams representing time evolution [58, 59, 60, 61, 62, 63, 64, 65]; examples include the class of dual unitarity circuits, which will be covered more in details in Chapter 1.4 and are the main focus of this thesis, as well with its generalizations [66, 67, 68], and some cellular automata, as the famous Rule 54 [69, 70], which can be used for a quantum dynamics starting from non-classical initial states, or the Floquet quantum East model [64, 71].

Explicit results for Haar-random circuits can be obtained for quantities that involve two replicas of the gate, such as the second moment of the reduced density matrix for a subsystem

$$Z^{(2)} = \text{tr} [\rho_A^2], \quad (1.19)$$

or out of time correlation functions (OTOCs), defined as

$$O^{\alpha,\beta}(x,t) = 1 - \frac{1}{d^L} \text{tr} [\sigma^\alpha(x,t) \sigma^\beta(0,0) \sigma^\alpha(x,t) \sigma^\beta(0,0)], \quad (1.20)$$

where $\sigma^\alpha_{\alpha=1,\dots,d^2-1}$ is an orthonormal basis of traceless hermitian operators such that

$$(\sigma^\alpha)^2 = \mathbb{1}_{d^2} \quad (1.21)$$

(for $d = 2$ a possible choice are the standard Pauli matrices) and L is the number of sites in the system. The idea is that both (1.19),(1.21) require two copies of the unitary operator \mathbb{U} defining the forward time evolution, together with two for the backward one (which corresponds to \mathbb{U}^\dagger). Alternatively, the evolution of these copies can be thought as a single copy evolved with a replica gate that includes four layers [41]:

$$V \otimes V^* \otimes V \otimes V^* \quad V \in U(d^2), \quad (1.22)$$

where V is a single gate acting on two qudits as represented in (1.17). This replicated, or *folded*, gate can be averaged over the Haar measure, assuming noise is uncorrelated in space and time, effectively reducing the degrees of freedom on a single site from d^4 to 2, since the only non-vanishing elements of the averaged gate corresponds to the two possible pairing of the forward copies with the backward ones.

This maps the circuit to an Ising-like statistical model (where the two pairings can be thought of as the two spin configurations), where the quantity of interest (such as the one in (1.21),(1.19)) is mapped to a partition function [42, 43, 44, 72]. Similarly to Ising, the leading contributions come from large domains of equal pairing, and the non-trivial part of the partition function can be thought of as some free energy cost at the interface between different domains.

Interestingly, one can extend this picture, which is exact only performing an average on the gates, to specific instances of gates, noting that fluctuations from the generic behaviour are suppressed in the scaling limit [73, 74], obtaining the so called *membrane picture* for the entanglement dynamics. The membrane picture postulates the existence of a function $\mathcal{E}_n[v]$ which specifies the free energy density at the interface between large domains corresponding to different pairings of replicas. In the case of a 1 + 1 dimensional system, the membrane between domains is a line (indeed \mathcal{E} is also called *line tension*) and has only a local degree of freedom, its slope v , while in larger dimensions one has more angles to specify. The function $\mathcal{E}[v]$ satisfies generic constraints [74]: it must be convex, meaning that

$$\mathcal{E}[v_1\lambda + (1 - \lambda)v_2] \leq \lambda\mathcal{E}[v_1] + (1 - \lambda)\mathcal{E}[v_2], \quad \lambda \in [0, 1] \quad (1.23)$$

and its Legendre transform must correspond to the local rate of entropy production

$$\Gamma[s] = \min_v \left\{ \mathcal{E}[v] - \frac{sv}{s_{eq}} \right\} \quad \frac{\partial S}{\partial t} = s_{eq}\Gamma \left[\frac{\partial S}{\partial x} \right], \quad (1.24)$$

where s_{eq} corresponds to the maximal entanglement density, which is equal to $\log(d)$ for a spin chain of qudits of local dimension d .

A useful quantity to measure the spreading of operators is the *butterfly velocity*, which defines, at a given value of t , the light-cone $x \in [-v^B t, v^B t]$ in which the OTOC (defined in Eq. (1.21)) is finite (meaning it is not exponentially suppressed): it can be extracted from the line tension with a self consistency equation

$$\mathcal{E}_2[v_B] = v_B, \tag{1.25}$$

while the entanglement growth for a Rényi entropy starting from a low entangled initial state is

$$v_n^E = \min_v \mathcal{E}_n[v]. \tag{1.26}$$

Equation (1.26) already gives a quantitative prediction: it implies that, in a scaling regime, the rate of growth of entanglement should converge to the same values, regardless of the initial state chosen, which is different to what is expected for non-chaotic systems, such as free or integrable systems [20, 75, 76, 77, 78].

An explicit expression for the line tension is extremely hard to obtain for a clean system; for dual unitary circuits, for example, it is constant and extremal for all values of v [73]. In the work in Chapter 4 we provide a different example of $\mathcal{E}[v]$ for a *clean system* evolved with a generalized dual unitary circuit and verify the constraints in (1.23),(1.25),(1.26); in this case the line tension is not constant and has a V shape.

We also mention that the membrane approach to compute entanglement has also been successfully applied to holographic theories [79, 80].

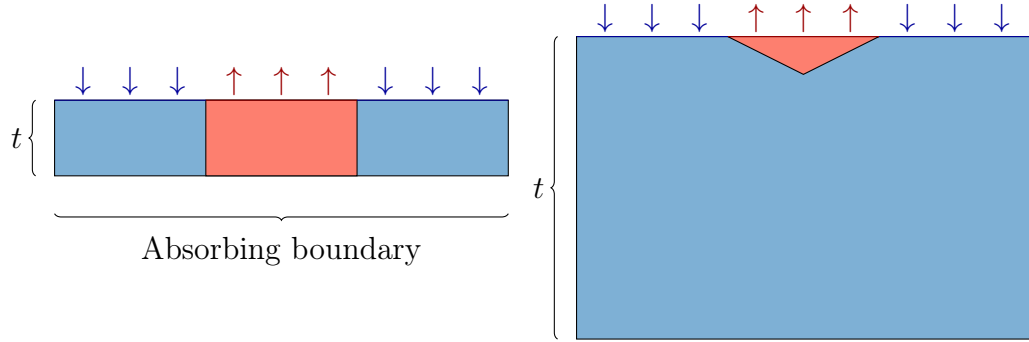


Figure 1.1: Entanglement dynamics using the membrane approach: the subsystem (spin up) corresponds to a different pairing of replicas than the rest (spin down). The bottom line represents the initial state and is essentially an open boundary with no interaction (energy cost) for any pairing. At short times, the free energy is minimized such that the domain of spin up touches the initial state; the size of the boundary separating the domains scales with t , implying a linear growth for the entanglement; at later times instead the free energy is minimized by wrapping the subsystem (in red) with a domain corresponding to the other pairing (blue), showing saturation in entanglement.

1.3.1 Entanglement growth for a subsystem: Membrane vs Quasiparticle picture

The membrane theory provides a quantitative prediction for the entanglement dynamics from a quantum quench. A sketch of its prediction in the simplest case of a finite, connected subsystem is reported in Fig. 1.1. Independently on the value of the line tension, the qualitative prediction is clear: there is an initial regime of linear growth of entanglement, which then saturates.

Interestingly, this is the same behaviour predicted by the *quasiparticle picture* [81], another powerful tool used to understand the entanglement spreading in many-body quantum systems after a quench, which was developed in the context of integrable systems and conformal field theories. The idea is that entanglement is generated by initially entangled local pairs of quasiparticles that then move ballistically in both directions (to conserve momentum). One can imagine these as forming a sort of Bell pair state, with the two qubits moving in opposite directions and spreading correla-

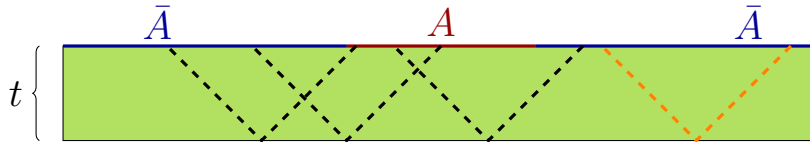


Figure 1.2: Entanglement dynamics at early times according to the quasiparticle picture for entanglement between a subsystem A and the rest of the system \bar{A} . The trajectories of pairs moving, originating from the initial state (bottom edge) are represented with dashed lines. In orange there is an example of a pair not contributing to the entanglement for this choice of bipartition. At later time the number of pairs connecting A with \bar{A} saturates.

tion throughout the system. Counting the number of pairs connecting a subsystem with the other quantifies the entanglement; an intuitive picture of this behaviour is present in Fig. 1.2.

The quasiparticle prediction can be made quantitative within the context of integrable systems [13, 82] by using the Yang-Yang entropy to express the contribution from each pair of quasiparticle, and the velocity of excitations to quantify their velocity, obtaining the explicit formula

$$S_n(t) = 2t \int_{2|v(\lambda)|t < \ell_A} v(\lambda) s(\lambda) d\lambda + \ell_A \int_{2|v(\lambda)|t > \ell_A} s(\lambda) d\lambda, \quad (1.27)$$

where the integration is over quasiparticle species.

Crucially, both approaches, although coming from very different perspectives, bear the same qualitative results in the geometry of a finite sized interval immersed on a large environment. However, the two pictures describe very different systems: the membrane picture is understood to work for chaotic ones, where destructive interference essentially forces the dominant configurations of diagrams to be pairings of replicas, while the quasiparticle should hold for systems with a large number of conserved quantities which propagate at some finite speed.

A change in the geometry of the subsystem can instead give a different qualitative result depending on the "picture" adopted. The simplest case is the one of a subsystem A made of two intervals of sizes ℓ_A , separated by a large enough distance x ; at early times, when the two parts of A are

causally disconnected, we have again a generic initial linear growth followed by saturation. This saturation, as per the minimal cut idea in Fig. 1.1, is preserved at later times according to the membrane picture, while the quasiparticle picture predicts a drop in the entanglement of A at times

$$t \in \left[\frac{x}{v_{qp}}, \frac{x + \ell_A}{v_{qp}} \right], \quad (1.28)$$

where v_{qp} is the speed of quasiparticle propagation, due to the fact that some quasiparticle pairs now end up on the two intervals making up the subsystem A and thus not contributing to the entanglement.

Divergence from the quasiparticle approach was first noted in the context of Holographic Conformal Field theories (CFT) [83]. These special class of CFTs display some chaotic features while maintaining conformal invariance [84, 85, 86, 87]; rational CFTs (such as the critical point of Ising model) instead behave as "integrable" and show agreement with the quasiparticle picture and are generated by a finite number of primary operators. In the work in Chapter 6 we provide rigorous result that agree with both these pictures in the context of Dual unitary circuits. Namely, we show that a quantum quench from the same, simple initial state, behaves according to each of the two predictions depending on whether the Dual Unitary gate is chaotic (meaning that we extract randomly from an ensemble) or has conserved charges, in the aforementioned geometry of two intervals separated by a large enough distance.

1.4 Dual Unitary circuits

The most well known example of exactly solvable, clean, interacting quantum circuit is the one made of Dual Unitary gates [65, 58]. In this Thesis, the focus will be on these gates implemented in a brickwork fashion, as

depicted in (1.18), although other geometries are possible [60, 88]. In this section, a brief, non-exhaustive overview of the results obtained so far for such circuits is presented.

A dual unitary gate U is defined as a gate that retains unitarity after a spacetime swap of indexes:

$$\langle i, j | \tilde{U} | k, l \rangle = \langle i, k | U | j, l \rangle \quad (1.29)$$

$$UU^\dagger = U^\dagger U = \mathbb{1}_d \otimes \mathbb{1}_d = \tilde{U}\tilde{U}^\dagger = \tilde{U}^\dagger\tilde{U}. \quad (1.30)$$

This spacetime duality was first observed in the many-body evolution operator of the kicked Ising model at a special point [89] and allowed for calculation of quantities such as the spectral form factor [56] and entanglement growth [90]. Then, Refs. [65, 58] noted that the duality held at the level of a single gate, allowing for the definition of the full class of Dual Unitary circuits [58]. A full parametrization of Dual Unitary gates is known for qubits [58], although there are known families in arbitrary local dimension [91, 92, 93, 94, 95], a complete classification in arbitrary local dimension is thought to be an exceedingly hard task [94].

A generic dual unitary gate does not have conserved quantities, and as such the only local operator which commutes with time evolution is the identity matrix; the GGE (1.9) is thus just the infinite temperature state. In [96] a special class of solvable initial states was introduced, and it was shown that they thermalize to the infinite temperature state in the shortest possible time for a connected subsystem. In turn, this shows that, for such states, the entanglement velocity

$$v^E = \frac{S(t)}{2t \log(d)}, \quad (1.31)$$

is equal to the largest possible value, 1, in the initial growth phase. In fact the converse also holds true: a quantum circuit with maximal entanglement

growth must be dual unitary [97]. In the work presented in Chapter 2, we extended these results on the entanglement growth rate to a quench from a generic state, choosing noisy dual unitary gates. Noise can be introduced on a dual unitary gate by adding one-site unitaries on each leg:

$$U \rightarrow (u_- \otimes v_-) U (u_+ \otimes v_+) \quad u_{\pm}, v_{\pm} \in U(d^2), \quad (1.32)$$

and then averaging the unitaries with the Haar measure. Among other noteworthy dynamical properties of generic dual unitary evolution, there are correlation functions, which only propagate along the light-cone, and have a generic exponential decay [58], the spectral form factor, which has the same expression of the one obtained for random matrices [98], and the butterfly velocity which is maximal and equal to the speed of light $v^B = 1$ [99].

More exotic quantities have also been investigated, such as quantum state designs [100, 101], quantum scars [102], temporal entanglement (Chapter 3 and [103]) and scrambling [104]; interestingly, Dual Unitary gates have also been implemented with real-world quantum computers [105, 106].

In the work presented in Chapter 5 we showed the general construction of dual unitary gates with commuting, conserved charges, with support on one site, finding notable differences with some of the previous results obtained for chaotic dual unitary gates. In particular, we showed how one can extend the class of solvable states in order to accommodate for the new charge structure, finding in general a slower entanglement growth $v^E < 1$, and, surprisingly, we found, in some cases, a two-step thermalization process for a single, connected, interval.

States now thermalize to a non-trivial GGE ensemble, and correlation functions of local operators do not, in general, decay exponentially, according to the classification presented in [58], showing that even just within the context of Dual Unitary gates, one can have quite different dynamics.

Chapter 2

Growth of entanglement of generic states under dual-unitary dynamics

2.1 Summary



In this work, we consider a quantum quench under dual unitary dynamics from a state which is not solvable. In order to obtain an explicit result, we introduce some noise on the gates, uncorrelated in time and space.

Similar noise for dual unitaries was introduced also in previous works [104] to compute different quantities, although here it was generalized to arbitrary local Hilbert space dimension d .

Interestingly, even though a generic parametrization of dual unitaries in arbitrary dimension is not known, after averaging two replicas of gates (meaning four layers, since a replica contains both the gate and the complex conjugate), the resulting gate has only one free parameter, which is known as the *entangling power* of the gate [93]. We show that in every dimension, for high enough entangling power, the entanglement growth from any pair-product initial state is the maximal one for *almost all* realizations

of the gate. Moreover, we show that there are explicit examples of dual unitary gate with entangling power in the range required for the bound, and we generalized the latter in the case of a quench from an MPS initial state.

As it will be clear from the results in Chapter 5, introducing an average is not only a useful technical trick, but it is necessary to rule out dual unitary gates with conserved charges, for which entanglement growth depends on the initial state.

Growth of entanglement of generic states under dual-unitary dynamicsAlessandro Foligno and Bruno Bertini *School of Physics and Astronomy, University of Nottingham, Nottingham NG7 2RD, United Kingdom
and Centre for the Mathematics and Theoretical Physics of Quantum Non-Equilibrium Systems, University of Nottingham,
Nottingham NG7 2RD, United Kingdom* (Received 12 August 2022; accepted 10 May 2023; published 24 May 2023)

Dual-unitary circuits are a class of locally interacting quantum many-body systems displaying unitary dynamics also when the roles of space and time are exchanged. These systems have recently emerged as a remarkable framework where certain features of many-body quantum chaos can be studied exactly. In particular, they admit a class of “solvable” initial states for which, in the thermodynamic limit, one can access the full nonequilibrium dynamics. This reveals a surprising property: when a dual-unitary circuit is prepared in a solvable state the quantum entanglement between two complementary spatial regions grows at the *maximal* speed allowed by the local structure of the evolution. Here we investigate the fate of this property when the system is prepared in a *generic* pair-product state. We show that in this case, the entanglement increment during a time step is submaximal for finite times, however, it approaches the maximal value in the infinite-time limit. This statement is proven rigorously for dual-unitary circuits generating high enough entanglement, while it is argued to hold for the entire class.

DOI: [10.1103/PhysRevB.107.174311](https://doi.org/10.1103/PhysRevB.107.174311)**I. INTRODUCTION**

The evolution of quantum entanglement gives a universal and unifying characterization of nonequilibrium dynamics in a wide range of quantum many-body systems ranging from lattice models to relativistic field theories [1–4]. Whereas the analysis of specific local observables is clouded by a plethora of system- and observable-specific effects, the evolution of entanglement over large scales does not depend on such inessential details and returns a clear portrait of the full (generalized) thermalization process [5,6]. Whenever a quantum many-body system with local interactions is prepared in an out-of-equilibrium state with low entanglement, and then let to follow its own unitary evolution, the entanglement between different spatial regions is observed to grow in time, signaling the proliferation of quantum correlations. In the course of this process, the entanglement entropy of a given subsystem is transformed into *thermodynamic entropy* and eventually saturates to a time-independent value indicating the onset of relaxation [5,7–10]. Unless specific competing mechanisms are introduced—such as disorder [11–13], confinement [14], or local measurements [15–17]—the entanglement grows linearly in time, irrespective of the nature of the system dynamics [5,6,10,18–33].

The linear growth of entanglement naturally defines a velocity—known as *entanglement velocity* [6,23,31]—which is obtained dividing the slope of the growth by the density

of stationary entropy. The entanglement velocity is the key emergent parameter of the thermalization process: it gives information on when subsystems start approaching stationarity and, at the same time, determines the feasibility of classical simulations of the quantum dynamics [34–37]. While it is clear that the entanglement velocity depends on geometry and couplings of a given system [10,28,38], it is less obvious whether it also depends on the initial configuration. One might expect that the dependence on the initial configuration should be mild, and all configurations leading to the same stationary state are characterized by the same entanglement velocity: some numerical observations supporting this expectation have been presented in Ref. [25]. On the other hand, the entanglement velocity describes a truly out-of-equilibrium regime taking place prior to relaxation and when a full scrambling of quantum information has yet to take place. For free systems, for instance, initial configurations leading to the same stationary state can have different entanglement velocities [19]. The same is expected for interacting integrable systems, where a formula for the entanglement velocity [10,38] is only known for a special class of initial states [39,40]. These examples show that, at least for integrable models, the entanglement velocity contains more information than the stationary state and the intuitive expectation discussed above fails. For quantum chaotic systems, however, the question is still open.

Here we analyze this question in the context of chaotic “local quantum circuits,” i.e., chains of qudits evolved by discrete applications of local unitary operators. These systems are useful idealizations of generic quantum matter and, over the last few years, have helped understanding information spreading [6,25,28,31,41–44], spectral statistics [45,45–55], and thermalization [26,32,51,56] in quantum many-body systems. Specifically, here we consider a particular class of local

Published by the American Physical Society under the terms of the Creative Commons Attribution 4.0 International license. Further distribution of this work must maintain attribution to the author(s) and the published article’s title, journal citation, and DOI.

quantum circuits known as “dual unitary circuits” [57], which are defined by the property that their bulk dynamics remain unitary also when exchanging the roles of space and time. The most remarkable feature of these systems is that, despite being quantum chaotic, they allow for exact calculations of many relevant many-body quantities [27,50,58–69]. Surprisingly, even the very quantum chaotic nature of dual-unitary circuits can be rigorously proven [45,49].

Dual-unitary circuits admit a class of “solvable” initial states [25,26], whose dynamics can be characterized exactly in the thermodynamic limit [25,26,65,70]. When evolving from solvable states dual-unitary circuits display *maximal* entanglement growth, namely they show the largest entanglement growth compatible with the local structure of the time-evolution [25,26]. In fact, it has been recently shown in Ref. [71] that such a maximal growth is only attainable in dual-unitary circuits. For generic initial states, however, dual-unitarity does not provide any obvious simplification and exact calculations fall out of reach. In addition, many of the special features of the dynamics of solvable states, including the maximal growth of entanglement, are observed to disappear in finite-time numerical experiments [25,26,65].

Here we show that, remarkably, some exact statements can be made also for generic initial states. In particular, we consider the entanglement evolution from “generic pair-product states,” i.e., nonsolvable states written as products of arbitrary two-site states, and show that the entanglement velocity is *maximal* for *almost all* dual-unitary circuits. Therefore it is *almost always* independent of the initial configuration.

To find these results, we introduce space-time-dependent noise that preserves dual-unitarity and show that the entanglement velocity averaged over the noise approaches the maximal value for large times. We then prove that this implies asymptotic maximality of the entanglement velocity for each realization. Our statements are established rigorously for circuits made of dual-unitary gates with high enough “entangling power,” which measures how much a gate can entangle two qubits. These include dual-unitary gates constructed with complex Hadamard matrices [72] and four-leg perfect tensors [73,74]. We also present a constructive way—supported by numerical checks—to extend them.

The rest of this paper is laid out as follows. In Sec. II, we introduce the systems and initial states considered in this work. In Sec. III, we introduce the entanglement velocity, which is the quantity of interest, and review its calculation for dual-unitary circuits evolving from solvable states. Section IV contains our main results: we begin by introducing the space-time dependent noise and show how maximality on average implies maximality for each single realization. In Sec. IV A, we bound from below the averaged entanglement entropy with a function depending on the gates solely through their entangling power. Then, in Sec. IV B, we prove maximality on average for circuits made of gates with large enough entangling power, while in Sec. IV C, we argue that the proof can be extended to all dual-unitary circuits, and in Sec. IV D, we present some supporting numerical evidence. Finally, in Sec. IV E, we show that our result is robust if one considers more general low-entangled initial states. Our conclusions and final remarks are reported in Sec. V. The four Appendixes contain a number of complementary technical points.

II. SETTING

A one-dimensional local quantum circuit is a chain of $2L$ qudits—with d internal states—where the evolution occurs in discrete time steps and describes local interactions. In particular, considering circuits where the time evolution is implemented in the so called “brickwork” geometry, we write the unitary operator evolving the system from time t to time $t + 1$ as

$$\mathbb{U}(t) = \mathbb{U}_2(t) \cdot \mathbb{U}_1(t), \quad (1)$$

where we introduced

$$\mathbb{U}_1(t) = \bigotimes_{x \in \mathbb{Z}_L} U_{x,t}, \quad \mathbb{U}_2(t) = \bigotimes_{x \in \mathbb{Z}_L + \frac{1}{2}} U_{x,t+1/2}. \quad (2)$$

The operator $U_{x,t}$ acts nontrivially, as the $d^2 \times d^2$ unitary matrix $U(x, t)$, only on the qudits at positions x and $x + 1/2$. The matrices $\{U(x, t)\}$ are known as “local gates” and encode the physical properties of the system. In particular, whenever

$$U(x, t) = U, \quad \forall x, t, \quad (3)$$

the evolution operator is invariant under two-site shifts in time and space. We will refer to this case as a space-time translational invariant quantum circuit.

Note that in Eq. (2), we labeled sites by half integers and assumed periodic boundary conditions so that the (half-odd) integers x and $x + L$ denote the same site. We also remark that the form (1) of the time-evolution operator implies that there is a strict maximal speed for the propagation of correlations. This means that any pair of local operators a_x and b_y evolved up to time t satisfy

$$[a_x(t), b_y(t)] = 0, \quad |[x] - [y]| > 2v_{\max}t, \quad (4)$$

where $[\bullet]$ denotes the ceiling function (smallest integer larger or equal to the argument). Moreover, our choice of units implies a maximal speed $v_{\max} = 1$.

We consider a particular class of local quantum circuits called dual-unitary circuits [57]. Their defining property is that they are generated by local gates that remain unitary under a particular reshuffling which corresponds to switching space and time. More precisely, defining a matrix \tilde{U} with elements

$$\tilde{U}_{(j,l);(i,k)} = U_{(i,j);(k,l)}, \quad i, j, k, l = 0, \dots, d - 1, \quad (5)$$

where we set $(i, j) = i * d + j$, we require

$$U^\dagger U = U U^\dagger = I, \quad \tilde{U}^\dagger \tilde{U} = \tilde{U} \tilde{U}^\dagger = I. \quad (6)$$

Whilst the first condition is the standard unitarity requirement for the local gate, the second one is imposing that the gate acts as a unitary matrix also when the roles of space and time are swapped. These constraints admit solution for all local Hilbert space dimensions $d \geq 2$, however, a full parametrization is only known for $d = 2$ [49,57,62,72,75,76]. It is also useful to recall that, even though some of the solutions to (6) are integrable [59,62,76,77], i.e., generate evolution operators with an extensive number of local conserved charges, the integrable instances can only form a lower dimensional sub-manifold of the total manifold of dual-unitary circuits. This can be intuitively understood by noting that the two equations (6) are

left invariant by the transformation

$$U \mapsto u_+ \otimes u_- \cdot U \cdot v_+ \otimes v_-, \tag{7}$$

with u_+, \dots, v_- arbitrary elements of the group of $d \times d$ unitary matrices, which we denote by $U(d)$. This transformation is generally enough to break any nontrivial conservation law. In other words, dual unitary circuits are *generally* nonintegrable or quantum chaotic.

A. Entangling power

A feature of the local gate U which will prove to be important in the following is its *entangling power*. The latter is a measure of the average entanglement produced by U when acting on Haar-random product states, see, e.g., Ref. [78]. In particular, as shown in Refs. [78–80], for dual-unitary circuits it can be expressed as

$$p = \frac{d^4 - \text{tr}[(\tilde{U}^{t_2}(\tilde{U}^{t_2})^\dagger)^2]}{d^2(d^2 - 1)}, \tag{8}$$

where $(\cdot)^{\dagger_2}$ denotes the partial transpose with respect to the second qudit. From (8), one can immediately verify that p is invariant under (7).

As we recall in Appendix A, the entangling power (8) fulfils

$$0 \leq p \leq 1. \tag{9}$$

The lower bound is attained when $\tilde{U}^{t_2}(\tilde{U}^{t_2})^\dagger/d^2$ is a rank-1 projector. This happens when, up to the transformation (7), U coincides with the SWAP gate. Namely, it merely swaps the states of the two qudits it acts on, generating no entanglement. Instead, the upper bound is attained for

$$\tilde{U}^{t_2}(\tilde{U}^{t_2})^\dagger = (\tilde{U}^{t_2})^\dagger \tilde{U}^{t_2} = I. \tag{10}$$

To understand this condition it is useful to think of U a state of four qudits with amplitudes $\{U_{(a_1, a_2); (a_3, a_4)}\}$. In this language, Eq. (10) means that the subset formed by the first and fourth qudits is maximally entangled with its complement. Recalling that the gate U also fulfils (6), we see that also the subsets formed by first and second and first and third qubits are maximally entangled with their complements. In fact, in the state defined by U any bipartition of the four qudits has maximal entanglement with its complement. Gates generating states with this property are called *perfect tensors* [81] or 2-unitary gates [82]. Perfect tensors with four entries exist for every local Hilbert space dimension strictly larger than $d = 2$ [73,74] and, therefore, for $d > 2$, the upper bound $p = 1$ can be attained. Instead, for $d = 2$ the maximal value that p can attain is [57]

$$p = \frac{d}{d + 1}, \tag{11}$$

and, up to (7), it is attained by local gates of the form

$$U_{(i,j),(k,l)} = \delta_{il} \delta_{jk} \exp\left(i \frac{2\pi ij}{d}\right). \tag{12}$$

The family (12) of dual-unitary gates has been constructed in Ref. [72] using complex Hadamard matrices. Here, for brevity, we call it the ‘‘Hadamard family.’’

B. Quantum quench

To study the out-of-equilibrium dynamics of the circuits we consider a standard quantum quench protocol: we prepare them in a nonequilibrium state $|\Psi_0\rangle$ and let them evolve according to their time-evolution operator. In particular, we consider generic ‘‘pair-product’’ states of the form

$$|\Psi_0\rangle = \frac{1}{d^{L/2}} \bigotimes_{x=1}^L \left(\sum_{i,j=0}^{d-1} m_{i,j} |i, j\rangle \right), \tag{13}$$

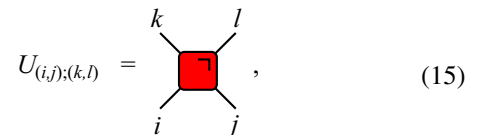
where $\{|i\rangle\}_{i=0}^d$ is a basis of the local Hilbert space and matrix m , with elements $m_{i,j}$, fulfils

$$\text{tr}(mm^\dagger) = d, \tag{14}$$

which ensures that $|\Psi_0\rangle$ is normalized to one. Apart from this condition, the matrix m is *completely generic*.

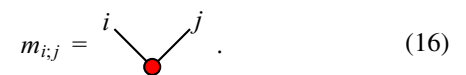
Although the family (13) does not represent the most general low-entangled state, it contains many physically relevant points—in particular it contains all translational invariant product states—and it is complex enough to show generic behavior. In most of the paper, we focus on this family to reduce to a minimum the technical complications, while in Sec. IV E, we show that our techniques can be applied to more general families of matrix product states leading to qualitatively similar results.

The evolution quantum circuits can be conveniently represented graphically. One depicts the local gates as a four-leg tensors



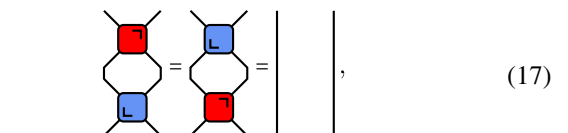
$$U_{(i,j),(k,l)} = \text{red square with legs } i, j, k, l, \tag{15}$$

and the initial state matrix m as a two-leg one

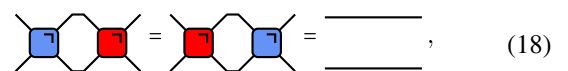


$$m_{i,j} = \text{red dot with legs } i, j. \tag{16}$$

When it does not lead to confusion the indices can be dropped to represent the actual tensor instead of its elements. For instance, (6) are conveniently represented as



$$\text{red square} = \text{blue square} = \text{vertical line}, \tag{17}$$



$$\text{blue square} = \text{red square} = \text{horizontal line}, \tag{18}$$

where we introduced the diagram



$$U^\dagger = \text{blue square with legs } i, j, k, l. \tag{19}$$

Instead, the state at time t is depicted as

$$U^t |\Psi_0\rangle = \text{[Diagram of a brickwork lattice with red nodes and dashed lines]} \quad (20)$$

where we took $L = 4$ and $t = 2$, we represented the matrix multiplication from bottom to top and we conveniently depicted the space-time translational invariant case with periodic boundary conditions. The representation in Eq. (20) makes it clear why this particular way of applying local gates is called brickwork geometry.

III. ENTANGLEMENT GROWTH

In this paper, we are interested in the evolution of the entanglement between a contiguous block of $2L_A$ qudits, $A = \{x_1, x_1 + 1/2, \dots, x_2\}$, and its complement, $\bar{A} = \{1/2, \dots, L\} \setminus A$, in the state (20). In particular, we will focus on the regime where the entanglement typically grows linearly

in time [5,6,10,18–33], i.e.,

$$2v_{\max}t \leq L_A \leq L - L_A. \quad (21)$$

Since we are considering systems with local interactions, the entanglement between A and \bar{A} is produced starting from the boundaries between the two sub-systems. In the regime of interest, the two boundaries between A and \bar{A} are causally disconnected and give identical contributions.

To quantify the entanglement of the bipartition we compute the reduced density matrix

$$\rho_A(t) = \text{tr}_{\bar{A}}[U^t |\Psi_0\rangle\langle\Psi_0| U^{-t}] \quad (22)$$

and evaluate its Rényi entropies

$$S_A^{(\alpha)}(t) = \frac{1}{1-\alpha} \ln \text{tr}[\rho_A(t)^\alpha], \quad \alpha \in \mathbb{R}. \quad (23)$$

Note that $S_A^{(\alpha)}(t)$ is nonincreasing in α

$$S_A^{(\alpha)}(t) \leq S_A^{(\beta)}(t), \quad \alpha \geq \beta, \quad (24)$$

and its limiting value for $\alpha \rightarrow 1$ corresponds to the celebrated *entanglement entropy*

$$\lim_{\alpha \rightarrow 1} S_A^{(\alpha)}(t) = -\text{tr}[\rho_A(t) \ln \rho_A(t)] \equiv S_A(t), \quad (25)$$

which is a bona fide measure of bipartite entanglement [1].

To analyze Rényi entropies in the regime (21) we note that the reduced density matrix can be represented as

$$\rho_A(t) = \frac{1}{d^{2t+L_A}} \text{[Diagram of a brickwork lattice with blue and red nodes and lines]} \quad (26)$$

where we used the two-site product form of the initial state (13), the normalization (14), the unitarity of the gates U , and we introduced the diagram

$$m^\dagger = \text{[Diagram of a blue node with two lines]} \quad (27)$$

Using the representation (26) and employing the unitarity relations (17) one can readily show that if

$$2t < |[x_2] - [x_1]|, \quad (28)$$

the traces of powers of the reduced density matrix $\rho_A(t)$ factorize as follows:

$$\text{Tr}[\rho_A(t)^\alpha] = \text{Tr}[(C_{2x_2}^\dagger C_{2x_2})^\alpha] \text{Tr}[(C_{2x_1}^\dagger C_{2x_1})^\alpha]. \quad (29)$$

Here $t_{x_i} = t - \{x_i\}$ ($\{\bullet\} \equiv [\bullet] - \bullet$ is the fractional part) and C_x is a $d^{x_2} \times d^{x_1}$ matrix corresponding to the following diagram

$$[C_x]_{a;b} = \frac{1}{d^{\frac{x}{2}}} \text{[Diagram of a brickwork lattice with red nodes and labels a_x, b_x, a_1, b_1]} \quad (30)$$

where q_j denotes the j th digit of q in base d . Thanks to the unitarity of the local gates, we have the condition

$$\text{Tr}[C_x C_x^\dagger] = 1, \quad \forall x. \quad (31)$$

To simplify the notation, from now on, we assume x_1, x_2 to be integers. Plugging (29) into (23), we can express the Rényi entropies as

$$S_A^{(\alpha)}(t) = \frac{2}{1-\alpha} \ln \text{Tr}[(C_{2t}^\dagger C_{2t})^\alpha], \quad (32)$$

where the factor of 2 occurs because the two independent boundaries between A and \bar{A} give the same contribution.

Since $C_x C_x^\dagger$ is Hermitian, positive definite, and fulfils (31), it is easy to find a bound for the powers of its trace. To see this, we diagonalize the matrix and express the above conditions in terms of its eigenvalues λ_i as follows:

$$\lambda_i \geq 0, \quad \sum_{i=1}^{\mathcal{N}} \lambda_i = 1, \quad (33)$$

where $\mathcal{N} = d^x$ is the dimension of the vector space on which the matrix acts. The constraints (33) on generic real numbers lead to the following bound:

$$\frac{1}{\mathcal{N}^{\alpha-1}} \leq \text{Tr}[(C_x^\dagger C_x)^\alpha] = \sum_i \lambda_i^\alpha \leq 1, \quad \forall \alpha \geq 1. \quad (34)$$

Using this in (32), we find

$$0 \leq S_A^{(\alpha)}(t) \leq 4t \ln d, \quad \forall \alpha \geq 1. \quad (35)$$

The lower bound is reached when $C_x^\dagger C_x$ is a projector on a one-dimensional space, while the upper bound is attained when it is maximally mixed, i.e.,

$$C_x C_x^\dagger = \frac{\mathbb{1}_x}{d^x}, \quad (36)$$

where $\mathbb{1}_x$ is the identity matrix on x qudits.

We are now in a position to introduce the quantity of interest in this paper, i.e., the *entanglement velocity*, which quantifies the asymptotic growth of entanglement in the out-of-equilibrium regime (21). In our setting, this quantity is defined as the ratio between half of the asymptotic slope of the entanglement entropy and the density of entropy of the stationary state—the additional factor of two is included to isolate the entanglement growth from a single boundary between A and \bar{A} . More formally, for a circuit without local conservation laws, we have

$$v_E \equiv \limsup_{t \rightarrow \infty} \lim_{L_A \rightarrow \infty} \lim_{L \rightarrow \infty} \frac{S_A(t)}{4t \ln d}. \quad (37)$$

Note that in (37), we used that the circuit has no local conservation laws to find the density of its thermodynamic entropy ($2 \ln d$) and we introduced the limit superior rather than the regular limit to make sure that v_E always exists. Analogously, we can introduce entanglement velocities for all Rényi entropies

$$v_{E,\alpha} \equiv \limsup_{t \rightarrow \infty} \lim_{L_A \rightarrow \infty} \lim_{L \rightarrow \infty} \frac{S_A^{(\alpha)}(t)}{4t \ln d}, \quad v_{E,1} = v_E. \quad (38)$$

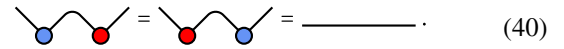
Using (24) and (35) we find the following general bound

$$0 \leq v_{E,\beta} \leq v_{E,\alpha} \leq 1, \quad \beta \geq \alpha. \quad (39)$$

Note that, up to now, we did not use the dual-unitarity of the gates at any point in the reasoning and, in fact, our discussion applies to any chaotic local quantum circuit. This is because

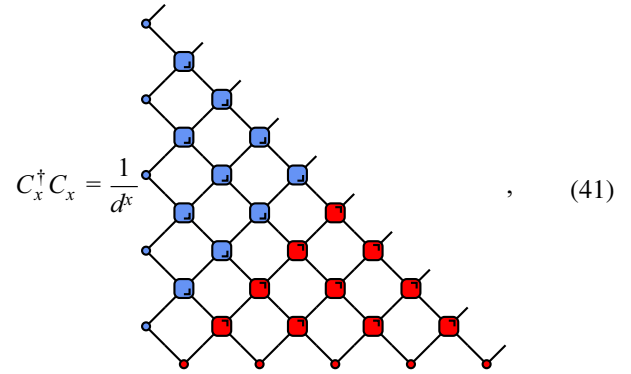
generic matrices m “break” the special dual-unitarity property of the local gates, preventing any direct simplification. On the other hand, as we shall now see, for a special class of compatible matrices, dual-unitarity immediately leads to an explicit expression for $S_A^{(\alpha)}(t)$.

Let us consider a subclass of pair-product states (13) characterized by *unitary* matrices m , i.e., matrices fulfilling the diagrammatic relations



$$\text{---} \text{---} \text{---} = \text{---} \text{---} \text{---} = \text{---}. \quad (40)$$

Repeatedly applying (40) and (18), we can fully contract the tensor network



$$C_x^\dagger C_x = \frac{1}{d^x}, \quad (41)$$

and find

$$C_x^\dagger C_x = \frac{\mathbb{1}_x}{d^x}. \quad (42)$$

Pair-product initial states with this property are part of a larger family of exactly treatable states, generically in MPS form, called *solvable states* [26].

We see that, for solvable pair product states, $C_x^\dagger C_x$ takes the maximally mixed form (36), therefore the entropies saturate the bound (35), i.e.,

$$S_A^{(\alpha)}(t) = 4t \ln d, \quad \forall \alpha, \quad (43)$$

or, equivalently, all entropies have the *maximal* increment over a time step

$$\Delta S_A^{(\alpha)}(t) \equiv \frac{S_A^{(\alpha)}(t) - S_A^{(\alpha)}(t-1)}{4 \ln d} = 1, \quad \forall \alpha. \quad (44)$$

This condition characterizes all solvable states for large enough subsystems [26]. A particular consequence of this is also

$$v_E = 1. \quad (45)$$

The goal of this paper is to show that, even if hidden, an effect of dual-unitarity is also present for generic initial states. As a consequence, even if (44) does not hold at finite times, the entanglement velocity *remains maximal*.

IV. ENTANGLEMENT VELOCITY FROM GENERIC PAIR-PRODUCT STATES

Our strategy to treat generic initial states is to introduce space-time-dependent noise and to show that our statements hold for arbitrary distributions of the noise. More specifically, we consider a space-time translational invariant, dual-unitary circuit characterized by a local gate U , and insert uncorrelated Haar-distributed $U(d)$ noise at each space-time point

through the transformation (7). Note that the family of random dual-unitary gates produced in this way is the direct generalization for generic d of the family introduced in the case $d = 2$ [83].

In this random setting, it is natural to consider the averaged Rényi entropies

$$\bar{S}_A^{(\alpha)}(t) = \frac{1}{1-\alpha} \mathbb{E}[\ln \text{tr}(\rho_A(t)^\alpha)], \quad (46)$$

where $\mathbb{E}[\cdot]$ is the average over the set of unitaries

$$\mathbf{u} \equiv \{u(\tau, x)\}_{\tau=1/2, 1, \dots, t; x=1/2, 1, \dots, L} \in U^{4Lt}(d), \quad (47)$$

and $U^x(d)$ denotes the direct product of x copies of $U(d)$.

Analogously, we define the averaged entanglement velocities as

$$\bar{v}_{E,\alpha} \equiv \limsup_{t \rightarrow \infty} \lim_{L_A \rightarrow \infty} \lim_{L \rightarrow \infty} \frac{\bar{S}_A^{(\alpha)}(t)}{4t \ln d}, \quad \bar{v}_E = \bar{v}_{E,1}. \quad (48)$$

With these definitions at hand, we are now in a position to state our main objective. Our goal is to prove the following property.

Property 1. For all states of the form (13)

$$\bar{v}_E = 1. \quad (49)$$

Before approaching the proof, let us analyze its implications. Recalling the bound in Eq. (39) we see that this property implies that the average entanglement velocity is maximal for any initial state (13). Since we find our bound saturated on average, we intuitively expect the entanglement velocity to be maximal for almost every choice of the unitaries \mathbf{u} , i.e., in the nonrandom case. To make this statement more precise, consider the function f whose limit superior for $t \rightarrow \infty$ is the entanglement velocity

$$f(t, \{u_\pm(t, x)\}, \{v_\pm(t, x)\}) \equiv \lim_{L_A \rightarrow \infty} \lim_{L \rightarrow \infty} \frac{S_A(t)}{4t \ln(d)}. \quad (50)$$

Note that, for any choice of the gates, we have

$$f(t, \{u_\pm(t, x)\}, \{v_\pm(t, x)\}) \in [0, 1]. \quad (51)$$

Here we make this function depend on an semi-infinite square grid of gates, labeled by (x, t) , with $t = 1, 2, \dots, \infty$ and $x = -\infty, \dots, \infty$ (at finite times t it actually depends only on a finite subset of such gates). This function is measurable for any t because it is continuous [84]: its associated measure Ω is the product of the Haar measures, we call them Ω_{loc} , of each unitary $u(t, x)$. Importantly, the measure Ω is fixed and does not depend on t because it is a countable product of Haar measures on the semi-infinite square grid described above. Since f is positive and measurable for any t , we can apply Fatou's lemma [84] and exchange the order between limsup and integral

$$\int d\Omega v_E = \int d\Omega \limsup_{t \rightarrow \infty} f \geq \limsup_{t \rightarrow \infty} \int d\Omega f = \bar{v}_E = 1, \quad (52)$$

where, in the last equality, we used property 1. Using the bound (51), we then find

$$\int d\Omega v_E = 1. \quad (53)$$

Since this saturates the bound on the velocity, it is implied that, for almost all choices of gates, the entanglement velocity is 1, i.e.,

$$\bar{v}_E = 1 \Rightarrow v_E \approx 1. \quad (54)$$

Here the symbol \approx indicates that the equality holds for *almost all* choices of gates.

Importantly, the statement (53) has strong implications also for the nonrandom case. Indeed, for any given nonrandom distribution of the one-site gates \mathbf{u} —for instance, one that is uniform in space and time—one can consider adding an arbitrary small distribution of “noise.” Namely, one modifies the one-site gates as

$$u^{(\epsilon)}(\tau, x) := u(\tau, x) \cdot w^{(\epsilon)}(\tau, x), \quad (55)$$

where, for each (τ, x) , $w^{(\epsilon)}(\tau, x)$ is a unitary matrix extracted at random from an ϵ -ball centered on the identity matrix. We emphasize that this ball is taken to have unit measure. For instance, one can take $w^{(\epsilon)}(\tau, x)$ distributed according to a Gaussian measure

$$d\Omega_{\text{loc}} \mapsto d\Omega_{\text{loc}}^{(\epsilon)} = \prod_{a=1}^{d^2-1} \frac{1}{\sqrt{2\pi}\epsilon} \exp\left(-\frac{1}{2} \frac{\theta_a^2}{\epsilon^2}\right) d\theta, \quad (56)$$

or a box measure

$$d\Omega_{\text{loc}} \mapsto d\Omega_{\text{loc}}^{(\epsilon)} = \prod_{a=1}^{d^2-1} \frac{1}{2\epsilon} \Theta(\epsilon - |\theta_a|) d\theta, \quad (57)$$

where $\theta = \{\theta_a\}_{a=1}^{d^2-1}$ are the Euler angles specifying $w^{(\epsilon)}(\tau, x)$.

The choice (55) implies that, by choosing small enough ϵ , one can make $u^{(\epsilon)}(\tau, x)$ arbitrarily close to $u(\tau, x)$. Then, Eq. (53) guarantees that for every $\epsilon > 0$ the entanglement velocity averaged over $u^{(\epsilon)}(\tau, x)$ is maximal, i.e., *it is maximal when we get arbitrarily close to the nonrandom case.*

In the upcoming subsections we prove property 1. In Sec. IV A, we show that $\bar{S}_A(t)$ can be bounded from below in terms of a function depending on the gates only through the entangling power of U . In Sec. IV B, we show that for

$$p \geq \bar{p}(d) \equiv \frac{d^2-1}{d^2} \left(1 - \frac{1}{\sqrt{2d+2}}\right), \quad (58)$$

this bound leads to a rigorous proof of property 1. In particular, recalling Sec. II A and noting that

$$\bar{p}(d) < \frac{d}{d+1} < 1, \quad (59)$$

we prove that property 1 holds for perfect tensors and for the Hadamard family (cf. Eq. (12)) while in Sec. IV C, we argue that property 1 can be extended to all p except for a neighborhood of $p = 0$. Instead, in Sec. IV D, we present numerical evidence supporting the claim that v_E is one for concrete individual realizations of the noise. Finally, in Sec. IV E, we show that similar statements can be made for a more general class of initial states in MPS form.

A. Bound on $\bar{S}_A(t)$

We aim to bound $\bar{S}_A(t)$ in the regime (21) by a function depending on the local gates only through p . We begin by

using (24) and (35) which give

$$\bar{S}_A^{(2)}(t) \leq \bar{S}_A(t) \leq 4t \ln d. \quad (60)$$

Noting now that the function

$$f(x) = -2 \ln x \quad (61)$$

is convex, we have

$$-2 \ln \mathcal{P}_{2t} \leq \bar{S}_A^{(2)}(t), \quad (62)$$

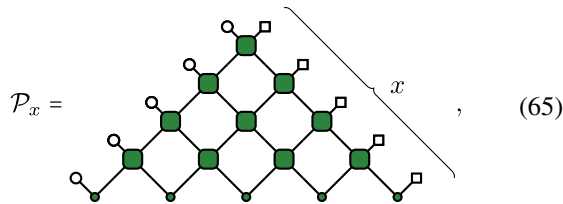
where we introduced the averaged purity for the matrix $C_x^\dagger C_x$

$$\mathcal{P}_x \equiv \mathbb{E}[\text{Tr}[(C_x^\dagger C_x)^2]]. \quad (63)$$

Putting all together, we have

$$-2 \ln \mathcal{P}_{2t} \leq \bar{S}_A(t) \leq 4t \ln d. \quad (64)$$

To conclude, we show that \mathcal{P}_x depends on the local gates only through their entangling power. To this end, we note that, since \mathbf{u} are independently distributed at each space-time point, the average $\mathbb{E}[\cdot]$ factorizes on each separate gate. This allows us to adopt a convenient tensor-network representation for \mathcal{P}_x , which is obtained by folding the four diagrams for $C_x, C_x^\dagger, C_x,$ and C_x^\dagger on top of each other and averaging (see Ref. [83] for a more detailed explanation of this ‘‘folded’’ diagrammatic representation)



where we introduced the vectors

$$\begin{aligned} |\circ\rangle &\equiv \frac{1}{d} \sum_{i,j,k,l} \delta_{ij} \delta_{kl} |ijkl\rangle, \\ |\square\rangle &\equiv \frac{1}{d} \sum_{i,j,k,l} \delta_{il} \delta_{jk} |ijkl\rangle, \end{aligned} \quad (66)$$

and the averaged gate

$$W = \text{[diagram]} = (P \otimes P) (U \otimes_r U^*)^{\otimes_r 2} (P \otimes P). \quad (67)$$

Here \otimes_r denotes the tensor product over replicas rather than spatial sites, and the operator

$$P = \mathbb{E}[(v \otimes_r v^*)^{\otimes_r 2}] \quad v \in U(d), \quad (68)$$

is a projector on a two-dimensional space spanned by the vectors (66) (see, e.g., Appendix G of Ref. [41] for an elementary proof). Note that these states are linearly independent but not orthogonal, indeed

$$\langle \square | \circ \rangle = \frac{1}{d}. \quad (69)$$

Since P is a projector, we used

$$P^2 = P, \quad (70)$$

to apply it also on the initial state matrix. Namely, we defined the averaged initial state matrix as

$$n = \text{[diagram]} = P(m \otimes_r m^*)^{\otimes_r 2} P. \quad (71)$$

The above discussion implies that all wires in (65) carry a two-dimensional vector space spanned by $|\circ\rangle$ and $|\square\rangle$. Almost all matrix elements of W and n in this basis are fixed solely by dual unitarity (6) and the normalization condition (14) and are hence independent of the specific U and m . The only exceptions are

$$\text{[diagram]} = 1 - p + \frac{p}{d^2}, \quad \text{[diagram]} \equiv \frac{c}{d}, \quad (72)$$

where the second equation defines the parameter c , which characterizes the averaged initial state matrix. In Appendix B, we show that c takes values in $[1, d]$ and it is equal to one only when the initial state is solvable.

Considering, for instance, the orthonormal bases

$$\{|\circ, \circ\rangle, |\circ, \bullet\rangle, |\bullet, \circ\rangle, |\bullet, \bullet\rangle\}, \quad \{|\circ\rangle, |\bullet\rangle\}, \quad (73)$$

where we introduced the state

$$|\bullet\rangle = \frac{d|\square\rangle - |\circ\rangle}{\sqrt{d^2 - 1}}, \quad (74)$$

we explicitly find

$$W = \begin{bmatrix} 1 & 0 & 0 & 0 \\ 0 & 0 & 1 - p & \frac{p}{\sqrt{d^2 - 1}} \\ 0 & 1 - p & 0 & \frac{p}{\sqrt{d^2 - 1}} \\ 0 & \frac{p}{\sqrt{d^2 - 1}} & \frac{p}{\sqrt{d^2 - 1}} & 1 - \frac{2p}{d^2 - 1} \end{bmatrix} \quad (75)$$

and

$$n = \begin{bmatrix} 1 & \frac{c-1}{\sqrt{d^2-1}} \\ \frac{c-1}{\sqrt{d^2-1}} & 1 - \frac{2(c-1)}{d^2-1} \end{bmatrix}. \quad (76)$$

Since W bares dependence on the gate only through p , the same holds for \mathcal{P}_x . We also stress that, since the averaged gate is symmetric and parity-invariant, we did not include a mark in its graphical representation.

B. Rigorous proof of property 1 for $p \geq \bar{p}(d)$

In this section, we make use of the bound (64) to prove property 1 for $p > \bar{p}(d)$ (cf. (58)). To this end, we introduce the following lemma.

Lemma 1. For $p \geq \bar{p}(d)$ and any state (13), there exist $A, B \geq 0$ such that

$$d^x \mathcal{P}_x \leq A + Bx. \quad (77)$$

The choice $B = 0$ can only be made for initial solvable states satisfying (40).

Equations (77) and (64) imply

$$1 - \frac{\ln(A + 2Bt)}{2t \ln d} \leq \frac{\bar{S}_A(t)}{4t \ln d} \leq 1. \quad (78)$$

Taking the infinite-time limit and using the bound (39), we obtain

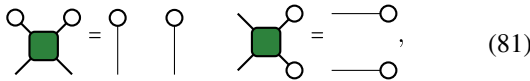
$$v_E = 1, \tag{79}$$

which proves property 1. Note that using lemma 1 one can also prove

$$v_{E,\alpha} = 1, \quad \alpha \leq 2, \tag{80}$$

by combining (62), (24), and (35).

To prove lemma 1, we derive a simple recursive relation for \mathcal{P}_x . We begin by noting that the dual-unitarity conditions (6) imply



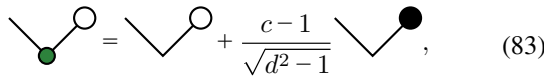
$$\tag{81}$$

and

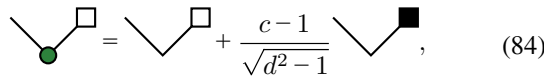


$$\tag{82}$$

Moreover, we have



$$\tag{83}$$



$$\tag{84}$$

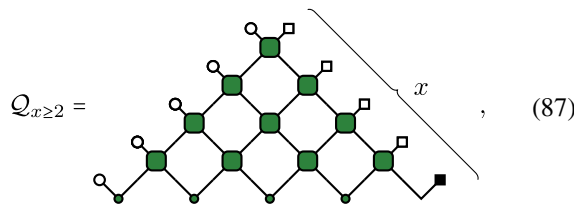
where we introduced

$$|\blacksquare\rangle = \frac{d|\circ\rangle - |\square\rangle}{\sqrt{d^2-1}}. \tag{85}$$

We now have all the fundamental ingredients for deriving the desired recursive relations. Using (84) in the bottom right corner of (65), telescoping (82), and using (69), we find

$$\mathcal{P}_x = \frac{1}{d}\mathcal{P}_{x-1} + \frac{c-1}{\sqrt{d^2-1}}\mathcal{Q}_x, \tag{86}$$

where we introduced

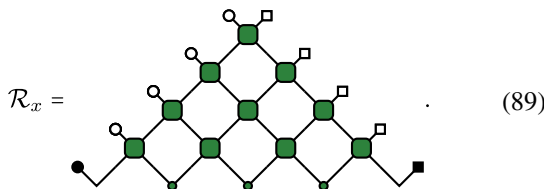


$$\tag{87}$$

and $\mathcal{Q}_1 = \langle \circ | \blacksquare \rangle = \sqrt{d^2-1}/d$. Applying now (83) to the bottom left corner of (87) and then telescoping (81), we have

$$\mathcal{Q}_x = \frac{1}{d}\mathcal{Q}_{x-1} + \frac{c-1}{\sqrt{d^2-1}}\mathcal{R}_x, \tag{88}$$

where



$$\tag{89}$$

To close the recursive system formed by (86) and (88), we now seek a bound for \mathcal{R}_x . In particular, a bound of the form

$$|\mathcal{R}_x| \leq \frac{C}{D^x}, \tag{90}$$

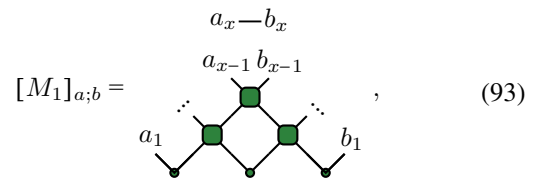
for some $C > 0$ and $D > d$, leads to

$$\mathcal{Q}_x \leq \frac{\alpha}{d^x} + \frac{\beta}{D^x}, \tag{91}$$

$$\mathcal{P}_x \leq \frac{\gamma}{d^x} + \frac{(c-1)\alpha}{\sqrt{d^2-1}} \frac{x}{d^x} + \frac{\delta}{D^x}, \quad \alpha, \beta, \gamma, \delta \in \mathbb{R}, \tag{92}$$

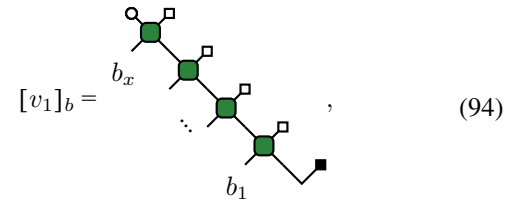
which immediately imply (77).

To find the bound in Eq. (90), we view \mathcal{R}_x as the matrix element of



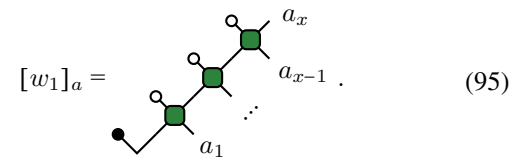
$$\tag{93}$$

between the vectors



$$\tag{94}$$

and

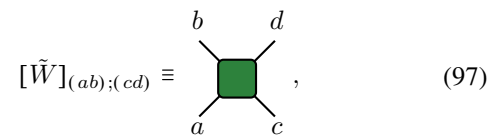


$$\tag{95}$$

Employing the Cauchy-Schwartz inequality, we then obtain

$$|\mathcal{R}_x| = |\langle v_1 | M_1 | w_1 \rangle| \leq \|M_1\|_\infty \sqrt{\langle v_1 | v_1 \rangle} \sqrt{\langle w_1 | w_1 \rangle}. \tag{96}$$

Let us now consider separately the three factors on the right-hand side. Since the gates are the average of dual-unitary gates, the operator norm of the dual averaged gate \tilde{W} , with elements



$$\tag{97}$$

is one. Therefore we have nontrivial contributions to the norm of M_1 only from the initial state row. This gives

$$\|M_1\|_\infty \leq \|n\|_\infty^{x-2} = \left(\frac{d+c}{d+1}\right)^{x-2}, \tag{98}$$

where the identity

$$\|n\|_\infty = \frac{d+c}{d+1}, \tag{99}$$

is proven in Appendix B.

Equation (98) is the *key simplification* provided by dual-unitarity in the current setting. Even though the bottom boundary of the tensor network (93) is “generic,” the dual-unitarity of the bulk tensors implies that its operator norm is bounded by a number that scales with the number of tensors on its edge. This should be contrasted with the non-dual-unitary case, where the dual gate \tilde{W} has operator norm greater than one [85], and, therefore, the operator norm of M_1 scales with the total number of tensors composing it. In summary, because of dual-unitarity, Eq. (98) shows an “area scaling” rather than a “volume scaling.” As we now see, for large enough entangling power p such an area scaling can be counter-balanced by the other two terms in (96), leading to the bound (90).

To treat the second factor in (96), we introduce the matrix

$$T_2 = \square \text{---} \diamond \text{---} \diamond \text{---} \square, \tag{100}$$

so that we can write

$$\langle v_1 | v_1 \rangle = \left(\begin{array}{c} \square \text{---} \diamond \text{---} \square \\ \square \text{---} \diamond \text{---} \square \\ \square \text{---} \diamond \text{---} \square \\ \square \text{---} \diamond \text{---} \square \end{array} \right)_{x-1} = \langle \text{O} \text{O} | T_2^{x-1} | \blacksquare \blacksquare \rangle, \tag{101}$$

where we used the fact that the averaged gate is real. As shown in Appendix D, the vector $|\blacksquare \blacksquare\rangle$ is an eigenvector of T_2 with eigenvalue

$$\lambda(p) = (1 - p)^2 + \frac{p^2}{d^2 - 1}. \tag{102}$$

Therefore we have

$$\langle v_1 | v_1 \rangle = \lambda(p)^{x-1} \langle \text{O} \text{O} | \blacksquare \blacksquare \rangle = \lambda(p)^{x-1} \frac{d^2 - 1}{d^2}. \tag{103}$$

Proceeding analogously (cf. Appendix D), we find

$$\langle w_1 | w_1 \rangle = \lambda(p)^{x-2}. \tag{104}$$

Finally, putting all together, we obtain the following bound:

$$|\mathcal{R}_x| \leq \left(\frac{d+1}{d+c} \right)^2 \sqrt{\frac{d^2-1}{d^2\lambda(p)^3}} \left(\frac{d+c}{d+1} \right)^x \lambda(p)^x \tag{105}$$

$$\leq \left(\frac{d+1}{d+c} \right)^2 \sqrt{\frac{d^2-1}{d^2\lambda(p)^3}} \left(\frac{2d}{d+1} \right)^x \lambda(p)^x, \tag{106}$$

where we used that $c \leq d$. Choosing p such that

$$\lambda(p) \frac{2d}{d+1} < \frac{1}{d}, \tag{107}$$

we then find the bound (90). Solving for p we find that (107) is indeed satisfied for all

$$p \geq \bar{p}(d). \tag{108}$$

This concludes the proof.

C. Extension to $p < \bar{p}(d)$

An obvious strategy to generalize our proof is to extend lemma 1 to $p \leq \bar{p}(d)$. To this end, a simple observation is that, for small enough values of c , one can use the tighter bound (105) for $|\mathcal{R}_x|$. The latter grants the validity of lemma 1 whenever

$$\left(\frac{d+c}{d+1} \right) \lambda(p) < \frac{1}{d}. \tag{109}$$

Recalling that $c \geq 1$ (cf. Appendix B), we find that this bound can be satisfied for some c only if

$$p > \tilde{p}(d) \equiv \frac{d^2 - 1}{d^2} \left(1 - \frac{1}{\sqrt{d+1}} \right). \tag{110}$$

In fact, the bound (109) can be easily refined. For instance, instead of Eq. (96), we can consider

$$|\mathcal{R}_x| \leq \sqrt{\langle w_2 | w_2 \rangle} \sqrt{\langle v_2 | v_2 \rangle} \|M_2\|, \tag{111}$$

with $|w_2\rangle, |v_2\rangle$, defined with an extra row of gates, i.e.,

$$v_2 = \begin{array}{c} \text{O} \text{---} \square \\ \square \text{---} \square \\ \square \text{---} \square \\ \square \text{---} \square \\ \square \text{---} \square \\ \square \text{---} \square \\ \square \text{---} \square \\ \square \text{---} \square \\ \square \text{---} \square \\ \square \text{---} \square \end{array}. \tag{112}$$

Comparing this with (94), we see that the norm $\langle v_2 | v_2 \rangle$ involves the matrix T_4 . One can directly verify that the eigenvalue of T_4 contributing to this norm corresponds to an eigenvector with support 4 and it is strictly smaller than $\lambda(p)$. This results in an immediate improvement of the bound. In fact, this procedure can be repeated considering increasingly “thicker” states $|w_x\rangle, |v_x\rangle$ for any $x \geq 2$ and leads to a systematic improvement.

The fact that the bound on \mathcal{R}_x can be improved is also suggested by numerical evidence. For instance, in Fig. 1, we show the behavior of $\mathcal{R}_x d^x$ as a function of time for $d = 5$. We see that the exponential decay (90)—which implies the validity of Lemma 1—is clearly shown by our numerical evaluations for $p > 0.3$, which should be compared with $\bar{p}(5) \approx 0.68$ and $\tilde{p}(5) \approx 0.57$. From the trend in the numerical data, it is reasonable to expect that, upon accessing larger values of x , the same decay would be observed for all $p \neq 0$. A different indication is shown in Fig. 2, which suggests that

$$\Delta \ln \mathcal{P}_x \equiv \ln \mathcal{P}_{x-1} - \ln \mathcal{P}_x, \tag{113}$$

approaches 1 for all values of p except for a neighborhood of $p = 0$. Consistently with lemma 1 the leading corrections at large x appear to be $\approx x^{-1}$.

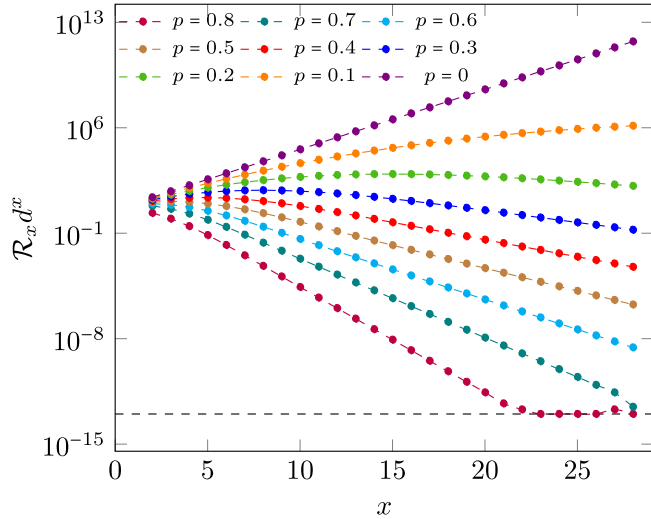


FIG. 1. Remainder $d^x \mathcal{R}_x$ [cf. (89)] for $c = 2.5$, $d = 5$, and several values of p . The exponential decay (90) with $D > d$ covers much more values than the range $p \gtrsim 0.62$, for which our rigorous bound (109) applies. The dotted line on the bottom indicates the limit of the numerical accuracy.

D. Numerical results for single realizations

In this section, we provide numerical evidence supporting the claim that v_E is maximal for essentially *any* single realization of the gates (47). For our numerical experiments we consider dual-unitary quantum circuits with a two-dimensional local Hilbert space. In this case, the most general local gate can be written as

$$U_{(ij);(kl)} = \sum_{i',j',k',l'=1}^2 \exp(iJ\delta_{i'j'}) u_{+i;i'} u_{-j;j'} v_{+k;k'} v_{-l;l'}, \quad (114)$$

where $\{v_{\pm}, u_{\pm}\}$ are fixed $U(2)$ matrices and $J \in [0, \pi/2]$. The angle J is in one-to-one correspondence with the entangling

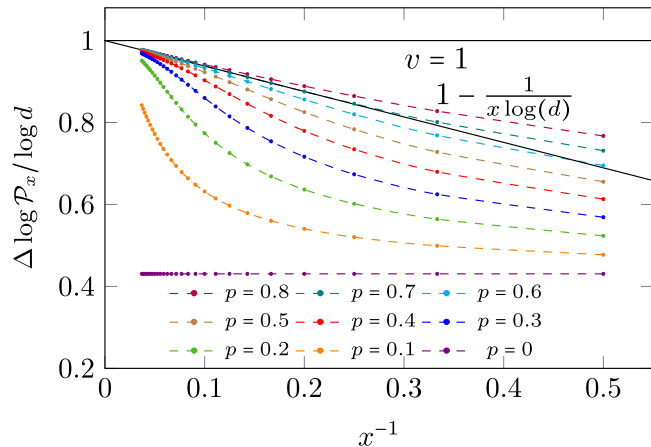


FIG. 2. Increment of the indicator $\Delta \ln(\mathcal{P}_x)$ in Eq. (113) per step for an initial state corresponding to $c = 2.5$ and $d = 5$. The quantity is expected to saturate at the averaged velocity value as $x \rightarrow \infty$. Note that our rigorous analytic bound (109) applies only if $p \gtrsim 0.62$. Assuming $d^x \mathcal{P}_x \sim A + Bx$ even for $p > 0.62$, we expect, for large x , $\Delta \ln \mathcal{P}_x \sim 1 - 1/(x \ln d)$.

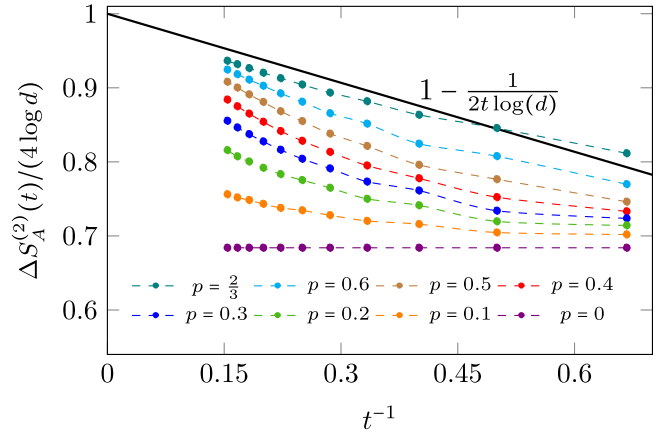


FIG. 3. $\Delta S_A^{(2)}(t)$ as a function of t^{-1} for a system prepared in a generic pair product state specified by the matrices (116) with $\theta = 0.35$ and evolved with a homogeneous dual-unitary quantum circuit with local gate (114), with fixed $\{v_{\pm}, u_{\pm}\}$ (their explicit form is reported in Appendix E) and different values of a [related to J through (115)]. This quantity saturates at the Rényi-2 entanglement velocity $v_{E,2}$ as $t \rightarrow \infty$. Assuming that for large times $S_A^{(2)}(t) \sim -2 \ln \mathcal{P}_{2t}$, we expect the various plots to reach asymptotically the line $1 - 1/(2t \ln(d))$ (black).

power [57]. Specifically, using the definition (8), we have

$$p = \frac{2}{3} \cos(J)^2. \quad (115)$$

In the following we use p , rather than J , to keep consistency with the previous sections. The initial state matrix is instead taken of the form

$$m_{i,j} = (1 - \delta_{ij}) \sin(\theta) + \delta_{ij} \cos \theta. \quad (116)$$

Focussing on a space-time translationally invariant circuit, i.e., a circuit where the local gate is the same at each space-time point, we compute the Rényi entropy $S_A^{(2)}(t)$ for $t \leq L_A/2$ by numerically constructing the matrix C_x [cf. (30)] and using (32). This direct approach allows us to reach values of x up to 14. Note that, due to the fast growth of entanglement in dual-unitary circuits, this is more efficient than tensor network methods based on the truncation of the time-evolving state, e.g., TEBD.

A representative example of our results is presented in Fig. 3, where we report $\Delta S_A^{(2)}(t)$ [cf. Eq. (44)] as a function of the inverse time. Our results suggest that at large times $\Delta S_A^{(2)}(t)$ approaches $4 \ln d$ with power law corrections that, as observed in the averaged case, are larger for smaller values of p . This implies

$$v_{E,2} = v_E = 1, \quad (117)$$

in accordance with our expectations.

E. More general initial states

In most of this paper, we considered for simplicity the family of pair-product states (13). However, our approach can be applied more generally. For instance, as a nontrivial example let us consider a family of MPS that are generic fixed

points of the RG flow [86], i.e., they can be written as

$$|\Psi_0\rangle = \frac{1}{d^{\frac{L}{2}}} \sum_{a_j \in \mathbb{Z}_d} \text{tr}[Z^{a_1, a_2} Z^{a_3, a_4} \dots Z^{a_{2N-1}, a_{2L}}] |a\rangle, \quad (118)$$

where $\{Z^{a,b}\}$ are $\chi \times \chi$ matrices such that

$$X \equiv \frac{1}{d} \sum_{a,b} Z^{a,b} \otimes (Z^{a,b})^* = |L\rangle\langle R|, \quad (119)$$

with

$$|L\rangle = \sum_{i=1}^{\chi} |i, i\rangle, \quad |R\rangle = \sum_{i=1}^{\chi} \lambda_i |i, i\rangle, \quad \sum_{i=1}^{\chi} \lambda_i = 1, \quad (120)$$

and $\lambda_i > 0$. Generalizing the discussion of Secs. IV A and IV B, in Appendix C, we show that for

$$\lambda(p)\chi \left(\frac{d+1}{d-1} + \sqrt{\frac{d+1}{d-1}} \right) < \frac{1}{d}, \quad (121)$$

Property 1 holds for all the MPS (118).

V. DISCUSSION

We studied the asymptotic growth of entanglement in dual-unitary circuits prepared in generic low-entangled states. These states are generally *nonsolvable*: they break the unitarity of the evolution in space and their entanglement dynamics cannot be accessed using the standard dual-unitarity-based approaches [25,26]. Moreover, as opposed to solvable states, they display a submaximal entanglement increment at short times.

By introducing dual-unitarity-preserving random noise we showed that, surprisingly, the entanglement dynamics of generic states remain *exactly tractable* for large times: one can still make exact statements for individual realizations of the noise, possibly excluding a subset with zero measure. In this way, we proved that for a class of dual-unitary circuits with large enough entangling power the growth-rate of entanglement approaches the maximal value as time increases—i.e., their entanglement velocity is always maximal irrespective of the initial conditions. We showed that this maximally entangling class exists for any number d of local degrees of freedom as it includes the Hadamard family of dual-unitary gates introduced in Ref. [72]. Moreover, for $d \geq 3$ it also contains four-leg perfect tensors [73,74,87–89]. In fact, we presented analytical and numerical arguments suggesting that all dual-unitary circuits with nonzero entangling power belong to this class.

Our results established an even tighter connection between dual-unitarity and maximal entanglement growth. While Ref. [71] recently showed that if there exists an initial state for which the asymptotic entanglement rate is maximal, then the circuit is dual unitary, here we showed that in generic dual-unitary circuits *every* initial state eventually approaches maximal entanglement growth. In this respect, our results show that dual-unitary circuits are the hardest quantum circuits to simulate with classical computers [34–37] making of them the optimal test bed for investigations on quantum supremacy in the nonequilibrium dynamics [90].

A natural question is whether our “generality” assumption—the fact that we excluded a zero-measure set of gates—is necessary or not. Namely, do we need to exclude some special dual-unitary gates (e.g., the integrable ones) or *any* dual-unitary circuit generates maximal entanglement growth at large times? This would establish whether quantum chaos is an essential ingredient to produce the observed initial-condition independence of the entanglement velocities or dual unitarity alone suffices.

Finally, we stress that the methods developed here provide a systematic way to investigate quenches from generic initial states in dual-unitary circuits. Interesting questions that one can tackle with them include (deep) thermalization timescales in dual-unitary circuits [25,26,65,70], and multiunitary quantum channels [91], or the “temporal entanglement” scaling in chaotic quantum circuits [92] (see also Refs. [77,93–95]). The latter question is currently under investigation [96].

ACKNOWLEDGMENTS

We thank Tianci Zhou for collaboration on a closely related project and for many useful comments on the manuscript. We also grateful to Lorenzo Piroli, Tomaž Prosen, Pavel Kos, and, especially, Katja Klobas for very valuable feedback on the manuscript. This work has been supported by the Royal Society through the University Research Fellowship No. 201101.

APPENDIX A: BOUNDS ON THE ENTANGLING POWER OF DUAL-UNITARY GATES

The values that the entangling power p can take are bounded by the unitarity of the matrix. To see this, consider $\text{tr}[(\tilde{U}^{t_2}(\tilde{U}^{t_2})^\dagger)^2]$ in the definition (8): the unitarity of the matrix fixes the value of

$$\text{tr}[\tilde{U}^{t_2}(\tilde{U}^{t_2})^\dagger] = \text{tr}[\tilde{U}\tilde{U}^\dagger] = d^2. \quad (A1)$$

Applying (34) to the matrix $\frac{\tilde{U}^{t_2}(\tilde{U}^{t_2})^\dagger}{d^2}$, we find

$$\text{tr}[(\tilde{U}^{t_2}(\tilde{U}^{t_2})^\dagger)^2] \in [d^2, d^4] \Rightarrow p \in [0, 1]. \quad (A2)$$

In particular, the case

$$\text{tr}[(\tilde{U}^{t_2}(\tilde{U}^{t_2})^\dagger)^2] = d^2 \quad (A3)$$

is attained if and only if \tilde{U}^{t_2} is unitary, having all eigenvalues with magnitude 1. This request, together with the dual unitarity conditions (6), means that U is unitary for any choice of couples of in/out indexes. Tensors with this property are known as 4-leg perfect tensors and they exist for all $d > 2$ [73,74]. There is, however, a nonexhaustive class of dual unitary gates which is well defined in any dimension [62]

$$U_{(ij),(kl)} = \delta_{il} \delta_{jk} \exp(iJ_{ij}), \quad (A4)$$

with J_{ij} being any set of d^2 real numbers. In terms of J_{ij} , we can write

$$\text{tr}[(\tilde{U}^{t_2}(\tilde{U}^{t_2})^\dagger)^2] = \sum_{i,j,k,l} \exp[i(J_{ij} + J_{kl} - J_{il} - J_{kj})]. \quad (A5)$$

As before, we can express the right-hand side as a matrix trace

$$\sum_{i,j,k,l} \exp[i(J_{ij} + J_{kl} - J_{il} - J_{kj})] = d^4 \text{tr}[(\xi\xi^\dagger)^2], \quad (A6)$$

with

$$\xi_{ij} \equiv \frac{\exp(iJ_{ij})}{d} \Rightarrow \text{Tr}[\xi \xi^\dagger] = 1. \quad (\text{A7})$$

Using again (34), we find

$$\text{tr}[(\tilde{U}^{t_2}(\tilde{U}^{t_2})^\dagger)^2] \in [d^3, d^4] \Rightarrow p \in \left[0, \frac{d}{d+1}\right]. \quad (\text{A8})$$

The choice $J_{ij} = 0$, which corresponds to a swap gate, gives $p = 0$. Instead, the choice

$$J_{ij} = \frac{2\pi ij}{d}, \quad (\text{A9})$$

corresponding to the Hadamard family considered in Sec. IV, gives

$$p = \frac{d}{d+1}. \quad (\text{A10})$$

We also note that, since the value of p depends continuously on J_{ij} , there must exist gates corresponding to all values in the range

$$p \in \left[0, \frac{d}{d+1}\right]. \quad (\text{A11})$$

Finally, we remark that this range is exhaustive in $d = 2$, since any dual unitary gate can be expressed as in Eq. (114).

APPENDIX B: AVERAGED INITIAL STATE MATRIX

Considering the averaged form of the initial state matrix in the basis $\{|\circ\rangle, |\bullet\rangle\}$, we have

$$n = \begin{pmatrix} 1 & \frac{c-1}{\sqrt{d^2-1}} \\ \frac{c-1}{\sqrt{d^2-1}} & 1 - 2\frac{c-1}{d^2-1} \end{pmatrix}, \quad (\text{B1})$$

with

$$c = \frac{1}{d} \text{tr}((m^\dagger m)^2). \quad (\text{B2})$$

We can bound the values that the constant c can take noting that the matrix m is subject to the constraint

$$\text{tr}(m^\dagger m) = d. \quad (\text{B3})$$

Therefore we can use (34) on $m^\dagger m / d$ with $\mathcal{N} = d$, $\alpha = 2$, finding

$$c \in [1, d]. \quad (\text{B4})$$

The matrix (B1) is Hermitian and, therefore, its operator norm coincides with the norm of its maximal eigenvalue. Computing it explicitly, we find

$$\begin{aligned} \lambda_{\max} &= 1 - \frac{c-1}{d^2-1} + \sqrt{\left(\frac{c-1}{\sqrt{d^2-1}}\right)^2 + \left(\frac{c-1}{d^2-1}\right)^2} \\ &= 1 - \frac{c-1}{d^2-1} (1 - \sqrt{d^2-1+1}) = \frac{d+c}{d+1}. \end{aligned} \quad (\text{B5})$$

In summary, we have

$$\|n\|_\infty = \frac{c+d}{d+1} \in \left[1, \frac{2d}{d+1}\right]. \quad (\text{B6})$$

APPENDIX C: INITIAL STATES IN MPS FORM

Consider an MPS which is a generic fixed point of the RG flow, i.e., it obeys Eqs (119), (120). This means we can write

$$X^\dagger X = \langle L|L\rangle |R\rangle \langle R| \quad (\text{C1})$$

implying that

$$\|X\|_\infty = \sqrt{\langle R|R\rangle} \sqrt{\langle L|L\rangle} \leq \sqrt{\chi}. \quad (\text{C2})$$

We can repeat the steps of Sec. IV B finding recurrence relations for $\mathcal{P}_x^{\text{MPS}}$, $\mathcal{Q}_x^{\text{MPS}}$ —the analogues of (65) and (87)—and bounding $\mathcal{R}_x^{\text{MPS}}$ —the analog of (89)—by means of the Cauchy-Schwartz inequality. In order to do so, we find the operator norm of the matrix representing the folded MPS after averaging over the local unitaries.

We begin by noting that the average restricts the upper indices (a_1, a_2, a_3, a_4) and (b_1, b_2, b_3, b_4) of the doubly folded tensor

$$Z^{a_1, b_1} \otimes (Z^{a_2, b_2})^* \otimes Z^{a_3, b_3} \otimes (Z^{a_4, b_4})^*, \quad (\text{C3})$$

to the subspace spanned by

$$|\circ\rangle = \frac{\delta_{a_1, a_2} \delta_{a_3, a_4}}{d} \quad (\text{C4})$$

and

$$|\square\rangle = \frac{\delta_{a_1, a_4} \delta_{a_3, a_2}}{d}. \quad (\text{C5})$$

We call \tilde{Z} the resulting tensor.

Grouping the indices (a, i) and (b, j) , the tensor $\tilde{Z}_{i,j}^{a,b}$ can be seen as a matrix of dimension $2\chi \times 2\chi$, acting on the vector space $V_{\circ, \bullet} \otimes V_\chi$, where $V_{\circ, \bullet}$ is the space spanned by (C4) and (C5), and $V_\chi = \mathbb{C}^\chi$ is the auxiliary space of the MPS. Our task is to find the operator norm of this matrix. To this end, we write it as

$$\tilde{Z} = \begin{pmatrix} \tilde{Z}^{\circ\circ} & \tilde{Z}^{\circ\bullet} \\ \tilde{Z}^{\bullet\circ} & \tilde{Z}^{\bullet\bullet} \end{pmatrix}, \quad (\text{C6})$$

and bound its norm as

$$\|Z\|_\infty \leq \max \left\{ \|\tilde{Z}^{\circ\circ}\|_\infty, \|\tilde{Z}^{\bullet\bullet}\|_\infty \right\} + \|\tilde{Z}^{\circ\bullet}\|_\infty. \quad (\text{C7})$$

Using Eqs. (119) and (C2), we find

$$\|\tilde{Z}^{\circ\circ}\|_\infty = \|\tilde{Z}^{\square\square}\|_\infty = (\|X\|_\infty)^2 \leq \chi. \quad (\text{C8})$$

Consider now the n th norm of $\tilde{Z}^{\circ\square}$ (where n is taken to be even): we can write it as

$$\|\tilde{Z}^{\circ\square}\|_n = \left(\text{Tr}(A_n A_n^\dagger A_n A_n^\dagger) \right)^{\frac{1}{n}}, \quad (\text{C9})$$

where we defined the matrix

$$(A_n)_{a,b} \equiv d^{-\frac{n}{2}} \text{Tr} \left[\prod_{i=1}^{n/2} Z^{a_{2i-1}, b_{2i-1}} (Z^{a_{2i}, b_{2i}})^\dagger \right]. \quad (\text{C10})$$

Here $a_i = 1, \dots, d$ and the trace is taken over the auxiliary space. Moreover, we have that

$$\text{Tr}(A_n A_n^\dagger) = \text{Tr}[(X X^\dagger)^{\frac{n}{2}}]. \quad (\text{C11})$$

The matrix $A_n A_n^\dagger$ is Hermitian and acts on a d^n -dimensional vector space, this means that

$$\frac{\text{Tr}(A_n A_n^\dagger A_n A_n^\dagger)}{\text{Tr}[(X X^\dagger)^{\frac{n}{2}}]^2} \in [d^{-n}, 1], \quad (\text{C12})$$

Taking the limit $n \rightarrow \infty$, and using Eq. (C2), we find

$$\|\tilde{Z}^{\square, \square}\|_\infty \in \left[\frac{\|X\|_\infty^2}{d}, \|X\|_\infty^2 \right] \implies \|\tilde{Z}^{\square, \square}\|_\infty < \chi. \quad (\text{C13})$$

Using Eqs. (74), (C13), and the triangular inequality, the norms of the submatrices are bounded as

$$\|\tilde{Z}^{\square, \bullet}\|_\infty \leq \chi \sqrt{\frac{d+1}{d-1}} \quad \|\tilde{Z}^{\bullet, \bullet}\|_\infty \leq \chi \frac{d+1}{d-1}, \quad (\text{C14})$$

finally, Eq. (C7) implies

$$\|\tilde{Z}\|_\infty \leq \chi \left(\frac{d+1}{d-1} + \sqrt{\frac{d+1}{d-1}} \right). \quad (\text{C15})$$

Using this result, we finally obtain condition (121).

APPENDIX D: TWO-SITE TRANSFER MATRIX

Consider the transfer matrix T_2 in Eq. (100): using the explicit expression for the averaged gate (75) (which has the same form in the square states basis), we see that its explicit form in the basis

$$\{|\square\square\rangle, |\blacksquare\square\rangle, |\square\blacksquare\rangle, |\blacksquare\blacksquare\rangle\}, \quad (\text{D1})$$

reads as

$$T_2 = \begin{pmatrix} 1 & 0 & 0 & 0 \\ 0 & 1-p & 0 & 0 \\ 0 & 0 & 1-p & 0 \\ 0 & 0 & 0 & (1-p)^2 + \frac{p^2}{d^2-1} \end{pmatrix}, \quad (\text{D2})$$

allowing us to immediately compute

$$\begin{aligned} \langle v_2 | v_2 \rangle &= \langle \square\square | T_2^{x-1} | \blacksquare\blacksquare \rangle \\ &= \lambda(p)^{x-1} \langle \square\square | \blacksquare\blacksquare \rangle = \\ &= \lambda(p)^{x-1} \frac{d^2-1}{d^2}. \end{aligned} \quad (\text{D3})$$

TABLE I. Parameters for the one-site unitaries used to produce the data in Fig. 3.

	θ	ϕ	α
u_-	0.774764	5.531527	4.534001
u_+	2.521203	3.352128	4.712387
v_-	1.768693	0.704289	5.567499
v_+	0.251880	1.607363	5.823117

Similarly, the transfer matrix

$$T'_2 = \begin{array}{c} \circ \\ | \\ \diamond \\ | \\ \diamond \\ | \\ \circ \end{array}, \quad (\text{D4})$$

can be put in the same form under a unitary change of basis $\{\square, \blacksquare\} \rightarrow \{\circ, \bullet\}$, allowing us to find

$$\begin{aligned} \langle w_2 | w_2 \rangle &= \langle \bullet\bullet | T_2^{x-2} | \circ \rangle \\ &= \lambda(p)^{x-2} \langle \bullet\bullet | \circ \rangle \\ &= \lambda(p)^{x-2}, \end{aligned} \quad (\text{D5})$$

where we used the notation for the arc state

$$|\circ\rangle = |\circ\circ\rangle + |\bullet\bullet\rangle. \quad (\text{D6})$$

APPENDIX E: DETAILS OF THE NUMERICS

In Fig. 3, we plotted the numerical evaluation of the Rényi-2 entropy for different values of the parameter p . We implemented the gates defined in Eq. (114), where the unitary matrices $u_\pm, v_\pm \in U(2)$ are obtained from a random Haar uniform extraction. Those matrices are kept fixed while varying the value of J (or p , which are connected through Eq. (115)). The explicit parametrization implemented is the following:

$$\begin{bmatrix} \cos(\alpha) + i \sin(\alpha) \cos(\theta) & i \sin(\alpha) \sin(\theta) e^{-i\phi} \\ i \sin(\alpha) \sin(\theta) e^{i\phi} & \cos(\alpha) - i \sin(\alpha) \cos(\theta) \end{bmatrix}. \quad (\text{E1})$$

The values used to produce Fig. 3 are reported in Table I.

[1] L. Amico, R. Fazio, A. Osterloh, and V. Vedral, Entanglement in many-body systems, *Rev. Mod. Phys.* **80**, 517 (2008).
[2] P. Calabrese, J. Cardy, and B. Doyon, Entanglement entropy in extended quantum systems, *J. Phys. A: Math. Theor.* **42**, 500301 (2009).
[3] P. Calabrese, Entanglement and thermodynamics in non-equilibrium isolated quantum systems, *Physica A* **504**, 31 (2018).
[4] N. Laflorencie, Quantum entanglement in condensed matter systems, *Phys. Rep.* **646**, 1 (2016).
[5] P. Calabrese and J. Cardy, Evolution of entanglement entropy in one-dimensional systems, *J. Stat. Mech.* (2005) P04010.

[6] A. Nahum, J. Ruhman, S. Vijay, and J. Haah, Quantum Entanglement Growth under Random Unitary Dynamics, *Phys. Rev. X* **7**, 031016 (2017).
[7] J. M. Deutsch, H. Li, and A. Sharma, Microscopic origin of thermodynamic entropy in isolated systems, *Phys. Rev. E* **87**, 042135 (2013).
[8] W. Beugeling, A. Andreanov, and M. Haque, Global characteristics of all eigenstates of local many-body hamiltonians: participation ratio and entanglement entropy, *J. Stat. Mech.* (2015) P02002.
[9] V. Gurarie, Global large time dynamics and the generalized gibbs ensemble, *J. Stat. Mech.* (2013) P02014.

- [10] V. Alba and P. Calabrese, Entanglement and thermodynamics after a quantum quench in integrable systems, *Proc. Natl. Acad. Sci. USA* **114**, 7947 (2017).
- [11] G. D. Chiara, S. Montangero, P. Calabrese, and R. Fazio, Entanglement entropy dynamics of Heisenberg chains, *J. Stat. Mech.* (2006) P03001.
- [12] M. Žnidarič, T. Prosen, and P. Prelovšek, Many-body localization in the Heisenberg XXZ magnet in a random field, *Phys. Rev. B* **77**, 064426 (2008).
- [13] R. Nandkishore and D. A. Huse, Many-body localization and thermalization in quantum statistical mechanics, *Annu. Rev. Condens. Matter Phys.* **6**, 15 (2015).
- [14] M. Kormos, M. Collura, G. Takács, and P. Calabrese, Real-time confinement following a quantum quench to a non-integrable model, *Nat. Phys.* **13**, 246 (2017).
- [15] B. Skinner, J. Ruhman, and A. Nahum, Measurement-Induced Phase Transitions in the Dynamics of Entanglement, *Phys. Rev. X* **9**, 031009 (2019).
- [16] Y. Li, X. Chen, and M. P. A. Fisher, Measurement-driven entanglement transition in hybrid quantum circuits, *Phys. Rev. B* **100**, 134306 (2019).
- [17] R. Vasseur, A. C. Potter, Y.-Z. You, and A. W. W. Ludwig, Entanglement transitions from holographic random tensor networks, *Phys. Rev. B* **100**, 134203 (2019).
- [18] M. Fagotti and P. Calabrese, Evolution of entanglement entropy following a quantum quench: Analytic results for the XY chain in a transverse magnetic field, *Phys. Rev. A* **78**, 010306(R) (2008).
- [19] B. Bertini, E. Tartaglia, and P. Calabrese, Entanglement and diagonal entropies after a quench with no pair structure, *J. Stat. Mech.* (2018) 063104.
- [20] V. Alba and P. Calabrese, Entanglement dynamics after quantum quenches in generic integrable systems, *SciPost Phys.* **4**, 017 (2018).
- [21] G. Lagnese, P. Calabrese, and L. Piroli, Entanglement dynamics of thermofield double states in integrable models, *J. Phys. A: Math. Theor.* **55**, 214003 (2022).
- [22] A. M. Läuchli and C. Kollath, Spreading of correlations and entanglement after a quench in the one-dimensional bose–hubbard model, *J. Stat. Mech.* (2008) P05018.
- [23] H. Kim and D. A. Huse, Ballistic Spreading of Entanglement in a Diffusive Nonintegrable System, *Phys. Rev. Lett.* **111**, 127205 (2013).
- [24] R. Pal and A. Lakshminarayan, Entangling power of time-evolution operators in integrable and nonintegrable many-body systems, *Phys. Rev. B* **98**, 174304 (2018).
- [25] B. Bertini, P. Kos, and T. Prosen, Entanglement Spreading in a Minimal Model of Maximal Many-Body Quantum Chaos, *Phys. Rev. X* **9**, 021033 (2019).
- [26] L. Piroli, B. Bertini, J. I. Cirac, and T. Prosen, Exact dynamics in dual-unitary quantum circuits, *Phys. Rev. B* **101**, 094304 (2020).
- [27] S. Gopalakrishnan and A. Lamacraft, Unitary circuits of finite depth and infinite width from quantum channels, *Phys. Rev. B* **100**, 064309 (2019).
- [28] T. Zhou and A. Nahum, Entanglement Membrane in Chaotic Many-Body Systems, *Phys. Rev. X* **10**, 031066 (2020).
- [29] H. Liu and S. J. Suh, Entanglement Tsunami: Universal Scaling in Holographic Thermalization, *Phys. Rev. Lett.* **112**, 011601 (2014).
- [30] C. T. Asplund, A. Bernamonti, F. Galli, and T. Hartman, Entanglement scrambling in 2d conformal field theory, *J. High Energy Phys.* **09** (2015) 110.
- [31] C. W. von Keyserlingk, T. Rakovszky, F. Pollmann, and S. L. Sondhi, Operator Hydrodynamics, OTOCs, and Entanglement Growth in Systems without Conservation Laws, *Phys. Rev. X* **8**, 021013 (2018).
- [32] K. Klobas, B. Bertini, and L. Piroli, Exact Thermalization Dynamics in the “Rule 54” Quantum Cellular Automaton, *Phys. Rev. Lett.* **126**, 160602 (2021).
- [33] K. Klobas and B. Bertini, Entanglement dynamics in Rule 54: Exact results and quasiparticle picture, *SciPost Phys.* **11**, 107 (2021).
- [34] N. Schuch, M. M. Wolf, F. Verstraete, and J. I. Cirac, Entropy Scaling and Simulability by Matrix Product States, *Phys. Rev. Lett.* **100**, 030504 (2008).
- [35] N. Schuch, M. M. Wolf, K. G. H. Vollbrecht, and J. I. Cirac, On entropy growth and the hardness of simulating time evolution, *New J. Phys.* **10**, 033032 (2008).
- [36] A. Perales and G. Vidal, Entanglement growth and simulation efficiency in one-dimensional quantum lattice systems, *Phys. Rev. A* **78**, 042337 (2008).
- [37] P. Hauke, F. M. Cucchietti, L. Tagliacozzo, I. Deutsch, and M. Lewenstein, Can one trust quantum simulators?, *Rep. Prog. Phys.* **75**, 082401 (2012).
- [38] B. Bertini, K. Klobas, V. Alba, G. Lagnese, and P. Calabrese, Growth of Rényi Entropies in Interacting Integrable Models and the Breakdown of the Quasiparticle Picture, *Phys. Rev. X* **12**, 031016 (2022).
- [39] S. Ghoshal and A. Zamolodchikov, Boundary S-matrix and boundary state in two-dimensional integrable quantum field theory, *Int. J. Mod. Phys. A* **09**, 3841 (1994).
- [40] L. Piroli, B. Pozsgay, and E. Vernier, What is an integrable quench?, *Nucl. Phys. B* **925**, 362 (2017).
- [41] A. Nahum, S. Vijay, and J. Haah, Operator Spreading in Random Unitary Circuits, *Phys. Rev. X* **8**, 021014 (2018).
- [42] A. Chan, A. De Luca, and J. T. Chalker, Solution of a Minimal Model for Many-Body Quantum Chaos, *Phys. Rev. X* **8**, 041019 (2018).
- [43] V. Khemani, A. Vishwanath, and D. A. Huse, Operator Spreading and the Emergence of Dissipative Hydrodynamics under Unitary Evolution with Conservation Laws, *Phys. Rev. X* **8**, 031057 (2018).
- [44] T. Rakovszky, F. Pollmann, and C. W. von Keyserlingk, Diffusive Hydrodynamics of Out-of-Time-Ordered Correlators with Charge Conservation, *Phys. Rev. X* **8**, 031058 (2018).
- [45] B. Bertini, P. Kos, and T. Prosen, Exact Spectral Form Factor in a Minimal Model of Many-Body Quantum Chaos, *Phys. Rev. Lett.* **121**, 264101 (2018).
- [46] A. J. Friedman, A. Chan, A. De Luca, and J. T. Chalker, Spectral Statistics and Many-Body Quantum Chaos with Conserved Charge, *Phys. Rev. Lett.* **123**, 210603 (2019).
- [47] A. Chan, A. De Luca, and J. T. Chalker, Spectral Statistics in Spatially Extended Chaotic Quantum Many-Body Systems, *Phys. Rev. Lett.* **121**, 060601 (2018).
- [48] A. Flack, B. Bertini, and T. Prosen, Statistics of the spectral form factor in the self-dual kicked Ising model, *Phys. Rev. Res.* **2**, 043403 (2020).

- [49] B. Bertini, P. Kos, and T. Prosen, Random matrix spectral form factor of dual-unitary quantum circuits, *Commun. Math. Phys.* **387**, 597 (2021).
- [50] F. Fritzsche and T. Prosen, Eigenstate thermalization in dual-unitary quantum circuits: Asymptotics of spectral functions, *Phys. Rev. E* **103**, 062133 (2021).
- [51] P. Kos, T. Prosen, and B. Bertini, Thermalization dynamics and spectral statistics of extended systems with thermalizing boundaries, *Phys. Rev. B* **104**, 214303 (2021).
- [52] B. Bertini, P. Kos, and T. Prosen, Exact spectral statistics in strongly localized circuits, *Phys. Rev. B* **105**, 165142 (2022).
- [53] S. J. Garratt and J. T. Chalker, Many-Body Delocalization as Symmetry Breaking, *Phys. Rev. Lett.* **127**, 026802 (2021).
- [54] S. J. Garratt and J. T. Chalker, Local Pairing of Feynman Histories in Many-Body Floquet Models, *Phys. Rev. X* **11**, 021051 (2021).
- [55] A. Chan, S. Shivam, A. Huse, David, and A. De Luca, Many-body quantum chaos and space-time translational invariance, *Nat. Commun.* **13**, 7484 (2022).
- [56] K. Klobas and B. Bertini, Exact relaxation to Gibbs and non-equilibrium steady states in the quantum cellular automaton Rule 54, *SciPost Phys.* **11**, 106 (2021).
- [57] B. Bertini, P. Kos, and T. Prosen, Exact correlation functions for dual-unitary lattice models in $1 + 1$ dimensions, *Phys. Rev. Lett.* **123**, 210601 (2019).
- [58] B. Bertini, P. Kos, and T. Prosen, Operator Entanglement in Local Quantum Circuits I: Chaotic Dual-Unitary Circuits, *SciPost Phys.* **8**, 067 (2020).
- [59] B. Bertini, P. Kos, and T. Prosen, Operator entanglement in local quantum circuits ii: Solitons in chains of qubits, *SciPost Phys.* **8**, 068 (2020).
- [60] P. W. Claeys and A. Lamacraft, Maximum velocity quantum circuits, *Phys. Rev. Res.* **2**, 033032 (2020).
- [61] I. Reid and B. Bertini, Entanglement barriers in dual-unitary circuits, *Phys. Rev. B* **104**, 014301 (2021).
- [62] P. W. Claeys and A. Lamacraft, Ergodic and Nonergodic Dual-Unitary Quantum Circuits with Arbitrary Local Hilbert Space Dimension, *Phys. Rev. Lett.* **126**, 100603 (2021).
- [63] R. Suzuki, K. Mitarai, and K. Fujii, Computational power of one- and two-dimensional dual-unitary quantum circuits, *Quantum* **6**, 631 (2022).
- [64] W. W. Ho and S. Choi, Exact Emergent Quantum State Designs from Quantum Chaotic Dynamics, *Phys. Rev. Lett.* **128**, 060601 (2022).
- [65] M. Ippoliti and W. W. Ho, Dynamical purification and the emergence of quantum state designs from the projected ensemble, [arXiv:2204.13657](https://arxiv.org/abs/2204.13657).
- [66] Y. Kasim and T. Prosen, Dual unitary circuits in random geometries, *J. Phys. A: Math. Theor.* **56**, 025003 (2023).
- [67] P. W. Claeys, M. Henry, J. Vicary, and A. Lamacraft, Exact dynamics in dual-unitary quantum circuits with projective measurements, *Phys. Rev. Res.* **4**, 043212 (2022).
- [68] C. Jonay, V. Khemani, and M. Ippoliti, Tri-unitary quantum circuits, *Phys. Rev. Res.* **3**, 043046 (2021).
- [69] R. Milbradt, L. Sheller, C. Assmus, and B. Mendl, Christian, Ternary unitary quantum lattice models and circuits in $2+1$ dimensions, *Phys. Rev. Lett.* **130**, 090601 (2023).
- [70] P. W. Claeys and A. Lamacraft, Emergent quantum state designs and biunitarity in dual-unitary circuit dynamics, *Quantum* **6**, 738 (2022).
- [71] T. Zhou and A. W. Harrow, Maximal entanglement velocity implies dual unitarity, *Phys. Rev. B* **106**, L201104 (2022).
- [72] B. Gutkin, P. Braun, M. Akila, D. Waltner, and T. Guhr, Local correlations in dual-unitary kicked chains, [arXiv:2001.01298](https://arxiv.org/abs/2001.01298).
- [73] F. Huber, C. Eltschka, J. Siewert, and O. Gühne, Bounds on absolutely maximally entangled states from shadow inequalities, and the quantum MacWilliams identity, *J. Phys. A: Math. Theor.* **51**, 175301 (2018).
- [74] S. A. Rather, A. Burchardt, W. Bruzda, G. Rajchel-Mieldzióć, A. Lakshminarayan, and K. Życzkowski, Thirty-six Entangled Officers of Euler: Quantum Solution to a Classically Impossible Problem, *Phys. Rev. Lett.* **128**, 080507 (2022).
- [75] T. Prosen, Many-body quantum chaos and dual-unitarity round-a-face, *Chaos* **31**, 093101 (2021).
- [76] M. Borsi and B. Pozsgay, Remarks on the construction and the ergodicity properties of dual unitary quantum circuits (with an Appendix by roland bacher and denis serre), *Phys. Rev. B* **106**, 014302 (2022).
- [77] G. Giudice, G. Giudici, M. Sonner, J. Thoenniss, A. Lerose, D. A. Abanin, and L. Piroli, Temporal Entanglement, Quasiparticles, and the Role of Interactions, *Phys. Rev. Lett.* **128**, 220401 (2022).
- [78] S. A. Rather, S. Aravinda, and A. Lakshminarayan, Creating Ensembles of Dual Unitary and Maximally Entangling Quantum Evolutions, *Phys. Rev. Lett.* **125**, 070501 (2020).
- [79] S. Aravinda, S. A. Rather, and A. Lakshminarayan, From dual-unitary to quantum bernoulli circuits: Role of the entangling power in constructing a quantum ergodic hierarchy, *Phys. Rev. Res.* **3**, 043034 (2021).
- [80] A. Rather, Suhail, S. Aravinda, and A. Lakshminarayan, Construction and local equivalence of dual-unitary operators: from dynamical maps to quantum combinatorial designs, *PRX Quantum* **3**, 040331 (2022).
- [81] F. Pastawski, B. Yoshida, D. Harlow, and J. Preskill, Holographic quantum error-correcting codes: Toy models for the bulk/boundary correspondence, *J. High Energy Phys.* **06** (2015) 149.
- [82] D. Goyeneche, D. Alsina, J. I. Latorre, A. Riera, and K. Życzkowski, Absolutely maximally entangled states, combinatorial designs, and multiunitary matrices, *Phys. Rev. A* **92**, 032316 (2015).
- [83] B. Bertini and L. Piroli, Scrambling in random unitary circuits: Exact results, *Phys. Rev. B* **102**, 064305 (2020).
- [84] T. Tao, *An Introduction to Measure Theory*, Graduate studies in mathematics (American Mathematical Society, Rhode Island, 2013).
- [85] M. Ippoliti and V. Khemani, Postselection-Free Entanglement Dynamics via space-time Duality, *Phys. Rev. Lett.* **126**, 060501 (2021).
- [86] F. Verstraete, J. I. Cirac, J. I. Latorre, E. Rico, and M. M. Wolf, Renormalization-Group Transformations on Quantum States, *Phys. Rev. Lett.* **94**, 140601 (2005).
- [87] P. Facchi, G. Florio, G. Parisi, and S. Pascazio, Maximally multipartite entangled states, *Phys. Rev. A* **77**, 060304(R) (2008).
- [88] D. Goyeneche and K. Życzkowski, Genuinely multipartite entangled states and orthogonal arrays, *Phys. Rev. A* **90**, 022316 (2014).

- [89] P. Hosur, X.-L. Qi, D. A. Roberts, and B. Yoshida, Chaos in quantum channels, *J. High Energy Phys.* **02** (2016) 004.
- [90] F. Arute, K. Arya, R. Babbush, D. Bacon, J. C. Bardin, R. Barends, R. Biswas, S. Boixo, F. G. Brandao, D. A. Buell *et al.*, Quantum supremacy using a programmable superconducting processor, *Nature (London)* **574**, 505 (2019).
- [91] P. Kos and G. Styliaris, Circuits of space-time quantum channels, [arXiv:2206.12155](https://arxiv.org/abs/2206.12155).
- [92] A. Lerose, M. Sonner, and D. A. Abanin, Influence Matrix Approach to Many-Body Floquet Dynamics, *Phys. Rev. X* **11**, 021040 (2021).
- [93] A. Lerose, M. Sonner, and D. A. Abanin, Scaling of temporal entanglement in proximity to integrability, *Phys. Rev. B* **104**, 035137 (2021).
- [94] M. Sonner, A. Lerose, and D. A. Abanin, Influence functional of many-body systems: Temporal entanglement and matrix-product state representation, *Ann. Phys.* **435**, 168677 (2021).
- [95] M. Sonner, A. Lerose, and D. A. Abanin, Characterizing many-body localization via exact disorder-averaged quantum noise, *Phys. Rev. B* **105**, L020203 (2022).
- [96] A. Foligno, T. Zhou, and B. Bertini, Temporal entanglement in chaotic quantum circuits, [arXiv:2302.08502](https://arxiv.org/abs/2302.08502) (2023).

Chapter 3

Temporal entanglement

3.1 Summary

In this paper we consider the folding algorithm introduced in [107] to simulate the time evolution of local observables in extensive systems. We quantify the approximability of a key element of this algorithm, the Influence matrix [108], by an MPO, computing its operatorial entanglement. Initially we work on a generic unitary circuit and assume the membrane picture holds, in order to obtain explicit results in terms of the line tension. In the second part of the paper we focus instead on Dual Unitary circuits and, using the explicit expression for the line tension, we find and compute their temporal entanglement, finding a volume law scaling for the entanglement entropy, and an area law scaling for higher Rényi entropies. Even though we predict the scaling for the entanglement entropy of the influence matrix, as corroborated by numerical simulation, a precise relation between this quantity and approximability of the influence matrix is still lacking.


Temporal Entanglement in Chaotic Quantum Circuits

Alessandro Foligno^{1,2}, Tianci Zhou,³ and Bruno Bertini^{1,2}

¹*School of Physics and Astronomy, University of Nottingham, Nottingham NG7 2RD, United Kingdom*

²*Centre for the Mathematics and Theoretical Physics of Quantum Non-Equilibrium Systems, University of Nottingham, Nottingham, NG7 2RD, United Kingdom*

³*Center for Theoretical Physics, Massachusetts Institute of Technology, Cambridge, Massachusetts 02139, USA*

 (Received 4 March 2023; revised 21 July 2023; accepted 21 August 2023; published 11 October 2023)

The concept of space evolution (or space-time duality) has emerged as a promising approach for studying quantum dynamics. The basic idea involves exchanging the roles of space and time, evolving the system using a space transfer matrix rather than the time evolution operator. The infinite-volume limit is then described by the fixed points of the latter transfer matrix, also known as influence matrices. To establish the potential of this method as a bona fide computational scheme, it is important to understand whether the influence matrices can be efficiently encoded in a classical computer. Here we begin this quest by presenting a systematic characterization of their entanglement—dubbed temporal entanglement—in chaotic quantum systems. We consider the most general form of space evolution, i.e., evolution in a generic spacelike direction, and present two fundamental results. First, we show that temporal entanglement always follows a volume law in time. Second, we identify two marginal cases—(i) pure space evolution in generic chaotic systems and (ii) any spacelike evolution in dual-unitary circuits—where Rényi entropies with index larger than one are sublinear in time while the von Neumann entanglement entropy grows linearly. We attribute this behavior to the existence of a product state with large overlap with the influence matrices. This unexpected structure in the temporal entanglement spectrum might be the key to an efficient computational implementation of the space evolution.

DOI: [10.1103/PhysRevX.13.041008](https://doi.org/10.1103/PhysRevX.13.041008)

Subject Areas: Quantum Physics,
Quantum Information,
Statistical Physics

I. INTRODUCTION

The first two decades of the new millennium witnessed extraordinary experimental progress in measuring dynamical properties of quantum many-body systems. Experiments are now able to probe, for instance, local relaxation of isolated systems [1–3] and out-of-equilibrium transport [4–8] over surprisingly long timescales. Theoreticians, however, can very rarely provide independent predictions to compare with these experiments, especially concerning dynamics beyond intermediate timescale. Indeed, characterizing a quantum many-body system out of equilibrium, or even simulating its state on a classical computer, remains to date a formidable task.

The situation is slightly more favorable in one dimension, where one can use an extension of the celebrated DMRG algorithm [9,10] to provide a faithful representation

of the time-evolving quantum state [11]. The initial state is represented as a matrix product state (MPS), and a suitable evolution algorithm (e.g., (time-dependent)Density Matrix Renormalization Group [12,13] or Time-Evolution Block-Decimation [14,15]) finds an MPS approximation of the state at time t for a given level of accuracy. The problem, however, is that the amount of resources required for such an approximation grows exponentially with the entanglement of the state and, in the absence of localization or other ergodicity-breaking mechanisms, the latter builds up very quickly as time elapses. In practice this means that one needs an exponentially growing amount of resources for an accurate representation of the state. This “entanglement barrier” is physical and cannot be avoided whenever one tries to characterize the whole quantum state. The key question, however, is whether or not it is necessary to simulate the evolution of the whole quantum state to compute its experimentally accessible properties, e.g., its correlation functions.

In the course of the past decade several algorithms have been proposed to circumvent the fast entanglement growth of nonequilibrium states [16–26]. The common theme is to sidestep the problem by exploiting the fact that one is

Published by the American Physical Society under the terms of the Creative Commons Attribution 4.0 International license. Further distribution of this work must maintain attribution to the author(s) and the published article's title, journal citation, and DOI.

typically only interested in the correlation functions of special observables, for instance, those that are *local* in space. A promising one, which motivates our work, is the so-called “folding algorithm” or “transverse folding algorithm” proposed in Ref. [26] (see also Refs. [27–31]), whose main idea is to evolve the system in space, rather than in time. Taking the one-point function in Fig. 1 as an example, this means that one has to contract its tensor-network representation horizontally, by means of an appropriate space transfer matrix rather than vertically using the time evolution operator. The name of the algorithm derives from the fact that this operation becomes much more efficient when considering the “folded representation” of the correlator, i.e., when folding the tensor network around the center as shown in Fig. 1(b), which doubles the local degrees of freedom but keeps the correlations short-ranged. Physically, the vertical column of tensors beneath the observable implements the unitary evolution of the subsystem of interest—the one where the observable acts—while the sections on its two sides encode the nonunitary action exerted on the subsystem by the rest of the system, i.e., the environment. For instance, in the example of Fig. 1 the system is a single spin (or qudit). Inspired by the Feynman-Vernon influence functional approach [32], Ref. [33] proposed to dub “influence matrices” the portions of the tensor network describing the action of the environment. Note that when the environment becomes very

large, the influence matrices become equal to the left and right fixed points of the space transfer matrix \mathcal{T}_t ; see Fig. 1.

The idea of exchanging space and time to describe infinite systems at finite times proved to be very successful and over the past few years has found interesting applications to the study of spectral statistics and quantum chaos [34–39], entanglement dynamics [40–43], impurity problems [44], and even full-counting statistics of many-body observables [45] and Loschmidt echo [46–48]. When considered as a computational tool for computing correlation functions, however, the folding algorithm has an important limitation: it can only deal with cases where the operator insertions break the translation symmetry in a single spatial point, i.e., one-point functions and, more generally, autocorrelations. In this way one cannot access, for instance, generic two-point functions—such as those needed to compute transport coefficients [49–51]—as they feature two operators separated in both time and space.

Another outstanding question concerns the computational complexity of the folding algorithm. Namely, how hard it is to implement this algorithm on a classical computer for increasingly large times. To answer this question one needs to understand what features of the influence matrices have to be retained to correctly describe expectation values of local operators and what is the amount of resources required to do so. An intuitive estimate can be obtained by studying their entanglement, dubbed “temporal entanglement” [28,52]. Indeed, roughly speaking, if the latter does not grow too fast one can efficiently approximate the influence matrices with matrix product states for arbitrarily high fidelity [55,56]. Following Refs. [28,33], one can argue that temporal entanglement should be small for generic systems. Indeed, the dephasing caused by the environment tends to align corresponding spins in the forward and backward copies (cf. Fig. 1) producing configurations that are diagonal and hence classical. Although plausible, this picture can be proven only in a few special cases. These include certain special chaotic quantum systems—dual-unitary circuits [57]—prepared in a special family of initial states [40,58] and in certain special classes of integrable models [30,59–62]. In generic cases the temporal entanglement is observed to grow in time, even though its growth appears slower than that of spatial entanglement [26,33].

In this work we fill both the aforementioned gaps: (1) We extend the folding algorithm to compute generic two-point functions and (2) we characterize the scaling of temporal entanglement in generic quantum many-body systems.

The main idea for extending the folding algorithm is to embed the two operators in the same system defined on a *timelike surface*, or path, γ , see the illustration in Fig. 2, and evolve it in the orthogonal spacelike direction. In a relativistic field theory one can imagine to implement our construction by boosting to a reference frame where the operators are measured at the same position and then

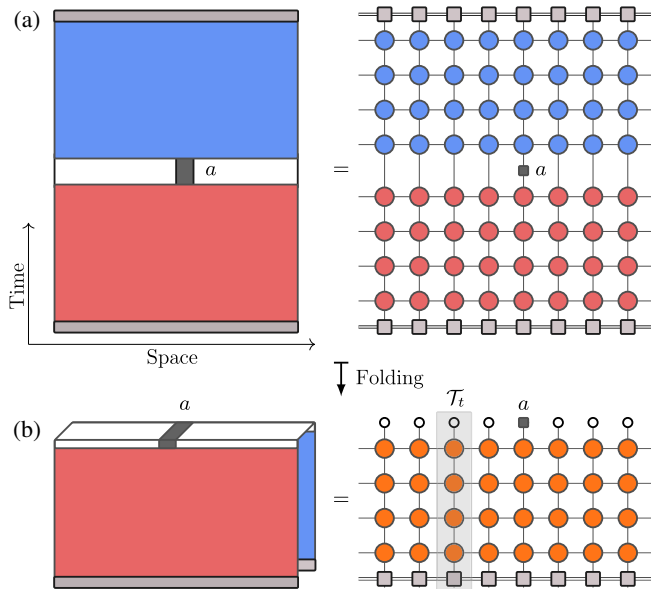


FIG. 1. (a) One-point function of the local operator a after a quantum quench and its tensor-network representation. Forward and backward time sheets are, respectively, depicted in red and blue. (b) The same one-point function of (a) after folding: in the folded tensor network the number of local degrees of freedom is doubled and the white circles at the top of the tensor network denote a loop. The gray shaded box highlights the space transfer matrix \mathcal{T}_t (acting from left to right on a lattice of t sites).

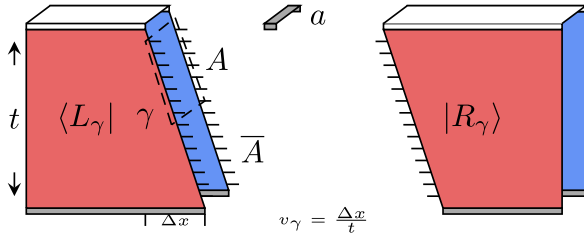


FIG. 2. Generalized influence matrices on a temporal slice γ . The (anti)slope of the path γ is $v_\gamma = \Delta x/t$. When $v_\gamma = 0$, they correspond to the regular influence matrices. A one-point or two-point function can be evaluated by contracting the left state $\langle L_\gamma|$, some relevant operators inserted along the path, and the right state $|R_\gamma\rangle$. The temporal entanglement is the larger among the entanglement of $\langle L_\gamma|$ and that of $|R_\gamma\rangle$ for a partition A, \bar{A} on a temporal slice.

use the usual folding algorithm. This setup allows us to treat generic two-point functions, and also gives the option to optimize the evaluation of one-point functions by varying the path on which the influence matrices are evaluated. Note that the extreme case of a timelike surface corresponding with the light cone edge has been considered in Ref. [63] and, for this case, Ref. [62] characterized the complexity of the corresponding influence matrices for integrable dual-unitary circuits.

To characterize the scaling of temporal entanglement, we compute the entanglement entropies of the generalized influence matrices $\langle L_\gamma|$ and $|R_\gamma\rangle$ across contiguous bipartitions of γ . We, respectively, denote them by

$$S_{L,A}^{(\alpha)}(\gamma) \quad \text{and} \quad S_{R,A}^{(\alpha)}(\gamma), \quad (1)$$

for subregion A and Rényi index α . Our findings are summarized in Table I.

Overall we find that the temporal von Neumann entropy ($\alpha = 1$) always grows linearly in time after a quench from a generic initial state. Nevertheless, we find cases in which Rényi entropies with index $\alpha > 1$ (higher Rényi entropies from now on) grow sublinearly. In particular, the higher Rényi entropies of vertical influence matrices (the regular ones) in *any* chaotic system are logarithmic in time, while those of *any* influence matrix in a dual-unitary circuit are

bounded by a constant. In these cases the slope of growth of von Neumann entropy is strictly smaller than that of regular state entanglement. These statements are proven analytically for dual-unitary circuits, while in the case of generic circuits they result from the combination of entanglement membrane theory [64,65] and numerical observations.

The observed linear growth of von Neumann entanglement entropy rules out an efficient high-fidelity approximation of the influence matrices via matrix product states [56]. Our findings, however, suggest that there are physically relevant cases where the temporal entanglement spectrum displays a strong separation of scales: There are a few large (at most linearly decaying) Schmidt values and many exponentially small ones. This remarkable structure might be the key for an efficient implementation of the folding algorithm.

In the following subsection, we sketch the key steps to obtain the scalings in Table I and discuss their consequences. A complete description of our setup begins in Sec. II.

A. Summary of approaches and results

We consider generic quantum many-body systems with local interactions modeled by local brickwork quantum circuits [66]. This is a class of locally interacting systems in discrete time that has recently played a key role in understanding many-body quantum dynamics. The enormous complexity of the latter implies that the theoretical description, or even the mere numerical simulation, of quantum matter out of equilibrium is practically possible only in the short-time regime. Brickwork quantum circuits simplify the picture by imposing strictly local interactions over a finite time step and give rare examples where local observables and information theoretical quantities can be determined at all times. The results obtained in these systems, for instance, through random averaging [64,67–70] and/or space-time duality [40,58,63,71–77], have significantly advanced our understanding of universal properties of the dynamics. Applications include, for instance, operator dynamics and information spreading [64,67–70,78–80], statistical properties of the spectrum [34–39,81–84], and, more broadly, thermalization [58–60,83,85–87]. We also note that quantum circuits are vital tools for experimental

TABLE I. Scaling of the temporal entanglement. We take the second Rényi entropy as a representative of higher Rényi entropies. The maximum is taken over L, R states and the possible contiguous regions A on γ for a given slope v_γ . All the circuits have a brickwork architecture (see Sec. II). Only vertical cuts or dual-unitary circuits give sublinear growth in higher Rényi entropy. Italic font denotes analytical results (obtained by membrane picture or exact calculation), bold font denotes numerical evidence.

	$\max[S_{L,A}^{(1)}(\gamma), S_{R,A}^{(1)}(\gamma)]$	$\max[S_{L,A}^{(2)}(\gamma), S_{R,A}^{(2)}(\gamma)]$
Generic circuit ($v_\gamma \neq 0$)	$\sim t$	$\sim t$
Generic circuit ($v_\gamma = 0$)	$\sim t$	$\lesssim \log t$
Generic dual-unitary circuit	$\sim t$	~ 1

simulation of quantum systems and quantum computation. For instance, they can be used to demonstrate quantum advantage [88–91], to perform randomized benchmarking [92–95], randomized measurements [96–101], shadow tomography [102–104], and, more generally, to study nonequilibrium dynamics of Floquet systems [105,106].

The structure of these circuits look like a Suzuki-Trotter [107,108] approximation of (local) Hamiltonian evolution, but the unitary gates are not necessarily infinitesimal in time or close to the identity: They can be arbitrary unitaries (see the detailed illustration of our setup in Sec. II).

To understand the behavior of $S_{L/R,A}^{(\alpha)}(\gamma)$ in generic circuits, we take the gates forming the brickwork structure to be independent Haar random matrices. By averaging over the random gates the calculation of entanglement related quantities is mapped into that of the free energy of a statistical mechanical model of emergent spins [64,65]. In particular, we find that the averaged temporal purity,

$$\overline{\exp\left(-S_{L/R,A}^{(2)}(\gamma)\right)}, \quad (2)$$

is the difference of free energies of the same statistical model subjected to different boundary conditions. By minimizing the free energies we find domain-wall configurations that give (cf. Sec. IV)

$$\overline{\exp\left(-S_{L/R,A}^{(2)}(\gamma)\right)} \simeq e^{-v_{\text{TE}}^{(2)} t \log d}, \quad (3)$$

where the linear coefficient $v_{\text{TE}}^{(2)} \geq 0$ is determined by the line tension $\mathcal{E}_H(v)$ of the membrane separating the different domains. The line tension is an intrinsic function of the membrane, which, in translational invariant systems (at least after disorder average), only depends on the space-time slope v . Although the explicit expression is complicated, we have a useful condition,

$$v_{\text{TE}}^{(2)} = 0 \Leftrightarrow \mathcal{E}_H(v_\gamma) = \mathcal{E}_H(0), \quad (4)$$

where v_γ is the antislope [109] of the path γ ; see Fig. 2.

Equation (3) results in a lower bound of the typical growth rates of the temporal entanglement entropies. In particular, we have

$$\begin{aligned} \overline{S_{L/R,A}^{(1)}(\gamma)} &\geq v_{\text{TE}}^{(2)} \log(d)t, \\ \overline{S_{L/R,A}^{(\alpha>1)}(\gamma)} &\geq \frac{1}{2} v_{\text{TE}}^{(2)} \log(d)t. \end{aligned} \quad (5)$$

In fact, following Ref. [69], we argue that this conclusion can be applied to generic Floquet circuits even in the absence of randomness. In this case the entanglement dynamics is still described by an emergent statistical mechanical model and the tension of the associated membrane can be determined perturbatively, dressing the

membrane tension of the Haar random circuit [69]. In practice this means that one can apply Eq. (5) without the average by replacing $\mathcal{E}_H(v)$ by $\mathcal{E}(v)$. Therefore, for generic Floquet circuits and generic paths γ , the temporal entanglement entropies with Rényi index $\alpha \geq 1$ grow linearly in time [110].

Equation (4), however, also suggests that there are two interesting marginal cases where temporal entanglement entropies can be sublinear.

(I) Constant line tension, i.e.,

$$\mathcal{E}(v) = \text{const.} \quad (6)$$

(II) Vertical path, i.e.,

$$v_\gamma = 0. \quad (7)$$

Condition (I) provides a very stringent constraint. Indeed, invoking general properties of the line-tension function [111], one can conclude that a constant line tension has to be equal to one. This in turn implies a maximal growth rate of the regular *spatial* entanglement after a quantum quench in the circuit. As shown in Refs. [69,112], circuits with this property have to be *dual unitary*.

On the contrary, condition (II) does not involve the line-tension function; it only requires the temporal surface to be vertical (i.e., it holds for regular influence matrices). This means that, intriguingly, the vanishing of the linear coefficient at $v_\gamma = 0$ should occur for generic circuits.

The two marginal cases (I) and (II) are studied in detail in Secs. V and VI. There we show that in both cases higher Rényi entropies ($\alpha > 1$) display a sublinear growth in time. Nevertheless, their von Neumann entropy ($\alpha = 1$) grows *linearly* (second and third rows of Table I). Namely, one cannot evaluate the scaling of von Neumann entropy via a replica trick as the replica limit does not commute with the large-time limit. Interestingly, a similar discrepancy in the scaling of Rényi entropies was also observed in Refs. [113,114] for the behavior of the “regular” spatial entanglement in circuits with conservation laws.

At the level of entanglement spectrum the mechanism driving the observed sublinear scaling is the same in both cases (I) and (II): the influence matrices have large overlap with a product state of the form $|\Psi'_A\rangle \otimes |\Psi''_{\bar{A}}\rangle$ on A and \bar{A} . Then, an immediate application of Eckart-Young’s theorem [115] implies that the reduced density matrices,

$$\rho_{L,\gamma,A} = \frac{\text{tr}_{\bar{A}}(|L_\gamma\rangle\langle L_\gamma|)}{\| |L_\gamma\rangle\|^2}, \quad \rho_{R,\gamma,A} = \frac{\text{tr}_{\bar{A}}(R_\gamma |R_\gamma\rangle)}{\| |R_\gamma\rangle\|^2}, \quad (8)$$

have at least one slowly decaying eigenvalue. This eigenvalue determines the slow growth of higher Rényi entropies. Meanwhile, we find exponentially many other eigenvalues of $\rho_{L/R,\gamma,A}$ that decay exponentially fast with time t . This produces a linearly growing entanglement

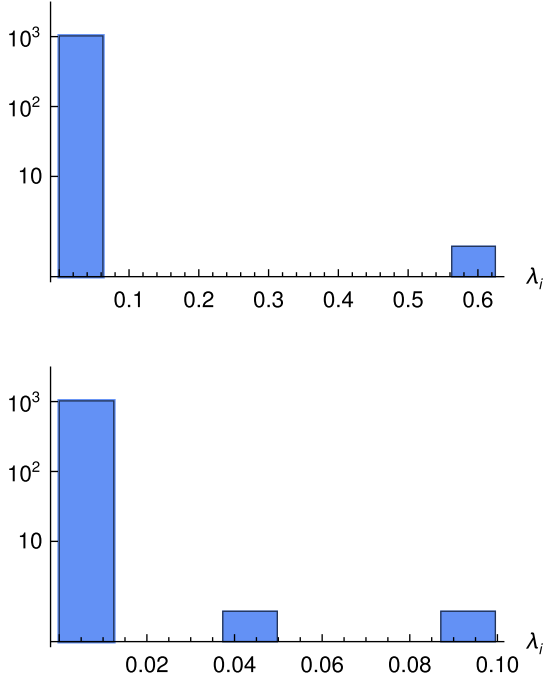


FIG. 3. Schmidt values λ_i for the bipartition of $\langle L_\gamma \rangle$ in two subsystems of equal size for $t = 5$. The y axis reports the number of Schmidt values within a small bin centered on λ_i . The top panel corresponds to the marginal case (I) [cf. Eq. (6)] while the bottom panel corresponds to the marginal case (II) [cf. Eq. (7)].

entropy $S_{L/R,A}^{(1)}(\gamma)$. Figure 3 shows the separation of scales in the entanglement spectrum of the temporal state in two representative examples.

In this situation one might be inclined to conclude that the singular states corresponding to the large Schmidt values represent the dominant part of the state. The linear growth of the von Neumann entropy, however, excludes the possibility of constructing a high-fidelity approximation of the state by keeping a polynomial number of Schmidt eigenvectors. Nevertheless, if the objective is to only approximate special observables, for instance, the one-point function $\text{tr}[\rho_0 a_x(t)]$, the answer might be different. More generally, it is interesting to ask how much physically relevant information can be extracted faithfully from the first few Schmidt eigenstates in cases with such a strong separation of scales. We leave these questions to future research.

The rest of this paper is laid out as follows. In Sec. II we introduce the precise setting considered in this work. In Sec. III we discuss the folding algorithm and explain its extension to nonvertical cuts. In Sec. IV we determine the scaling of temporal entanglement in generic quantum circuits using the entanglement-membrane approach of Refs. [64,65,69]. The two marginal cases with sublinear growth of higher Rényi entropies are analyzed in Secs. V and VI. In particular, in Sec. V we discuss the scaling of temporal entanglement in dual-unitary circuits evolving from generic initial states, while in Sec. VI we study the scaling of regular temporal entanglement, i.e., of the

influence matrix on the vertical cut, in generic circuits. In Sec. VII we compare the growth of temporal entanglement and that of regular state entanglement. Our conclusions and final remarks are reported in Sec. VIII.

II. SETTING

We consider the quantum dynamics generated by local quantum circuits acting on a chain of $2L$ qudits (d internal states) placed at half integer positions. These circuits have nearest-neighbor interactions, and are often dubbed “brickwork” quantum circuits. The operator performing one step of evolution alternatively evolves the even and odd sublattices:

$$\mathbb{U} = \mathbb{U}_1 \mathbb{U}_2. \quad (9)$$

Here we introduced

$$\mathbb{U}_1 = \bigotimes_{x \in \mathbb{Z}_L} U_{x,x+1/2}, \quad \mathbb{U}_2 = \bigotimes_{x \in \mathbb{Z}_L+1/2} U_{x,x+1/2}, \quad (10)$$

with $U_{x,x+1/2}$ acting nontrivially, as the $d^2 \times d^2$ unitary matrix U , only on the qudits at positions x and $x + 1/2$. The matrix U is known as “local gate” and specifies the local interactions. Local gates can in principle be different at each space-time point, i.e.

$$U \mapsto U(t, x), \quad (11)$$

representing a disordered system undergoing aperiodic quantum dynamics. In contrast, in the special case where all local gates coincide, the quantum circuit constitutes a clean (two-site shift invariant), periodically driven system.

A useful property of the local gate, which we use later to identify quantum circuits with similar dynamical features, is its *entangling power*. Roughly speaking, the latter is a measure of the ability of the gate to entangle two qubits [116]. Normalizing it to be in $[0, 1]$, the entangling power can be expressed as [116]

$$p(U) = \frac{d^4 + d^2 - \text{tr}(U^R U^{R\dagger})^2 - \text{tr}[(US)^R (US)^{R\dagger}]^2}{d^2(d^2 - 1)}. \quad (12)$$

Here U^R indicates the gate obtained by rotating the original gate U by a right angle

$$\langle lj|U^R|ki \rangle = \langle kl|U|ij \rangle, \quad i, j, k, l = 0, \dots, d-1, \quad (13)$$

and S denotes the SWAP gate,

$$\langle ij|S|lk \rangle = \delta_{i,k} \delta_{j,l}. \quad (14)$$

Here we are interested in the evolution of the system for $t > 0$. At $t = 0$ the system is prepared in a generic “pair-product” state,

$$|\Psi_0\rangle = \frac{1}{d^{L/2}} \bigotimes_{x=1}^L \left(\sum_{i,j=0}^{d-1} m_{ij} |i\rangle \otimes |j\rangle \right), \quad (15)$$

where $\{|i\rangle\}_{i=0}^{d-1}$ is a basis of the configuration space of a single qudit—the “local” Hilbert space. The matrix m , with elements m_{ij} , fulfills

$$\text{tr}[mm^\dagger] = d, \quad (16)$$

which ensures that $|\Psi_0\rangle$ is normalized to one. We consider general pair-product states, rather than simple product states, to keep the staggered structure of the brickwork quantum circuit. Note that a product state is recovered by the choice

$$m_{ij} \propto \delta_{i,i_0} \delta_{j,j_0}, \quad i_0, j_0 \in \{0, \dots, d-1\}, \quad (17)$$

while generically one can think of Eq. (15) as a product state which has been subject to half a step of evolution.

The evolution in a quantum circuit can be conveniently illustrated using a tensor-network-inspired graphical representation [117]. In particular, depicting the components of the local gate and the initial state matrix as

$$U_{(k,l);(i,j)} = \begin{array}{c} k \quad l \\ \diagup \quad \diagdown \\ \square \\ \diagdown \quad \diagup \\ i \quad j \end{array}, \quad m_{ij} = \begin{array}{c} i \quad j \\ \diagup \quad \diagdown \\ \bullet \\ \diagdown \quad \diagup \end{array}, \quad (18)$$

we can represent the state of the system at time t as follows:

$$|\Psi_t\rangle = \frac{1}{d^{L/2}} \begin{array}{c} \text{Diagram of a brickwork quantum circuit with red squares and legs} \end{array}, \quad (19)$$

where we considered $t = 3$. As illustrated in the above diagram, we depicted the periodic boundary conditions by connecting left and right boundaries, and used the convention that when legs of different tensors are joined together the index of the corresponding local space is summed over. Moreover, we drop the indices to represent the full vector rather than its components. We will use this convention whenever it does not lead to confusion.

Let us consider the evolution of the reduced density matrix of a finite region A . Representing it diagrammatically, we have

$$\rho_A(t) = \frac{1}{d^{|A|}} \begin{array}{c} \text{Diagram of a brickwork quantum circuit with red and blue squares and legs} \end{array}, \quad (20)$$

where we took $A = \{1, 3/2, 2, 5/2\}$ and introduced a diagrammatic representation for the Hermitian conjugate of the local gate,

$$U^\dagger = \begin{array}{c} \text{Diagram of a blue square with legs} \end{array}, \quad (21)$$

and the complex conjugate of the initial state matrix,

$$m^* = \begin{array}{c} \text{Diagram of a blue dot with legs} \end{array}. \quad (22)$$

Using this representation we can depict the unitarity of the local gate with the following diagrammatic relations

$$\begin{array}{c} \text{Diagrammatic relations showing unitarity of the local gate} \end{array}. \quad (23)$$

To simplify the diagrams it is convenient to fold them in two. In particular, folding the blue part of the circuit underneath the red one, we can represent the reduced density matrix in Eq. (20) as follows,

$$\rho_A(t) = \frac{1}{d^{|A|/2}} \begin{array}{c} \text{Diagram of a folded brickwork quantum circuit with orange squares and legs} \end{array}, \quad (24)$$

where we introduced the *double gate*,

$$\begin{array}{c} \diagup \\ \boxed{\text{orange}} \\ \diagdown \end{array} := W = U \otimes_r U^*, \quad (25)$$

the *double initial-state matrix*,

$$\begin{array}{c} \diagup \\ \bullet \\ \diagdown \end{array} = m \otimes_r m^*, \quad (26)$$

the *loop state*,

$$\begin{array}{c} \diagup \\ \bigcirc \\ \diagdown \end{array} = \frac{1}{\sqrt{d}} \bigcup := |\bigcirc\rangle, \quad (27)$$

and, finally, the shorthand notation,

$$|A| := (\text{no of sites in } A). \quad (28)$$

In the above equations \otimes_r denotes the tensor product between different copies or *replicas* of the time sheet (different from \otimes which is the one between different spatial sites in the same copy).

In this folded representation, the unitarity relations (23) are depicted as

$$\begin{array}{c} \diagup \\ \boxed{\text{orange}} \\ \diagdown \end{array} = \begin{array}{c} \diagup \\ \bullet \\ \diagdown \end{array}, \quad \begin{array}{c} \diagdown \\ \boxed{\text{orange}} \\ \diagup \end{array} = \begin{array}{c} \diagdown \\ \bullet \\ \diagup \end{array}. \quad (29)$$

Moreover, since the double gate is itself unitary, we also have

$$\begin{array}{c} \diagup \\ \boxed{\text{orange}} \\ \diagdown \\ \boxed{\text{green}} \\ \diagup \end{array} = \begin{array}{c} \diagup \\ \boxed{\text{green}} \\ \diagdown \\ \boxed{\text{orange}} \\ \diagup \end{array} = \begin{array}{|c|} \hline \\ \hline \end{array}, \quad (30)$$

where we introduced

$$\begin{array}{c} \diagdown \\ \boxed{\text{green}} \\ \diagup \end{array} := W^\dagger = U^\dagger \otimes_r U^T. \quad (31)$$

III. GENERALIZED FOLDING ALGORITHM AND GENERALIZED TEMPORAL ENTANGLEMENT

A standard class of observables in quantum circuits are correlation functions of local operators. In particular, let us focus on nonequilibrium dynamical two-point functions of the form

$$C_{ab}(x_1, x_2, t_1, t_2) = \text{tr}[\rho_0 a_{x_1}(t_1) b_{x_2}(t_2)], \quad (32)$$

where we took $t_2 \geq t_1 \geq 0$, $a_x := a_x(0)$ and $b_x := b_x(0)$ are local operators, and $\rho_0 = |\Psi_0\rangle\langle\Psi_0|$ is the initial state [cf. Eq. (15)]. Note that Eq. (32) contains nonequilibrium one-point functions as a special case that is obtained by setting $a_x = \mathbb{1}$.

In fact, the upcoming discussion will also be applicable to the case where ρ_0 is the infinite-temperature state, which, in generic situations, is the only stationary state of the system. In this case the correlation takes the following equilibrium form:

$$C_{ab}^{\text{eq}}(x_1, x_2, t) = \text{tr}[a_{x_1} b_{x_2}(t)]. \quad (33)$$

Because of the strict light cone structure of the quantum circuit, the correlation function (32) is nontrivial (i.e., causally connected) only if [see Fig. 5(b)]

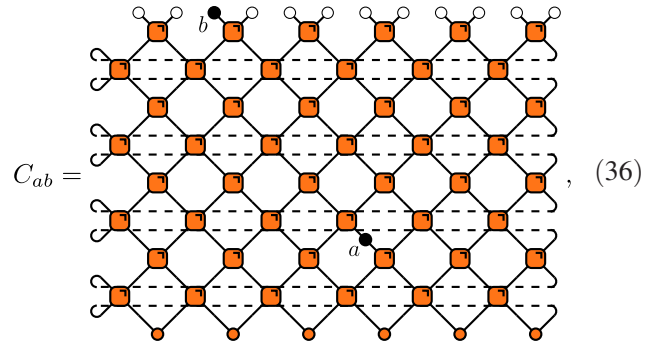
$$|[x_1] - [x_2]| \leq t_1 + t_2. \quad (34)$$

while Eq. (33) only if

$$|[x_1] - [x_2]| \leq t. \quad (35)$$

For the sake of definiteness from now on we assume $x_2 < x_1$ and $x_1, x_2 \in \mathbb{Z}_L$, while to lighten the notation we drop the dependence of the correlation on x_1, x_2, t_1, t_2 .

Considering this case we can represent Eq. (32) diagrammatically as



where, for simplicity, we assumed that a_x and b_x act nontrivially only on one site, we depicted them as

$$a \bullet = a \otimes_r \mathbb{1}, \quad b \bullet = b \otimes_r \mathbb{1}, \quad (37)$$

and set

$$a \bullet = \bullet a. \quad (38)$$

Let us now illustrate how the diagram (36) can be evaluated using the folding algorithm of Ref. [26]. The starting point is to represent it in terms of transfer matrices “in space.” Namely, one introduces three different transfer matrices

$$\mathcal{T}_x = \text{[diagram]}, \quad \mathcal{T}_x^{(a)} = \text{[diagram]}, \quad \mathcal{T}_x^{(b)} = \text{[diagram]}, \quad (39)$$

$$|R_x\rangle = \text{[diagram]}, \quad (43)$$

so that the diagram (36) can be written as

$$C_{ab} = \text{tr}[\mathcal{T}_1 \cdots \mathcal{T}_{x_2-1} \mathcal{T}_{x_2}^{(b)} \mathcal{T}_{x_2+1} \cdots \mathcal{T}_{x_1-1} \mathcal{T}_{x_1}^{(a)} \mathcal{T}_{x_1+1} \cdots \mathcal{T}_L], \quad (40)$$

where we consider the generic case of nontranslational invariant circuits. We remark that the space transfer matrices in Eq. (39) are matrix product operators (MPOs) with finite bond dimension $\chi = d^2$.

The next step is to note that unitarity can simplify products of transfer matrices. To illustrate this point, let us write down the product of $2t_2$ transfer matrices $[\mathcal{T}_x$ in Eq. (39)]. In diagrams it takes the following form:

$$\text{[diagram]} \quad (41)$$

Unitarity [cf. Eq. (30)] allows us to cancel all the gates above the red dashed lines and propagate the bullets to the legs crossing the dashed lines. We therefore have the following rank-1 decomposition,

$$\mathcal{T}_{y_1} \cdots \mathcal{T}_{y_{2t_2}} = |R_{y_1}\rangle \langle L_{y_{2t_2}}|, \quad \forall y_j, \quad (42)$$

where we introduced the following vectors on the folded time lattice,

$$\langle L_x| = \text{[diagram]} \quad (44)$$

This means that, for $L > x_2 - x_1 + 2t_2$, Eq. (51) can be written as

$$C_{ab} = \langle L_{x_1-1} | \mathcal{T}_{x_1}^{(a)} \mathcal{T}_{x_1+1} \cdots \mathcal{T}_{x_2-1} \mathcal{T}_{x_2}^{(b)} | R_{x_2+1} \rangle. \quad (45)$$

This representation sheds light on the physical interpretation of the two vectors $\langle L_x|$ and $|R_x\rangle$. These objects encode the effect of the rest of the system on the subsystem of size $x_2 - x_1$ where a_x and b_x act. Since their role is analogous to that of the influence functional of Feynman and Vernon [32], they have been dubbed “influence matrices” [33]. Note that in the translational invariant case one can use Eq. (42) to show that $\langle L_x|$ and $|R_x\rangle$ are the unique *fixed points*, i.e., eigenvectors corresponding to eigenvalue one, of the space transfer matrix \mathcal{T} (which is x independent in translational invariant circuits).

The representation (45) is the main instrument of the folding algorithm. Assuming that one can find an efficient MPS representation for the influence matrices (see Sec. III B), Eq. (45) gives a way to compute two-point functions as matrix elements of an MPO—the product of $x_2 - x_1 + 1$ space transfer matrices—between two MPSs. Since the bond dimension of the MPO is bounded by $d^{2(x_2-x_1+1)}$, this operation can be performed efficiently for small distances $x_2 - x_1$. On the other hand, the computation becomes rapidly unfeasible when the distance increases. This represents a serious limitation as, for instance, two-point functions for arbitrary distances fulfilling Eq. (34) are needed to compute transport coefficients in linear response [49–51]. To circumvent this problem we propose an alternative method for contracting the diagram in Eq. (36): Instead of contracting it

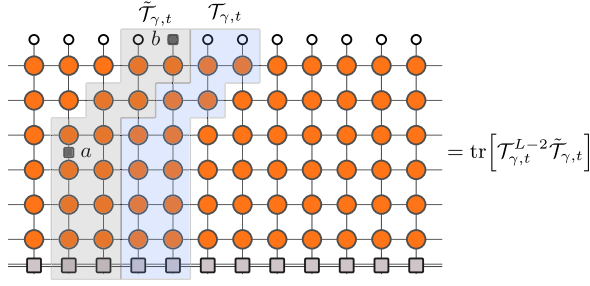


FIG. 4. Folded tensor-network representation of a dynamical two-point function of two operators a and b after a quantum quench. The tensor network can be contracted using nonvertical transfer matrices that follow the timelike path γ and propagate in the spacelike direction orthogonal to γ . The two different transfer matrices used are highlighted in the boxes.

in the space direction, we contract it in a more general spacelike direction such that the two points lie on the same timelike surface; see the macroscopic-scale illustration in Fig. 2; an example in terms of the associated tensor network is depicted instead in Fig. 4. The only relevant macroscopic feature of the timelike surface is its the space-time slope v_γ . A more precise lattice definition is given in Sec. III A, while in Sec. III B we discuss the computational complexity of encoding the influence matrices in an MPS.

A. Generalized folding algorithm

For a precise definition of the generalized folding algorithm it is useful to distinguish between two different regimes:

- (I) $0 \leq x_2 - x_1 \leq t_2 - t_1$,
- (II) $t_2 - t_1 < x_2 - x_1 \leq t_2 + t_1$.

Note that regime (II) only arises out of equilibrium: the equilibrium correlation in Eq. (33) exists only in the regime (I). Moreover, regime (I) is also the only regime arising for nonequilibrium one-point functions.

1. Regime (I)

In this regime there exists a path $\tilde{\gamma}$ connecting a and b that is entirely contained in the causal light cone emanating

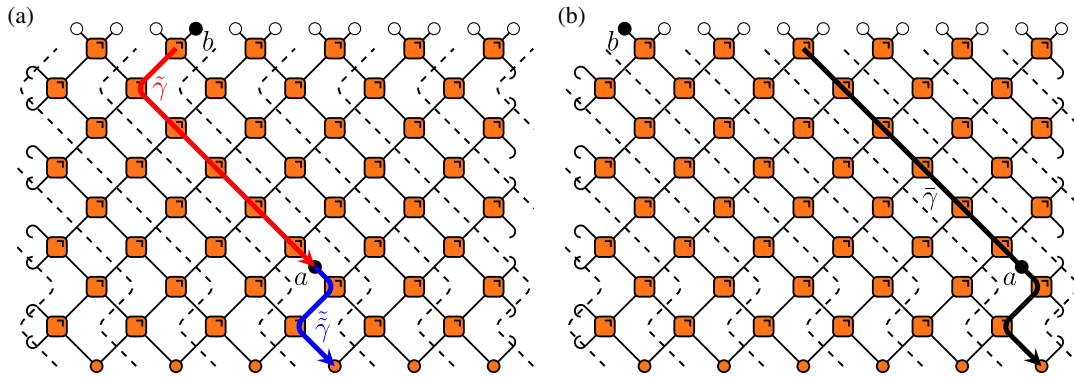


FIG. 5. Diagrammatic representation of the path to contract correlation functions. Panels (a) and (b) depict examples of paths used in the contraction of the correlation functions in the regimes I and II, respectively. Dashed lines help to identify the transfer matrix and time slices to cut open the diagram.

from a ; i.e., it goes from a to b without ever “turning back.” We call this kind of paths *timelike paths*, because all the space-time points they reach are causally connected.

To specify $\tilde{\gamma}$ we start from the gate below b and move down in discrete jumps; see Fig. 5(a). At each jump we reach one neighboring gate: either the one at southeast or the one at southwest. Using the variable $\tilde{\gamma}_i = \pm$ to keep track of whether on the i th step we jump on the left or on the right, we can represent the path by means of the following sequence,

$$\tilde{\gamma} = \{\tilde{\gamma}_1, \dots, \tilde{\gamma}_N\}, \quad (46)$$

where $N = 2(t_2 - t_1) - 1$ is the length of the path. For instance,

$$\tilde{\gamma} = \{-, +, +, +, +\} \quad (47)$$

is the path depicted in red in Fig. 5(a). The path $\tilde{\gamma}$ can be extended to a path γ that reaches the initial state by concatenating it with another timelike path $\tilde{\tilde{\gamma}}$ from (x_1, t_1) to $(y, 0)$ for some $y \in [x_1 - t_1, x_1 + t_1]$. The total length of the path γ , i.e., the total number of jumps, is then $2t_2$. For instance, in the example of Fig. 5 one can consider

$$\gamma = \{-, +, +, +, +\} \circ \{+, -, +\}, \quad (48)$$

where \circ denotes the composition operator. The average slope of a given path γ is given by

$$v_\gamma = \frac{1}{|\gamma|} \sum_{i=1}^{|\gamma|} \gamma_i, \quad (49)$$

where $|\gamma|$ is the length of the path. As mentioned before, v_γ is the only bit of information required for a coarse grained description of the path.

Since the path γ does not turn back, we can use it to “slice” the diagram of the correlation function. Namely, we

subdivide it in a number of timelike slices by cutting the bonds in a direction parallel to γ (see the black dashed lines in Fig. 5) and connect them with suitably defined transfer matrices. In particular, for the configuration in Fig. 5(a) the transfer matrices are given by

$$\mathcal{T}_{\gamma,x} = \text{[Diagram]}, \quad \mathcal{T}_{\gamma,x}^{(ab)} = \text{[Diagram]}. \quad (50)$$

In this way we can write Eq. (36) as

$$C_{ab} = \text{tr}[\mathcal{T}_{\gamma,1} \cdots \mathcal{T}_{\gamma,x_1-1} \mathcal{T}_{\gamma,x_1}^{(ab)} \mathcal{T}_{\gamma,x_1+1} \cdots \mathcal{T}_{\gamma,L}]. \quad (51)$$

This expression can again be simplified using the unitarity of the gates. In particular, we again have

$$\mathcal{T}_{\gamma,y_1} \cdots \mathcal{T}_{\gamma,y_2} = |R_{\gamma,y_1}\rangle \langle L_{\gamma,y_2}|, \quad \forall y_j, \quad (52)$$

where we introduced the generalized or “boosted” influence matrices:

$$\langle L_{\gamma,x}| = \text{[Diagram]}, \quad (53)$$

$$|R_{\gamma,x}\rangle = \text{[Diagram]}. \quad (54)$$

Therefore, for $L > 2t_2$, we find

$$C_{ab} = \langle L_{\gamma,x_1-1} | \mathcal{T}_{\gamma,x_1}^{(ab)} | R_{\gamma,x_1+1} \rangle. \quad (55)$$

As opposed to Eq. (45), this expression can always be efficiently contracted if $\langle L_{\gamma,x}|$ and $|R_{\gamma,x}\rangle$ admit an efficient MPS representation.

2. Regime (II)

In this regime there is no timelike path connecting a and b . This means that we cannot embed both a and b in the same “thin” transfer matrix as done in Eq. (55). The best strategy in this case is to slice the diagram (36) using transfer matrices corresponding to the path $\tilde{\gamma} = \gamma_{\text{lc}} \circ \tilde{\gamma}$, where

$$\gamma_{\text{lc}} = \{+, \dots, +\} \quad (56)$$

is the fastest path allowed by causality (i.e., on the edge of the light cone) and $\tilde{\gamma}$ is an arbitrary timelike path between the initial state and a [cf. Fig. 5(b)]. Repeating the above analysis we find that for $L > x_2 - x_1 + t_2 + t_1$ the correlations can be expressed as

$$C_{ab} = \langle L_{\tilde{\gamma},x_1-1} | \mathcal{T}_{\tilde{\gamma},x_1}^{(a)} \mathcal{T}_{\tilde{\gamma},x_1+1} \cdots \mathcal{T}_{\tilde{\gamma},x_2-t_2+t_1-1} \mathcal{T}_{\tilde{\gamma},x_2-t_2+t_1}^{(b)} | R_{\tilde{\gamma},x_2-t_2+t_1+1} \rangle, \quad (57)$$

where we introduced

$$\mathcal{T}_{\gamma,x}^{(a)} = \text{[Diagram]}, \quad \mathcal{T}_{\gamma,x}^{(b)} = \text{[Diagram]}. \quad (58)$$

We see that the expression (57) involves the product of

$$n = x_2 - x_1 - t_2 + t_1 + 1 \quad (59)$$

transfer matrices, which means $0 \leq n \leq 2t_1$. This has two immediate implications. First, the representation (57) gives an advantage over Eq. (45) because it involves fewer transfer matrices. Second, when both $x_2 - x_1$ and t_1 are large the contraction of Eq. (57) becomes inefficient.

B. Generalized temporal entanglement

In extreme summary, the upshot of the previous subsection is that an efficient representation of the generalized

influence matrices does indeed lead to an efficient computational scheme for the calculation of correlation functions in many physically relevant cases [118]. This motivates us to investigate whether an efficient representation of the generalized influence matrices is possible. In particular, here we assess whether these objects admit an efficient MPS representation by computing their entanglement. This is the fundamental question to which the rest of this paper is devoted.

The entanglement of the influence matrices is computed in three steps.

- (i) We define reduced density matrices corresponding to an arbitrary nondisjoint bipartition $A\bar{A}$ of the lattice along the path γ :

$$\rho_{H,\gamma,A} = \text{tr}_{\bar{A}} \frac{|H_{\gamma,x}\rangle\langle H_{\gamma,x}|}{\| |H_{\gamma,x}\rangle \|^2}, \quad H = L, R. \quad (60)$$

- (ii) We compute their Rényi entropies,

$$S_{H,A}^{(\alpha)}(\gamma) := S^{(\alpha)}(\rho_{H,\gamma,A}), \quad H = L, R, \quad \alpha \in \mathbb{R}, \quad (61)$$

where we introduced the function

$$S^{(\alpha)}(\rho) := \frac{1}{1-\alpha} \log \text{tr}[\rho^\alpha]. \quad (62)$$

- (iii) We maximize them over all possible bipartitions $A\bar{A}$ where A is a contiguous region.

Before proceeding we note that

$$\rho_{L,\gamma,A}(W) = \rho_{R,\bar{\gamma},A}(W'), \quad (63)$$

where we highlighted the dependence on the double gate (25), introduced

$$W' = \begin{array}{|c|} \hline \text{L} \\ \hline \end{array}, \quad (64)$$

and denoted by $\bar{\gamma} = \{-\gamma_1, \dots, -\gamma_{2l_2}\}$ the mirror image of the path γ with respect to the vertical line passing through b .

In the following we will use this relation to focus only on the entanglement properties of one of $\langle L_{\gamma,x} |$ and $|R_{\gamma,x}\rangle$: the remaining case can be easily inferred from Eq. (63) upon replacing W with W' . Therefore, from now on we will only look at the entanglement of $\langle L_{\gamma,x} |$, and, to lighten the notation, we set

$$\rho_{L,\gamma,A} \mapsto \rho_{\gamma,A}, \quad S_{L,A}^{(\alpha)}(\gamma) \mapsto S_A^{(\alpha)}(\gamma). \quad (65)$$

Moreover, we also drop the dependence of $\langle L_{\gamma,x} |$ on the point x at which it is computed, i.e.,

$$\langle L_{\gamma,x} | \mapsto \langle L_\gamma |. \quad (66)$$

IV. TEMPORAL ENTANGLEMENT IN GENERIC UNITARY CIRCUITS

In this section we specify the unitary gates in Eq. (18) to be (independent) Haar random matrices. We consider the temporal entanglement of the state in Eq. (53) for a typical realization of the disorder and in the long time limit. In our analysis we focus on initial states in product form; i.e., we take m as in Eq. (17). Indeed, we expect that the choice of the initial state, as long as it is short-range entangled, does not affect the general scaling of entanglement in a random circuit.

The use of the Haar random unitaries follows from the philosophy of random matrix theory. By dispensing with all system-specific details, these strongly chaotic gates allow for analytic calculations while retaining the universal properties of entanglement in strongly interacting systems. Recently, there have been various applications of random unitary circuits to explain aspects of quantum chaos and other nonequilibrium features of generic quantum systems; see, for instance, Refs. [64,67,82,119–125] and the review [66] for a more comprehensive list of references.

The (Rényi) entanglement in a random unitary circuit is described by a statistical mechanical model written in terms of permutation degrees of freedom [65,111,126]. The von Neumann entropy is at the replica limit of the model. The permutations originate from pairings of the unitary evolution with its time reversal. To be more specific, let us consider the example of the n th Rényi entropy, with $\mathbb{N} \ni n \geq 2$, of $\rho_A(t)$: the regular density matrix reduced to a subregion A [cf. Eq. (20)]. In each copy of the time-evolved reduced density matrix $\rho_A(t)$, there is one forward and one backward time sheet [cf. Eq. (24)]. Therefore, in total, there are n forward and n backward time sheets. When performing random averaging over the gates, each copy of a given gate and its Hermitian conjugate are paired in a fashion similar to the Wick theorem of the free fields. The boundary conditions for the Rényi entropies are domain walls between different types of pairings. If we view the pairings as spin degrees of freedom, the effective statistical mechanical model describing the entanglement is in the ordered phase, and the domain wall continues to exist in the bulk, possibly splitting in a cascade of more elementary domain walls. The (Rényi) entanglement entropy is given by the free energy of these generically interacting domain walls. All these microscopic details can be encoded in a coarse grained line tension of the domain wall, which gives rise to the growth rate of entanglement in the long time limit.

In the upcoming subsections we obtain the general scaling of temporal entanglement in three steps

- (1) We show that the boundary conditions to evaluate the purity of $\langle L_\gamma |$ correspond to domain walls in the statistical problem (Sec. IV A).
- (2) Averaging over the random unitary gates, we show that the minimal-energy configurations are those

where the domains penetrate in the bulk. Minimizing the free energies by means of the line-tension formalism we find a linear growth of temporal entanglement (Sec. IV B).

- (3) Recalling the arguments of Ref. [69] we infer that the domain-wall picture can be applied also to a single realization of random circuit (without averaging) or, equivalently, to systems without randomness (Sec. IV C).

A technical note: in the upcoming calculations we consider the state $\langle L_\gamma |$, with the (anti)slope $v \geq 0$; see Fig. 7. Indeed, the $v \geq 0$ condition gives rise to nontrivial domain-wall configurations. In the case $v < 0$ our analysis can be applied to $|R_\gamma\rangle$.

A. Boundary conditions for temporal entanglement

The expression of the n th Rényi entropy contains n copies of the forward and backward evolution by the circuit. The pairings emerge naturally on the boundary when contracting copies of these circuits to evaluate Rényi entropies, with or without random averaging.

Let us illustrate this idea in the example of the purity $\text{tr}[\rho_A^2(t)]$ of the quantum state $\rho_A(t)$; see Fig. 6(a). To form the reduced density matrix $\rho_A(t)$, we take partial trace in each copy of $\rho(t)$. The partial trace operation is denoted as a contraction of the corresponding indices from the forward and backward copies of the circuit. Multiplying two copies of $\rho_A(t)$ and taking the trace, we obtain the SWAP contraction in region A . In this quantity, there are two copies of the unitary gate U and two copies of U^* . There are two ways to contract them, which we denote as $\mathbb{1}$ and (12) permutations:

$$\mathbb{1}: \overbrace{U \otimes U^* \otimes U \otimes U^*}, \quad (12): \overbrace{U \otimes U^* \otimes U \otimes U^*}. \quad (67)$$

The top boundary thus has a domain-wall boundary condition between $\mathbb{1}$ and (12) permutations.

Temporal entanglement is defined for an ‘‘operator state,’’ namely a state in the folded space. Therefore, the ket itself involves a forward and a backward evolution: see, e.g., Eq. (53). The permutation boundary conditions are the same if we were to consider an operator state on a spatial slice, which have been computed explicitly in Ref. [80]. For completeness, we repeat the derivation for the second Rényi entropy for the operator state $\langle L_\gamma |$. The boundary conditions involve permutations in the symmetric group S_4 . The purity of a subregion on the temporal slice is

$$\frac{\text{tr}_A(\text{tr}_{\bar{A}}(|L_\gamma\rangle\langle L_\gamma|)^2)}{\langle L_\gamma | L_\gamma \rangle^2}. \quad (68)$$

Here we choose the initial product state in the diagrams to be normalized to 1, which is different from the m state in Eq. (18). To be consistent with the random circuit literature,

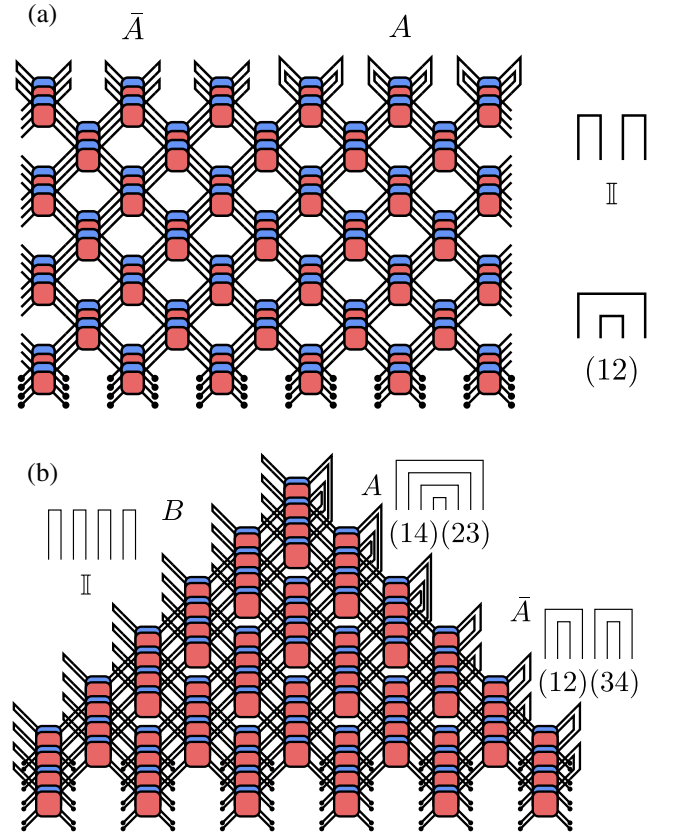


FIG. 6. Permutation boundary conditions for (a) the state purity $\text{tr}[\rho_A^2(t)]$ and (b) the operator purity $\text{tr}_A[\text{tr}_{\bar{A}}(|L_\gamma\rangle\langle L_\gamma|)^2]$. The dots at the bottom represent a generic product initial state. Red gates are forward evolution u ; blue gates are backward evolution u^* . (a) The top boundary conditions implement the partial trace, the matrix multiplication of ρ_A with itself and the trace in \bar{A} . Right: region A has boundary condition $\mathbb{1}$, region \bar{A} has boundary condition (12). (b) The top boundary conditions are permutation elements in S_4 . They are, respectively, given by $\mathbb{1}$, (12)(34), and (14)(23). We consider a general contiguous partition. The ratio of size $|A|$ and the total size $|A| + |\bar{A}|$ is set to be $r \in [0, 1]$.

we choose to normalize the boundary condition as shown in Fig. 6 for upward pointing legs. For downward pointing legs, we use permutations normalized as the loop state as in Eq. (27). The temporal Rényi-2 entropy thus has two terms,

$$S_A^{(2)}(\gamma) = -\log(\text{tr}_A[\text{tr}_{\bar{A}}(|L_\gamma\rangle\langle L_\gamma|)^2]) + 2\log(\langle L_\gamma |), \quad (69)$$

where the second term is twice the Rényi-2 entropy of $A\bar{A}$. The boundary conditions for the first term is shown in Fig. 6(b).

B. Entanglement in terms of domain-wall line tension: Disorder average

In Fig. 6, we see that pairings (permutations) emerge naturally as boundary conditions when evaluating entanglement-related quantities. In fact, in quantum chaotic

systems these pairings are also the dominant degrees of freedom in the interior of the multilayer unitary evolution. One simple way to introduce pairings in the bulk is through random averaging of the gate over Haar ensemble. Indeed, the latter are the only degrees of freedom surviving the average.

Taking the purity diagram in Fig. 6(a) as an example, each four-layer gate after random averaging can only give a tensor of $\mathbb{1}$ or (12) as the output at its bottom legs. Hence we can label the gate with “spin” variables taking values in $\mathbb{1}$ or (12) . The $\mathbb{1}$ and (12) can form contiguous domains connecting to the $\mathbb{1}$ and (12) on the boundary. We label a general domain wall between a pairing σ on the left and a pairing μ on the right as $\sigma^{-1}\mu$. The domain wall between $\mathbb{1}$ and (12) is thus $\mathbb{1}^{-1}(12) = (12)$. Because of constraints from unitarity and locality of the interactions, this (12) domain wall can only wander within the light cone and cannot branch. The entanglement is the free energy, or tension, of the domain wall. Since disorder fluctuations are negligible over large enough scales, the system is asymptotically translationally invariant and the domain wall macroscopically should be a straight line. Using v to denote the inverse of the domain wall’s slope, we can write the Rényi entropy at leading order as

$$-\log \overline{\text{tr}[\rho_A^2(t)]} \simeq s_{\text{eq}} \min_v \mathcal{E}_H(v) t, \quad (70)$$

where $\overline{\cdot}$ denotes the average over Haar random gates, $\mathcal{E}_H(v)$ is the line tension of a domain wall in the Haar random circuit [127],

$$\mathcal{E}_H(v) = \frac{\log \frac{d^2+1}{d} + \frac{1+v}{2} \log \frac{1+v}{2} + \frac{1-v}{2} \log \frac{1-v}{2}}{\log d}, \quad (71)$$

and s_{eq} is the infinite temperature equilibrium entropy $\log d$ (we recall that d is the local Hilbert space dimension). For a generic product initial state, the domain-wall end point at the bottom is not fixed and the Rényi entropy is obtained by minimizing over different slopes.

Since the random circuit is left-right symmetric after disorder averaging, the minimum in Eq. (70) is taken at $v = 0$, i.e., a vertical line; see Fig. 7(a). This gives a linear growth where the line tension is the entanglement growth rate, which is called entanglement velocity [128].

Let us now consider the entanglement of the operator state $\langle L_\gamma \rangle$. In particular, we consider the following averaged version of it:

$$\bar{S}_A^{(2)}(\gamma) := -\log \overline{\text{tr}_A[\text{tr}_{\bar{A}}(|L_\gamma\rangle\langle L_\gamma|)^2]} + \log \overline{(\langle L_\gamma | L_\gamma \rangle)^2}. \quad (72)$$

As noted above, this quantity involves permutations in S_4 . In this case the leading contribution is again given by suitable domain walls; however, differently from before

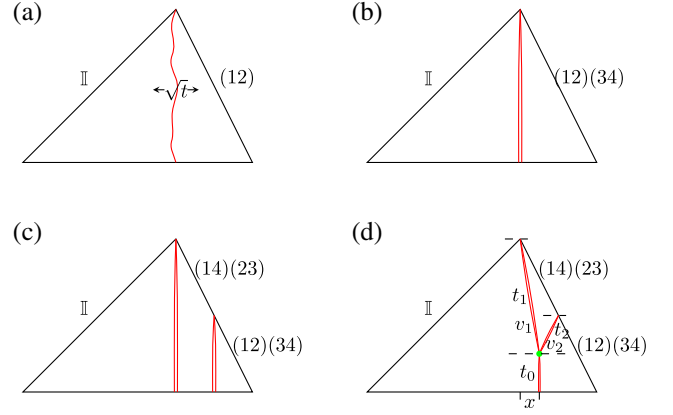


FIG. 7. Domain-wall configurations for puritylike diagrams. (a) Domain wall for purity $\text{tr}(\rho_A^2)$. The single domain wall [a transposition (12)] undergoes a random walk down to the bottom boundary. The size fluctuation is \sqrt{t} , which is subleading to t and ignored in other panels. (b) Domain walls for $(\text{tr}\rho_A^2)^2$. The two transpositions are independent. (c) Configurations when the two sets of domain wall do not interact. (d) The two sets of domain wall meet in a middle time slice. The three segments have time duration t_1 , t_2 , and t_0 , and antislopes v_1 , v_2 , and 0 respectively. The antislope of the right edge of the triangle is v . The green vertex represents the fusion. It can have a nontrivial weight, but only affects the free energy by an $\mathcal{O}(1)$ amount.

these domain walls will involve multiple elementary transpositions.

For instance, let us consider the second term on the right-hand side of Eq. (72):

$$F_2(t) := -\log \overline{(\langle L_\gamma | L_\gamma \rangle)^2}. \quad (73)$$

The boundary condition is $\mathbb{1}$ on subsystem B and $(12)(34)$ on subsystem $A\bar{A}$ [cf. boundary conditions of the first term in Fig. 6(b)]. Hence it has two commutative domain walls at the intersection of B and $A\bar{A}$. These two domain walls are independent; each of them go vertically down to the bottom [Fig. 7(b)] and give a contribution of $\mathcal{E}_H(0)t$. And thus the second term corresponds to twice the state Rényi entropy:

$$F_2(t) \simeq 2s_{\text{eq}} \mathcal{E}_H(0)t. \quad (74)$$

The boundary conditions of the first term in Eq. (69) contain four domain walls. There are two commutative transpositions $(14)(23)$ at the tip of the diagram (cut between B and $A\bar{A}$), and other two transpositions $(13)(24)$ at the entanglement cut between A and \bar{A} . The two transpositions $(14)(23)$ alone are independent, so are $(13)(24)$. If the two sets do not meet at an intermediate time slice before reaching the bottom boundary, we can separately minimize their free energies. The equilibrium configuration is that all the domain walls go down vertically [Fig. 7(c)], giving total free energy,

$$F_{1,\text{vert}}(t) := -\log \left\{ \overline{\text{tr}_A[\text{tr}_{\bar{A}}(|L_\gamma\rangle\langle L_\gamma|^2)]} \right\} \\ \simeq 2s_{\text{eq}}\mathcal{E}_H(0)t + 2s_{\text{eq}}\mathcal{E}_H(0)(1-r)t, \quad (75)$$

where $r \in [0, 1]$ is the ratio of size $|A|$ and total size $|A| + |\bar{A}|$. The difference with $F_2(t)$ in Eq. (74) is then $\mathcal{E}_H(0)t$: This gives us the following upper bound,

$$\bar{S}_A^{(2)}(\gamma) \lesssim 2(1-r)\mathcal{E}(0)t. \quad (76)$$

If the two sets meet in the middle, the domain walls can fuse to different permutations according to the group multiplication rules. For example, if (13)(24) and (14)(23) completely fuse together, the domain wall becomes (13)(24) \times (14)(23) = (12)(34). We see that the number of domain walls reduces to two, thus reducing the energy cost. For this reason a configuration like the one displayed in Fig. 7(d) can compete for the minimal free energy.

We now set up the minimization problem assuming the two sets to have (anti)slope v_1 and v_2 before they meet in the middle. After the fusion, the resulting domain wall (12)(34) is composed by two independent components. They cost free energy $2\mathcal{E}_H(0)t_0$ for the remaining duration of t_0 . The vertex can have a nontrivial weight, but, as long as it is not zero, it only brings in a $\mathcal{O}(1)$ correction and can be neglected when considering the leading order free energy in the long time limit. The geometry is depicted in Fig. 7(d). Therefore, we can write the free energy as

$$F_{1,Y}(t, t_0) \simeq 2s_{\text{eq}}[\mathcal{E}_H(v_1)t_1 + \mathcal{E}_H(v_2)t_2 + \mathcal{E}_H(0)t_0], \quad (77)$$

where t_0 , t_1 , and t_2 are the duration of the two sets of domain walls and satisfy the geometric relations. The subscript Y denotes the merging configuration.

$$v_1 = \frac{x}{t_1}, \quad v_2 = \frac{x - rv_\gamma t}{t_2}. \quad (78)$$

To parametrize time, we set

$$t_0 = r_0 t, \quad t_1 - t_2 = rt, \quad t_1 + t_0 = t, \quad (79)$$

where $r \in [0, 1]$ is the ratio of size $|A|$ with respect to $|A| + |\bar{A}|$, and $r_0 \in [0, 1-r]$ is the portion of the merged domain wall. $r_0 = 0$ corresponds to merge at the bottom; $r_0 = 1-r$ corresponds to taking $v_1 = v_\gamma$, i.e., merge immediately when available. To minimize $F_1(t, t_0)$, we first fix t_0 and vary x . The implicit x derivative gives

$$\mathcal{E}'_H\left(\frac{x}{t_1}\right) + \mathcal{E}'_H\left(x - \frac{v_\gamma r t}{t_2}\right) = \mathcal{E}'_H(v_1) + \mathcal{E}'_H(v_2) = 0. \quad (80)$$

For a reflection symmetric system the physical solution is

$$v_1 = -v_2; \quad (81)$$

namely, the two sets of domain walls in Fig. 7(d) meet symmetrically from left and right toward each other.

The minimization with respect to t_0 depends on the explicit form of the line-tension function. In particular, an explicit calculation for the case of the random circuit line tension \mathcal{E}_H is carried out in Appendix A. The resulting expression of $\min_{t_0} F_{1,Y}(t, t_0)$ is piecewise continuous in v and depends on d . Nevertheless, it is still linear in t [cf. Eq. (A6)]. Combining with the linear bound in Eq. (76), we conclude that in a Haar random circuit,

$$\bar{S}_A^{(2)}(\gamma) \simeq s_{\text{eq}}v_{\text{TE,H}}^{(2)}t. \quad (82)$$

where the temporal Rényi entanglement velocity $v_{\text{TE,H}}^{(2)} > 0$. The explicit expressions of $v_{\text{TE,H}}^{(2)}$ for Haar random circuit can be found in Eq. (A12).

C. Typical circuit without averaging

In this subsection, we argue that the line-tension formalism discussed above can be applied to the calculation of temporal entanglement in generic chaotic circuits without introducing disorder averaging. The recipe is to replace $\mathcal{E}_H(v)$ with a “dressed” line-tension function $\mathcal{E}(v)$ characterized by the following general properties [111],

$$\mathcal{E}(v) \geq |v|, \quad \mathcal{E}''(v) \geq 0, \quad \mathcal{E}(v) = \mathcal{E}(-v), \quad (83)$$

where the last one follows from the parity symmetry of the system.

The basic arguments follow Ref. [69], where the concept of line-tension function is generalized to nonrandom circuits and we will briefly recall them here. The key observation is that the pairings between a unitary gate and its Hermitian conjugate continue to dominate the configuration sum, or “path integral,” that determines the Rényi entropies. Indeed, these are real positive quantities that do not suffer from phase cancellation. A single domain wall, such as (12), will be dressed by nonpairing degrees of freedom, but only perturbatively to have an $\mathcal{O}(1)$ width.

Our problem is slightly more complicated than the one discussed in Ref. [69] because the contributions generating temporal entanglement involve composite domain walls [for instance, a domain wall (123) can appear]. Nevertheless, the two sets of domain walls (14)(23) and (13)(24) have the same dressed line-tension function $\mathcal{E}(v)$ when they do not interact. Indeed, (14)(23) can be mapped to (12)(34) by relabelling the third and fourth copies of the unitary and its complex conjugate—it is a symmetry of the multireplica dynamics if we look at the patch of (14)(23) alone. The symmetry no longer holds when the two sets of domain walls meet each other and interact. This process, however, only dresses the interaction vertex in Fig. 7(d), which introduces an order $\mathcal{O}(1)$ correction to the free energy. Below the interaction vertex, the two sets of domain walls

fuse to (12)(34), which again has the same line-tension function $\mathcal{E}(v)$. This justifies the use of a single line-tension function $\mathcal{E}(v)$ to characterize the scaling of the temporal Rényi-2 in Eq. (69).

Specifically, following the steps discussed in the previous section, we obtain

$$S_A^{(2)}(\gamma) \simeq s_{\text{eq}} v_{\text{TE}}^{(2)} t, \quad (84)$$

where the temporal Rényi entanglement velocity is determined by

$$v_{\text{TE}}^{(2)} = \min_{r_0 \in [0, r]} [\min_{r_0} \mathcal{F}(r_0), 2(1-r)\mathcal{E}(0)]. \quad (85)$$

The parameters r_0 and r are defined in Eq. (79) and

$$\mathcal{F}(r_0) = 2[\mathcal{E}[v_1(r_0)] - \mathcal{E}(0)](1-r_0) \quad (86)$$

$$+ 2\mathcal{E}[v_1(r_0)](1-r_0-r). \quad (87)$$

In this case, the remaining minimization over r_0 cannot be performed explicitly as the minimum depends on the precise form of the line tension. However, we can show that for $\mathcal{E}(0) > 0$,

$$\min_{r_0 \in [0, r]} \mathcal{F}(r_0) = 0 \Leftrightarrow \mathcal{E}(v_\gamma) = \mathcal{E}(0), \quad (88)$$

which implies generic linear growth of the temporal Rényi-2 entropy apart from marginal cases.

We begin to prove this property by noting that the two terms in Eqs. (86) and (87) are both non-negative,

$$\begin{aligned} [\mathcal{E}[v_1(r_0)] - \mathcal{E}(0)](1-r_0) &\geq 0, \\ \mathcal{E}[v_1(r_0)](1-r_0-r) &\geq 0, \end{aligned} \quad (89)$$

in the relevant range $r_0 \in [0, r]$, because of the convexity and parity of line-tension function. Indeed, these two properties imply that the function is either constant or has a unique local minimum in $v = 0$, i.e.,

$$\mathcal{E}(v) \geq \mathcal{E}(0) > 0, \quad \forall v. \quad (90)$$

In fact, the above inequality indicates that Eq. (89) can both be zero for generic r only if $r_0 = r$ and

$$\mathcal{E}(v_\gamma) = \mathcal{E}(0). \quad (91)$$

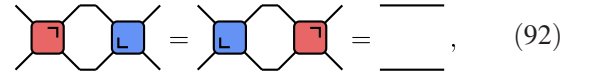
Noting that the reversed implication is obvious, we conclude the proof.

In fact, due to the general properties (83) of the line-tension function, Eq. (91) admits solution only in two cases: either constant line-tension function [Eq. (6)] or

$v_\gamma = 0$ [Eq. (7)]. These are the two marginal cases mentioned in Sec. IA.

V. TEMPORAL ENTANGLEMENT IN CHAOTIC DUAL-UNITARY CIRCUITS

In this section we consider the first of the two marginal cases identified in Eq. (91): the one in which the line-tension function is constant. As discussed in Sec. IA [cf. the discussion around Eq. (6)], this situation can only be realized when the local gates forming the time evolution operator in Eq. (10) are dual unitary [57]. In terms of our diagrammatic representation, the dual-unitarity condition means that the gates fulfill



$$\text{[Red Gate][Blue Gate]} = \text{[Blue Gate][Red Gate]} = \text{---}, \quad (92)$$

in addition to the standard unitarity conditions (23). Without additional fine-tuning, the gates fulfilling Eqs. (23) and (92) are quantum chaotic [35,57,71].

Imposing the condition (92) enables one to make a number of exact statements concerning dynamics and spectral properties of the quantum circuit [34,35,38,40,58,62,63,71–73,75,76,78,79,85,86]. In particular, dual-unitary circuits have been shown to admit a class of “solvable” initial states for which one can compute exactly the full time evolution of any local subsystem [58]. For solvable initial states the generalized influence matrices $\langle L_\gamma \rangle$ and $|R_\gamma\rangle$ [cf. Eqs. (54) and (53)] take the following product form:

$$\langle L_\gamma \rangle = \langle \bigcirc \rangle^{\otimes |\gamma|}, \quad |R_\gamma\rangle = |\bigcirc\rangle^{\otimes |\gamma|}, \quad (93)$$

where $|\bigcirc\rangle$ is the loop state of Eq. (27). This form immediately implies a strictly vanishing temporal entanglement.

Here, however, we are interested in the behavior of temporal entanglement for *generic*, nonsolvable, initial states. Specifically—recalling that for the family of initial states Eq. (15) considered here the solvable instances correspond to the cases where the matrix m is unitary [77]—we consider the case where m is *not* unitary.

Since the time evolution in a chaotic system should not depend on the initial configuration, one might expect that the behavior of solvable states is somewhat representative of the generic situation. Namely, that the temporal entanglement is always small for dual-unitary circuits. In fact, as we now discuss, this intuition turns out to be incorrect: Even though higher temporal Rényi entropies are bounded by a sublinear function of time (in agreement with our entanglement-membrane analysis of the previous section), the von Neumann temporal entanglement entropy is always linear for non-fine-tuned dual-unitary circuits. In the upcoming subsections we show these facts by

analyzing separately the cases of higher Rényi entropies and von Neumann entropy.

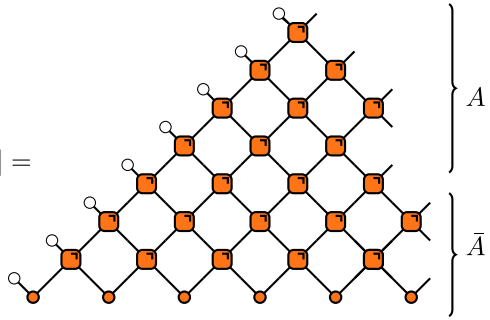
For simplicity, in the main text we consider paths $\gamma = A\bar{A}$ with *constant* slope v_γ . This means that the slope is the same in both A and \bar{A} . This assumption is lifted in Appendixes B and C where we present the most general form of our results.

A. Bound on temporal higher Rényi entropies

In this subsection we show that higher temporal Rényi entropies are *sublinear* in time, in agreement with the entanglement membrane analysis of the previous section. More precisely, we prove the following bound,

$$S_A^{(\alpha>1)}(\gamma) \leq \frac{\alpha}{\alpha-1} \log \left[\frac{d^{\tau_A} \mathcal{P}(\tau/2)}{\mathcal{P}(\tau_{\bar{A}}/2)} \right], \quad (94)$$

where A, \bar{A} correspond to a contiguous bipartition of the $2t$ legs of the influence matrix,



$$\langle L_\gamma | = \left. \begin{array}{c} \text{Lattice structure} \\ \text{Region A} \\ \text{Region } \bar{A} \end{array} \right\} , \quad (95)$$

τ_A ($\tau_{\bar{A}}$) is the number of up-pointing legs in A (\bar{A}) fulfilling

$$\tau_A + \tau_{\bar{A}} = (1 + v_\gamma)t \equiv \tau, \quad (96)$$

while

$$\mathcal{P}(t) = \text{tr}[\rho_{[0,\infty)}(t)^2] \quad (97)$$

is the purity of the “regular” reduced density matrix $\rho_{[0,\infty)}(t)$ [cf. Eq. (24)] corresponding to a half-infinite subsystem $[0, \infty)$ with open boundary conditions.

To prove Eq. (94) we proceed in two steps, which are detailed in Appendix B.

Step 1. General bound on higher Rényi entropies.—We take advantage of the unitarity of the gates and of the Eckart-Young theorem [115] to bound the temporal Rényi entropies in terms of the norm of the state $\langle L_\gamma |$:

$$S_A^{(\alpha)}(\gamma) \leq \frac{\alpha}{\alpha-1} \log \left(\frac{\langle L_{\bar{A}} | L_{\bar{A}} \rangle}{\langle L_\gamma | L_\gamma \rangle} \right). \quad (98)$$

Step 2. Dual-unitary case.—Specializing the treatment to the dual-unitary case we can relate $\langle L_\gamma | L_\gamma \rangle$ to the spatial purity [cf. Eq. (97)]. In particular, we find

$$\langle L_\gamma | L_\gamma \rangle = d^r \mathcal{P}(\tau/2). \quad (99)$$

Plugging it into Eq. (98) we obtain Eq. (94).

The physical interpretation of Eq. (94) is immediate: in dual-unitary circuits the growth of higher temporal Rényi entropies is controlled by that of spatial purity. If the initial state is solvable, then the purity is minimized to d^{-2t} and the temporal entanglement is zero. For more general, nonsolvable states the purity is no longer strictly d^{-2t} , but—since dual-unitary circuits maintain a maximal entanglement velocity [77]—it can only acquire subexponential corrections. This implies that all higher temporal Rényis are *sublinear* in time.

To make further progress we introduce the following assumption.

Assumption 1.—For any generic dual-unitary circuit evolving from a non solvable state, we have

$$\mathcal{P}(t) \simeq \frac{Ct}{d^{2t}}, \quad (100)$$

where \simeq denotes the leading order in the asymptotic expansion for large times and $C > 0$ a time independent constant.

The scaling in Eq. (100) can be proven by averaging each dual-unitary gate of the circuit over random single qubit rotations of its legs (see Ref. [77] and Appendix D). Thus, we expect it to hold for typical dual-unitary circuits: This is in agreement with our numerical investigations, as shown in Fig. 8 for some representative examples.

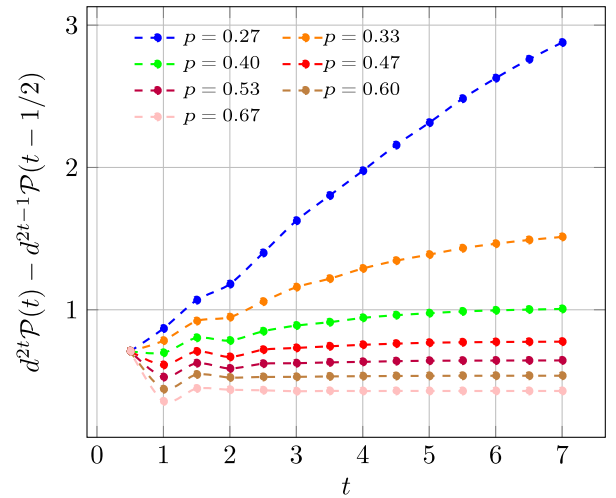


FIG. 8. Evolution of $d^{2t}\mathcal{P}(t) - d^{2(t-1)}\mathcal{P}(t-1)$ as a function of t for homogeneous dual-unitary circuits with different entangling power p [cf. Eq. (12)]. If the scaling (100) holds, this quantity should saturate to the constant $C/2$. We considered $d = 2$ and parametrized the gates as described in Appendix E. Note that C grows upon decreasing p : this is consistent with the fact that at the noninteracting point $p = 0$ the purity decays with an exponent $\lambda < 2 \log d$.

As discussed in Appendix D we expect the case $C = 0$ to hold only for solvable initial states, for which $\mathcal{P}(t) = d^{-2t}$ and the temporal entanglement is identically 0 for any bipartition [58]. The discussion in Appendix D, however, also shows that these states are “unstable” from the point of view of purity scaling: for any arbitrary small perturbation of a solvable state one has Eq. (100) with $C > 0$ and the behavior of temporal entanglement is the one we discuss here.

Using Assumption 1 and considering an appropriate scaling of the bipartition,

$$r \equiv \frac{|A|}{2t} < 1, \quad (101)$$

it is immediate to show that the higher Rényi entropies saturate to a constant [129],

$$S_A^{(\alpha)}(\gamma) \simeq \frac{\alpha}{\alpha-1} \log(1-r). \quad (102)$$

A direct numerical test of Eq. (102) is not straightforward as we have only access to short times. Therefore, we can only consider gates for which the asymptotic form Eq. (100) is attained early. With this restriction the bound appears convincingly obeyed. For instance, in Fig. 9 we consider a comparison between Eq. (102) and the four gates of Fig. 8 with higher entangling power.

B. Linear growth of temporal entanglement entropy

In Sec. VA, we showed that the higher Rényi entropies are bounded by a constant for any partition with ratio $r < 1$. However, since Rényi entropies are nonincreasing functions of the Rényi index, this result only provides a lower bound for the temporal entanglement entropy, i.e.,

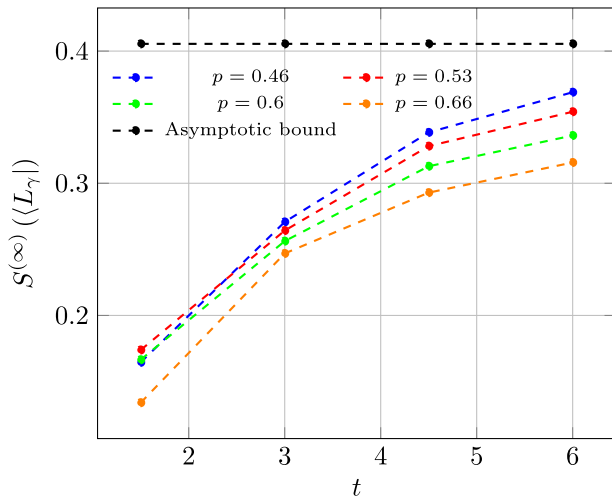


FIG. 9. Growth of $S^{(\infty)}$ for the state L_γ , taken with $v_\gamma = 1$, for gates of various entangling power p , compared with the asymptotic bound given by Eq. (102), for a fixed value of $r = 1/3$.

$$S_A(\gamma) = \lim_{\alpha \rightarrow 1} S_A^{(\alpha)}(\gamma). \quad (103)$$

In this subsection, we show that $S_A(\gamma)$ in a typical dual-unitary circuit grows linearly in time for nonsolvable initial states.

Denoting again by r the ratio between the number of legs in region A and the total [cf. Eq. (101)], we can bound $S_A(\gamma)$ from above and below,

$$s(r)t \log d \leq S_A(\gamma) \leq s(r)t \log d + \mathcal{O}(\log t), \quad (104)$$

with the same function:

$$s(r) = \begin{cases} (1 + v_\gamma)r^2 & r \in [0, \frac{2}{v_\gamma+3}] \\ \frac{4(1-r)[(2+v_\gamma)r-1]}{1+v_\gamma} & r \in (\frac{2}{v_\gamma+3}, 1]. \end{cases} \quad (105)$$

The $\log(t)$ margin in Eq. (104) is subleading with respect to the linear scaling of $s(r)t \log d$ and therefore the latter determines the long timescaling of $S_A(\gamma)$.

In the derivation of the upper bound, we only use Assumption 1. For the lower bound, we additionally employ Assumption 2.

Assumption 2.—The membrane picture of entanglement holds for the second Rényi entropy of the state in Eq. (119).

This assumption is in line with general expectations from the membrane theory [69] and can be verified numerically. A representative example is reported in Fig. 10. We see that, even though there are strong deviations for short times, the numerical results seem to approach the membrane theory predictions as time increases (see Appendix C 3 for a more thorough discussion of the validity of this assumption).

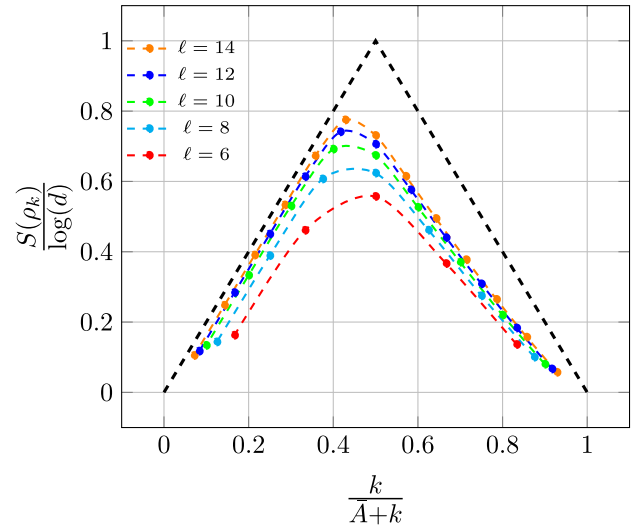
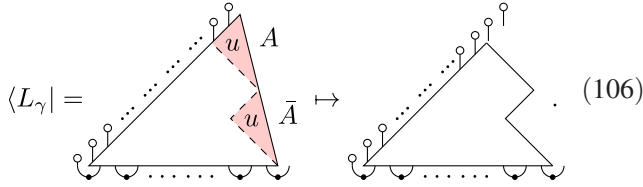


FIG. 10. Slope of the entanglement entropy of the matrices ρ_k as a function of k , for various values of $\ell \equiv \bar{A} + k$ accessible numerically. The dashed line represents the asymptotic profile of the curve according to Eq. (123) as per Assumption 2. The path chosen is the one at the edge of the lightcone.

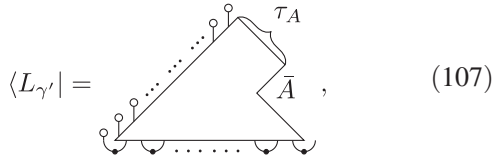
We sketch the proof in three steps.

Step 1. Reduction.—First we observe that the entanglement of a state, for a given bipartition, is unaffected by the action of unitary matrices acting locally on the two separate bipartitions. Thanks to this observation and the dual unitarity of the gates, we can consider a simplified version of our state $\langle L_\gamma | \mapsto \langle L_{\gamma'} |$ where the new path γ' corresponds to the edges of the light cones of the two bipartitions (see the detailed derivation in Appendix C 1). This is easily understood graphically by looking at the diagram below and noting that the area in red corresponds to matrices that, when viewed horizontally, are unitary. Therefore, removing them will not affect its entanglement.



After this operation we end up with some bullet states on the top of region A , which do not entangle with any other part of the system: They can also be removed without affecting the result.

To sum up, as far as the entanglement is concerned, we can reduce $\langle L_\gamma |$ to the following state,

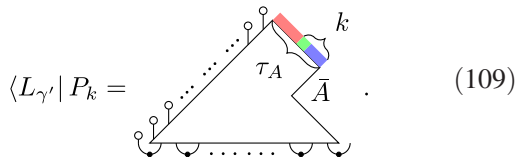


in which region A has $\tau_A = (1 + v_\gamma)|A|/2$ sites and region \bar{A} has $|\bar{A}|$ sites.

Step 2. Lower and upper bounds.—We define $\tau_A + 1$ orthogonal projectors in region A :

$$\begin{aligned} P_0 &= |\circ\rangle\langle\circ| \otimes |\circ\rangle\langle\circ| \otimes \cdots |\circ\rangle\langle\circ| \otimes \mathbb{1}_{\bar{A}}, \\ P_1 &= |\circ\rangle\langle\circ| \otimes |\circ\rangle\langle\circ| \otimes \cdots (\mathbb{1}_{d^2} - |\circ\rangle\langle\circ|) \otimes \mathbb{1}_{\bar{A}}, \\ P_k &= |\circ\rangle\langle\circ|^{\otimes \tau_A - k} \otimes (\mathbb{1}_{d^2} - |\circ\rangle\langle\circ|) \mathbb{1}_{d^2}^{\otimes k-1} \otimes \mathbb{1}_{\bar{A}}, \\ P_{\tau_A} &= (\mathbb{1}_{d^2} - |\circ\rangle\langle\circ|) \otimes \mathbb{1}_{d^2} \otimes \cdots \mathbb{1}_{d^2} \otimes \mathbb{1}_{\bar{A}}. \end{aligned} \quad (108)$$

In words, the projector has three different actions, which we highlight by different colors in the following graphical equation:



The k th projector P_k keeps the bottom $k - 1$ sites (blue) intact, projects each of the top $\tau_A - k$ sites (red) to a bullet state and the k th site (green) to the orthogonal complement of the bullet state.

One can easily verify that the projectors are orthogonal and form a complete basis, i.e.,

$$P_i P_j = \delta_{ij} P_i, \quad \sum_{k=0}^{\tau_A} P_k = \mathbb{1}_A \otimes \mathbb{1}_{\bar{A}}. \quad (110)$$

These projectors decompose $|L_{\gamma'}\rangle$ into $\tau_A + 1$ states, which are orthogonal in A . Namely,

$$\text{tr}_A(P_i |L_{\gamma'}\rangle \langle L_{\gamma'}| P_j) = 0, \quad i \neq j. \quad (111)$$

The reduced density matrix,

$$\rho_{\bar{A}} = \frac{1}{\langle L_{\gamma'} | L_{\gamma'} \rangle} \text{tr}_A(|L_{\gamma'}\rangle \langle L_{\gamma'}|), \quad (112)$$

is then written as a classical mixture of $\tau_A + 1$ reduced density matrices,

$$\rho_{\bar{A}} = \sum_{k=0}^{\tau_A} P_k \rho_k, \quad (113)$$

where the classical probability is

$$p_k = \frac{\text{tr}(P_k |L_{\gamma'}\rangle \langle L_{\gamma'}|)}{\langle L_{\gamma'} | L_{\gamma'} \rangle}, \quad (114)$$

and the reduced density matrices are

$$\rho_k = \frac{\text{tr}_A(P_k |L_{\gamma'}\rangle \langle L_{\gamma'}|)}{\text{tr}(P_k |L_{\gamma'}\rangle \langle L_{\gamma'}|)}. \quad (115)$$

The concavity lower bound and mixing upper bound of $S(\rho_{\bar{A}})$ confine the von Neumann entropy to the following interval:

$$\sum_{k=0}^{\tau_A} p_k S(\rho_k) \leq S_A(\gamma) \leq \sum_{k=0}^{\tau_A} p_k S(\rho_k) - \sum_{k=0}^{\tau_A} p_k \log p_k. \quad (116)$$

The Shannon entropy of the classical probability p_k is at most $\log(\tau_A + 1) \sim \mathcal{O}(\log t)$. Therefore, we conclude that

$$\sum_{k=1}^{\tau_A} p_k S(\rho_k) \leq S_A(\gamma) \leq \sum_{k=1}^{\tau_A} p_k S(\rho_k) + \mathcal{O}(\log t), \quad (117)$$

where we also removed $k = 0$ from the summation since $S(\rho_0) = 0$.

Step 3. Evaluation of $\sum_{k=1}^{\tau_A} p_k S(\rho_k)$.—We evaluate p_k in Appendix C 2 using Assumption 1. The asymptotic expression reads as

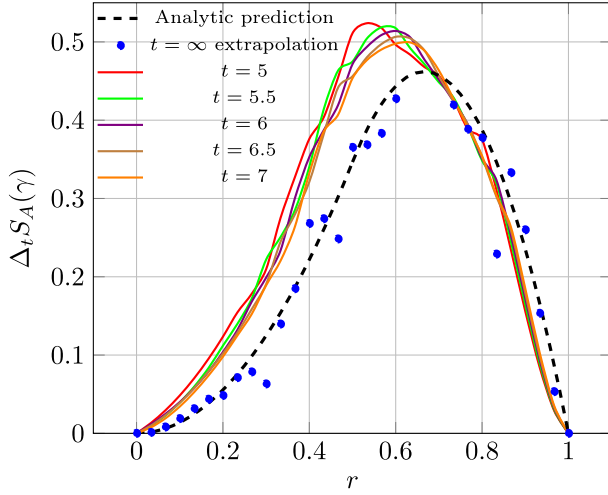


FIG. 13. Slope of the entanglement entropy for the state $\langle L_\gamma |$, obtained by taking finite differences of $S_A(\gamma)$ for two subsequent time steps. Given the discrete nature of the states, only some rational values of r are allowed at each time, so we interpolated between those in order to take the difference. In blue, we show an extrapolation of these data in the limit $t \rightarrow \infty$, which we ultimately compare with the asymptotic prediction, in black [obtained from Eq. (105)]. The extrapolation is attained by observing that, due to the logarithmic form of the corrections to $S_A(\gamma)$, for large enough t we have $\Delta_t S_A(\gamma) \simeq A + B/t$, where A is the desired asymptotic value. Then, we performed a linear fit of the data in $1/t$ to estimate A .

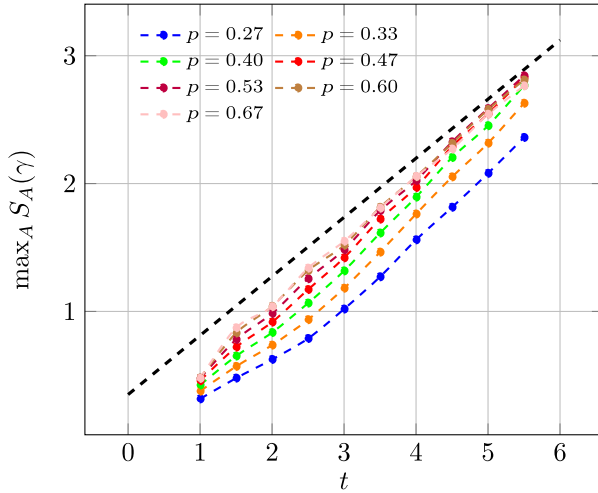


FIG. 14. Maximal entanglement of the influence matrix on the diagonal path γ_{lc} [cf. Eq. (56)] versus the length of the path $|\gamma_{lc}|$ for different values of the entangling power p . The entanglement reported is the maximum attained among all the possible non-disjoint bipartitions. The gates are parametrized as explained in Appendix E. The asymptotic growth seems to be independent of the entangling power. The initial p -dependent transient is larger for smaller values of p . This is consistent with the fact that for $p = 0$ the gates are SWAPS and $\langle L_{\gamma_{lc}} |$ is a product state for all initial states Eq. (15). The black dashed line corresponds to the theoretical prediction of the growth, as in Eq. (105), plus an arbitrary constant chosen for convenience.

VI. TEMPORAL ENTANGLEMENT OF THE VERTICAL STATE

In this section, we consider the second marginal case of Eq. (91) in which the timelike surface is vertical ($v_\gamma = 0$) and the chaotic quantum circuit is arbitrary. Namely, we look at the scaling in $|\gamma| = 2t$ of the temporal entanglement of the original influence matrix for generic circuits.

We find that higher Rényi entropies grow logarithmically in time:

$$S_A^{(\alpha)}(\gamma) \sim \log(t), \quad \alpha > 1. \quad (124)$$

We begin by showing the sublinear growth via a direct application of the Eckart-Young strategy employed in Appendix B 1. Specifically, we use the upper bound,

$$\begin{aligned} S_A^{(\alpha)}(\gamma) &\leq \frac{\alpha}{1-\alpha} \log \frac{[\langle L_\gamma | (|\Psi_A\rangle \otimes |\Psi_{\bar{A}}\rangle)]^2}{\langle L_\gamma | L_\gamma \rangle \langle \Psi_A | \Psi_A \rangle \langle \Psi_{\bar{A}} | \Psi_{\bar{A}} \rangle} \\ &:= \frac{2\alpha}{1-\alpha} \log r_t, \end{aligned} \quad (125)$$

by means of the overlap of the state $\langle L_\gamma |$ and a factorized state $\langle \Psi_A | \otimes \langle \Psi_{\bar{A}} |$.

To find a product state with large overlap we employ the membrane theory. Specifically, we consider the state

$$\langle \Psi_A | \otimes \langle \Psi_{\bar{A}} | = \langle L_{\gamma/2} | \otimes \langle L_{\gamma/2} |, \quad (126)$$

which is depicted in Fig. 15(b). Assuming the circuit to be Haar random, the norm of these states are determined by the line tension at $v = 0$ as follows,

$$\begin{aligned} \overline{\langle L_\gamma | L_\gamma \rangle} &\sim \exp[-\mathcal{E}_H(0) \log(d)t], \\ \overline{\langle \Psi_A | \Psi_A \rangle} &\sim \exp[-\mathcal{E}_H(0) \log(d)t/2], \\ \overline{\langle \Psi_{\bar{A}} | \Psi_{\bar{A}} \rangle} &\sim \exp[-\mathcal{E}_H(0) \log(d)t/2], \end{aligned} \quad (127)$$

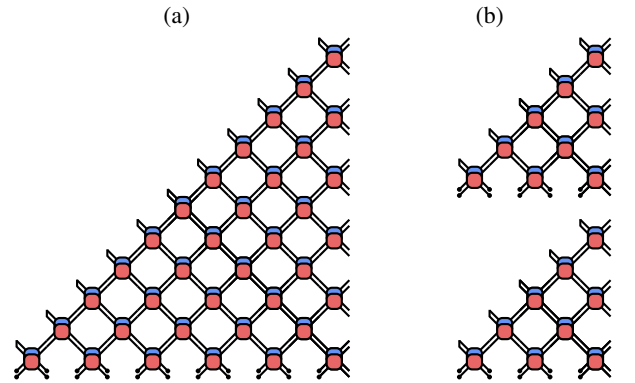


FIG. 15. (a) The vertical state. (b) A tensor product state on A and \bar{A} . The state is written as a tensor product of two vertical states defined on a time lattice with half of the sites.

where we recall [cf. Eq. (71)]

$$\mathcal{E}_H(0) = \frac{\log(d^2 + 1) - \log 2d}{\log d}. \quad (128)$$

The average of the overlap is

$$\overline{\langle L_\gamma | (|\Psi_A\rangle \otimes |\Psi_{\bar{A}}\rangle)} \sim \exp[-\mathcal{E}_H(0) \log(d)t]. \quad (129)$$

The estimation in Eq. (129) relies upon evaluating the random averaging in Fig. 16(c), where the region in which the two states differ is only populated by the permutation $\mathbb{1}$. Thus, the minimal free-energy configuration continues to have a domain wall going vertically down. Combining Eqs. (127) and (129) we find

$$\bar{r}_t = \frac{|\overline{\langle L_\gamma | (|\Psi_A\rangle \otimes |\Psi_{\bar{A}}\rangle)}|}{\sqrt{\langle L_\gamma | L_\gamma \rangle \langle \Psi_A | \Psi_A \rangle \langle \Psi_{\bar{A}} | \Psi_{\bar{A}} \rangle}} = O(t^\alpha), \quad (130)$$

The exponent α can be found by studying the subleading contributions from the random walk of the domain wall. All the domain walls in Fig. 16 are subject to the noncrossing condition at the right boundary. If we view from bottom to top, this is the random walk that first hit $x = 0$ (the

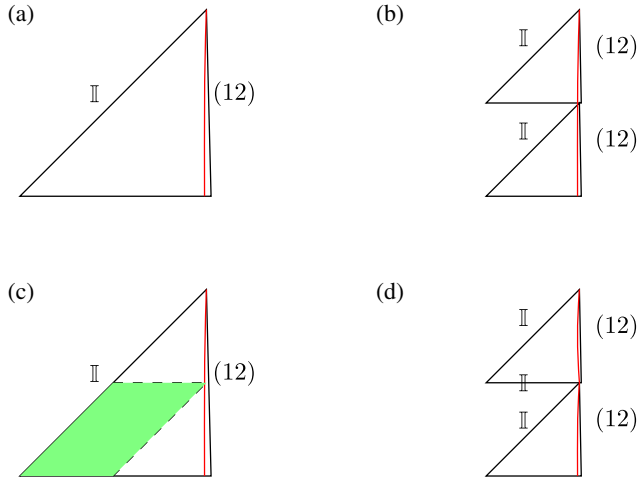


FIG. 16. The domain-wall analysis that produces Eqs. (127) and (129). (a) $\overline{\langle L_\gamma | L_\gamma \rangle}$: the dominant configuration is one domain wall going down vertically at equilibrium. (b) $\overline{\langle \Psi_A | \otimes \langle \Psi_{\bar{A}} | (|\Psi_{\bar{A}}\rangle \otimes |\Psi_A\rangle)}$: the two parts of the product state factorize so there are two independent vertical domain walls with half the size of (a). (c) $\overline{\langle L_\gamma | (|\Psi_A\rangle \otimes |\Psi_{\bar{A}}\rangle)}$: the green region is where $\langle L_\gamma |$ and $\langle \Psi_{\bar{A}} | \otimes \langle \Psi_A |$ differ. It has only one copy of $u \times u^*$, which, upon averaging, generates a patch of $\mathbb{1}$. The domain wall will avoid the green region and goes down vertically. (d) The green region after average provides the $\mathbb{1}$ boundary conditions for the two dashed lines in (c) (see main text for the bottom rim of the upper triangle; also see Appendix F). The top triangle has a pinned domain wall ending at the rightmost point, the bottom triangle still host a free random walk.

coordinate of the right boundary) for $t = 0$ (the final time when viewing from bottom to top). The probability distribution for this process is known as the Lévy-Smirnov distribution and reads as

$$p(x) = \frac{x}{t^{3/2}} e^{-x^2/t}. \quad (131)$$

The three independent averages inside the square root in the numerator of Eq. (130) [one in Fig. 16(a), the other two in Fig. 16(b)] correspond to a free boundary condition at the bottom, each of which contributes a polynomial factor $t^{-1/2}$ (integrate the Lévy-Smirnov distribution in x). For the average of the overlap, the green region in Fig. 16(c) represents the missing part in $\langle \Psi_A | \langle \Psi_{\bar{A}} |$ compared with $\langle L_\gamma |$. It can only produce $\mathbb{1}$, which becomes the boundary condition of the lower triangle and bottom rim of the top triangle in Fig. 16(d) (the boundary condition for the bottom rim after random averaging is $|\mathbb{O}\rangle$ tensor product with the vectorized density matrix of the initial state in the folded space. Once we project this state in the space spanned by $\mathbb{1}$ and (12), as prescribed by the Haar average of the gates, it becomes $|\mathbb{O}\mathbb{O}\rangle$, i.e., a $\mathbb{1}$ boundary). The lower triangle contributes a $t^{-1/2}$ factor as we argued above. Instead, because of the $\mathbb{1}$ boundary condition at the bottom rim, the domain wall in the top triangle is penalized by a factor of $1/d$ when it further moves to the left. Thus the domain wall is pinned to a slope of $v = 0$. We end up with a $t^{-3/2}$ factor in the Lévy-Smirnov distribution for the pinned domain wall. Putting it all together, we have

$$\bar{r}_t \simeq \frac{t^{-3/2} t^{-1/2}}{\sqrt{t^{-1/2} t^{-1/2} t^{-1/2}}} = t^{-5/4}. \quad (132)$$

These random wall arguments can be made more precise by solving a set of recursive relations of the averaged terms in Eq. (130); see Appendix F. The prediction (132) is compared with exact solution of the recursive relations in Fig. 17. The power-law decay of \bar{r}_t suggests that also r_t in Eq. (125) should decay as a power law, leading to Eq. (124).

On the other hand, a direct numerical evaluation is still compatible with a linear growth in time of $S_A(\gamma)$; see Fig. 18. Interestingly, we see that for certain choices of gates the growth of temporal entanglement entropy is slower than the lower bound for dual-unitary circuits (see Sec. VB). This indicates that dual-unitary circuits do not produce an extremal temporal entanglement growth.

VII. TEMPORAL VERSUS SPATIAL ENTANGLEMENT

Having argued that temporal entanglement grows linearly after a quench in generic quantum circuits, the natural question is whether its growth is faster or slower than that of “spatial entanglement,” i.e., regular state entanglement.

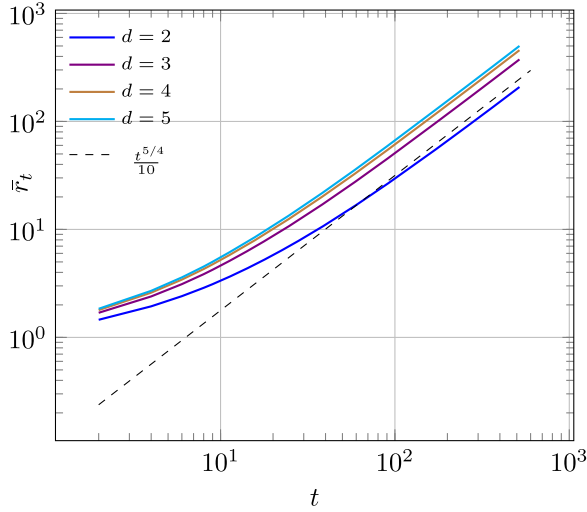


FIG. 17. Polynomial decay of \bar{r}_t . According to Eq. (F29) we show the asymptotic expected behavior $\propto t^{-5/4}$ as a dotted line. In the calculation we considered sites of local dimension d and an initial product state.

This question can be addressed precisely in the case of dual-unitary circuits. Indeed, for these circuits we have that state entanglement grows at the maximal possible speed for generic initial states [77], i.e.,

$$S_{\text{sp}}(t) \simeq 2t \log d. \quad (133)$$

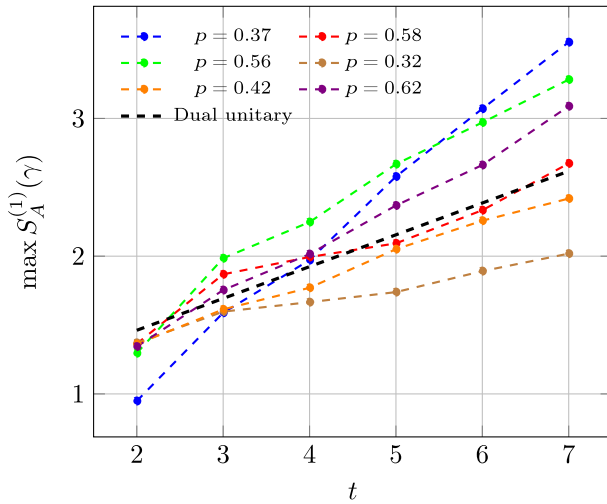


FIG. 18. Growth of the entanglement entropy for the vertical cut state $\langle L_\gamma \rangle$, given random choices of the dual-unitary gate (kept constant in space and time) with entangling power p . We considered the contiguous bipartition $A\bar{A}$ of γ yielding the maximum entanglement. The entangling power is computed according to Eq. (5) in Ref. [130], which has been normalized by a factor $(d+1)/(d-1)$ in order to have $p \in [0, 1]$. The black line represents the growth of $S_A^{(1)}(\gamma)$ in dual-unitary circuits [Eq. (105)].

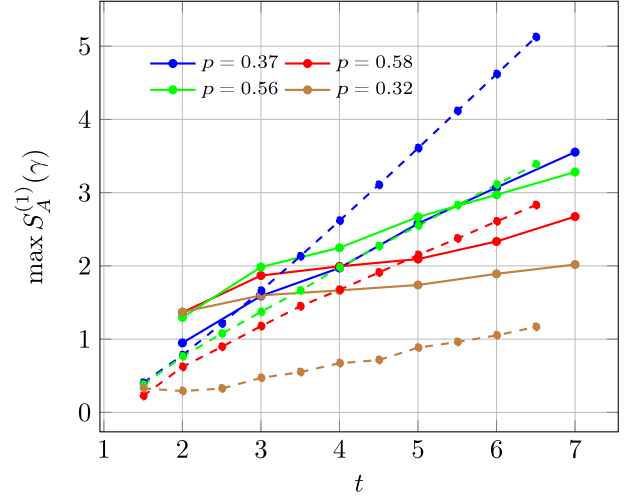


FIG. 19. Comparison between the growth of spatial and temporal entanglement along the vertical path for generic unitary gates. The continuous lines report temporal entanglement of unitary gates with different entangling power (normalized such that $p \in [0, 1]$) while the dashed lines report the corresponding state entanglement. The plot suggests a faster asymptotic growth for the spatial entanglement.

On the other hand, we can use our asymptotic result of Sec. VB to see that

$$S_A(\gamma) \lesssim \max_r S(r)t = \frac{(1+v_\gamma)t}{(2+v_\gamma)} \log d \leq \frac{2t}{3} \log d, \quad (134)$$

where in the first step we computed the maximum of Eq. (105) and in the second we used that it is monotonic in v_γ .

Comparing Eqs. (133) and (134) we see that the temporal entanglement is lower than the spatial entanglement for every path γ . Our numerical investigations suggest that, for small enough v_γ , temporal entanglement grows slower than spatial entanglement also in generic quantum circuits. For instance, in Fig. 19 we report a comparison between the entanglement of the vertical state ($v_\gamma = 0$) and that of the regular time-evolving state for different times: We see that the former has a consistently smaller growth rate for all the gates considered. When the slope of the path is increased, however, the growth of temporal entanglement appears to match that of state entanglement. See, for instance, the comparison between spatial entanglement and temporal entanglement of the diagonal path ($v_\gamma = 1$) reported in Fig. 20.

VIII. DISCUSSION

In this work we studied spacelike propagation approaches to quantum nonequilibrium dynamics. The main idea is to compute the time evolution of relevant observables by exchanging the roles of space and time. For

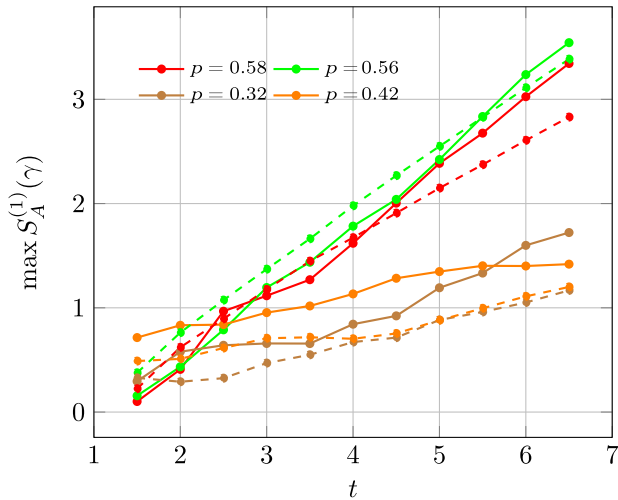


FIG. 20. Comparison between the growth of spatial and temporal entanglement along the diagonal path for generic unitary gates. The continuous lines report temporal entanglement of unitary gates with different entangling power (normalized such that $p \in [0, 1]$) while the dashed lines report the corresponding state entanglement.

large enough volumes, the “dual system” living in the time direction—also known as space-time swapped system [43,45]—reaches (left and right) stationary states dubbed “influence matrices” [33]. Since in many-body systems characterizing a stationary state is often easier and more efficient than characterizing a time-evolving state at intermediate times, spacelike propagation approaches are particularly promising and are attracting an increasing amount of attention [26–30,34,40–45,57–62,87,131,132].

Here we studied whether these ideas can be used to devise an efficient computational scheme to access correlation functions of local operators in generic systems. Our starting point has been the “folding algorithm” of Ref. [26], which uses the above idea to compute autocorrelation functions of local operators in one-dimensional quantum systems. The algorithm represents the time-evolving expectation value as a two-dimensional tensor network and proceeds by embedding the local operator in a system on the vertical time lattice which is then evolved in the space direction. To also access two-point functions between causally connected operators, we generalized the folding algorithm by considering propagation in a generic spacelike direction, i.e., in any direction in the two-dimensional space-time forming an angle α smaller than $\pi/4$ with the space direction. The idea is to consider the system on the lattice along a timelike slice, or path, connecting the two points and evolve it in the orthogonal spacelike direction.

We then investigated the efficiency of the generalized folding algorithm by computing the scaling in time of the temporal entanglement, i.e., the entanglement of the influence matrices [28]. Performing a comprehensive investigation in chaotic quantum circuits, we showed that for

generic spacelike evolutions (or states on timelike slice) the entanglement of the influence matrices grows linearly in time, preventing an efficient classical storing. However, we also showed that the volume-law scaling of temporal entanglement is much more subtle than one might expect due to the nontrivial structure of the temporal entanglement spectrum. Indeed, we found physically relevant cases where it separates into a few large Schmidt values (decaying at most polynomially in time) and many small ones (decaying exponentially). This means that the growth of temporal entanglement cannot be characterized via a replica trick.

More specifically, we identified two cases where all temporal Rényi entropies with index larger than one grow sublinearly in time: (i) standard space evolution (the one of the original folding algorithm of Ref. [26], where the timelike surface is vertical) in *generic quantum circuits* and (ii) any spacelike evolution in dual-unitary circuits. This phenomenon is very similar in nature to the sub-ballistic scaling of spatial Rényi entropies observed in circuits with diffusive conservation laws [113,114]. As in the latter case, the time-evolving state has large overlap with a product state over a spatial bipartition of the system; in our case, the influence matrices have large overlap with a product state (which we identified) over a temporal bipartition of the system. This means that the reduced density matrix has a small number of slowly decaying eigenvalues controlling the scaling of higher Rényi entropies.

On the other hand, we showed that the von Neumann temporal entanglement entropy grows *linearly* in time in both the cases (i) and (ii), but it has a strictly smaller rate of growth compared to regular state entanglement. Specifically, while for generic circuits we argued for a linear growth based on the absence of physical constraints and we characterized it numerically, for dual-unitary circuits we were able to provide a closed form expression for the slope of growth. This expression is always nonzero and smaller than the slope of growth of state entanglement. We stress that a strictly positive growth rate of temporal entanglement in dual-unitary circuits is particularly surprising because—due to their maximally fast dephasing [58,83]—these systems are expected to be the chaotic system generating the lowest temporal entanglement [33]. We also emphasize that, to the best of our knowledge, this is the first analytical account of the noncommutativity of replica and large-time limit generating different scalings of Rényi entropies.

Combined with the results of Ref. [62], our findings suggest that the behavior of temporal entanglement after a quantum quench is a dynamical chaos indicator; i.e., it discriminates between integrable and chaotic dynamics. Indeed, while Ref. [62] provided evidence for a generic sublinear scaling of temporal entanglement in integrable models, here we showed that it grows linearly in chaotic systems (modulo some genericity assumption on the initial state). This scenario is in agreement with the

characterization put forward in Ref. [133], which proposed volume-law spatiotemporal entanglement as the defining feature of quantum chaotic systems. From this point of view, temporal entanglement seems to behave similarly to the operator space entanglement of local operators [16,134–136]—another conjectured dynamical chaos indicator [71,72,137,138].

Our work opens several directions for future research. An obvious one is to understand whether it is possible to exploit our findings on the structure of the temporal entanglement spectrum to devise efficient computational schemes. In particular, the fact that influence matrices have a large product-state component might be used to extract information on the large-time dynamics of certain special observables.

Another compelling question is to confirm our numerical observation that the von Neumann entropy of the standard influence matrix grows linearly in time for generic circuits, but its growth is slower than that of regular state entanglement. Because of the noncommutativity of large-time and replica limits this cannot be achieved by a direct application of the entanglement membrane approach. Indeed, in this case the membrane approach can only describe higher Rényi entropies and not von Neumann: one cannot perform the analytic continuation. One possible strategy is to use the approach developed here for dual-unitary circuits: decompose the reduced density matrix as a convex combination and use data processing inequality and convexity of the von Neumann entropy to bound it.

Finally, a further avenue for future research is to assess the performance of our generalized folding algorithm in nonergodic systems, like nearly integrable ones, where the temporal entanglement grows slowly. This could provide a very efficient way to extract numerically linear transport coefficients and, more generally, characterize nonlinear transport in such systems. For instance, it could be applied to the characterization of anomalous transport in integrable systems with non-Abelian charges [139].

ACKNOWLEDGMENTS

We thank Lorenzo Piroli, Pavel Kos, and Alessio Leroche for helpful discussions and valuable comments on the manuscript. T. Z. acknowledges discussion with and comments from Adam Nahum and Dmitry Abanin on the initial preprint. This work has been supported by the Royal Society through the University Research Fellowship No. 201101 (A. F. and B. B.) and by the National Science Foundation under Grant No. NSF PHY-1748958 (B. B. and T. Z.). T. Z. is supported as a postdoctoral researcher from NTT Research Award No. AGMT DTD 9.24.20 and the Massachusetts Institute of Technology. We acknowledge the accommodation of the KITP program “Quantum Many-Body Dynamics and Noisy Intermediate-Scale Quantum Systems” in which part of the work took place.

APPENDIX A: MINIMIZATION OF THE FREE-ENERGY TERM FOR HAAR RANDOM CIRCUIT

Here we explicitly carry out the minimization of $F_{1,Y}(t, t_0)$ with respect to t_0 using the random circuit line tension in Eq. (71). We recall that, setting $v_1 = -v_2$ in Eq. (77), we have

$$F_{1,Y}(t, r_0) \simeq 4s_{\text{eq}}t \left[\mathcal{E}_H(v_1(r_0)) \left[1 - r_0 - \frac{r}{2} \right] + \mathcal{E}_H(0) \frac{r_0}{2} \right], \quad (\text{A1})$$

where

$$v_1(r_0) = \frac{rv_\gamma}{2 - r - 2r_0} \in \left[\frac{r}{2 - r - 2r_0} v_\gamma, v_\gamma \right], \quad (\text{A2})$$

and we use $r_0 = t_0/t \in [0, r]$. The expression of the free energy in this case is

$$F_{1,Y}(t, r_0) - F_2(t) \simeq 2s_{\text{eq}}t \left[\{ \mathcal{E}_H(v_1(r_0)) - \mathcal{E}_H(0) \} (1 - r_0) + \mathcal{E}_H(v_1(r_0)) (1 - r - r_0) \right]. \quad (\text{A3})$$

We now solve this final minimization using the explicit random circuit line tension \mathcal{E}_H . We set the r_0 derivative of the above expression to zero,

$$\mathcal{E}_H(0) - 2\mathcal{E}_H(v_1) + 2v_1\mathcal{E}'_H(v_1) = 0, \quad (\text{A4})$$

and find that the equation is solved for $v_1 = v_d$, where

$$v_d := \frac{d-1}{\sqrt{d^2+1}}. \quad (\text{A5})$$

The derivative $\partial_{r_0} F_{1,Y}(t, r_0)$ is negative for $v_1 \in [0, v_d]$ and positive for $v_1 \in (v_d, 1]$. So $v_1 = v_d$ is the minimal for $v_1 \in [0, 1]$. However, since $v_1 \in [(r/2 - r)v_\gamma, v_\gamma]$, depending on the choice of r , the free energy falls into three cases:

$$\begin{aligned} & \min_{r_0 \in [0, r]} F_{1,Y}(t, r_0) - F_2(t) \\ & \simeq 2s_{\text{eq}}t \begin{cases} r[\mathcal{E}_H(v_\gamma) - \mathcal{E}_H(0)] & v_\gamma \in [0, v_d] \\ r[\mathcal{E}_H(v_d) \frac{v_\gamma}{v_d} - \mathcal{E}_H(0) \frac{v_d+v_\gamma}{2v_d}] & v_\gamma \in [v_d, \frac{2-r}{r} v_d] \\ (2-r)\mathcal{E}_H(\frac{r}{2-r} v_\gamma) - \mathcal{E}_H(0) & v_\gamma \in (\frac{2-r}{r} v_d, 1]. \end{cases} \end{aligned} \quad (\text{A6})$$

To obtain $\bar{S}_A^{(2)}(\gamma)$, we further compare this minimum with the free energy of decoupled configurations in Fig. 7, i.e., $2s_{\text{eq}}t(1-r)\mathcal{E}(0)$ from Eq. (76).

We first note that

$$(2-r)\mathcal{E}_H\left(\frac{r}{2-r}v_\gamma\right) - \mathcal{E}_H(0) \geq (1-r)\mathcal{E}_H(0), \quad (\text{A7})$$

due to $\mathcal{E}(v) \geq \mathcal{E}(0)$. So for the case of $v_\gamma \in ((2-r/r)v_d, 1]$ the Y-shaped configuration can never dominate. Physically, the minimal for the Y shape here corresponds to taking $r_0 = 0$, which represents two tilted sets of domain walls meeting at the very bottom. Its free energy can always be lowered if all the domain walls go down vertically.

Then we compare the expression for $v_\gamma \in [v_d, (2-r)v_d/r]$ and $2s_{\text{eq}}t(1-r)\mathcal{E}(0)$. Setting

$$r\left[\mathcal{E}_H(v_d)\frac{v_\gamma}{v_d} - \mathcal{E}_H(0)\frac{v_d+v_\gamma}{2v_d}\right] \leq (1-r)\mathcal{E}_H(0), \quad (\text{A8})$$

gives $v_\gamma \leq (2-r)v'_d/r$, where

$$v'_d := \frac{1}{2} \frac{\log \frac{d^2+1}{2d}}{\text{arctanh}(v_d)}. \quad (\text{A9})$$

We have $v'_d \leq v_d$ and $\lim_{d \rightarrow \infty} (v'_d - v_d) = 0$. For $v_d < (2-r)v'_d/r$ to hold, we require $r \leq 2v'_d/(v_d + v'_d)$.

Finally, the case of $v_\gamma \in [0, v_d)$. For the Y-shaped configuration to dominate, we should have

$$r[\mathcal{E}_H(v_\gamma) - \mathcal{E}_H(0)] \leq (1-r)\mathcal{E}_H(0). \quad (\text{A10})$$

This requires $r \leq \mathcal{E}_H(0)/\mathcal{E}_H(v_\gamma)$.

In summary, we conclude that Haar random circuits have

$$\bar{S}_A^{(2)}(\gamma) \simeq s_{\text{eq}}v_{\text{TE,H}}^{(2)}t, \quad (\text{A11})$$

where

$$v_{\text{TE,H}}^{(2)} = \begin{cases} 2r[\mathcal{E}_H(v_\gamma) - \mathcal{E}_H(0)] & r \leq \frac{\mathcal{E}_H(0)}{\mathcal{E}_H(v_\gamma)}v_\gamma < v_d \\ 2(1-r)\mathcal{E}_H(0) & r > \frac{\mathcal{E}_H(0)}{\mathcal{E}_H(v_\gamma)}v_\gamma < v_d \\ 2r\left[\mathcal{E}_H(v_d)\frac{v_\gamma}{v_d} - \mathcal{E}_H(0)\frac{v_d+v_\gamma}{2v_d}\right] & r \leq \frac{2v'_d}{v_d+v'_d}v_\gamma \geq v_d \\ 2(1-r)\mathcal{E}_H(0) & r > \frac{2v'_d}{v_d+v'_d}v_\gamma \geq v_d. \end{cases} \quad (\text{A12})$$

APPENDIX B: RÉNYI ENTROPIES IN DUAL-UNITARY CIRCUITS

In this appendix we present the detailed calculations leading to the bounds on temporal higher Rényi entropies discussed in Sec. VA.

1. Upper bound on temporal Rényi entropies for generic quantum circuits

In this subsection we bound $S_A^{(\alpha)}(\gamma)$ in terms of the norm of the state $\langle L_\gamma |$. We begin by writing the Schmidt decomposition of the state $\langle L_\gamma |$ between the region A and the rest \bar{A} . Namely,

$$\frac{\langle L_\gamma |}{\sqrt{\langle L_\gamma | L_\gamma \rangle}} = \sum_{r=1}^{\min(d^{|A|}, d^{|\bar{A}|})} \Lambda_r \langle A_r |_A \otimes \langle B_r |_{\bar{A}}, \quad (\text{B1})$$

where $\{|A_r\rangle_A\}$ and $\{|B_r\rangle_{\bar{A}}\}$ are orthogonal states, while the Schmidt values $\{\Lambda_r\}$ fulfill

$$0 \leq \Lambda_r \leq \dots \leq \Lambda_{r-1}, \quad \sum_{r=1}^{\min(d^{|A|}, d^{|\bar{A}|})} \Lambda_r^2 = 1. \quad (\text{B2})$$

The integer

$$n = \min\{r \mid \Lambda_r = 0\} \quad (\text{B3})$$

is referred to as the Schmidt rank of the state.

Next, we invoke the Eckart-Young theorem [115] to bound from below the largest Schmidt value. To this end we first recall the statement of the theorem

Theorem 1 (Eckart-Young).—The scalar product of an unnormalized state $|\Phi_n\rangle$ of Schmidt rank n over the bipartition $B\bar{B}$ and a normalized state $|\Phi_k\rangle$ with rank $k < n$ fulfills the following lower bound,

$$|\langle \Phi_n | \Phi_k \rangle| \leq \sqrt{\sum_{j=1}^k \Lambda_j^2}, \quad (\text{B4})$$

where $\{\Lambda_r\}$ are the Schmidt values of $|\Phi_n\rangle$. The state saturating the bound is unique up to a global phase and reads as

$$|\Phi_k^*\rangle = \frac{1}{\sqrt{\sum_{j=1}^k \Lambda_j^2}} \sum_{r=1}^k \Lambda_r |a_r\rangle_B \otimes |b_r\rangle_{\bar{B}}, \quad (\text{B5})$$

where $\{|a_r\rangle_B\}$ and $\{|b_r\rangle_{\bar{B}}\}$ are sets of orthogonal states.

This formulation of the Eckart-Young theorem can be directly proven using the von Neumann trace inequality [140].

Using Theorem 1 we have that the largest Schmidt value Λ_1 of any state $|\Phi_n\rangle$ fulfills

$$\Lambda_1 \geq |\langle \Phi_n | \Phi_1 \rangle|, \quad (\text{B6})$$

for any normalized product state $|\Phi_1\rangle$. Specializing the theorem to our case, we consider a bipartition of the $2t$ sites in τ_A on the top and $\tau_{\bar{A}} = 2t - \tau_A$ on the bottom halves.

In particular, we fix

$$\frac{\tau_A}{2t} \equiv r, \quad (\text{B7})$$

and consider the following product state in this bipartition,

$$\langle \tilde{L} | = \langle \bigcirc |^{\otimes \tau_A} \otimes \langle L_{\gamma_{\bar{A}}} |, \quad (\text{B8})$$

where $\gamma_{\bar{A}}$ is the second part of the path γ , which comprises $\tau_{\bar{A}}$ steps. Using only the unitarity of the gates, it is immediate to see that the scalar product of the state with $\tau_A |\bigcirc\rangle$ states leads to a cancellation of the first τ_A diagonal rows. Namely,

$$\begin{aligned} \langle L_{\gamma} | \left(|\bigcirc\rangle^{\otimes \tau_A} \right) &= \text{[Diagram: A triangular lattice of orange and white nodes with a path of orange nodes starting from the top and moving down-left. The first \tau_A rows are highlighted with a dashed line.]} \\ &= \text{[Diagram: A triangular lattice of orange and white nodes with a path of orange nodes starting from the top and moving down-left. The first \tau_A rows are highlighted with a dashed line.]} \\ &= \langle L_{\gamma_{\bar{A}}} | \end{aligned} \quad (\text{B9})$$

So that we find

$$\Lambda_1 \geq \frac{\langle L_{\gamma} | \tilde{L} \rangle}{\sqrt{\langle L_{\gamma} | L_{\gamma} \rangle \langle \tilde{L} | \tilde{L} \rangle}} = \sqrt{\frac{\langle L_{\gamma_{\bar{A}}} | L_{\gamma_{\bar{A}}} \rangle}{\langle L_{\gamma} | L_{\gamma} \rangle}}. \quad (\text{B10})$$

This gives

$$\max_A S_A^{(\infty)}(\gamma) = -\log \Lambda_1^2 \leq \log \frac{\langle L_{\gamma_{\bar{A}}} | L_{\gamma_{\bar{A}}} \rangle}{\langle L_{\gamma} | L_{\gamma} \rangle}. \quad (\text{B11})$$

Next, we use the known inequality [141],

$$S^{(\alpha)}(\rho) \leq \frac{\alpha}{\alpha-1} S^{(\infty)}(\rho), \quad \alpha > 1, \quad (\text{B12})$$

fulfilled by the function in Eq. (62), to obtain Eq. (98).

2. Norm of $\langle L_{\gamma} | L_{\gamma} \rangle$ for dual-unitary circuits

Here we compute $\langle L_{\gamma} | L_{\gamma} \rangle$ in the special case of dual-unitary circuits. Using the dual-unitarity relations for double gates,

$$\text{[Diagram: A double gate with orange and green nodes.]} = \text{[Diagram: A double gate with green and orange nodes.]} = \text{[Diagram: Two horizontal lines.]}, \quad (\text{B13})$$

one can easily show that

$$\begin{aligned} \langle L_{\gamma} | L_{\gamma} \rangle &= \text{[Diagram: A triangular lattice of orange and green nodes with a path of orange nodes starting from the top and moving down-left. The path is highlighted with a dashed line.]} \\ &= \text{[Diagram: A triangular lattice of orange and green nodes with a path of orange nodes starting from the top and moving down-left. The path is highlighted with a dashed line.]} \\ &= \langle L_{\gamma_{lc}} | L_{\gamma_{lc}} \rangle := \mathcal{N}_{\tau}, \end{aligned} \quad (\text{B14})$$

where we introduced the diagonal path [cf. Eq. (56)],

$$\gamma_{lc} = \{+, +, \dots, +\}, \quad (\text{B15})$$

with length $\tau = (1 + v_{\gamma})t$ and denoted by \mathcal{N}_{τ} the norm of $\langle L_{\gamma_{lc}} |$.

We now observe that the latter quantity is directly related to spatial entanglement. Indeed, computing the purity of the regular density matrix $\rho_A(t)$ [cf. Eq. (24)] and choosing $A = [t - x, \infty]$, we find

$$\mathcal{P}(t) = \frac{1}{d^{2t}} \mathcal{N}_{2t}. \quad (\text{B16})$$

Combining this equation with Eqs. (B14), (B11), and (B12) we recover the bound in Eq. (94).

APPENDIX C: LINEAR GROWTH OF TEMPORAL ENTANGLEMENT ENTROPY IN DUAL-UNITARY CIRCUITS

In this appendix we present the detailed calculations leading to the bound on temporal entanglement entropy discussed in Sec. VB.

1. Reduction

Consider a generic bipartition of a state L_{γ} , $\gamma = \gamma_A \circ \gamma_{\bar{A}}$:

$$\langle L_{\gamma} | = \text{[Diagram: A triangular lattice of orange and green nodes with a path of orange nodes starting from the top and moving down-left. The path is highlighted with a dashed line. A red arrow points to the path, and a black arrow points to the path.]}. \quad (\text{C1})$$

Now we observe that, since the entanglement is invariant under local unitary transformations, the entanglement between A and \bar{A} is not changed by the transformation,

$$\langle L_\gamma | \mapsto \langle L_\gamma | (U_A^\dagger \otimes U_{\bar{A}}^\dagger), \quad (\text{C2})$$

for any unitary matrices U_A and $U_{\bar{A}}$ acting, respectively, only in A and \bar{A} . We consider the transformations U_A and $U_{\bar{A}}$ removing the largest number of gates; in the example shown in Eq. (C1), this corresponds to

$$[U_{\bar{A}}]_{i,j} = \begin{array}{ccc} i_1 & \text{---} & j_1 \\ & \diagdown & \diagup \\ i_2 & \bullet & j_2 \\ & \diagup & \diagdown \\ i_3 & & j_3 \\ & \text{---} & \\ i_4 & & j_4 \end{array}, \quad [U_A]_{i,j} = \begin{array}{ccc} i_1 & \bullet & j_1 \\ & \diagdown & \diagup \\ i_2 & \bullet & j_2 \\ & \diagdown & \diagup \\ i_3 & \bullet & j_3 \\ & \diagdown & \diagup \\ i_4 & \bullet & j_4 \\ & \diagdown & \diagup \\ i_5 & & j_5 \end{array}, \quad (\text{C3})$$

where i_a/j_a correspond to the a th digit of i/j in base d^2 . The corresponding $\langle L_{\gamma'} |$ state has the following form,

$$\langle L_{\gamma'} | = \text{Diagram of a triangular lattice with two paths highlighted: } \gamma'_A \text{ (black) and } \gamma'_{\bar{A}} \text{ (red)}. \quad (\text{C4})$$

where we highlighted the new paths γ'_A and $\gamma'_{\bar{A}}$ forming the edge of $\langle L_{\gamma'} |$. This new state has now effectively $\tau_A = |A|(1 + v_A)/2$ sites in the bipartition $|A|$, since the remaining product bullet states are disentangled with the rest.

2. Evaluation of p_k

Let us evaluate $\langle L_{\gamma'} | P_k | L_{\gamma'} \rangle$ in order to compute Eq. (114). We are considering states $\langle L_{\gamma'} |$ as the one shown in Eq. (C4), corresponding to a path (we ignore the bullet states disentangled from the rest),

$$\gamma' = \underbrace{\{+, +, \dots, +\}}_{\tau_A} \circ \underbrace{\{-, -, \dots, -\}}_{|\bar{A}|(1-v_{\bar{A}})/2} \circ \underbrace{\{+, +, \dots, +\}}_{|\bar{A}|(1+v_{\bar{A}})/2}, \quad (\text{C5})$$

of total length $\tau_A + |\bar{A}|$.

Graphically, it is easy to see that, using the unitarity of the gates, any scalar product of the type $\langle L_{\gamma'} | (|\circ\rangle^{\otimes x})$, where the x bullet states are applied from the top, deletes the first x main diagonal of the state $\langle L_{\gamma'} |$:

$$\langle L_{\gamma'} | (|\circ\rangle^{\otimes x}) = \text{Diagram of a triangular lattice with a path and } x \text{ bullet states at the top.} \quad (\text{C6})$$

$$= \langle L_{\gamma \setminus x} |, \quad (\text{C7})$$

where with $\gamma \setminus x$ we indicate the path γ , where the first x jumps have been deleted. Using the definition of the projectors P_k in Eq. (108), we then find

$$\langle L_{\gamma'} | P_k | L_{\gamma'} \rangle = \langle L_{\gamma' \setminus \tau_A - k} | L_{\gamma' \setminus \tau_A - k} \rangle - \langle L_{\gamma' \setminus (\tau_A - k + 1)} | L_{\gamma' \setminus (\tau_A - k + 1)} \rangle, \quad (\text{C8})$$

for $k > 0$, and

$$\langle L_{\gamma'} | P_0 | L_{\gamma'} \rangle = \langle L_{\gamma' \setminus \tau_A} | L_{\gamma' \setminus \tau_A} \rangle. \quad (\text{C9})$$

Finally, using Eq. (B14) and the shape of γ' in Eq. (C5), we find

$$\begin{aligned} \langle L_{\gamma'} | P_k | L_{\gamma'} \rangle &= \mathcal{N}_{|\bar{A}|(1+v_{\bar{A}})/2+k} - \mathcal{N}_{|\bar{A}|(1+v_{\bar{A}})/2+k-1}, \\ \langle L_{\gamma'} | P_0 | L_{\gamma'} \rangle &= \mathcal{N}_{|\bar{A}|(1+v_{\bar{A}})/2}. \end{aligned} \quad (\text{C10})$$

Using again Eq. (B14), we also have

$$\langle L_{\gamma'} | L_{\gamma'} \rangle = \mathcal{N}_{(1+v_{\bar{A}})t}, \quad (\text{C11})$$

where we used the fact that

$$|A| \frac{1+v_A}{2} + |\bar{A}| \frac{1+v_{\bar{A}}}{2} = \frac{1+v_{\bar{A}}}{2} 2t. \quad (\text{C12})$$

Finally, using Assumption 1, we find the asymptotic scaling,

$$\langle L_{\gamma'} | P_k | L_{\gamma'} \rangle \sim C > 0, \quad (\text{C13})$$

$$\langle L_{\gamma'} | P_0 | L_{\gamma'} \rangle \sim C |\bar{A}| \frac{1+v_{\bar{A}}}{2} > 0, \quad (\text{C14})$$

$$\langle L_{\gamma'} | L_{\gamma'} \rangle \sim C(1+v)t, \quad (\text{C15})$$

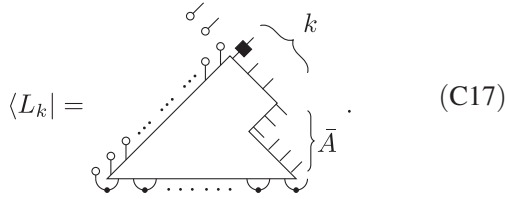
which, putting back in the definition of p_k in Eq. (114), gives

$$p_k = \begin{cases} \frac{1}{(1+v_\gamma)t} & k \neq 0 \\ \frac{|\bar{A}|(1+v_{\gamma\bar{A}})}{2(1+v_\gamma)t} & k = 0 \end{cases}; \quad (\text{C16})$$

in the main text we considered a coarse grained constant slope for the path γ , which corresponds to the substitution, in Eq. (C16), $v_{\gamma_A} = v_{\gamma_{\bar{A}}} = v_\gamma$, that leads to Eq. (118).

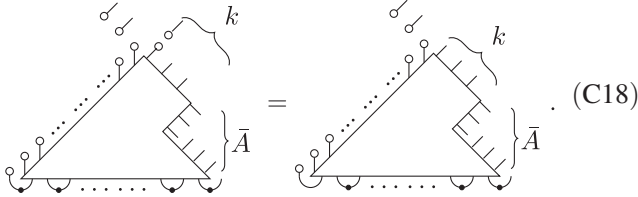
3. Entropy of the state $|L_k\rangle$ via membrane approach

In this appendix we use the entanglement membrane approach to compute the second Rényi entropy of the state in Eq. (119) which we call $|L_k\rangle$ and repeat the expression here:



$$\langle L_k | = \quad (\text{C17})$$

The projector (black box) is $\mathbb{1}_{d^2} - |\circ\rangle\langle\circ|$. By using the dual-unitary property, the action of the $|\circ\rangle\langle\circ|$ is equivalent to replacing the left boundary state via a solvable EPR state:

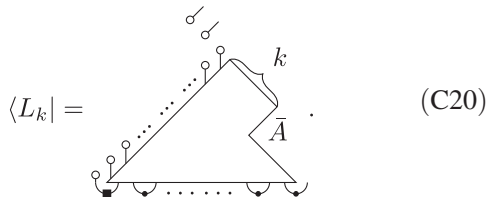


$$= \quad (\text{C18})$$

Therefore this is the part to be projected out. We decompose the initial state on the bottom left of the diagram into a component of the solvable state (EPR state) and a remainder term (box state):

$$\text{loop with dot} = \frac{1}{d} \text{loop} + \text{box state}. \quad (\text{C19})$$

From Eq. (C18), $\langle L_k |$ can be simplified to



$$\langle L_k | = \quad (\text{C20})$$

We then closely follow the discussion of Sec. IV B. The evaluation follows exactly as in Eq. (69) when the state $\langle L_\gamma |$ is replaced by $\langle L_k |$; namely,

$$S^{(2)}(|L_k\rangle) = F_1(x) - F_2(x), \quad (\text{C21})$$

with

$$F_1(x) = -\log(\text{tr}_A[\text{tr}_{\bar{A}}(|L_k\rangle\langle L_k|)^2]), \quad (\text{C22})$$

and

$$F_2(x) = -2 \log \text{tr}(|L_k\rangle\langle L_k|). \quad (\text{C23})$$

Here A is the subsystem formed by the top τ_A sites (of which the top $\tau_A - k$ sites are decoupled product states though, so it is as if A contained only k sites for what concerns entanglement calculations).

The calculation follows the same lines as the one outlined in Sec. IV B with one main difference: since the square state



$$(\text{C24})$$

in the bottom left corner of $|L_k\rangle$ is orthogonal to the loop state $|\circ\rangle$, its fourfold copy is orthogonal to the identity permutation in S_4 . This means that the optimal domain-wall configurations are not those reported in Fig. 7 but, instead, look like those reported in Fig. 22. This gives

$$F_1(x) = F_2(x) + 2 \min(k, |\bar{A}|) \log d, \quad (\text{C25})$$

where we used that for dual-unitary circuits the line tension is equal to one. Plugging in Eq. (C21) and using the monotonicity in α of the Rényi entropies we arrive at Eq. (123).

In Fig. 21, we checked the validity of Eq. (123), by comparing the maximum value of $S^{(1)}(\rho_k)$ as a function of $\ell \equiv k + |\bar{A}|$ (i.e., the number of sites defining the corresponding Hilbert space) for $v_\gamma = 1$. From the membrane theory [cf. Eq. (123)] we expect an asymptotic growth of the peak to be equal to

$$\sup_{\substack{k, \\ k+|\bar{A}|=\text{const}}} \min(k, |\bar{A}|) \log(d^2) = \frac{k + |\bar{A}|}{2} \log(d^2) \\ = \ell \log(d). \quad (\text{C26})$$

This prediction agrees with the data for the higher values of the entanglement power p . For lower values of the entangling power we expect the asymptotic form to arise at larger system sizes. The growth rate of the sup in Eq. (C26) is actually a necessary and sufficient condition

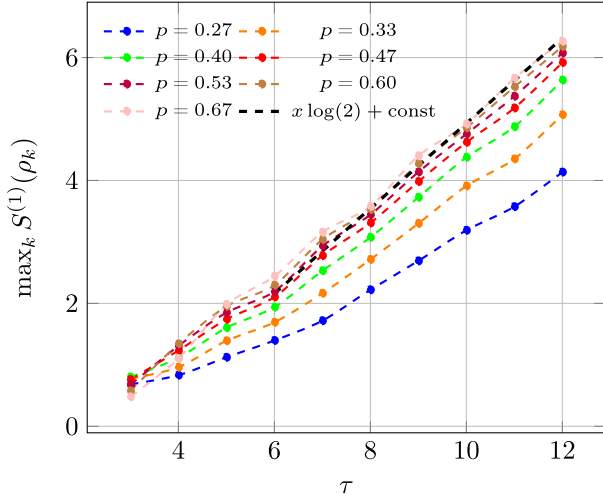


FIG. 21. Entanglement entropy for the matrix ρ_k , obtained by maximizing the value over all possible choices of k , keeping $\tau = |\bar{A}| + k$ fixed, for generic dual-unitary gates of different entangling power, local Hilbert space dimension $d = 2$, and $v_\gamma = 1$.

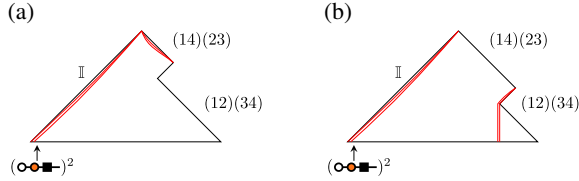


FIG. 22. Domain-wall configuration giving the leading contribution to Eq. (C22). (a) When $k < |A|$, the two domain walls (14)(23) split into four domain walls (12)(34) \times (13)(24). Two of them go to the left to contract with the orthogonal states. The other two (12)(34) go to the right and cancel with the two domain walls at the interactions of A and \bar{A} . (b) The domain walls at the tip do not split. They go to the left to contract with the orthogonal states.

for the validity of Eq. (123). This is because, using the positivity of mutual information one has:

$$|S(\rho_k^{(\ell)}) - S(\rho_{k-1}^{(\ell)})| \leq \log(d^2), \quad (\text{C27})$$

where we stressed for clarity that here we consider a density matrix with ℓ sites and a bipartition (on which entanglement is defined) with $k, \ell - k$ sites. Combining Eq. (C27) with Eq. (C26), one must have

$$S(\rho_k^{(\ell)}) = \min(k, \ell - k) \log(d^2) + o(k) + o(\ell), \quad (\text{C28})$$

which is indeed Eq. (123).

APPENDIX D: ASYMPTOTIC BEHAVIOR OF $\mathcal{P}(t)$ UNDER RANDOM DUAL-UNITARY GATES

In this appendix we characterize the asymptotic behavior of the purity in dual-unitary circuits with random local

gates. In particular, following Ref. [77] we consider local gates of the form

$$u_+(\tau, x) \otimes u_-(\tau, x) \cdot U \cdot v_+(\tau, x) \otimes v_-(\tau, x), \quad (\text{D1})$$

where U is a fixed two-site dual-unitary gate and u_\pm, v_\pm are random single-site matrices $\in U(d)$ distributed independently in the space-time. In this setting, Ref. [77] proved that if

$$p(U) \geq \frac{d^2 - 1}{d^2} \left(1 - \frac{1}{\sqrt{2d + 2}} \right) \quad (\text{D2})$$

[cf. Eq. (12)], then

$$d^x \mathbb{E}_u[\mathcal{P}(x/2)] \leq A + Bx, \quad A, B \geq 0, \quad (\text{D3})$$

where $\mathbb{E}_u[\cdot]$ is the average over \mathbf{u} drawn from the full $U^{\otimes 4L_t}(d)$ group (Haar average).

Here we want to show that for nonsolvable states $d^x \mathbb{E}_u[\mathcal{P}(x/2)]$ is bounded by a linearly growing function also from below. Namely,

$$d^x \mathbb{E}_u[\mathcal{P}(x/2)] \geq Cx. \quad (\text{D4})$$

Defining the convenient auxiliary quantity,

$$\mathcal{M}_x = d^x \mathcal{P}(x/2) - d^{x-1} \mathcal{P}(x/2 - 1/2), \quad (\text{D5})$$

our goal is to show

$$\lim_{x \rightarrow \infty} \mathbb{E}_u[\mathcal{M}_x] = \mathbb{E}_u[\mathcal{M}_\infty] > 0. \quad (\text{D6})$$

This proves Assumption 1 in the random dual-unitary setting.

First, we note that $\mathbb{E}_u[\mathcal{M}_x]$ can be related to the function \mathcal{Q}_x —introduced in Eq. (85) of Ref. [77]—as follows:

$$\mathbb{E}_u[\mathcal{M}_x] = d^x \frac{c - 1}{\sqrt{d^2 - 1}} \mathcal{Q}_x. \quad (\text{D7})$$

Here the parameter c is defined in terms of the initial state matrix m [cf. Eq. (15)]:

$$c = \frac{1}{d} \text{tr}[(mm^\dagger)^2] \in [1, d]. \quad (\text{D8})$$

In particular, the value $c = 1$ corresponds to a unitary initial state matrix m , i.e., a solvable initial state. In this case, noting that \mathcal{Q}_x is finite for $c = 1$, Eq. (D7) gives $\mathcal{M}_x = 0$. This is the expected result for solvable states: the norm of $\langle L_\gamma \rangle$ is equal to one and its increment \mathcal{M}_{r^*} is zero. From now on we consider $c > 1$ and argue that in this case $\mathbb{E}_u[\mathcal{M}_x]$ is always strictly larger than zero.

We begin by noting that a direct application of Eq. (86) of Ref. [77] gives

$$\mathbb{E}_u[\mathcal{M}_x] = \mathbb{E}_u[\mathcal{M}]_{x_0} + \sum_{i=x_0+1}^x \mathcal{S}_i. \quad (\text{D9})$$

Here we introduced

$$\mathcal{S}_x = d^x \frac{c-1}{\sqrt{d^2-1}} \mathcal{R}_x, \quad (\text{D10})$$

where \mathcal{R}_x is the function defined in Eq. (87) of Ref. [77].

Next, using Eq. (103) of Ref. [77] we conclude

$$|\mathcal{S}_x| \leq Aa^x, \quad (\text{D11})$$

where p is the entangling power of U [cf. Eq. (12)] and we introduced

$$\lambda = (1-p)^2 + \frac{p^2}{d^2-1}, \quad (\text{D12})$$

$$a = \frac{d+c}{d+1} d\lambda, \quad (\text{D13})$$

$$A = \frac{(c-1)^2 d+1}{(d+c)^2 d-1} \sqrt{\frac{d^2-1}{d^2\lambda^3}}. \quad (\text{D14})$$

For high enough values of the entangling power,

$$p > \bar{p}(d) = \frac{d^2-1}{d^2} \left(1 - \frac{1}{\sqrt{2d+2}}\right), \quad (\text{D15})$$

it is immediate to verify that $a < 1$ for any value of c in the range $[1, d]$, which allows us to find an upper bound for $\mathbb{E}_u[\mathcal{M}_x]$. Namely,

$$\begin{aligned} \mathbb{E}_u[\mathcal{M}_x] &\leq \mathbb{E}_u[\mathcal{M}_{x_0}] + \sum_i |\mathcal{S}_i| \\ &\leq \mathbb{E}_u[\mathcal{M}_{x_0}] + \frac{A}{1-a} a^{x_0+1}. \end{aligned} \quad (\text{D16})$$

This bound was first presented in Ref. [77]. Our goal here is to bound $\mathbb{E}_u[\mathcal{M}_x]$ also from below, showing that it is always strictly larger than 0. To this end we combine Eqs. (D9), (D11), and the triangle inequality to write

$$\begin{aligned} \mathbb{E}_u[\mathcal{M}_x] &\geq \mathbb{E}_u[\mathcal{M}_{x_0}] - \sum_i |\mathcal{S}_i| \\ &\geq \mathbb{E}_u[\mathcal{M}_{x_0}] - A \frac{a^{x_0+1} - a^{x+1}}{1-a}. \end{aligned} \quad (\text{D17})$$

For p fulfilling the bound (D15) one has $a < 1$. This implies that, if we find an x_0 such that

$$\mathbb{E}_u[\mathcal{M}_{x_0}] > A \frac{a^{x_0+1}}{1-a}, \quad (\text{D18})$$

then

$$\lim_{x \rightarrow \infty} \mathbb{E}_u[\mathcal{M}_x] = \mathbb{E}_u[\mathcal{M}_\infty] > 0. \quad (\text{D19})$$

In order to get some intuition it is useful to consider two limiting cases. First, we fix the values of x , p , d , and restrict ourselves to a neighborhood of the solvable case, which corresponds to $c = 1$. We choose the neighborhood to be small compared to the other parameters, so that we can treat everything perturbatively around the lowest nontrivial order of the solvable case:

$$c \in [1, 1 + \epsilon], \quad \epsilon \ll \frac{1}{x}, \quad 1 - a. \quad (\text{D20})$$

In this situation, it is easy to see that

$$\mathbb{E}_u[\mathcal{M}_x] = O(c-1), \quad A = O[(c-1)^2], \quad (\text{D21})$$

which immediately imply the validity of condition (D18) if $c \neq 1$. This shows that some properties of the solvable case are not stable under perturbations.

The other useful limit is $d \gg 1$, which makes the expressions (D14) and (D13) much easier to handle. We consider $\mathbb{E}_u[\mathcal{M}_4]$ at leading order in d , expanded at the first relevant order for $1-p$. We consider gates with entangling power close to the one of the Hadamard gate, or larger, meaning that

$$1-p \lesssim O(d^{-1}). \quad (\text{D22})$$

The asymptotic expression at the lowest relevant order is

$$\begin{aligned} \mathbb{E}_u[\mathcal{M}_4] &= (c-1)[1+c(1-p)] > (c-1) \\ &= O(d^0). \end{aligned} \quad (\text{D23})$$

Expanding Eqs. (D14) and (D13), we find

$$A = \frac{(c-1)^2}{(d+c)^2} \frac{d^3}{[(1-p)^2 d^2 + 1]^{3/2}} \lesssim O(d^3), \quad (\text{D24})$$

$$a = \frac{d+c}{d} \frac{(1-p)^2 d^2 + 1}{d} = O(d^{-1}). \quad (\text{D25})$$

Putting together everything in condition (D18), we see the left-hand side is $O(d^0)$ and the right-hand side is $O(d^{-2})$, so the condition is respected. Finally, to address the general case, we compute $\mathbb{E}_u[\mathcal{M}_{x_0}]$ numerically for a high value of x_0 , showing that the bound (D18) holds for a nontrivial interval of entangling powers.

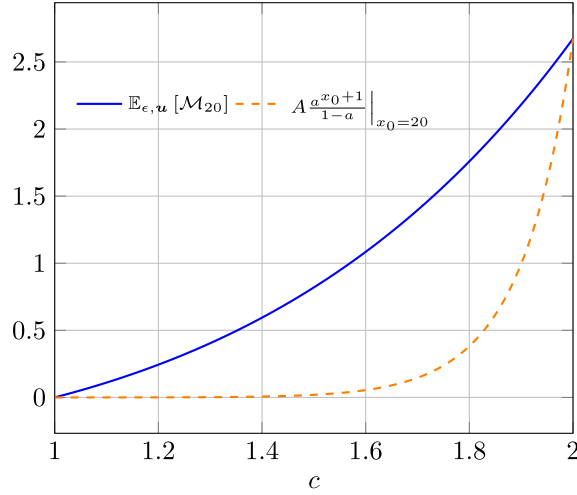


FIG. 23. $\mathbb{E}_u[\mathcal{M}_{x_0}]$ and $A(a^{x_0+1}/1-a)$ versus c for $x_0 = 20$, $p = \bar{n}$, and $d = 2$. Note the linear and quadratic growth around $c = 1$ according to Eq. (D21).

In particular, we consider the case $d = 2$. In this case, the values of the entangling power p fulfilling the bound (D15) are given by

$$\frac{2}{3} > p > \bar{p}(2) \approx 0.4438, \quad (\text{D26})$$

where we used that for $d = 2$ the maximal attainable value of p is $2/3$ [77].

Computing $\mathbb{E}_u[\mathcal{M}_x]$ for $x = 20$, we verify the inequality (D18) holds for any c if we pick p in the interval

$$\frac{2}{3} > p \geq \bar{n} \approx 0.47660548. \quad (\text{D27})$$

Note that, to verify the equality for p close to $\bar{p}(d)$ one would need to consider arbitrarily large values of x_0 . Indeed the denominator $(1-a)^{-1}$ diverges at $p = \bar{p}(d)$. As an example, we show in Fig. 23 the value of $Aa^{x_0+1}/(1-a)$ versus $\mathbb{E}_u[\mathcal{M}_{x_0}]$, for $x_0 = 20$ as a function of c .

APPENDIX E: PARAMETRIZATION OF DUAL-UNITARY GATES FOR NUMERICAL EXPERIMENTS

To produce the data presented in plots involving dual unitary gates (i.e., Figs. 8–14), we parametrized the gates as in Eq. (D1), with fixed one-site unitaries u_{\pm}, v_{\pm} :

$$u_+ = \begin{pmatrix} 0.204 - 0.971i & -0.108 - 0.068i \\ 0.125 + 0.0254i & -0.524 + 0.842i \end{pmatrix}, \quad (\text{E1})$$

$$u_- = \begin{pmatrix} -0.279 - 0.921i & 0.238 + 0.132i \\ -0.272 + 0.017i & -0.649 + 0.710i \end{pmatrix}, \quad (\text{E2})$$

$$v_+ = \begin{pmatrix} -0.025 - 0.367i & -0.921 - 0.127i \\ 0.908 - 0.202i & 0.005 + 0.368i \end{pmatrix}, \quad (\text{E3})$$

$$v_- = \begin{pmatrix} 0.380 - 0.321i & 0.436 + 0.750i \\ 0.807 + 0.318i & 0.260 - 0.424i \end{pmatrix}, \quad (\text{E4})$$

and two-site dual-unitary given by

$$U(p) = \begin{pmatrix} e^{-iJ(p)} & 0 & 0 & 0 \\ 0 & 0 & -ie^{iJ(p)} & 0 \\ 0 & -ie^{iJ(p)} & 0 & 0 \\ 0 & 0 & 0 & e^{-iJ(p)} \end{pmatrix}, \quad (\text{E5})$$

where

$$J(p) = \arcsin\left(\sqrt{1 - \frac{3p}{2}}\right), \quad (\text{E6})$$

and $p \in [0, 1]$. Using the definition of entangling power in Eq. (12) one can immediately verify that

$$p[U(p)] = p. \quad (\text{E7})$$

APPENDIX F: RECURRENCE RELATION FOR $\langle L_{\gamma} | L_{\gamma} \rangle$

In this appendix we consider the Haar averages in Eq. (130). A doubly folded averaged unitary is projected on two-dimensional local vector space, spanned by the normalized vectors

$$|\circ_2\rangle = \frac{|\uparrow\uparrow\rangle}{d}, \quad |\square_2\rangle = \frac{|(12)\rangle}{d}, \quad (\text{F1})$$

where $|(12)\rangle, |\uparrow\uparrow\rangle$ refer to the permutation vectors represented in Fig. 6(a).

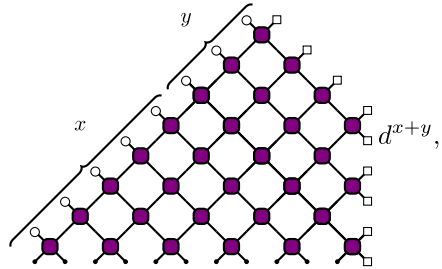
Moreover, a Haar averaged unitary gate fulfills the following relations:

$$\begin{aligned} & \text{Gate with 4 legs} = \text{Purple square gate}, \\ & \text{Purple square gate with 2 legs} = \frac{d}{d^2 + 1} \left(\text{Red circle} + \text{Blue square} \right), \\ & \text{Purple square gate with 2 legs} = \text{Red circle} + \text{Blue square}. \end{aligned} \quad (\text{F2})$$

Here, we choose a specific normalization for the initial state such that

$$\begin{array}{c} \circ \\ | \\ \bullet \end{array} = \begin{array}{c} \square \\ | \\ \bullet \end{array} := 1. \quad (\text{F3})$$

We can define the quantity



$$\mathcal{A}_{x,y} = d^{x+y}, \quad (\text{F4})$$

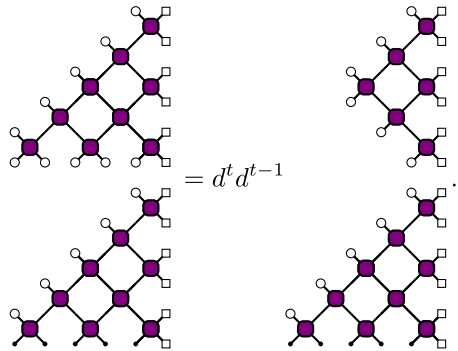
with $y \leq x + 1$. It is immediate to see that

$$\overline{\langle L_{\gamma_{t+1}} | L_{\gamma_{t+1}} \rangle} = \mathcal{A}_{t,t+1}. \quad (\text{F5})$$

Using Eqs. (F2) and (F3), one finds the following recurrence relations:

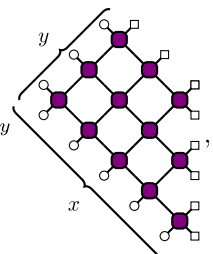
$$\mathcal{A}_{x,y} = \begin{cases} \frac{d^2}{d^2+1} (\mathcal{A}_{x-1,y-1} + \mathcal{A}_{x,y-1}) & y = x + 1 \\ \frac{d^2}{d^2+1} (\mathcal{A}_{x-1,y} + \mathcal{A}_{x,y-1}) & 0 < y \leq x \\ \left(\frac{2d^2}{d^2+1}\right)^x & y = 0. \end{cases} \quad (\text{F6})$$

The treatment for the average $\overline{\langle L_{\gamma} | L_{\gamma/2} \rangle \otimes | L_{\gamma/2} \rangle}$ is similar: the average corresponds to the diagram



$$d^{2t-1} = d^t d^{t-1}. \quad (\text{F7})$$

The top diagram can be expressed again with recursive relation, defining the quantity $\mathcal{B}_{x,y}$:



$$\mathcal{B}_{x,y} = d^{x+y}, \quad (\text{F8})$$

which fulfills

$$\mathcal{B}_{x,y} = \begin{cases} \frac{d^2}{d^2+1} (\mathcal{B}_{x-1,y-1} + \mathcal{B}_{x,y-1}) & y = x \\ \frac{d^2}{d^2+1} (\mathcal{B}_{x-1,y} + \mathcal{B}_{x,y-1}) & y < x \\ 1 & y = 0. \end{cases} \quad (\text{F9})$$

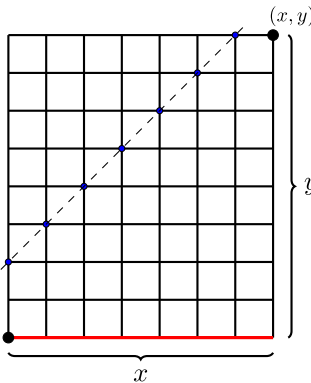
Equation (130) can then be expressed in terms of these quantities as (assuming a generic bipartition of the temporal state at time t in $t = t_1 + t_2$)

$$\bar{r}_t = \frac{\mathcal{B}_{t_1,t_1} \sqrt{\mathcal{A}_{t_2,t_2+1}}}{\sqrt{\mathcal{A}_{t,t+1} \mathcal{A}_{t_1,t_1+1}}}. \quad (\text{F10})$$

Interestingly, we can map the recurrence relation (F6) in a different problem. First, we slightly change normalization by defining

$$\mathcal{A}_{x,y} = \tilde{\mathcal{A}}_{x,y} \left(\frac{d^2}{d^2+1}\right)^{x+y}, \quad (\text{F11})$$

then the quantity $\tilde{\mathcal{A}}_{x,y}$ can be thought of as the number of paths connecting the two black dots in the following grid, without crossing the dashed line $y = x + 2$ and in the minimum number of steps:



$$. \quad (\text{F12})$$

Each path gains a weight $1 + 1/d^2$ every time it touches the top boundary and a factor 2 for every crossed red link of the bottom boundary. To compute the asymptotic scaling of this quantity we can ignore the $1 + 1/d^2$ weight, which does not change the scaling for d large enough, since the number of paths touching the top boundary exactly p times is exponentially suppressed in p with respect to the total number of paths, which balances the

$$\left(\frac{d^2+1}{d^2}\right)^p \quad (\text{F13})$$

weight (this holds for $d > 1$). This statement can be made more precise using Theorem 2 of Ref. [142]. It is possible to show then that the number of paths touching the boundary p times is the following (the convention is to

set a binomial coefficient to 0 if the top argument is lower than the bottom one, or the latter is < 0):

$$\binom{x+y-p}{x} - \binom{x+y-p}{x+2}, \quad (\text{F14})$$

so that, considering the appropriate weight for these paths, and setting $x = y - 1 = t$ (we ignore the weights for the red links on the bottom for the sake of this argument), the total is

$$\sum_{p=0}^t \left[\binom{2t+1-p}{t} - \binom{2t+1-p}{t+2} \right] \left(1 + \frac{1}{d^2}\right)^p. \quad (\text{F15})$$

Studying the asymptotic scaling of this sum (using the Stirling formula and approximating the sum with an integral, expanded around the maximum), we can see the scaling at leading order in t is unaffected as long as $d > 1$. We can call a_n the number of paths connecting (x, y) to $(n, 0)$, then we can write

$$\tilde{A}_{x,y} \sim \sum_{n=0}^x (a_n - a_{n+1}) 2^n, \quad (\text{F16})$$

with

$$a_n = \begin{cases} \binom{x+y-n}{x-n} - \binom{x+y-n}{x+3} & 0 \leq n \leq x, n \leq y-3 \\ \binom{x+y-n}{y} & 0 \leq n, n \geq y-2 \\ 0 & n < 0, n > x. \end{cases} \quad (\text{F17})$$

In particular, we can rewrite Eq. (F10) as

$$\sum_{n=0}^x (a_n - a_{n+1}) 2^n = a_0 + \sum_{n=1}^x a_n 2^{n-1}, \quad (\text{F18})$$

and find an asymptotic expression for a_n using Stirling's formula [we take $(x, y) = (t, t+1)$]:

$$a_n 2^{n-1} \sim \frac{1}{2} f\left(\frac{n}{t}\right),$$

$$f(z) = \frac{2^{zt}}{\sqrt{2\pi t}} \frac{(2-z)^{(2-z)t}}{(1-z)^{(1-z)t}} \left[\frac{6}{t} + 2z - z^2 + O\left(\frac{z}{t}\right) \right]. \quad (\text{F19})$$

Finally, we can estimate the sum in Eq. (F18) with an integral, computed with the saddle point approximation:

$$\sum_{n=1}^t a_n 2^{n-1} = O\left(t \int_0^\infty f(z) dz\right). \quad (\text{F20})$$

We expand $\log[f(z)]$ around its minimum z_0 , at the leading orders in t :

$$z_0 = \sqrt{\frac{2}{t}} - \frac{11}{4t} + o\left(\frac{1}{t}\right),$$

$$\frac{d \log(f)}{dz} \Big|_{z=z_0} = O\left(\frac{1}{\sqrt{t}}\right),$$

$$\frac{d^2 \log(f)}{dz^2} \Big|_{z=z_0} = -t + o(t),$$

$$\log[f(z_0)] = t \log(4) - \log(t) + \frac{1}{2} \left[\log\left(\frac{4}{\pi}\right) - 1 \right]. \quad (\text{F21})$$

Using the saddle point approximation, for large t we find

$$\int_0^\infty f(z) dz \sim \frac{4^t}{t^{-3/2}} \frac{2}{\sqrt{e\pi}} \int_{-\sqrt{2}}^\infty e^{-x^2/2} dx, \quad (\text{F22})$$

which gives

$$\mathcal{A}_{t,t+1} = O\left(\left(\frac{2d^2}{d^2+1}\right)^{2t} t^{-1/2}\right). \quad (\text{F23})$$

We can compute $\mathcal{B}_{t,t}$ with a similar approach: in this case we need to consider the paths connecting a point (x, y) to the origin without crossing the line $x = y + 1$. As before, we approximate this quantity by ignoring the weights obtained touching the top boundary $1 + 1/d^2$. We can then write

$$\mathcal{B}_{x,y} = O\left(\left(\frac{d^2}{d^2+1}\right)^{x+y} \sum_{n=0}^x b_n \left(\frac{d^2+1}{d^2}\right)^n\right), \quad (\text{F24})$$

where b_n is the number of paths connecting (x, y) to $(n, 1)$:

$$b_n = \begin{cases} \binom{x+y-n-1}{y-1} - \binom{x+y-n-1}{x+1} & 0 \leq n \leq x, n \leq y-2 \\ \binom{x+y-n-1}{y-1} & 0 \leq n \leq x, n \geq y-1 \\ 0 & n < 0, n > x. \end{cases} \quad (\text{F25})$$

As before, we estimate the sum (F24) with an integral, in the case $(x, y) = (t, t)$:

$$\mathcal{B}_{t,t} = O\left(t \int_0^\infty g(z) dz\right),$$

$$g\left(\frac{n}{t}\right) \sim b_n \left(\frac{d^2+1}{d^2}\right)^n, \quad (\text{F26})$$

$$g(z) = \left(\frac{d^2}{d^2+1}\right)^{zt} \frac{1}{t\sqrt{2\pi t}} \frac{(2-z)^{(2-z)t}}{(1-z)^{(1-z)t}} [4 + 2z + O(z^2)].$$

The difference with the previous case is that $g'(z) \neq 0$ in the domain we are interested in, as long as $d > 1$. The maximum value attained is $g(z=0)$; thus we can estimate the integral expanding $\log(g)$ around $z=0$ at first order,

$$\int_0^\infty g(z) dz \sim \frac{g^2(0)}{g'(0)} = O(4^t t^{-5/2}), \quad (\text{F27})$$

finding the scaling

$$\mathcal{B}_{t,t} = O\left(\left(\frac{2d^2}{d^2+1}\right)^{2t} t^{-3/2}\right). \quad (\text{F28})$$

Plugging Eqs. (F23)–(F28) into Eq. (F10), we find

$$\bar{r}_t = O(t^{-5/4}). \quad (\text{F29})$$

-
- [1] I. Bloch, J. Dalibard, and W. Zwerger, *Many-Body Physics with Ultracold Gases*, *Rev. Mod. Phys.* **80**, 885 (2008).
- [2] T. Kinoshita, T. Wenger, and D. S. Weiss, *A Quantum Newton's Cradle*, *Nature (London)* **440**, 900 (2006).
- [3] T. Langen, S. Erne, R. Geiger, B. Rauer, T. Schweigler, M. Kuhnert, W. Rohringer, I. E. Mazets, T. Gasenzer, and J. Schmiedmayer, *Experimental Observation of a Generalized Gibbs Ensemble*, *Science* **348**, 207 (2015).
- [4] M. Schemmer, I. Bouchoule, B. Doyon, and J. Dubail, *Generalized Hydrodynamics on an Atom Chip*, *Phys. Rev. Lett.* **122**, 090601 (2019).
- [5] P. N. Jepsen, J. Amato-Grill, I. Dimitrova, W. W. Ho, E. Demler, and W. Ketterle, *Spin Transport in a Tunable Heisenberg Model Realized with Ultracold Atoms*, *Nature (London)* **588**, 403 (2020).
- [6] N. Malvania, Y. Zhang, Y. Le, J. Dubail, M. Rigol, and D. S. Weiss, *Generalized Hydrodynamics in Strongly Interacting 1D Bose Gases*, *Science* **373**, 1129 (2021).
- [7] D. Wei, A. Rubio-Abadal, B. Ye, F. Machado, J. Kemp, K. Srakaew, S. Hollerith, J. Rui, S. Gopalakrishnan, N. Y. Yao, I. Bloch, and J. Zeiher, *Quantum Gas Microscopy of Kardar-Parisi-Zhang Superdiffusion*, *Science* **376**, 716 (2022).
- [8] M. K. Joshi, F. Kranzl, A. Schuckert, I. Lovas, C. Maier, R. Blatt, M. Knap, and C. F. Roos, *Observing Emergent Hydrodynamics in a Long-Range Quantum Magnet*, *Science* **376**, 720 (2022).
- [9] S. R. White, *Density Matrix Formulation for Quantum Renormalization Groups*, *Phys. Rev. Lett.* **69**, 2863 (1992).
- [10] S. R. White, *Density-Matrix Algorithms for Quantum Renormalization Groups*, *Phys. Rev. B* **48**, 10345 (1993).
- [11] U. Schollwöck, *The Density-Matrix Renormalization Group in the Age of Matrix Product States*, *Ann. Phys. (Amsterdam)* **326**, 96 (2011).
- [12] A. J. Daley, C. Kollath, U. Schollwöck, and G. Vidal, *Time-Dependent Density-Matrix Renormalization-Group Using Adaptive Effective Hilbert Spaces*, *J. Stat. Mech.* (2004) P04005.
- [13] S. R. White and A. E. Feiguin, *Real-Time Evolution Using the Density Matrix Renormalization Group*, *Phys. Rev. Lett.* **93**, 076401 (2004).
- [14] G. Vidal, *Efficient Classical Simulation of Slightly Entangled Quantum Computations*, *Phys. Rev. Lett.* **91**, 147902 (2003).
- [15] G. Vidal, *Efficient Simulation of One-Dimensional Quantum Many-Body Systems*, *Phys. Rev. Lett.* **93**, 040502 (2004).
- [16] T. Prosen and M. Žnidarič, *Is the Efficiency of Classical Simulations of Quantum Dynamics Related to Integrability?*, *Phys. Rev. E* **75**, 015202(R) (2007).
- [17] J. Haegeman, J. I. Cirac, T. J. Osborne, I. Pižorn, H. Verschelde, and F. Verstraete, *Time-Dependent Variational Principle for Quantum Lattices*, *Phys. Rev. Lett.* **107**, 070601 (2011).
- [18] J. Haegeman, C. Lubich, I. Oseledets, B. Vandereycken, and F. Verstraete, *Unifying Time Evolution and Optimization with Matrix Product States*, *Phys. Rev. B* **94**, 165116 (2016).
- [19] E. Leviatan, F. Pollmann, J. H. Bardarson, D. A. Huse, and E. Altman, *Quantum Thermalization Dynamics with Matrix-Product States*, [arXiv:1702.08894](https://arxiv.org/abs/1702.08894).
- [20] B. Kloss, Y. B. Lev, and D. Reichman, *Time-Dependent Variational Principle in Matrix-Product State Manifolds: Pitfalls and Potential*, *Phys. Rev. B* **97**, 024307 (2018).
- [21] C. D. White, M. Zaletel, R. S. K. Mong, and G. Refael, *Quantum Dynamics of Thermalizing Systems*, *Phys. Rev. B* **97**, 035127 (2018).
- [22] M. Žnidarič, *Nonequilibrium Steady-State Kubo Formula: Equality of Transport Coefficients*, *Phys. Rev. B* **99**, 035143 (2019).
- [23] C. Krumnow, J. Eisert, and O. Legeza, *Towards Overcoming the Entanglement Barrier When Simulating Long-Time Evolution*, [arXiv:1904.11999](https://arxiv.org/abs/1904.11999).
- [24] T. Rakovszky, C. W. von Keyserlingk, and F. Pollmann, *Dissipation-Assisted Operator Evolution Method for Capturing Hydrodynamic Transport*, *Phys. Rev. B* **105**, 075131 (2022).
- [25] C. von Keyserlingk, F. Pollmann, and T. Rakovszky, *Operator Backflow and the Classical Simulation of Quantum Transport*, *Phys. Rev. B* **105**, 245101 (2022).
- [26] M. C. Bañuls, M. B. Hastings, F. Verstraete, and J. I. Cirac, *Matrix Product States for Dynamical Simulation of Infinite Chains*, *Phys. Rev. Lett.* **102**, 240603 (2009).
- [27] A. Müller-Hermes, J. I. Cirac, and M. C. Bañuls, *Tensor Network Techniques for the Computation of Dynamical Observables in One-Dimensional Quantum Spin Systems*, *New J. Phys.* **14**, 075003 (2012).
- [28] M. B. Hastings and R. Mahajan, *Connecting Entanglement in Time and Space: Improving the Folding Algorithm*, *Phys. Rev. A* **91**, 032306 (2015).
- [29] M. Sonner, A. Leroze, and D. A. Abanin, *Characterizing Many-Body Localization via Exact Disorder-Averaged Quantum Noise*, *Phys. Rev. B* **105**, L020203 (2022).
- [30] M. Frías-Pérez and M. C. Bañuls, *Light Cone Tensor Network and Time Evolution*, *Phys. Rev. B* **106**, 115117 (2022).
- [31] A. Leroze, M. Sonner, and D. A. Abanin, *Overcoming the Entanglement Barrier in Quantum Many-Body Dynamics via Space-Time Duality*, *Phys. Rev. B* **107**, L060305 (2023).
- [32] R. Feynman and F. Vernon, *The Theory of a General Quantum System Interacting with a Linear Dissipative System*, *Ann. Phys. (N.Y.)* **24**, 118 (1963).

- [33] A. Leroose, M. Sonner, and D. A. Abanin, *Influence Matrix Approach to Many-Body Floquet Dynamics*, *Phys. Rev. X* **11**, 021040 (2021).
- [34] B. Bertini, P. Kos, and T. Prosen, *Exact Spectral Form Factor in a Minimal Model of Many-Body Quantum Chaos*, *Phys. Rev. Lett.* **121**, 264101 (2018).
- [35] B. Bertini, P. Kos, and T. Prosen, *Random Matrix Spectral Form Factor of Dual-Unitary Quantum Circuits*, *Commun. Math. Phys.* **387**, 597 (2021).
- [36] A. Flack, B. Bertini, and T. Prosen, *Statistics of the Spectral Form Factor in the Self-Dual Kicked Ising Model*, *Phys. Rev. Res.* **2**, 043403 (2020).
- [37] S. J. Garratt and J. T. Chalker, *Local Pairing of Feynman Histories in Many-Body Floquet Models*, *Phys. Rev. X* **11**, 021051 (2021).
- [38] F. Fritzsche and T. Prosen, *Eigenstate Thermalization in Dual-Unitary Quantum Circuits: Asymptotics of Spectral Functions*, *Phys. Rev. E* **103**, 062133 (2021).
- [39] S. J. Garratt and J. T. Chalker, *Many-Body Delocalization as Symmetry Breaking*, *Phys. Rev. Lett.* **127**, 026802 (2021).
- [40] B. Bertini, P. Kos, and T. Prosen, *Entanglement Spreading in a Minimal Model of Maximal Many-Body Quantum Chaos*, *Phys. Rev. X* **9**, 021033 (2019).
- [41] M. Ippoliti and V. Khemani, *Postselection-Free Entanglement Dynamics via Spacetime Duality*, *Phys. Rev. Lett.* **126**, 060501 (2021).
- [42] M. Ippoliti, T. Rakovszky, and V. Khemani, *Fractal, Logarithmic, and Volume-Law Entangled Nonthermal Steady States via Spacetime Duality*, *Phys. Rev. X* **12**, 011045 (2022).
- [43] B. Bertini, K. Klobas, V. Alba, G. Lagnese, and P. Calabrese, *Growth of Rényi Entropies in Interacting Integrable Models and the Breakdown of the Quasiparticle Picture*, *Phys. Rev. X* **12**, 031016 (2022).
- [44] J. Thoenniss, M. Sonner, A. Leroose, and D. A. Abanin, *Efficient Method for Quantum Impurity Problems Out of Equilibrium*, *Phys. Rev. B* **107**, L20115 (2023).
- [45] B. Bertini, P. Calabrese, M. Collura, K. Klobas, and C. Rylands, *Nonequilibrium Full Counting Statistics and Symmetry-Resolved Entanglement from Space-Time Duality*, [arXiv:2212.06188](https://arxiv.org/abs/2212.06188) [*Phys. Rev. Lett.* (to be published)].
- [46] B. Pozsgay, *The Dynamical Free Energy and the Loschmidt Echo for a Class of Quantum Quenches in the Heisenberg Spin Chain*, *J. Stat. Mech.* (2013) P10028.
- [47] L. Piroli, B. Pozsgay, and E. Vernier, *From the Quantum Transfer Matrix to the Quench Action: The Loschmidt Echo in XXZ Heisenberg Spin Chains*, *J. Stat. Mech.* (2017) 023106.
- [48] L. Piroli, B. Pozsgay, and E. Vernier, *Non-Analytic Behavior of the Loschmidt Echo in XXZ Spin Chains: Exact Results*, *Nucl. Phys.* **B933**, 454 (2018).
- [49] G. Mahan, *Many-Particle Physics* (Plenum Press, New York, 1990).
- [50] A. Altland and B. Simons, *Condensed Matter Field Theory* (Cambridge University Press, Cambridge, England, 2010).
- [51] B. Bertini, F. Heidrich-Meisner, C. Karrasch, T. Prosen, R. Steinigeweg, and M. Žnidarič, *Finite-Temperature Transport in One-Dimensional Quantum Lattice Models*, *Rev. Mod. Phys.* **93**, 025003 (2021).
- [52] Not to be confused with the “timelike entanglement” studied in the context of conformal field theory and AdS/CFT correspondence; see Refs. [53,54].
- [53] K. Doi, J. Harper, A. Mollabashi, T. Takayanagi, and Y. Taki, *Pseudoentropy in dS/CFT and Timelike Entanglement Entropy*, *Phys. Rev. Lett.* **130**, 031601 (2023).
- [54] K. Doi, J. Harper, A. Mollabashi, T. Takayanagi, and Y. Taki, *Timelike Entanglement Entropy*, *J. High Energy Phys.* **05** (2023) 052.
- [55] F. Verstraete and J.I. Cirac, *Matrix Product States Represent Ground States Faithfully*, *Phys. Rev. B* **73**, 094423 (2006).
- [56] N. Schuch, M.M. Wolf, F. Verstraete, and J.I. Cirac, *Entropy Scaling and Simulability by Matrix Product States*, *Phys. Rev. Lett.* **100**, 030504 (2008).
- [57] B. Bertini, P. Kos, and T. Prosen, *Exact Correlation Functions for Dual-Unitary Lattice Models in 1 + 1 Dimensions*, *Phys. Rev. Lett.* **123**, 210601 (2019).
- [58] L. Piroli, B. Bertini, J.I. Cirac, and T. Prosen, *Exact Dynamics in Dual-Unitary Quantum Circuits*, *Phys. Rev. B* **101**, 094304 (2020).
- [59] K. Klobas, B. Bertini, and L. Piroli, *Exact Thermalization Dynamics in the, “Rule 54” Quantum Cellular Automaton*, *Phys. Rev. Lett.* **126**, 160602 (2021).
- [60] K. Klobas and B. Bertini, *Exact Relaxation to Gibbs and Non-Equilibrium Steady States in the Quantum Cellular Automaton Rule 54*, *SciPost Phys.* **11**, 106 (2021).
- [61] A. Leroose, M. Sonner, and D. A. Abanin, *Scaling of Temporal Entanglement in Proximity to Integrability*, *Phys. Rev. B* **104**, 035137 (2021).
- [62] G. Giudice, G. Giudici, M. Sonner, J. Thoenniss, A. Leroose, D. A. Abanin, and L. Piroli, *Temporal Entanglement, Quasiparticles, and the Role of Interactions*, *Phys. Rev. Lett.* **128**, 220401 (2022).
- [63] S. Gopalakrishnan and A. Lamacraft, *Unitary Circuits of Finite Depth and Infinite Width from Quantum Channels*, *Phys. Rev. B* **100**, 064309 (2019).
- [64] A. Nahum, J. Ruhman, S. Vijay, and J. Haah, *Quantum Entanglement Growth under Random Unitary Dynamics*, *Phys. Rev. X* **7**, 031016 (2017).
- [65] T. Zhou and A. Nahum, *Emergent Statistical Mechanics of Entanglement in Random Unitary Circuits*, *Phys. Rev. B* **99**, 174205 (2019).
- [66] M. P. A. Fisher, V. Khemani, A. Nahum, and S. Vijay, *Random Quantum Circuits*, *Annu. Rev. Condens. Matter Phys.* **14**, 335 (2023).
- [67] C. W. von Keyserlingk, T. Rakovszky, F. Pollmann, and S. L. Sondhi, *Operator Hydrodynamics, OTOCs, and Entanglement Growth in Systems without Conservation Laws*, *Phys. Rev. X* **8**, 021013 (2018).
- [68] T. Rakovszky, F. Pollmann, and C. W. von Keyserlingk, *Diffusive Hydrodynamics of Out-of-Time-Ordered Correlators with Charge Conservation*, *Phys. Rev. X* **8**, 031058 (2018).
- [69] T. Zhou and A. Nahum, *Entanglement Membrane in Chaotic Many-Body Systems*, *Phys. Rev. X* **10**, 031066 (2020).
- [70] V. Khemani, A. Vishwanath, and D. A. Huse, *Operator Spreading and the Emergence of Dissipative Hydrodynamics under Unitary Evolution with Conservation Laws*, *Phys. Rev. X* **8**, 031057 (2018).

- [71] B. Bertini, P. Kos, and T. Prosen, *Operator Entanglement in Local Quantum Circuits I: Chaotic Dual-Unitary Circuits*, *SciPost Phys.* **8**, 67 (2020).
- [72] B. Bertini, P. Kos, and T. Prosen, *Operator Entanglement in Local Quantum Circuits II: Solitons in Chains of Qubits*, *SciPost Phys.* **8**, 68 (2020).
- [73] P. W. Claeys and A. Lamacraft, *Maximum Velocity Quantum Circuits*, *Phys. Rev. Res.* **2**, 033032 (2020).
- [74] B. Bertini and L. Piroli, *Scrambling in Random Unitary Circuits: Exact Results*, *Phys. Rev. B* **102**, 064305 (2020).
- [75] C. Jonay, V. Khemani, and M. Ippoliti, *Triunitary Quantum Circuits*, *Phys. Rev. Res.* **3**, 043046 (2021).
- [76] T. Zhou and A. W. Harrow, *Maximal Entanglement Velocity Implies Dual Unitarity*, *Phys. Rev. B* **106**, L201104 (2022).
- [77] A. Foligno and B. Bertini, *Growth of Entanglement of Generic States under Dual-Unitary Dynamics*, *Phys. Rev. B* **107**, 174311 (2023).
- [78] A. Chan, A. De Luca, and J. T. Chalker, *Solution of a Minimal Model for Many-Body Quantum Chaos*, *Phys. Rev. X* **8**, 041019 (2018).
- [79] I. Reid and B. Bertini, *Entanglement Barriers in Dual-Unitary Circuits*, *Phys. Rev. B* **104**, 014301 (2021).
- [80] H. Wang and T. Zhou, *Barrier from Chaos: Operator Entanglement Dynamics of the Reduced Density Matrix*, *J. High Energy Phys.* **12** (2019) 020.
- [81] A. J. Friedman, A. Chan, A. De Luca, and J. T. Chalker, *Spectral Statistics and Many-Body Quantum Chaos with Conserved Charge*, *Phys. Rev. Lett.* **123**, 210603 (2019).
- [82] A. Chan, A. De Luca, and J. T. Chalker, *Spectral Statistics in Spatially Extended Chaotic Quantum Many-Body Systems*, *Phys. Rev. Lett.* **121**, 060601 (2018).
- [83] P. Kos, T. Prosen, and B. Bertini, *Thermalization Dynamics and Spectral Statistics of Extended Systems with Thermalizing Boundaries*, *Phys. Rev. B* **104**, 214303 (2021).
- [84] B. Bertini, P. Kos, and T. Prosen, *Exact Spectral Statistics in Strongly Localized Circuits*, *Phys. Rev. B* **105**, 165142 (2022).
- [85] P. W. Claeys and A. Lamacraft, *Ergodic and Nonergodic Dual-Unitary Quantum Circuits with Arbitrary Local Hilbert Space Dimension*, *Phys. Rev. Lett.* **126**, 100603 (2021).
- [86] R. Suzuki, K. Mitarai, and K. Fujii, *Computational Power of One- and Two-Dimensional Dual-Unitary Quantum Circuits*, *Quantum* **6**, 631 (2022).
- [87] K. Klobas and B. Bertini, *Entanglement Dynamics in Rule 54: Exact Results and Quasiparticle Picture*, *SciPost Phys.* **11**, 107 (2021).
- [88] F. Arute, K. Arya, R. Babbush, D. Bacon, J. C. Bardin, R. Barends, R. Biswas, S. Boixo, F. G. S. L. Brandao, D. A. Buell *et al.*, *Quantum Supremacy Using a Programmable Superconducting Processor*, *Nature (London)* **574**, 505 (2019).
- [89] S. Boixo, S. V. Isakov, V. N. Smelyanskiy, R. Babbush, N. Ding, Z. Jiang, M. J. Bremner, J. M. Martinis, and H. Neven, *Characterizing Quantum Supremacy in Near-Term Devices*, *Nat. Phys.* **14**, 595 (2018).
- [90] A. Deshpande, B. Fefferman, M. C. Tran, M. Foss-Feig, and A. V. Gorshkov, *Dynamical Phase Transitions in Sampling Complexity*, *Phys. Rev. Lett.* **121**, 030501 (2018).
- [91] G. Muraleedharan, A. Miyake, and I. H. Deutsch, *Quantum Computational Supremacy in the Sampling of Bosonic Random Walkers on a One-Dimensional Lattice*, *New J. Phys.* **21**, 055003 (2019).
- [92] Y. Liu, M. Otten, R. Bassirianjahromi, L. Jiang, and B. Fefferman, *Benchmarking Near-Term Quantum Computers via Random Circuit Sampling*, [arXiv:2105.05232](https://arxiv.org/abs/2105.05232).
- [93] E. Magesan, J. M. Gambetta, and J. Emerson, *Characterizing Quantum Gates via Randomized Benchmarking*, *Phys. Rev. A* **85**, 042311 (2012).
- [94] E. Magesan, J. M. Gambetta, and J. Emerson, *Scalable and Robust Randomized Benchmarking of Quantum Processes*, *Phys. Rev. Lett.* **106**, 180504 (2011).
- [95] T. Proctor, K. Rudinger, K. Young, M. Sarovar, and R. Blume-Kohout, *What Randomized Benchmarking Actually Measures*, *Phys. Rev. Lett.* **119**, 130502 (2017).
- [96] T. Brydges, A. Elben, P. Jurcevic, B. Vermersch, C. Maier, B. P. Lanyon, P. Zoller, R. Blatt, and C. F. Roos, *Probing Rényi Entanglement Entropy via Randomized Measurements*, *Science* **364**, 260 (2019).
- [97] A. Elben, J. Yu, G. Zhu, M. Hafezi, F. Pollmann, P. Zoller, and B. Vermersch, *Many-Body Topological Invariants from Randomized Measurements in Synthetic Quantum Matter*, *Sci. Adv.* **6**, eaaz3666 (2020).
- [98] A. Elben, B. Vermersch, M. Dalmonte, J. I. Cirac, and P. Zoller, *Rényi Entropies from Random Quenches in Atomic Hubbard and Spin Models*, *Phys. Rev. Lett.* **120**, 050406 (2018).
- [99] H. Pichler, G. Zhu, A. Seif, P. Zoller, and M. Hafezi, *Measurement Protocol for the Entanglement Spectrum of Cold Atoms*, *Phys. Rev. X* **6**, 041033 (2016).
- [100] B. Vermersch, A. Elben, L. M. Sieberer, N. Y. Yao, and P. Zoller, *Probing Scrambling Using Statistical Correlations between Randomized Measurements*, *Phys. Rev. X* **9**, 021061 (2019).
- [101] B. Vermersch, A. Elben, M. Dalmonte, J. I. Cirac, and P. Zoller, *Unitary n -Designs via Random Quenches in Atomic Hubbard and Spin Models: Application to the Measurement of Rényi Entropies*, *Phys. Rev. A* **97**, 023604 (2018).
- [102] S. Aaronson, *Shadow Tomography of Quantum States*, [arxiv:1711.01053](https://arxiv.org/abs/1711.01053).
- [103] H.-Y. Huang, R. Kueng, and J. Preskill, *Predicting Many Properties of a Quantum System from Very Few Measurements*, *Nat. Phys.* **16**, 1050 (2020).
- [104] M. Ohliger, V. Nesme, and J. Eisert, *Efficient and Feasible State Tomography of Quantum Many-Body Systems*, *New J. Phys.* **15**, 015024 (2013).
- [105] N. Keenan, N. Robertson, T. Murphy, S. Zhuk, and J. Goold, *Evidence of Kardar-Parisi-Zhang Scaling on a Digital Quantum Simulator*, *Quantum Inf.* **9**, 72 (2023).
- [106] A. Morvan, T. Andersen, X. Mi, C. Neill, A. Petukhov, K. Kechedzhi, D. Abanin, A. Michailidis, R. Acharya, F. Arute *et al.*, *Formation of Robust Bound States of Interacting Microwave Photons*, *Nature (London)* **612**, 240 (2022).
- [107] H. F. Trotter, *On the Product of Semi-Groups of Operators*, *Proc. Am. Math. Soc.* **10**, 545 (1959).

- [108] M. Suzuki, *General Theory of Fractal Path Integrals with Applications to Many-Body Theories and Statistical Physics*, *J. Math. Phys. (N.Y.)* **32**, 400 (1991).
- [109] The dimension of slope in space time is time/distance = 1/velocity.
- [110] Here we assumed reflection symmetry of the gate [hence, $\tilde{\mathcal{E}}(v) = \tilde{\mathcal{E}}(-v)$]. In the absence of this property Eq. (4) takes a different form, but our conclusion about linear growth of temporal entanglement continues to apply.
- [111] C. Jonay, D. A. Huse, and A. Nahum, *Coarse-Grained Dynamics of Operator and State Entanglement*, [arXiv:1803.00089](https://arxiv.org/abs/1803.00089).
- [112] T. Zhou and A. W. Harrow, *Maximal Entanglement Velocity Implies Dual Unitarity*, *Phys. Rev. B* **106**, L201104 (2022).
- [113] T. Rakovszky, F. Pollmann, and C. W. von Keyserlingk, *Sub-ballistic Growth of Rényi Entropies due to Diffusion*, *Phys. Rev. Lett.* **122**, 250602 (2019).
- [114] Y. Huang, *Dynamics of Rényi Entanglement Entropy in Diffusive Qudit Systems*, *IOP SciNotes* **1**, 035205 (2020).
- [115] C. Eckart and G. Young, *The Approximation of One Matrix by Another of Lower Rank*, *Psychometrika* **1**, 211 (1936).
- [116] S. A. Rather, S. Aravinda, and A. Lakshminarayanan, *Creating Ensembles of Dual Unitary and Maximally Entangling Quantum Evolutions*, *Phys. Rev. Lett.* **125**, 070501 (2020).
- [117] J. I. Cirac, D. Pérez-García, N. Schuch, and F. Verstraete, *Matrix Product States and Projected Entangled Pair States: Concepts, Symmetries, Theorems*, *Rev. Mod. Phys.* **93**, 045003 (2021).
- [118] This is always true for two-point functions on equilibrium states [cf. (33)] (which encode linear response coefficients [51]) and one-point functions. For nonequilibrium two-point functions this is the case away from the regime $t_2 - t_1 < x_2 - x_1 \leq t_2 + t_1$.
- [119] A. Nahum, S. Vijay, and J. Haah, *Operator Spreading in Random Unitary Circuits*, *Phys. Rev. X* **8**, 021014 (2018).
- [120] M. Žnidarič, *Exact Convergence Times for Generation of Random Bipartite Entanglement*, *Phys. Rev. A* **78**, 032324 (2008).
- [121] A. W. Harrow and R. A. Low, *Random Quantum Circuits Are Approximate 2-Designs*, *Commun. Math. Phys.* **291**, 257 (2009).
- [122] J. Emerson, Y. S. Weinstein, M. Saraceno, S. Lloyd, and D. G. Cory, *Pseudo-Random Unitary Operators for Quantum Information Processing*, *Science* **302**, 2098 (2003).
- [123] B. Skinner, J. Ruhman, and A. Nahum, *Measurement-Induced Phase Transitions in the Dynamics of Entanglement*, *Phys. Rev. X* **9**, 031009 (2019).
- [124] Y. Li, X. Chen, and M. P. A. Fisher, *Measurement-Driven Entanglement Transition in Hybrid Quantum Circuits*, *Phys. Rev. B* **100**, 134306 (2019).
- [125] A. Chan, R. M. Nandkishore, M. Pretko, and G. Smith, *Unitary-Projective Entanglement Dynamics*, *Phys. Rev. B* **99**, 224307 (2019).
- [126] A. Nahum, J. Ruhman, S. Vijay, and J. Haah, *Quantum Entanglement Growth under Random Unitary Dynamics*, *Phys. Rev. X* **7**, 031016 (2017).
- [127] Here we use \mathcal{E}_H to denote the line tension for the average purity decay (annealed average). The expression is exact. The line tension for the average second Rényi entanglement (quenched average) has $\mathcal{O}(d^{-4})$ correction on top of this; see Ref. [65].
- [128] H. Kim and D. A. Huse, *Ballistic Spreading of Entanglement in a Diffusive Nonintegrable System*, *Phys. Rev. Lett.* **111**, 127205 (2013).
- [129] This holds for r strictly smaller than 1. For $r = 1 - A/r^\alpha$, logarithmic violations may occur.
- [130] P. Zanardi, C. Zalka, and L. Faoro, *Entangling Power of Quantum Evolutions*, *Phys. Rev. A* **62**, 030301(R) (2000).
- [131] B. Bertini, K. Klobas, and T.-C. Lu, *Entanglement Negativity and Mutual Information after a Quantum Quench: Exact Link from Space-Time Duality*, *Phys. Rev. Lett.* **129**, 140503 (2022).
- [132] K. Klobas and T. Prosen, *Space-like Dynamics in a Reversible Cellular Automaton*, *SciPost Phys. Core* **2**, 10 (2020).
- [133] N. Dowling and K. Modi, *An Operational Metric for Quantum Chaos and the Corresponding Spatiotemporal Entanglement Structure*, [arXiv:2210.14926](https://arxiv.org/abs/2210.14926).
- [134] T. Prosen and I. Pižorn, *Operator Space Entanglement Entropy in a Transverse Ising Chain*, *Phys. Rev. A* **76**, 032316 (2007).
- [135] I. Pižorn and T. Prosen, *Operator Space Entanglement Entropy in xy Spin Chains*, *Phys. Rev. B* **79**, 184416 (2009).
- [136] J. Dubail, *Entanglement Scaling of Operators: A Conformal Field Theory Approach, with a Glimpse of Simulability of Long-Time Dynamics in $1 + 1d$* , *J. Phys. A* **50**, 234001 (2017).
- [137] V. Alba, J. Dubail, and M. Medenjak, *Operator Entanglement in Interacting Integrable Quantum Systems: The Case of the Rule 54 chain*, *Phys. Rev. Lett.* **122**, 250603 (2019).
- [138] V. Alba, *Diffusion and Operator Entanglement Spreading*, *Phys. Rev. B* **104**, 094410 (2021).
- [139] V. B. Bulchandani, S. Gopalakrishnan, and E. Ilievski, *Superdiffusion in Spin Chains*, *J. Stat. Mech.* (2021) 084001.
- [140] L. Mirsky, *A Trace Inequality of John von Neumann*, *Mon. Hefte Math.* **79**, 303 (1975).
- [141] H. Wilming, M. Goihl, I. Roth, and J. Eisert, *Entanglement-Ergodic Quantum Systems Equilibrate Exponentially Well*, *Phys. Rev. Lett.* **123**, 200604 (2019).
- [142] M. Z. Spivey, *Enumerating Lattice Paths Touching or Crossing the Diagonal at a Given Number of Lattice Points*, *Electron. J. Comb.* **19**, P24 (2012).

Chapter 4

Quantum information spreading in generalized dual unitary

4.1 Summary

In this work, we consider a class of circuits introduced in [66] which obey a strictly weaker condition than dual unitarity. We compute exactly two quantities that characterize the spreading of information in the system: the entanglement velocity (from a special class of solvable states) and the butterfly velocity. We also show the explicit expression of the line tension mentioned in Sec. 1.3, using it to re-derive the two previous velocities.

The shape of the line tension obtained is extremal meaning that is the smallest possible one, after fixing the entanglement and butterfly velocity, which pin its value at $v = 0$ and $v = 1$, respectively, and it is in general non-constant, differing in this from dual unitary circuits. Moreover, we show that the weakened condition on the gates forces the entanglement spectrum to be flat.


Quantum Information Spreading in Generalized Dual-Unitary Circuits

Alessandro Foligno^{1,2}, Pavel Kos³, and Bruno Bertini^{1,2}

¹*School of Physics and Astronomy, University of Nottingham, Nottingham, NG7 2RD, United Kingdom*

²*Centre for the Mathematics and Theoretical Physics of Quantum Non-Equilibrium Systems, University of Nottingham, Nottingham, NG7 2RD, United Kingdom*

³*Max-Planck-Institut für Quantenoptik, Hans-Kopfermann-Str. 1, 85748 Garching, Germany*

 (Received 17 December 2023; revised 26 February 2024; accepted 8 May 2024; published 21 June 2024)

We study the spreading of quantum information in a recently introduced family of brickwork quantum circuits that generalizes the dual-unitary class. These circuits are unitary in time, while their spatial dynamics is unitary only in a restricted subspace. First, we show that local operators spread at the speed of light as in dual-unitary circuits, i.e., the butterfly velocity takes the maximal value allowed by the geometry of the circuit. Then, we prove that the entanglement spreading can still be characterized exactly for a family of compatible initial states (in fact, for an extension of the compatible family of dual-unitary circuits) and that the asymptotic entanglement slope is again independent on the Rényi index. Remarkably, however, we find that the entanglement velocity is generically smaller than 1. We use these properties to find a closed-form expression for the entanglement-membrane line tension.

DOI: [10.1103/PhysRevLett.132.250402](https://doi.org/10.1103/PhysRevLett.132.250402)

In recent years, quantum circuits have emerged as useful effective models to understand generic quantum many-body dynamics [1–13], and as concrete platforms for quantum simulation [14–24]. From a theoretical point of view their most appealing feature is that, contrary to generic many-body systems in continuous time, their dynamics are sometimes amenable to analytical descriptions. This is particularly significant in light of the current lack of computational approaches able to efficiently characterize out-of-equilibrium quantum matter.

The approaches to obtain analytical insights in quantum circuits can be divided in two groups. The first involves introducing a certain degree of randomness in the system to simplify treatment [2,5,25]. This approach is inspired by random matrix theory [26] and has its most representative example in Haar-random circuits [2], which led to several important results on operator dynamics and information spreading [2–6,9–11,25,27–36]. The second route, instead, is to derive exact results for special classes of systems obtained by imposing certain conditions on the elementary quantum gates without affecting the nature of the dynamics [8,37–42]. The appeal of this second approach is that it is arguably more fundamental—it allows one to study truly closed quantum many-body systems—and its most representative example is that of dual-unitary (DU) circuits [8].

Importantly, the latter are not artificial theoretical abstractions: they can implement standard Floquet dynamics, e.g., the kicked Ising model [7,43], and have been implemented in real-world quantum computers [44,45].

The defining property of DU circuits is that their local gates remain unitary upon exchanging the roles of space and time. This gives access to measures of quantum information spreading and operator growth that are notoriously hard to compute in general; see, e.g., Refs. [7,43,46–59]. Despite their solvability, DU circuits are provably quantum chaotic [3,60] and display almost generic dynamics. The only macroscopic effect of dual unitarity is that it enforces maximal velocity for the spreading of quantum correlations. Specifically, in DU circuits both the velocity characterizing operator spreading and the entanglement velocity of any state are equal to the speed of light [46,50,51]. In fact, the second property implies conversely the dual unitarity [61].

The fact that both scrambling and thermalization occur at the fastest possible rate in DU circuits leaves a distinct mark on the dynamics of quantum information. This is true even at the coarse-grained level where quantum information spreading is described by the so-called entanglement membrane [29,35,36] (see also [62,63]). DU circuits have been shown to exhibit an extremal, constant membrane line tension [29], rather than the general convex function observed numerically in generic systems [29], where scrambling and thermalization occur at different, submaximal rates with the only constraint that the former occurs before the latter. The natural question is then whether the dual unitarity condition can somehow be weakened, leading to a more generic, yet solvable, quantum information flow.

Published by the American Physical Society under the terms of the Creative Commons Attribution 4.0 International license. Further distribution of this work must maintain attribution to the author(s) and the published article's title, journal citation, and DOI.

In this Letter we address this question by characterizing the dynamics of quantum information in a class of “hierarchical generalizations” of DU circuits recently proposed in Ref. [64]. The idea is to construct a hierarchy of increasingly weaker conditions, with dual unitarity being at the bottom as the strongest one. Here, we consider the second level of the hierarchy, DU2 from now on, and find the following results. First, the operator-scrambling velocity continues to be equal to 1 (in fact we show that this is true for all levels of the hierarchy). Second, the entanglement velocity is still independent of the Rényi index and can still be computed exactly. It is, however, generically *submaximal*; we interpret this by noting that the dual dynamics of the gate is proportional to an isometry. This constrains the exchange of correlations between different parts of the system and, ultimately, reduces the entanglement growth. Finally, we recover these results by computing the entanglement membrane of DU2 and finding that it has nontrivial line tension. To the best of our knowledge the one provided here is the first explicit expression of a nonconstant line tension derived in a clean, interacting system.

More specifically, we consider a one-dimensional quantum circuit, made of $2L$ sites of qudits (quantum systems with d internal states), with a discrete, local unitary evolution. Neighboring sites are by definition at distance of $1/2$ apart, and their positions, labeled by half-integers, take periodic values on a ring of length L ($0 \equiv L$). A single time step is determined by the unitary operator $\mathbb{U} = \mathbb{U}_e \mathbb{U}_o$ with

$$\mathbb{U}_e = \bigotimes_{x \in \mathbb{Z}_L} U_{x,x+1/2}, \quad \mathbb{U}_o = \bigotimes_{x \in \mathbb{Z}_L} U_{x-1/2,x}. \quad (1)$$

$U_{a,b}$ is a two site unitary gate that acts on sites a, b .

We consider a subclass of unitary gates fulfilling the DU2 conditions [64]. These can be expressed by defining a spacetime-swapped gate \tilde{U} as $\langle kl|\tilde{U}|ij\rangle = \langle lj|U|ki\rangle$. In terms of these gates the DU2 condition becomes (cf. Fig. 1)

$$\begin{aligned} (\tilde{U} \otimes \mathbb{1}_d)(\mathbb{1}_d \otimes \tilde{U}\tilde{U}^\dagger)(\tilde{U}^\dagger \otimes \mathbb{1}_d) &= \tilde{U}\tilde{U}^\dagger \otimes \mathbb{1}_d, \\ (\mathbb{1}_d \otimes \tilde{U})(\tilde{U}\tilde{U}^\dagger \otimes \mathbb{1}_d)(\mathbb{1}_d \otimes \tilde{U}^\dagger) &= \mathbb{1}_d \otimes \tilde{U}\tilde{U}^\dagger, \end{aligned} \quad (2)$$

where $\mathbb{1}_x$ is the identity on a space of dimension x . This property is satisfied for DU gates where \tilde{U} is unitary;

however, it admits also families of non-DU solutions [64]. Note that Eq. (2) implies the validity of the analogous relations with \tilde{U}^\dagger and \tilde{U} exchanged [64].

Let us begin computing the speed of operator spreading, i.e., the “butterfly velocity” v_B . The latter can be quantified by looking at the following OTOC

$$O_{\alpha\beta}(x, t) = 1 - \frac{1}{d^{2L}} \text{tr}[\sigma_0^{(\alpha)}(t)\sigma_x^{(\beta)}(0)\sigma_0^{(\alpha)}(t)\sigma_x^{(\beta)}(0)], \quad (3)$$

where $\{\sigma^{(\alpha)}\}_{\alpha=1,\dots,d^2-1}$ are a basis for local traceless hermitian operators [65]. In chaotic systems, this out-of-time-order correlator (OTOC) approaches asymptotically 1 for $|x| \leq v_B t$, and 0 otherwise. In particular, Haar-random circuits have $v_B = (d^2 - 1)/(d^2 + 1)$ [4,6], while DU circuits $v_B = 1$ [46,47]. Note that the latter is the largest possible v_B because the strict causality encoded in Eq. (1) assures $O_{\alpha\beta}(x, t) = 0$ for $|x| > t$.

To compute v_B we use the strategy of Refs. [46,47]. Namely, we compute the limit $x, t \rightarrow \infty$ with $x_- = t - x$ fixed: if $O_{\alpha\beta}(x, t)$ is nonzero in this limit we have $v_B = 1$ otherwise $v_B < 1$ [66]. The limit is conveniently computed writing $1 - O_{\alpha\beta}(x, t)$ in terms of a suitable transfer matrix and expressing its asymptotic scaling in terms of the transfer-matrix fixed points. This procedure becomes particularly transparent by introducing a diagrammatic representation, similar to the one used in tensor networks, where one depicts single local gates as boxes with legs corresponding to the qudits they act on; see, e.g., [8,43,47]. In particular, since here we are interested in multireplica quantities we consider a graphical representation of “folded” quantum gates, i.e., tensor products of n replicas of U and its conjugate,

$$\boxed{n} \equiv (U \otimes U^*)^{\otimes n}. \quad (4)$$

The Hilbert spaces associated to each leg have dimension d^n . For $|x| < t$ one can express the quantity of interest in terms of (4) as follows [67]:

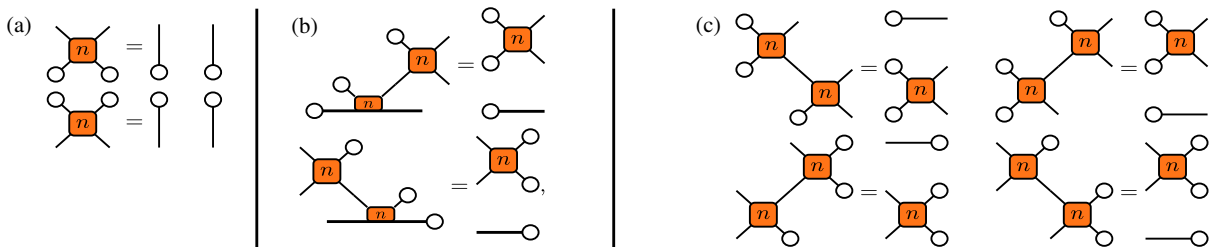


FIG. 1. Graphical representations of unitarity (a), compatibility relations for the initial state [cf. Eq. (15)] (b), and DU2 conditions [cf. Eq. (2)] (c).

$$1 - O_{\alpha\beta}(x, t) = \frac{1}{d^{2t}} \langle \bullet_{\alpha} | T_1^x | \bullet_{\beta} \rangle \quad (5)$$

Here, $x_{\pm} = t \pm x$, joined legs imply matrix product, and we introduced a graphical representation for two different index contractions that can be seen as states in the replicated Hilbert space, i.e.,

$$|\circ\rangle = \sum_{i_k=1}^d |i_1 i_1 \dots i_n i_n\rangle, \quad |\square\rangle = \sum_{i_k=1}^d |i_n i_1 i_1 \dots i_n\rangle, \quad (6)$$

where we used the shorthand notation $|i_1 i_2 \dots i_{2n}\rangle \equiv |i_1\rangle \otimes |i_2\rangle \otimes \dots \otimes |i_{2n}\rangle$. These states are neither orthogonal nor normalized and one has $\langle \circ | \square \rangle = d$ and $\langle \circ | \circ \rangle = \langle \square | \square \rangle = d^n$. Similarly we set

$$|\bullet_{\alpha}\rangle = (\alpha^{(\alpha)} \otimes \mathbb{1}_d)^{\otimes n} |\circ\rangle, \quad |\blacksquare_{\beta}\rangle = (\alpha^{(\beta)} \otimes \mathbb{1}_d)^{\otimes n} |\square\rangle. \quad (7)$$

For the sake of compactness, we suppressed the n dependence from the lhs of Eqs. (6) and (7) because in the diagrams the value of n is specified in the gates.

From the diagram (5) we see that $1 - O_{\alpha\beta}(x, t)$ is written as

$$1 - O_{\alpha\beta}(x, t) = \frac{1}{d^{x_-}} \langle \square \dots \blacksquare_{\beta} | T_{x_-}^{x_+} | \bullet_{\alpha} \dots \circ \rangle, \quad (8)$$

where we introduced

$$T_x = \frac{1}{d} \circ \text{---} \text{---} \text{---} \text{---} \diamond \quad (9)$$

This matrix has maximal eigenvalue 1 fixed by unitarity [46,47]. Therefore, in the limit of interest we can replace it by $\sum_i |r_i\rangle \langle l_i| / \langle l_i | r_i \rangle$ in Eq. (8), where $\langle l_i|$ and $|r_i\rangle$ denote respectively its right and left fixed points. Generically T_{x_-} has unique left and right fixed points guaranteed by unitarity, i.e., $|\circ \dots \circ\rangle$, $\langle \square \dots \square|$ [this can be seen graphically using the conditions in Fig. 1(a)]. The latter, however, contribute with a 1 in the rhs of Eq. (8). Therefore, the OTOC can have a nonzero value in the limit of interest only if T_x has at least another nontrivial fixed point for some x_- .

We now show that DU2 provides such an additional fixed point. We consider $x_- = 1$ and employ Eq. (2) (cf. Fig. 1) to show that

$$\langle l| = \langle \circ | T_1 = \circ \text{---} \text{---} \diamond, \quad |r\rangle = T_1 |\square\rangle = \circ \text{---} \text{---} \diamond, \quad (10)$$

are fixed points of T_1 . These vectors have nonzero overlap with states orthogonal to $|\square\rangle$ and $|\circ\rangle$, respectively, and therefore contribute to the rhs of Eq. (8) for some α and β . In particular, defining

$$|\bullet\rangle = d|\square\rangle - |\circ\rangle, \quad |\blacksquare\rangle = d|\circ\rangle - |\square\rangle, \quad (11)$$

we have [68]

$$\langle l | \blacksquare \rangle = \langle \bullet | r \rangle = d^4 \left(1 - \frac{1}{n_{\Lambda}} \right), \quad (12)$$

where $n_{\Lambda} = 1, \dots, d^2$ depending on the specific choice of the DU2 gate. The case $n_{\Lambda} = 1$ corresponds to a trivial gate with no entangling power, i.e., $U = u \otimes v$. Assuming $n_{\Lambda} \neq 1$, we find that $\lim_{t \rightarrow \infty} O_{\alpha\beta}(t-1, t) \neq 0$ and the butterfly velocity for DU2 gates is indeed maximal. This reasoning can be extended to the full hierarchy of Ref. [64] (focusing again on entangling gates) by considering

$$\langle l| = \langle \circ | (T_1)^{m-1}, \quad |r\rangle = (T_1)^{m-1} |\square\rangle, \quad (13)$$

for gates at the m th level of the hierarchy. This is the first main result of this Letter: all generalized dual-unitary circuits have butterfly velocity pinned at 1. This property shows that generalized dual-unitary circuits can never be fully generic when it comes to operator spreading. A maximal butterfly velocity, however, is not a very constraining feature by itself. Intuitively one can always think of achieving it by applying enough steps of tensor network renormalization to the quantum circuit [69].

Let us now move on to the calculation of the entanglement velocity by looking at a quantum quench from a class of initial states compatible with the DU2 property [64]. The latter are expressed as two-site shift invariant matrix product states (MPS) with bond dimension χ , namely

$$|\Psi_0\rangle = \frac{1}{d^{L/2}} \sum_{i_k=1}^d \text{tr}[M^{[i_1 i_2]} \dots M^{[i_{2L-1} i_{2L}]}] |i_1 \dots i_{2L}\rangle, \quad (14)$$

where the $\chi \times \chi$ matrices $\{M^{[a,b]}\}$ are chosen such that the MPS transfer matrix $\sum_{i,j=1}^d M^{[i,j]} \otimes (M^{[i,j]})^*$ has maximal, nondegenerate eigenvalue d , corresponding to eigenvectors $\langle \Omega_L|$ and $|\Omega_R\rangle$. Moreover, the $d\chi \times d\chi$ matrices W with elements $\langle ia | W | jb \rangle = \langle i | M^{(ab)} | j \rangle$ fulfill

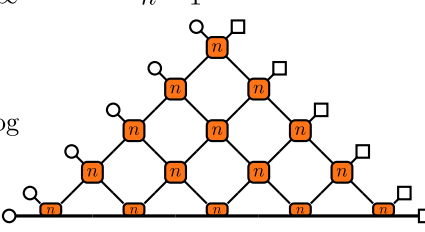
$$\begin{aligned} (\tilde{U} \otimes \mathbb{1}_{\chi})(\mathbb{1}_d \otimes WW^{\dagger})(\tilde{U}^{\dagger} \otimes \mathbb{1}_{\chi}) &= \tilde{U} \tilde{U}^{\dagger} \otimes \mathbb{1}_{\chi}, \\ (\tilde{U}^{\dagger} \otimes \mathbb{1}_{\chi})(\mathbb{1}_d \otimes W^{\dagger}W)(\tilde{U} \otimes \mathbb{1}_{\chi}) &= \tilde{U}^{\dagger} \tilde{U} \otimes \mathbb{1}_{\chi}; \end{aligned} \quad (15)$$

see Fig. 1(b). These relations are solved by the initial states compatible with dual unitarity introduced in Ref. [50]; however, these are not the only solutions. Note that (15) also implies $|\Omega_R\rangle = (\langle\Omega_L|)^\dagger = \sum_{i=1}^{\chi} |ii\rangle$.

Considering the evolution of the Rényi entropies of a block A (of length L_A), namely

$$S_A^{(n)}(t) = \frac{1}{1-n} \log(\text{tr}_A[\rho_A^n(t)]), \quad (16)$$

where $\rho_A(t)$ is the state at time t reduced to A , and taking the limit $L \rightarrow \infty$ followed by $L_A \rightarrow \infty$ we obtain [68]

$$\lim_{L_A \rightarrow \infty} \lim_{L \rightarrow \infty} S_A^{(n)}(t) = \frac{2n}{n-1} \log \chi d^{(2t+1)} - \frac{2}{n-1} \log \left(\text{Diagram} \right), \quad (17)$$


where we introduced the following symbol for the tensor product of n copies of W and W^* ,

$$\text{Diagram} = (W \otimes W^*)^{\otimes n}, \quad (18)$$

and the thicker line at the bottom corresponds to $2n$ copies of the MPS' auxiliary space.

The physical meaning of (17) is that for early times ($4t \leq L_A + 2t \leq L$) the entanglement between A and the rest is only produced at the two boundaries between the two subsystems and the latter are causally disconnected [70].

Next we observe that, by repeated applications of the DU2 property and the diagrammatic version of the compatibility condition (15) [Figs. 1(b) and 1(c)] we can simplify the triangular diagram in Eq. (17) to

$$\left(\text{Diagram} \right)^t \times \text{Diagram}. \quad (19)$$

This gives the following asymptotic entanglement velocity:

$$v_E^{(n)} \equiv \lim_{t \rightarrow \infty} \lim_{L_A \rightarrow \infty} \lim_{L \rightarrow \infty} \frac{S_A^{(n)}(t)}{4t \log(d)} = \frac{\log \text{tr}[(\tilde{U}\tilde{U}^\dagger/d^2)^n]}{2(1-n) \log(d)}. \quad (20)$$

This result generalizes the one for DU circuits [7,50], i.e., $v_E^{(n)} = 1$, which is recovered setting $\tilde{U}\tilde{U}^\dagger = \mathbb{1}_{d^2}$. Remarkably, however, Eq. (20) continues to be n -independent for all DU2 circuits. Indeed the spectrum of the matrix $\tilde{U}\tilde{U}^\dagger$ is *constant* for all DU2 gates [68].

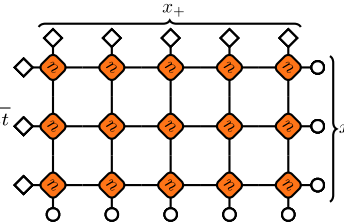
Property 1.—For DU2 circuits the eigenvalues of $\tilde{U}\tilde{U}^\dagger$ are all either equal to 0 or to a positive constant Λ^2 .

Since the trace of $\tilde{U}\tilde{U}^\dagger$ is fixed by the unitarity of U , the dimension of the nontrivial eigenspace, $n_\Lambda = 1, \dots, d^2$, is such that $n_\Lambda \Lambda^2 = d^2$. This allows us to rewrite Eq. (20) as

$$v_E^{(n)} = \frac{\log(\frac{d}{\Lambda})}{\log(d)} = \frac{\log(n_\Lambda)}{2 \log(d)}, \quad n_\Lambda = 1, \dots, d^2. \quad (21)$$

This exact expression represents our second main result and, in contrast with that on the butterfly velocity, cannot be directly extended to the full hierarchy of Ref. [64]: beyond DU2 the triangular diagram in Eq. (17) does not simplify and Property 1 does not hold. In fact, the validity of Property 1 seems to be the key to solvability as it implies that the spacetime-swapped gate \tilde{U} is proportional to an isometry. Consequently, when swapping space and time the dynamics are unitary in a reduced subspace. This reduction lowers the entanglement velocity, which can now attain different discrete values (but not arbitrary ones as in the generic case).

We now recover our exact results using the entanglement membrane picture [29,35,36]. The idea of this approach is to view the entanglement as the energy of a coarse-grained curve (which depends only on its slope). Namely, one can write a Rényi entropy as $S_n(x, t) = \min_y (\mathcal{E}_n((x-y)/t) + S_n(y, 0))$ [35]. The function $\mathcal{E}_n(v)$ can be computed by evaluating the scaling limit of a suitable matrix element in the replicated space [29]. More precisely, we have

$$e^{\frac{t \mathcal{E}_n(v) \log d}{(1-n)^{-1}}} \simeq \frac{1}{d^{2nt}} \left(\text{Diagram} \right)_{x_+ x_-}, \quad (22)$$


where \simeq denotes equality at leading order in t . The matrix element on the rhs is typically very hard to evaluate analytically and closed-form expressions have only been found in the presence of randomness and for large d [35,36,71], in the dual-unitary case [29], or for holographic quantum field theories [72]. In our case, instead, the calculation is straightforward: Eq. (22) can be explicitly contracted using the DU2 property [cf. Fig. 1(c)] starting from the top-left and bottom-right corners. A direct application of Property 1 then leads to our third main result,

$$\mathcal{E}_n(v) = \left(|v| + \frac{1 - |v| \log(n_\Lambda)}{2 \log(d)} \right). \quad (23)$$

We see that $\mathcal{E}_n(v)$ shows a nontrivial dependence on v but is convex as it should be for consistency. Specifically, it is generically linear in $|v|$ and becomes constant only in the DU case $n_\Lambda = d^2$ [see Fig. 2(a)]. As shown in Ref. [72],

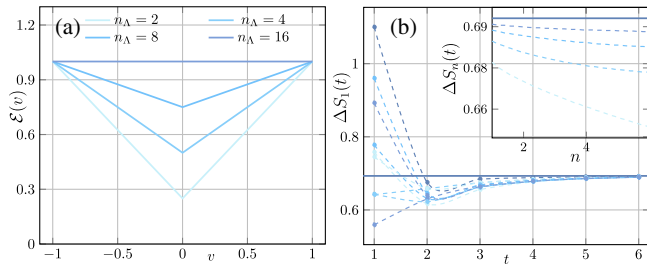


FIG. 2. (a) Line tension of DU2 circuits [cf. Eq. (23)], for $d = 4$, and n_A taking all possible values (except the trivial value 1) corresponding to different gates. (b) Entanglement slopes from random dimer-product states compared with the expected slope from solvable states (solid line). Inset: slope of Rényi entropies for increasing values of t (darker shade) as a function of the Rényi index n , compared to the n -independent result from solvable states (solid line).

this form maximizes the growth of the entanglement for fixed v_E and v_B . This extremal form of the membrane is again connected with the isometric nature of the spacetime-swapped dynamics.

Equation (23) allows us to recover our exact results for butterfly and entanglement velocities within the membrane approach [35]: the solution to $\mathcal{E}(v) = v$ is indeed $v = v_B = 1$ and $v_E^{(n)} = \mathcal{E}(v = 0)$ coincides with Eq. (21). In fact, the membrane approach suggests that this result does not depend on the initial state, as long as it is low entangled, and should apply also for states that do not satisfy Eq. (15). This is confirmed by our numerics; see Fig. 2(b).

In this Letter we presented an explicit characterization of the quantum information flow in a class of unitary circuits, dubbed DU2 circuits, that generalizes dual-unitary circuits. We showed that although local operators spread at the maximal speed and the entanglement spectrum after a quench is asymptotically flat, the entanglement velocity is submaximal and its value depends on additional properties of the gate. Finally, we showed that these results can be recovered using the entanglement-membrane approach by deriving an exact expression for the line tension.

Our exact results put DU2 circuits forward as a general class of chaotic, yet solvable quantum circuits characterized by local and isometric space dynamics. Some immediate questions for future research are to establish whether DU2 circuits enjoy the same degree of solvability as dual-unitary circuits by investigating different properties (e.g., spectral correlations or temporal entanglement) and whether one can achieve some form of exact solvability by imposing even weaker constraints on the space dynamics, perhaps reducing its degree of locality. Another interesting generalization would be to consider dynamics that are different isometric evolutions in the time and space directions. This could give possible new solvable families of circuits with measurements.

Note added.—While this manuscript was being finalized, we became aware of the related work [73], which will soon appear on arXiv.

We thank Katja Klobas for collaboration in the early stages of this project and for valuable comments on the manuscript. We also thank Xie-Hang Yu and Sarang Gopalakrishnan for useful discussions. We acknowledge financial support from the Royal Society through the University Research Fellowship No. 201101 (A.F. and B.B.). P.K. is supported by the Alexander von Humboldt Foundation. We warmly acknowledge the hospitality of the Simons Center for Geometry and Physics during the program “Fluctuations, Entanglements, and Chaos: Exact Results,” where part of this work has been performed.

- [1] P. Hosur, X.-L. Qi, D. A. Roberts, and B. Yoshida, Chaos in quantum channels, *J. High Energy Phys.* **02** (2016) 004.
- [2] A. Nahum, J. Ruhman, S. Vijay, and J. Haah, Quantum entanglement growth under random unitary dynamics, *Phys. Rev. X* **7**, 031016 (2017).
- [3] B. Bertini, P. Kos, and T. Prosen, Exact spectral form factor in a minimal model of many-body quantum chaos, *Phys. Rev. Lett.* **121**, 264101 (2018).
- [4] A. Nahum, S. Vijay, and J. Haah, Operator spreading in random unitary circuits, *Phys. Rev. X* **8**, 021014 (2018).
- [5] A. Chan, A. De Luca, and J. T. Chalker, Solution of a minimal model for many-body quantum chaos, *Phys. Rev. X* **8**, 041019 (2018).
- [6] C. W. von Keyserlingk, T. Rakovszky, F. Pollmann, and S. L. Sondhi, Operator hydrodynamics, OTOCs, and entanglement growth in systems without conservation laws, *Phys. Rev. X* **8**, 021013 (2018).
- [7] B. Bertini, P. Kos, and T. Prosen, Entanglement spreading in a minimal model of maximal many-body quantum chaos, *Phys. Rev. X* **9**, 021033 (2019).
- [8] B. Bertini, P. Kos, and T. Prosen, Exact correlation functions for dual-unitary lattice models in $1 + 1$ dimensions, *Phys. Rev. Lett.* **123**, 210601 (2019).
- [9] A. J. Friedman, A. Chan, A. De Luca, and J. T. Chalker, Spectral statistics and many-body quantum chaos with conserved charge, *Phys. Rev. Lett.* **123**, 210603 (2019).
- [10] Y. Li, X. Chen, and M. P. A. Fisher, Measurement-driven entanglement transition in hybrid quantum circuits, *Phys. Rev. B* **100**, 134306 (2019).
- [11] B. Skinner, J. Ruhman, and A. Nahum, Measurement-induced phase transitions in the dynamics of entanglement, *Phys. Rev. X* **9**, 031009 (2019).
- [12] T. Rakovszky, F. Pollmann, and C. W. von Keyserlingk, Sub-ballistic growth of Rényi entropies due to diffusion, *Phys. Rev. Lett.* **122**, 250602 (2019).
- [13] A. Zabalo, M. J. Gullans, J. H. Wilson, S. Gopalakrishnan, D. A. Huse, and J. H. Pixley, Critical properties of the measurement-induced transition in random quantum circuits, *Phys. Rev. B* **101**, 060301(R) (2020).
- [14] T. Brydges, A. Elben, P. Jurcevic, B. Vermersch, C. Maier, B. P. Lanyon, P. Zoller, R. Blatt, and C. F. Roos, Probing

- Rényi entanglement entropy via randomized measurements, *Science* **364**, 260 (2019).
- [15] A. Elben, J. Yu, G. Zhu, M. Hafezi, F. Pollmann, P. Zoller, and B. Vermersch, Many-body topological invariants from randomized measurements in synthetic quantum matter, *Sci. Adv.* **6**, eaaz3666 (2020).
- [16] A. Elben, B. Vermersch, M. Dalmonte, J. I. Cirac, and P. Zoller, Rényi entropies from random quenches in atomic Hubbard and spin models, *Phys. Rev. Lett.* **120**, 050406 (2018).
- [17] H. Pichler, G. Zhu, A. Seif, P. Zoller, and M. Hafezi, Measurement protocol for the entanglement spectrum of cold atoms, *Phys. Rev. X* **6**, 041033 (2016).
- [18] B. Vermersch, A. Elben, L. M. Sieberer, N. Y. Yao, and P. Zoller, Probing Scrambling using statistical correlations between randomized measurements, *Phys. Rev. X* **9**, 021061 (2019).
- [19] B. Vermersch, A. Elben, M. Dalmonte, J. I. Cirac, and P. Zoller, Unitary n -designs via random quenches in atomic Hubbard and spin models: Application to the measurement of Rényi entropies, *Phys. Rev. A* **97**, 023604, 2018.
- [20] S. Aaronson, Shadow tomography of quantum states, *arXiv:1711.01053*.
- [21] H.-Y. Huang, R. Kueng, and J. Preskill, Predicting many properties of a quantum system from very few measurements, *Nat. Phys.* **16**, 1050 (2020).
- [22] M. Ohliger, V. Nesme, and J. Eisert, Efficient and feasible state tomography of quantum many-body systems, *New J. Phys.* **15**, 015024 (2013).
- [23] N. Keenan, N. Robertson, T. Murphy, S. Zhuk, and J. Goold, Evidence of Kardar-Parisi-Zhang scaling on a digital quantum simulator, *npj Quantum Inf.* **9**, 72 (2023).
- [24] A. Morvan, T. Andersen, X. Mi, C. Neill, A. Petukhov, K. Kechedzhi, D. Abanin, A. Michailidis, R. Acharya, F. Arute *et al.*, Formation of robust bound states of interacting microwave photons, *Nature (London)* **612**, 240 (2022).
- [25] M. P. Fisher, V. Khemani, A. Nahum, and S. Vijay, Random quantum circuits, *Annu. Rev. Condens. Matter Phys.* **14**, 335 (2023).
- [26] M. Mehta, *Random Matrices* (Academic Press, New York, 1991).
- [27] V. Khemani, A. Vishwanath, and D. A. Huse, Operator spreading and the emergence of dissipative hydrodynamics under unitary evolution with conservation laws, *Phys. Rev. X* **8**, 031057 (2018).
- [28] T. Rakovszky, F. Pollmann, and C. W. von Keyserlingk, Diffusive hydrodynamics of out-of-time-ordered correlators with charge conservation, *Phys. Rev. X* **8**, 031058 (2018).
- [29] T. Zhou and A. Nahum, Entanglement membrane in chaotic many-body systems, *Phys. Rev. X* **10**, 031066 (2020).
- [30] H. Wang and T. Zhou, Barrier from chaos: Operator entanglement dynamics of the reduced density matrix, *J. High Energy Phys.* **12** (2019) 001.
- [31] A. Chan, R. M. Nandkishore, M. Pretko, and G. Smith, Unitary-projective entanglement dynamics, *Phys. Rev. B* **99**, 224307 (2019).
- [32] A. Chan, A. De Luca, and J. T. Chalker, Spectral statistics in spatially extended chaotic quantum many-body systems, *Phys. Rev. Lett.* **121**, 060601 (2018).
- [33] S. J. Garratt and J. T. Chalker, Many-body delocalization as symmetry breaking, *Phys. Rev. Lett.* **127**, 026802 (2021).
- [34] S. J. Garratt and J. T. Chalker, Local pairing of Feynman histories in many-body Floquet models, *Phys. Rev. X* **11**, 021051 (2021).
- [35] C. Jonay, D. A. Huse, and A. Nahum, Coarse-grained dynamics of operator and state entanglement, *arXiv:1803.00089*.
- [36] T. Zhou and A. Nahum, Emergent statistical mechanics of entanglement in random unitary circuits, *Phys. Rev. B* **99**, 174205 (2019).
- [37] K. Klobas, B. Bertini, and L. Piroli, Exact thermalization dynamics in the “Rule 54” quantum cellular automaton, *Phys. Rev. Lett.* **126**, 160602 (2021).
- [38] T. Prosen, Many-body quantum chaos and dual-unitarity round-a-face, *Chaos* **31**, 093101 (2021).
- [39] P. Kos, B. Bertini, and T. Prosen, Correlations in perturbed dual-unitary circuits: Efficient path-integral formula, *Phys. Rev. X* **11**, 011022 (2021).
- [40] B. Bertini, P. Kos, and T. Prosen, Exact spectral statistics in strongly localized circuits, *Phys. Rev. B* **105**, 165142 (2022).
- [41] P. Kos and G. Styliaris, Circuits of space and time quantum channels, *Quantum* **7**, 1020 (2023).
- [42] B. Bertini, C. De Fazio, J. P. Garrahan, and K. Klobas, Exact quench dynamics of the Floquet quantum East model at the deterministic point, *Phys. Rev. Lett.* **132**, 120402 (2024).
- [43] S. Gopalakrishnan and A. Lamacraft, Unitary circuits of finite depth and infinite width from quantum channels, *Phys. Rev. B* **100**, 064309 (2019).
- [44] E. Chertkov, J. Bohnet, D. Francois, J. Gaebler, D. Gresh, A. Hankin, K. Lee, D. Hayes, B. Neyenhuis, R. Stutz *et al.*, Holographic dynamics simulations with a trapped-ion quantum computer, *Nat. Phys.* **18**, 1074 (2022).
- [45] X. Mi *et al.*, Information scrambling in quantum circuits, *Science* **374**, 1479 (2021).
- [46] P. W. Claeys and A. Lamacraft, Maximum velocity quantum circuits, *Phys. Rev. Res.* **2**, 033032 (2020).
- [47] B. Bertini and L. Piroli, Scrambling in random unitary circuits: Exact results, *Phys. Rev. B* **102**, 064305 (2020).
- [48] N. Dowling, P. Kos, and K. Modi, Scrambling is necessary but not sufficient for chaos, *Phys. Rev. Lett.* **131**, 180403 (2023).
- [49] M. A. Rampp, R. Moessner, and P. W. Claeys, From dual unitarity to generic quantum operator spreading, *Phys. Rev. Lett.* **130**, 130402 (2023).
- [50] L. Piroli, B. Bertini, J. I. Cirac, and T. Prosen, Exact dynamics in dual-unitary quantum circuits, *Phys. Rev. B* **101**, 094304 (2020).
- [51] A. Foligno and B. Bertini, Growth of entanglement of generic states under dual-unitary dynamics, *Phys. Rev. B* **107**, 174311 (2023).
- [52] G. Giudice, G. Giudici, M. Sonner, J. Thoenniss, A. Lerose, D. A. Abanin, and L. Piroli, Temporal entanglement, quasiparticles, and the role of interactions, *Phys. Rev. Lett.* **128**, 220401 (2022).
- [53] A. Foligno, T. Zhou, and B. Bertini, Temporal entanglement in chaotic quantum circuits, *Phys. Rev. X* **13**, 041008 (2023).

- [54] B. Bertini, P. Kos, and T. Prosen, Operator entanglement in local quantum circuits I: Chaotic dual-unitary circuits, *SciPost Phys.* **8**, 67 (2020).
- [55] B. Bertini, P. Kos, and T. Prosen, Operator entanglement in local quantum circuits II: Solitons in chains of qubits, *SciPost Phys.* **8**, 68 (2020).
- [56] I. Reid and B. Bertini, Entanglement barriers in dual-unitary circuits, *Phys. Rev. B* **104**, 014301 (2021).
- [57] W. W. Ho and S. Choi, Exact emergent quantum state designs from quantum chaotic dynamics, *Phys. Rev. Lett.* **128**, 060601 (2022).
- [58] P. W. Claeys and A. Lamacraft, Emergent quantum state designs and biunitarity in dual-unitary circuit dynamics, *Quantum* **6**, 738 (2022).
- [59] M. Ippoliti and W. W. Ho, Dynamical purification and the emergence of quantum state designs from the projected ensemble, *PRX Quantum* **4**, 030322 (2023).
- [60] B. Bertini, P. Kos, and T. Prosen, Random matrix spectral form factor of dual-unitary quantum circuits, *Commun. Math. Phys.*, **387**, 597 (2021).
- [61] T. Zhou and A. W. Harrow, Maximal entanglement velocity implies dual unitarity, *Phys. Rev. B* **106**, L201104 (2022).
- [62] M. Mezei and J. Virrueta, Exploring the membrane theory of entanglement dynamics, *J. High Energy Phys.* **01** (2020) 186.
- [63] C. A. Agón and M. Mezei, Bit threads and the membrane theory of entanglement dynamics, *J. High Energy Phys.* **01** (2021) 193.
- [64] X.-H. Yu, Z. Wang, and P. Kos, Hierarchical generalization of dual unitarity, *Quantum* **8**, 1260 (2024).
- [65] We take them to be orthogonal with respect to the Hilbert-Schmidt product, i.e., $\text{tr}[\sigma^{(\alpha)}\sigma^{(\beta)}] = d\delta_{\alpha,\beta}$.
- [66] Here, we assume parity symmetry. If there is no parity symmetry one has to consider also the limit $|x|, t \rightarrow \infty$ with $x_{\pm} = t + x$ fixed. The treatment is completely analogous.
- [67] In Eq. (5) we assumed x to be half-integer. The case of integer x leads to identical considerations.
- [68] See Supplemental Material at <http://link.aps.org/supplemental/10.1103/PhysRevLett.132.250402> for (i) an explicit calculation of the scalar product in Eq. (12), (ii) a characterization of Rényi entropies at early times, i.e., for $L \geq L_A + 2t \geq 4t$ and a proof of Eq. (17), (iii) a proof that the matrix $\tilde{U}\tilde{U}^\dagger$ has flat spectrum, and (iv) the parametrization considered in our numerical experiments.
- [69] G. Evenbly and G. Vidal, Tensor network renormalization, *Phys. Rev. Lett.* **115**, 180405 (2015).
- [70] B. Bertini, K. Klobas, and T.-C. Lu, Entanglement negativity and mutual information after a quantum quench: Exact link from space-time duality, *Phys. Rev. Lett.* **129**, 140503 (2022).
- [71] Z. Gong, A. Nahum, and L. Piroli, Coarse-grained entanglement and operator growth in anomalous dynamics, *Phys. Rev. Lett.* **128**, 080602 (2022).
- [72] M. Mezei, Membrane theory of entanglement dynamics from holography, *Phys. Rev. D* **98**, 106025 (2018).
- [73] M. A. Rampp, S. A. Rather, and P. W. Claeys, The entanglement membrane in exactly solvable lattice models, [arXiv:2312.12509](https://arxiv.org/abs/2312.12509).

Supplemental Material: "Quantum information spreading in generalised dual-unitary circuits"

Here we report some useful information complementing the main text. In particular

- In Sec. I we compute explicitly the scalar products $\langle l|\blacksquare\rangle = \langle \bullet|r\rangle$ in Eq. (12) of the main text.
- In Sec. II we characterise Rényi entropies at early times, i.e., for $L \geq L_A + 2t \geq 4t$ and prove Eq. (17) of the main text.
- In Sec. III we show that the matrix $\tilde{U}\tilde{U}^\dagger$ has flat spectrum.
- In Sec. IV we report the parameterisation used for our numerical experiments.

I. EXPLICIT CALCULATION OF THE SCALAR PRODUCT IN EQ. (12)

Consider the vectors $|l\rangle$ and $|\blacksquare\rangle$ in Eqs. (10) and (11). Their scalar product can be compute by decomposing $|\blacksquare\rangle$

$$\langle l|\blacksquare\rangle = d \langle l|\circ\rangle - \langle l|\square\rangle = d \text{ (diagram)} - \text{ (diagram)} \quad (1)$$

The first term can be immediately simplified using unitarity and obtaining d^4 , while the second one can be written in terms of \tilde{U} as

$$\langle l|\bullet\rangle = d^4 - \text{tr} \left[\left(\tilde{U}\tilde{U}^\dagger \right)^2 \right] = d^4 \left(1 - \frac{1}{n_\Lambda} \right), \quad (2)$$

where we used Eq. (23) to simplify the second term; identical considerations apply to $\langle \blacksquare|r\rangle$.

II. ENTANGLEMENT DYNAMICS AT EARLY TIMES

In order to compute the Rényi entropy from Eq. (16), we can express the trace of the n -th power of the reduced density matrix as a contracted network:

$$\begin{aligned} \text{tr} [\rho_A^n] &= \frac{1}{d^{nL}} \text{ (diagram)} \\ &= \frac{1}{d^{nL}} \text{ (diagram)} \end{aligned} \quad (3)$$

where now the states $|\circ\rangle, |\square\rangle$ represent two different contractions in the space of replicas, defined as in (6). Equation (3) can be further simplified, by noting that the matrix MPS transfer matrix has an eigenvalue fixed by the compatibility condition (15). Using the unitarity of the gate, it is easy to show that

$$\text{ (diagram)} = d^n \text{ (diagram)} \quad \text{ (diagram)} = d^n \text{ (diagram)}, \quad (4)$$

where, due to the global replica symmetry, the same relation holds if we replace all the circles with squares. If we assume this eigenvalue of the transfer matrix is nondegenerate and maximal, then we can further simplify (3) as

$$\text{tr}[\rho_A^n] = \frac{1}{\chi^n d^{n(L_A+2t+1)}} \underbrace{\text{Diagram 1}}_{2t+1} \underbrace{\text{Diagram 2}}_{2t+1}. \quad (5)$$

Our last step consists into taking the scaling limit $L_A, t \rightarrow \infty$; keeping the ratio $t/L_A = \text{const} < 1/2$, in such a way that the two edges of the subsystem A are not causally connected. In this limit, the $L_A - 2t - 1$ MPS transfer matrices in between the two triangles in (5) can be substituted by the projector on their largest eigenvalue; explicitly we can write

$$\lim_{m \rightarrow \infty} \left(\frac{1}{d^n} \text{Diagram 3} \right)^m = \frac{1}{\chi^n} \text{Diagram 4}, \quad (6)$$

which allows to simplify Eq. (5) as

$$\text{tr}[\rho_A^n] = \left(\frac{1}{\chi^n d^{n(2t+1)}} \text{Diagram 5} \right)^2, \quad (7)$$

leading to Eq. (17).

III. SPECTRUM OF $\tilde{U}\tilde{U}^\dagger$

In this section we want to study the spectrum of $\tilde{U}\tilde{U}^\dagger$, where \tilde{U} is obtained by a reshuffling of the indexes of the gate U , explicitly

$$\langle kl | \tilde{U} | ij \rangle = \langle lj | U | ki \rangle. \quad (8)$$

Since it is convenient to use diagrammatic calculus for our calculations here, we begin by introducing a few more useful diagrams. We represent a single gate as

$$\langle kl | U | ij \rangle \equiv \text{Diagram 6a} = \left(\text{Diagram 6b} \right)^*. \quad (9)$$

Therefore, unitarity and DU2 property (2) correspond to

$$\text{Diagram 7a} = \text{Diagram 7b} = \text{Diagram 7c} = \text{Diagram 7d} = \text{Diagram 7e} = \text{Diagram 7f}. \quad (10)$$

In fact, DU2 also implies

$$\text{Diagram 8a} = \text{Diagram 8b} = \text{Diagram 8c} = \text{Diagram 8d}. \quad (11)$$

where now we have $n - m$ blue gates on the bottom and $m + 1$ on top. Using Eqs. (13) and (16), we can simplify the gates on top to write

$$\begin{aligned}
 B &= \sum_{\Lambda} \Lambda^{2(m+1)} \frac{\text{tr}[P_{\Lambda}]}{d^2} \text{Diagram} = \\
 &= \sum_{\Lambda, \Lambda'} \Lambda'^{2(n-m)} \Lambda^{2(m+1)} \frac{\text{tr}[P_{\Lambda}] \text{tr}[P_{\Lambda'}]}{d^2}.
 \end{aligned} \tag{21}$$

Combining Eqs. (18) and (21), we get

$$\forall n, m \quad \sum_{\Lambda, \Lambda'} \Lambda'^{2(n-m)} \Lambda^{2(m+1)} \frac{\text{tr}[P_{\Lambda}] \text{tr}[P_{\Lambda'}]}{d^2} = \sum_{\Lambda} \Lambda^{2n} \text{tr}[P_{\Lambda}] \tag{22}$$

which implies there can be only one nonzero Λ . In turn, this implies

$$\text{tr}[P_{\Lambda}] \Lambda = d^2 \quad \text{tr}[(\tilde{U}\tilde{U}^{\dagger})^n] = \Lambda^{2(n-1)} d^2 \tag{23}$$

Substituting (23) in (20) and setting $n_{\Lambda} = \text{tr}[P_{\Lambda}]$ this gives Eq. (21).

IV. PARAMETERISATION FOR NUMERICAL EXPERIMENTS

In order to produce the plots in Fig. 2, we used a DU2 gate with $d = 2$ and $n_{\Lambda} = 2$, parameterized as follows

$$\begin{aligned}
 U &= u_0(v_1 \otimes v_2), \tag{24} \\
 u_0 &= \begin{pmatrix} e^{i\pi/4} & 0 & 0 & 0 \\ 0 & 0 & e^{-i\pi/4} & 0 \\ 0 & e^{-i\pi/4} & 0 & 0 \\ 0 & 0 & 0 & e^{i\pi/4} \end{pmatrix}, \quad v_{1/2} = \frac{1}{\sqrt{2}} \begin{pmatrix} e^{i\alpha_{1/2}} & -e^{-i\alpha_{1/2}} \\ e^{i\alpha_{1/2}} & e^{-i\alpha_{1/2}} \end{pmatrix}, \tag{25}
 \end{aligned}$$

where the α s have been fixed to the values $\alpha_1 = 0.2, \alpha_2 = 0.3$. The initial states chosen are random dimer states

$$|\Psi_0\rangle = \left(\sum_{i,j} m_{ij} |i, j\rangle \right)^{\otimes L}, \tag{26}$$

where the matrix m_{ij} is the normalized matrix whose elements, in the computation basis, are pseudo-random numbers distributed uniformly in $[0, 1]$.

Chapter 5

Non-equilibrium dynamics of charged dual-unitary circuits

5.1 Summary

In this work, we show a general construction for dual unitary gates with conserved charges. Since for these gates charge densities move ballistically, starting from elementary charge (which we call solitons) one can always build an exponential number of conserved charges in the system size. The solitons allow to break the gates into generalized dual unitary blocks, which can act on neighbouring qudits with different dimensions.

Moreover, we define and fully characterize charged initial states which behave similarly to the ones introduced for chaotic unitary gates [109] meaning that again they have a maximal entanglement speed, although they do not thermalize to the infinite temperature state. We also construct a class of states solvable only on one side, which can only be defined in the presence of conserved solitons, showing that it has a peculiar thermalization dynamics for a single interval, with it being divided into two different phases.

Finally, using the membrane picture in each charge sector, we compute the

entanglement and entanglement asymmetry dynamics from generic initial states, showing again a two-step thermalization process. Our findings are supported by numerical evidence.

Non-equilibrium dynamics of charged dual-unitary circuits

Alessandro Foligno,^{1,2} Pasquale Calabrese,^{3,4} and Bruno Bertini⁵

¹*School of Physics and Astronomy, University of Nottingham, Nottingham, NG7 2RD, UK*

²*Centre for the Mathematics and Theoretical Physics of Quantum Non-Equilibrium Systems, University of Nottingham, Nottingham, NG7 2RD, UK*

³*SISSA and INFN Sezione di Trieste, via Bonomea 265, 34136 Trieste, Italy*

⁴*International Centre for Theoretical Physics (ICTP), Strada Costiera 11, 34151 Trieste, Italy*

⁵*School of Physics and Astronomy, University of Birmingham, Edgbaston, Birmingham, B15 2TT, UK*

The interplay between symmetries and entanglement in out-of-equilibrium quantum systems is currently at the centre of an intense multidisciplinary research effort. Here we introduce a setting where these questions can be characterised exactly by considering dual-unitary circuits with an arbitrary number of $U(1)$ charges. After providing a complete characterisation of these systems we show that one can introduce a class of solvable states, which extends that of generic dual unitary circuits, for which the non-equilibrium dynamics can be solved exactly. In contrast to the known class of solvable states, which relax to the infinite temperature state, these states relax to a family of non-trivial generalised Gibbs ensembles. The relaxation process of these states can be simply described by a linear growth of the entanglement entropy followed by saturation to a non-maximal value but with maximal entanglement velocity. We then move on to consider the dynamics from non-solvable states, combining exact results with the entanglement membrane picture we argue that the entanglement dynamics from these states is qualitatively different from that of the solvable ones. It shows two different growth regimes characterised by two distinct slopes, both corresponding to sub-maximal entanglement velocities. Moreover, we show that non-solvable initial states can give rise to the quantum Mpemba effect, where less symmetric initial states restore the symmetry faster than more symmetric ones.

CONTENTS

I. Introduction	1	A. Charge Propagation in Dual-Unitary Circuits	20
II. Setting and Summary of the Results	2	B. Proof of Theorem 1	21
III. \mathcal{G} -Symmetric Dual Unitary Circuits	4	C. Proof of Theorems 2-3	23
A. Explicit parameterisation of dual-unitary transformations	6	1. Left solvability	23
B. Diagrammatic representation	6	2. Charged solvability	24
IV. Charged solvable states	7	D. Late time regime for left charged solvable states	24
V. Entanglement dynamics from charged solvable states	9	1. Leading eigenvectors of the transfer matrix	24
A. Early-time Regime	9	2. Bound between left/right entanglement entropies	26
B. Late-time Regime	10	3. Bound on the rate of growth of entanglement in the second phase	27
VI. Entanglement dynamics from non-charged-solvable states	11	E. Simplification of Eq. (133)	28
A. Entanglement dynamics from left charged solvable states	11	References	29
B. Entanglement dynamics from generic states	13		
1. Early time growth	14		
2. Asymptotic entanglement value	16		
3. Second phase of thermalisation	17		
VII. Asymmetry dynamics and Mpemba effect	18		
VIII. Discussion and Outlook	20		
Acknowledgments	20		

I. INTRODUCTION

Understanding the non-equilibrium dynamics of interacting many-particle systems, classical or quantum, has been a key open question in theoretical physics for almost two centuries. Since the turn of the millennium, however, an interdisciplinary research effort involving experts from condensed matter physics, quantum information, and particle physics has started to crack the nut.

For instance, one aspect that made the study of many-body systems out of equilibrium particularly hard is that

the standard probes used to analyse systems at equilibrium, like Hamiltonian gaps or correlation functions of local observables, are either ill-defined or return obscure non-universal information in the non-equilibrium setting. Recent research, however, has finally identified a convenient probe in *quantum entanglement* [1–7]. The latter gives an observable-independent characterisation of the correlations between the different finite parts of the system and displays universal time evolution even in out-of-equilibrium settings. For example, under very general conditions on the microscopic dynamics, after a quantum quench the entanglement between a finite subsystem and the rest shows an irreversible linear growth followed by saturation [8–20].

At the same time researchers began to find minimal interacting models where the entanglement dynamics can be characterised exactly [18–24]. These can be considered as the out-of-equilibrium analogues of the solved models of statistical mechanics [25], and, just like their equilibrium counterparts, they can be used to define and characterise suitable universality classes for dynamical behaviours. The aforementioned minimal models have been found in the context of *quantum circuits*, i.e., many-body systems in discrete space-time [18–22, 26–36], owing to the more symmetric treatment of space and time provided by this setting. Specifically, there have been two main strategies to find solvable quantum circuits. The first is to introduce noise [27, 29, 30, 37] (see also Ref. [38] and references therein). In this case one can compute the average of relevant physical quantities by mapping them to classical partition functions, which can sometimes be solved exactly. The second is to impose additional constraints, or symmetries, on the dynamics [31, 39–45]. This second approach has the advantage of being more fundamental — it does not require any external influence — but the additional constraints can make these minimal models non-generic. Remarkably, however, among the constrained minimal models there are some exhibiting, ergodic, i.e., generic, dynamics. The simplest class with this property are dual unitary circuits [31], which are constrained to generate unitary dynamics also when the roles of space and time are exchanged.

Having obtained a blueprint of the thermalisation process through the entanglement the research has now shifted to seek more refined probes. A natural next step has been to investigate the fluctuations of globally conserved quantities within local subsystems, as they should also show a universal dynamics, and their interplay with the entanglement [46–53, 55, 56, 89]. For example, a simple but instructive problem studied in this context is that of symmetry restoration when a symmetric system is prepared in a non-equilibrium initial state that explicitly breaks the symmetry. This process can be characterised in a universal way by measuring the distance between the time-evolving state and its symmetrised counterpart via the so called *entanglement asymmetry* [51] (see also Refs. [53, 57–75]). This revealed, for instance, that a symmetry can sometimes be restored more rapidly when

it is broken more by the initial state, providing a quantum analogue of the famous Mpemba effect [76].

To sustain this effort it is again crucial to identify minimal models where these questions can be studied exactly. Some progress in this direction has been achieved in the context of noisy quantum circuits [68, 72, 73], however, for the case of clean systems the results are scarce. Essentially, only existing partial results in this direction [77] are for a class of Yang-Baxter integrable dual unitary circuits [78, 79]. Here we introduce and characterise a class of symmetric dual-unitary circuits class of quantum circuits, which are chaotic in each symmetry sector. We then use these systems to provide exact results on the interplay between entanglement and charge fluctuations. We do so by first introducing a class of initial states with exactly solvable quench dynamics. This extends the known class of solvable states of dual-unitary circuits [19]. We then study the dynamics of states that, instead, are not solvable, by combining exact bounds with the entanglement membrane theory. We prove that these two classes of states show a qualitatively different entanglement dynamics and that the latter can display the quantum Mpemba effect.

The rest of the paper is laid out as follows. In Sec. II we present a summary and a discussion of our main results. In Sec. III we report a systematic characterisation of dual unitary circuits with $U(1)$ charges for arbitrary local Hilbert space dimension. In Sec. IV we introduce the class of solvable states for charged dual-unitary circuits, which we dub “charged solvable states”. In Sec. V we present an exact solution of the quench dynamics of charged solvable states. In Sec. VI we instead study the dynamics of non-solvable states while in Sec. VII we discuss the dynamics of entanglement asymmetry. Our conclusions are reported in Sec. VIII. The main text is complemented by a number of appendices containing the proofs of some of the theorems presented in the main text and some explicit calculations.

II. SETTING AND SUMMARY OF THE RESULTS

We consider brickwork quantum circuits, i.e., quantum many-body systems defined on a lattice where the time evolution is discrete and the interactions are local. A step of time evolution is implemented by the many-body unitary operator \mathbb{U} constructed in terms of a two-qudit gate U according to the following staggered pattern

$$\mathbb{U} = \mathbb{U}_e \mathbb{U}_o, \quad \mathbb{U}_e = \bigotimes_{x=0}^L U_{x,x+1/2}, \quad \mathbb{U}_o = \bigotimes_{x=0}^L U_{x+1/2,x}. \quad (1)$$

Here the sites are labelled by half integers, $U_{a,b}$ acts on the qudits located at a and b , and we denoted by $2L$ the size of the system. Moreover, we take periodic boundary conditions, so that sites 0 and L coincide, and indicate by d the local dimension (number of states of each qudit) on each site.

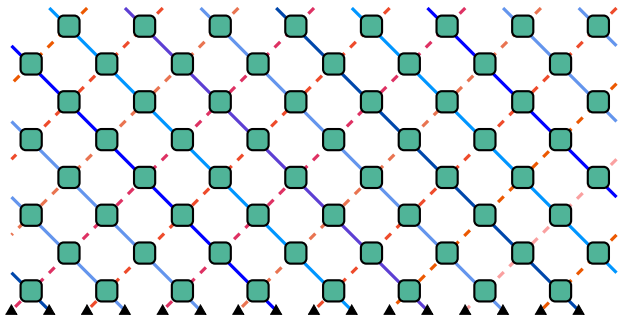


FIG. 1. Graphical representation of the state of a \mathcal{G} -symmetric dual-unitary circuit in a given charge sector. Left-moving (blue shades) and right-moving (red shades) legs have generically different local dimensions. See Sec. III B for a detailed explanation of the diagrammatic notation.

We take our local gate U be *dual-unitary* [31], meaning that both U and \tilde{U} — the gate corresponding to U upon exchange of space and time — are unitary matrices. More formally, the spacetime swapped gate \tilde{U} is defined through the following matrix element reshuffling

$$\langle ij | \tilde{U} | kl \rangle \equiv \langle jl | U | ik \rangle, \quad (2)$$

and dual unitarity corresponds to requiring

$$UU^\dagger = U^\dagger U = \mathbb{1}_{d^2} \quad \tilde{U}\tilde{U}^\dagger = \tilde{U}^\dagger\tilde{U} = \mathbb{1}_{d^2}, \quad (3)$$

where $\mathbb{1}_x$ represents the identity operator in \mathbb{C}^x . A quantum circuit composed of gates with this property is typically referred to as dual-unitary circuit. Specifically, in this work we consider dual unitary circuits with n independent $U(1)$ symmetries (hence having n independent conservation laws with 1-local density). In fact, since left and right moving charges are independent in dual unitary circuits [80] (see also the review in Appendix A), it is natural to consider independent symmetry groups for left (ℓ) and right (r) movers. Therefore, we consider circuits with a symmetry group given by

$$\mathcal{G} = U(1)_\ell^{n_\ell} \times U(1)_r^{n_r}, \quad (4)$$

where $n_{\ell/r}$ can take any value from 0 to $d-1$ (since we require our charges to commute with each other). The lower bound corresponds to circuits with no symmetry, while the upper bound to circuits with the maximal number of commuting 1-local charge densities.

In Sec. III we show that in \mathcal{G} -symmetric dual unitary circuits the local gate U can be decomposed in different charge sectors as

$$U = \bigoplus_{\alpha=1}^{n_r+1} \bigoplus_{\beta=1}^{n_\ell+1} U^{(\alpha,\beta)}, \quad (5)$$

where the blocks $U^{(\alpha,\beta)}$ have dimension $d_\alpha^{(r)} d_\beta^{(\ell)}$ and $d_\alpha^{(\ell/r)} > 0$ are such that

$$\sum_{\alpha=1}^{n_r+1} d_\alpha^{(r)} = \sum_{\beta=1}^{n_\ell+1} d_\beta^{(\ell)} = d. \quad (6)$$

Note that $U^{(\alpha,\beta)}$ implements unitary transformations with different domains and codomains, i.e.,

$$U^{(\alpha,\beta)} : \mathbb{C}^{d_\alpha^{(r)}} \otimes \mathbb{C}^{d_\beta^{(\ell)}} \rightarrow \mathbb{C}^{d_\beta^{(\ell)}} \otimes \mathbb{C}^{d_\alpha^{(r)}}. \quad (7)$$

Since domain and codomain of $U^{(\alpha,\beta)}$ are isomorphic, however, one can still think of it as a square unitary matrix. In fact, whenever U is dual unitary, also the blocks $U^{(\alpha,\beta)}$ are dual-unitary, meaning that both $U^{(\alpha,\beta)}$ and its space-time swapped counterpart are unitary.

In passing we note that unitary transformations with different (but isomorphic) domain and codomain can be used to define quantum cellular automata generalising the concept of brickwork quantum circuits [81]. These systems arise at the boundary of certain Floquet systems displaying many-body localisation in the bulk [82–85], and can be shown to generate a qualitatively different quantum information spreading [86, 87]. Here we find that the dual unitary version of these systems emerge naturally in the charge sectors of \mathcal{G} -symmetric dual unitary circuits. A schematic representation of the state of the system in a given charge sector is presented in Fig. 1.

Next, in Sec. IV, we show that for \mathcal{G} -symmetric dual unitary circuits one can extend the family of solvable states introduced in Ref. [19]. We dub this larger family *charged solvable* states and, in Sec. V, we present the exact solution of their many body dynamics. We show that in contrast with the solvable states of Ref. [19], which always relax to the infinite temperature state, charged solvable states relax to non-trivial generalised Gibbs ensembles. Their entanglement velocity, however, is still maximal. Specifically, at the leading order the entanglement entropy of an interval A of length L_A is described by the standard linear-growth/sharp relaxation form

$$S_A(t) = 2s \min(2t, L_A), \quad (8)$$

where $2s$ is the entropy density of the GGE. In fact, we find that $S_A(\infty)$ can be split into a “number” and a “configurational” part, where the former measures the average of the entanglement in the charge sectors and the latter the fluctuations of the charge [88–90]. The emergence of this splitting at infinite times is a typical feature of quantum many-body systems with conserved charges [52], however, in our case it takes a special form: the number part of $S_A(\infty)$ is extensive rather than logarithmic in L_A . One can understand this by noting that \mathcal{G} -symmetric dual unitary circuits have exponentially many (in L_A) charged sectors as opposed to the polynomially many occurring in generic systems with conservation laws.

Then, in Sec. VI, we consider the dynamics of \mathcal{G} -symmetric dual unitary circuits from states that are *not* charged solvable. Combining exact results with the entanglement membrane approach [91, 92] we find that the entanglement dynamics is *qualitatively different* from the one described by Eq. (8) as it shows a *two step relaxation*. More precisely, we find that left and right movers give different contributions to the entanglement growth (they

contribute equally for charged solvable states). Calling their respective contributions $s^{(r)}$ and $s^{(\ell)}$ and considering $s^{(r)} < s^{(\ell)}$ we have

$$S_A(t) = \begin{cases} 4ts^{(r)} & t \leq L_A/2 \\ 4ts^{(r)} - (2t - L_A)s_{\text{num}}^{(r)} & L_A/2 < t \leq t_{\text{th}} \\ L_A(s^{(r)} + s^{(\ell)}) & t > t_{\text{th}} \end{cases} \quad (9)$$

where $s_{\text{num}}^{(r)}$ is the number entropy density of right movers and the thermalisation time t_{th} is fixed by continuity to be

$$t_{\text{th}} = \frac{L_A}{2} \left(1 + \frac{s^{(\ell)} - s^{(r)}}{2s^{(r)} - s_{\text{num}}^{(r)}} \right). \quad (10)$$

Eq. (9) implies that, for a given GGE entropy density $2s = s^{(r)} + s^{(\ell)}$ non-solvable states show a slower (state dependent) entanglement growth compared to the solvable ones. Namely their entanglement velocity is not 1 despite the circuit being dual unitary. Moreover, the slope in the second phase is always lower than the one in the first as long as $s_{\text{num}}^{(r)} \neq 0$. This behaviour arises because the charge structure acts as a constraint that can create an imbalance on the amount of entanglement available for left- and right-moving charges: While solvable states are forced to have no imbalance, non-solvable ones are generically imbalanced and their thermalisation process is slower. The occurrence of the second stage of thermalisation is another interesting consequence of the charge structure, this time in concurrence with the non-integrable nature of the system. Indeed, this phase corresponds to a time regime where a simple quasiparticle picture would predict the entanglement to be already saturated. The growth is only observed because the creation and destruction of quasiparticles generates a scrambling of quantum information. This scrambling, however, cannot be maximal because all the creation/annihilation processes have to conserve the charge. Therefore, the slope in the second phase is generically smaller than in the first. A schematic representation of the entanglement growth from solvable and non-solvable states is reported in Fig. 2, while a numerical simulation confirming this picture is presented in Fig. 7 (cf. Sec. VI B).

Finally, in Sec. VII, we study symmetry restoration in \mathcal{G} -symmetric dual-unitary circuits. Namely, we quantify how a non-symmetric initial state becomes gradually more symmetric in the course of the time evolution. We do so by computing the entanglement asymmetry $\Delta S_A(t)$ defined as the relative entropy between the reduced state of A and its symmetrised version (cf. Sec. VII).

An interesting aspect of this process is the possible occurrence of the *quantum Mpemba effect*, which means that a symmetry is restored faster for states breaking it more at $t = 0$ [51]. Its name is due to the conceptual similarity that this process has with the ‘‘classical’’ Mpemba effect, arising when hot water freezes faster than cold water [76]. Since its first observation in Ref. [51] this effect has been observed in a range of different physical

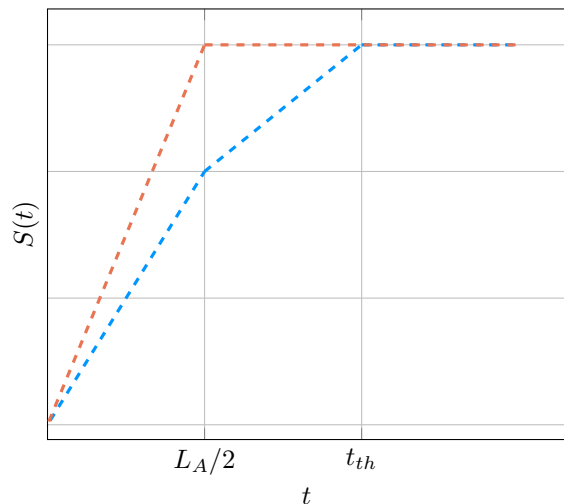


FIG. 2. Entanglement growth of a finite, connected interval of size L_A from a charged solvable state (orange) and a generic one (blue). Solvable charged states behave as those studied in [19], meaning they thermalise at the fastest possible rate and the entanglement saturates at $t = L_A/2$. In the generic case, instead, there is a secondary growth phase which is always slower than the first.

settings [51, 53, 57–73], including trapped ion quantum simulators [93]. Here we find that for non-charged solvable initial states in \mathcal{G} -symmetric dual-unitary circuits show the quantum Mpemba effect owing to their two step relaxation process. In particular, we provide an explicit example where the quantum Mpemba effect is controlled by the number entropy of right movers: larger number entropy implies larger initial asymmetry and faster relaxation.

III. \mathcal{G} -SYMMETRIC DUAL UNITARY CIRCUITS

In this work we are interested in dual-unitary circuits with continuous internal symmetries. In other words, we require the existence of extensive operators

$$Q = \sum_{x \in \mathbb{Z}_{2L}/2} q_x, \quad (11)$$

with q_x acting nontrivially only at site x , that commute with \mathbb{U} in Eq. (1).

In dual-unitary circuits, conserved charges as the one in Eq. (11) split in two independent components supported respectively on integer and half-odd integer sites, i.e.

$$Q^{(\ell)} = \sum_{x \in \mathbb{Z}_L} q_{x+1/2}^{(\ell)}, \quad Q^{(r)} = \sum_{x \in \mathbb{Z}_L} q_x^{(r)}. \quad (12)$$

Note that these operators are two-site shift invariant like the time evolution operator. Moreover, we denoted the

two charges in Eq. (12) by the labels ℓ and r as their densities are respectively left- and right-moving [80].

To see how this occurs we recall that, as a consequence of charge conservation, the charge density obeys an operatorial continuity equation of the form

$$\mathbb{U}^\dagger q_x \mathbb{U} = q_x - J_{x+1/2} + J_{x-1/2}, \quad (13)$$

where J_x is a local operator with support at most on two sites starting at site x . For dual unitary circuits, however, this operator takes the following special form [80] (for completeness, we report a proof of the relevant facts in Appendix A)

$$J_x = \begin{cases} -q_{x+1/2}, & x \in \mathbb{Z} \\ q_{x-1/2}, & x \in \mathbb{Z} + 1/2 \end{cases}, \quad (14)$$

meaning that the charge densities are simply shifted by the time evolution

$$\mathbb{U} q_x^{(r)} \mathbb{U}^\dagger = \begin{cases} q_{x+1}, & x \in \mathbb{Z} \\ q_{x-1}, & x \in \mathbb{Z} + 1/2 \end{cases}, \quad (15)$$

and the charges in Eq. (12) are independently conserved.

Operators evolving as in Eq. (15) have been referred to as ‘‘solitons’’ [94] or ‘‘gliders’’ [95] in the literature and their presence immediately implies that the circuit has far more conserved operators than those in Eq. (12). Indeed if the circuit admits a non-trivial soliton, for any given $\ell \geq 1$ one can produce $2^{\ell+1} - 2$ independent charge densities with support on at most 2ℓ sites (cf. App. A), each of which obeys (15). Physically, this happens because the solitons are effectively ‘‘fragmenting’’ the dynamics of the circuit in different charge sectors. The goal of this paper is to characterise this fragmentation and investigate its effects on the many-body dynamics. In the rest, we will use the word ‘‘soliton’’ to designate the fundamental building block of these charge densities, that is those with support on a single site.

Considering circuits with the symmetry group \mathcal{G} (cf. Eq. (4)) we then have $m_\ell = 1 + n_\ell$ independent left moving solitons and $m_\ell = 1 + n_\ell$ solitons. Indeed, Eq. (15) is fulfilled by the charges associated to the $U(1)$ symmetries and, trivially, by the identity operator. Noting then that Eq. (15) is linear in the charge density, we have that the space of solitons on each site is a vector space. Therefore we introduce the following bases of solitons

$$\mathcal{S}^{(r/\ell)} = \{\sigma_1^{(r/\ell)}, \dots, \sigma_{m_{\ell/r}}^{(r/\ell)}\}, \quad (16)$$

where the subscript denotes the element of the basis and we suppressed the position index x : unless explicitly stated position indices for solitons will be suppressed from now on. This basis can be taken to be Hilbert-Schmidt orthogonal.

The bases of solitons in Eq. (16) are characterised by means of the following theorem, proven in Appendix B.

Theorem 1. *In a dual unitary circuit with commuting solitons supported on a single site one can always choose a basis where the solitons are mutually orthogonal projectors. In addition, the bases in Eq. (16) can be taken to be*

$$\mathcal{S}^{(r/\ell)} = \{\{\Pi_\alpha^{(r/\ell)}\}, \{P_{+,\beta}^{(r/\ell)}, P_{-,\beta}^{(r/\ell)}\}\}, \quad (17)$$

where the two types of solitons, Π_α and $P_{+/-,\beta}$, respectively fulfil

$$\begin{aligned} U \left(\Pi_\alpha^{(r)} \otimes \mathbb{1}_d \right) U^\dagger &= \mathbb{1}_d \otimes \Pi_\alpha^{(r)}, \\ U \left(\mathbb{1}_d \otimes \Pi_\alpha^{(\ell)} \right) U^\dagger &= \Pi_\alpha^{(\ell)} \otimes \mathbb{1}_d, \end{aligned} \quad (18)$$

and

$$\begin{aligned} U \left(P_{\pm,\alpha}^{(r)} \otimes \mathbb{1}_d \right) U^\dagger &= \mathbb{1}_d \otimes P_{\mp,\alpha}^{(r)}, \\ U \left(\mathbb{1}_d \otimes P_{\pm,\alpha}^{(\ell)} \right) U^\dagger &= P_{\mp,\alpha}^{(\ell)} \otimes \mathbb{1}_d. \end{aligned} \quad (19)$$

Note that Eq. (18) implies that $\Pi_\alpha^{(\ell)/(r)}$ fulfil a stronger version of Eq. (15): rather than being shifted by two sites every time step they are shifted by one site each half step of the evolution. Besides being shifted by one site, the projectors $P_{+,\alpha}^{(r)}$ and $P_{-,\alpha}^{(r)}$ are swapped into one another each half step. We also remark that, since the set of solitons includes the identity operator, the basis in Eq. (17) fulfils the following completeness relation

$$\sum_\alpha \Pi_\alpha^{(r/\ell)} + \sum_\beta P_{+,\beta}^{(r/\ell)} + P_{-,\beta}^{(r/\ell)} = \mathbb{1}_d. \quad (20)$$

For the sake of simplicity here we only consider the case of commuting solitons, i.e., circuits where the symmetry group is abelian (this excludes, for example, circuits made of SWAP gates as they have non-abelian symmetry groups). Moreover, we restrict to solitons of the type Π_α . The latter is not a real restriction as the solitons of type $P_{\pm,\alpha}$ are mapped into Π_α by ‘‘renormalising’’ the quantum circuit, i.e., combining together two subsequent time steps and two neighbouring qudits (see the discussion at end of App. D 1 for an explicit example).

Under these conditions Theorem 1 implies that one decompose the local gates in a number of blocks corresponding to the charge sectors. Namely, using the completeness relations in Eq. (20), the strong soliton condition in Eq. (18), and the projector property of $\Pi_\alpha^{(\ell/r)}$ one can write

$$U = \sum_{\alpha,\beta} (\Pi_\beta^{(\ell)} \otimes \Pi_\alpha^{(r)}) U = \sum_{\alpha,\beta} U^{(\alpha,\beta)}, \quad (21)$$

where we introduced

$$U^{(\alpha,\beta)} \equiv (\Pi_\beta^{(\ell)} \otimes \Pi_\alpha^{(r)}) U (\Pi_\alpha^{(r)} \otimes \Pi_\beta^{(\ell)}). \quad (22)$$

Note that domain and codomain of this transformation are different. Specifically, we have

$$U^{(\alpha,\beta)} : \mathbb{C}^{d_\alpha^{(r)}} \otimes \mathbb{C}^{d_\beta^{(\ell)}} \rightarrow \mathbb{C}^{d_\beta^{(\ell)}} \otimes \mathbb{C}^{d_\alpha^{(r)}}, \quad (23)$$

where we set

$$d_\alpha^{(r/\ell)} = \text{tr} \left[\Pi_\alpha^{(r/\ell)} \right]. \quad (24)$$

These spaces, however, are isomorphic. Moreover, using Eq. (18) and the projector property of $\Pi_\alpha^{(r/\ell)}$ one can show that $U^{(\alpha,\beta)}$ is a unitary transformation between the two spaces, i.e.

$$\begin{aligned} (U^{(\alpha,\beta)})^\dagger U^{(\alpha,\beta)} &= \Pi_\alpha^{(r)} \otimes \Pi_\beta^{(\ell)}, \\ U^{(\alpha,\beta)} (U^{(\alpha,\beta)})^\dagger &= \Pi_\beta^{(r)} \otimes \Pi_\alpha^{(\ell)}. \end{aligned} \quad (25)$$

In fact, noting that

$$\begin{aligned} \widetilde{U^{(\alpha,\beta)}} &= (\Pi_\alpha^{(\ell)} \otimes \Pi_\beta^{(r)}) \widetilde{U} \\ &= (\Pi_\alpha^{(\ell)} \otimes \Pi_\beta^{(r)}) \widetilde{U} (\Pi_\beta^{(r)} \otimes \Pi_\alpha^{(\ell)}), \end{aligned} \quad (26)$$

and using again Eq. (18) and the projector property of $\Pi_\alpha^{(\ell)/(r)}$ one can show that also $\widetilde{U^{(\alpha,\beta)}}$ is unitary, i.e.

$$\begin{aligned} (\widetilde{U^{(\alpha,\beta)}})^\dagger \widetilde{U^{(\alpha,\beta)}} &= \Pi_\beta^{(r)} \otimes \Pi_\alpha^{(\ell)}, \\ \widetilde{U^{(\alpha,\beta)}} (\widetilde{U^{(\alpha,\beta)}})^\dagger &= \Pi_\alpha^{(\ell)} \otimes \Pi_\beta^{(r)}. \end{aligned} \quad (27)$$

Therefore, each one of the blocks on the r.h.s. of Eq. (21) is a *dual-unitary transformation*. This provides a full characterisation of \mathcal{G} -symmetric dual-unitary circuits: they are circuits in which the gate is decomposed in a number of dual unitary blocks. The precise decomposition depends on the soliton content of the circuit, and the local spaces on which the blocks act can have different local dimensions ($d_\alpha^{(r)} \neq d_\alpha^{(\ell)}$).

Before proceeding with the study of the properties of these circuits, in the two upcoming subsections we present an example of explicit parameterisation of such dual-unitary transformations and introduce a useful diagrammatic representation that will be extensively used in the rest of the paper.

A. Explicit parameterisation of dual-unitary transformations

A simple class of dual-unitary transformations can be constructed following Ref. [96]. Namely, one can set

$$U \left(|a\rangle_{(r)} \otimes |b\rangle_{(\ell)} \right) \equiv e^{iJ_{ab}} u |b\rangle_{(\ell)} \otimes v |a\rangle_{(r)} \quad (28)$$

where $|a\rangle_R$ and $|b\rangle_L$ are bases of $\mathbb{C}^{d_\alpha^{(r)}}$ and $\mathbb{C}^{d_\beta^{(\ell)}}$, $u \in U(d_\alpha^{(r)})$, $v \in U(d_\beta^{(\ell)})$, and $J_{ab} \in \mathbb{R}$. It is immediate to see that the map in Eq. (28) is of the type in Eq. (23) and fulfils both Eqs. (25) and (27); however it is possible to find other examples of such gates outside of this family. For concreteness, we will consider $U^{(\alpha,\beta)}$ in Eq. (22) to be of the form in Eq. (28). We will assume that u and v are taken to be generic enough such that $U^{(\alpha,\beta)}$ does not admit non-trivial solitons and, therefore, cannot be further decomposed.

B. Diagrammatic representation

The study of quantum circuits is significantly facilitated by the introduction of the following diagrammatic representation borrowed from the theory of tensor networks [97]. The matrix elements of the local gate U and its complex conjugate are represented as

$$\langle kl|U|ij\rangle = \begin{array}{c} k \quad l \\ \diagdown \quad \diagup \\ \square \\ \diagup \quad \diagdown \\ i \quad j \end{array}, \quad \langle kl|U^*|ij\rangle = \begin{array}{c} k \quad l \\ \diagdown \quad \diagup \\ \square \\ \diagup \quad \diagdown \\ i \quad j \end{array}. \quad (29)$$

Matrix multiplication is represented connecting the legs of indices summed over and acts bottom to top. For example, the unitary conditions for U and \widetilde{U} (cf. Eq. (3)) are expressed as

$$\begin{array}{c} \begin{array}{c} \square \\ \diagdown \quad \diagup \\ \square \\ \diagup \quad \diagdown \\ \square \\ \diagdown \quad \diagup \\ \square \\ \diagup \quad \diagdown \end{array} = \begin{array}{c} \square \\ \diagdown \quad \diagup \\ \square \\ \diagup \quad \diagdown \\ \square \\ \diagdown \quad \diagup \\ \square \\ \diagup \quad \diagdown \end{array} = \begin{array}{c} | \\ | \\ | \\ | \end{array}, \\ \begin{array}{c} \square \\ \diagdown \quad \diagup \\ \square \\ \diagup \quad \diagdown \\ \square \\ \diagdown \quad \diagup \\ \square \\ \diagup \quad \diagdown \end{array} = \begin{array}{c} \square \\ \diagdown \quad \diagup \\ \square \\ \diagup \quad \diagdown \\ \square \\ \diagdown \quad \diagup \\ \square \\ \diagup \quad \diagdown \end{array} = \begin{array}{c} \square \\ \diagdown \quad \diagup \\ \square \\ \diagup \quad \diagdown \end{array}, \end{array} \quad (30)$$

where we removed the indices to represent the full matrix, rather than its elements. Also note that in the second line we rotated two of the diagrams to arrange them along a horizontal line.

Many body operators are obtained by composing the above building blocks via the above rules. For example, the time evolution operator in Eq. (1) for a system of $2L = 10$ qudits is represented as

$$U = \begin{array}{c} \square \\ \diagdown \quad \diagup \\ \square \\ \diagup \quad \diagdown \\ \square \\ \diagdown \quad \diagup \\ \square \\ \diagup \quad \diagdown \\ \square \\ \diagdown \quad \diagup \\ \square \\ \diagup \quad \diagdown \\ \square \\ \diagdown \quad \diagup \\ \square \\ \diagup \quad \diagdown \end{array}. \quad (31)$$

We also introduce the so called ‘‘folded representation’’, which helps representing multi-replica quantities needed, e.g., for entanglement calculations. To this end we introduce symbols for the replicated local gate

$$(U \otimes U^*)^{\otimes n} = \begin{array}{c} \square \\ \diagdown \quad \diagup \\ \square \\ \diagup \quad \diagdown \\ \square \\ \diagdown \quad \diagup \\ \square \\ \diagup \quad \diagdown \end{array} = \begin{array}{c} \square \\ \diagdown \quad \diagup \\ \square \\ \diagup \quad \diagdown \end{array}, \quad (32)$$

and the replicated solitons

$$\bigotimes_{i=1}^n (q_i^{(r)} \otimes \mathbf{1}_d) = \begin{array}{c} \bullet \\ \diagdown \quad \diagup \\ \square \\ \diagup \quad \diagdown \end{array}, \quad \bigotimes_{i=1}^n (q_i^{(\ell)} \otimes \mathbf{1}_d) = \begin{array}{c} \bullet \\ \diagdown \quad \diagup \\ \square \\ \diagup \quad \diagdown \end{array}, \quad (33)$$

where we used the symbol q_i for the soliton in each replica i as it can be any linear combination of the basis of Π_α (we will specify to what it refers in each case) and

we assumed to have in general different solitons on each replica (also this will be specified in each case).

To represent contractions between replicas it is useful to introduce symbols for two special states in the multi replica space. The first one is the ‘‘circle state’’

$$|\circ_{d,n}\rangle = \left(\sum_{i=1}^d |i, i\rangle \right)^{\otimes n} \equiv \text{---}\bigcirc. \quad (34)$$

The second one is the ‘‘square state’’ $|\square_{d,n}\rangle$. Labelling the $2n$ replicas as $(1, 1^*, 2, 2^*, \dots, n, n^*)$ we can represent it as

$$|\square_{d,n}\rangle = \bigotimes_{a=1}^n \left(\sum_{i=1}^d |i\rangle_a |i\rangle_{(a+1)^*} \right) \equiv \text{---}\square, \quad (35)$$

where the replica indexes are understood to be cyclic, so that $n+1 \equiv 1$.

In the folded representation the unitarity conditions for U and \tilde{U} are represented as

$$\begin{array}{c} \text{---}\bigcirc \text{---} \\ \text{---}\bigcirc \text{---} \end{array} = \begin{array}{c} \bigcirc \\ \bigcirc \end{array}, \quad \begin{array}{c} \text{---}\square \text{---} \\ \text{---}\square \text{---} \end{array} = \begin{array}{c} \square \\ \square \end{array}, \quad (36)$$

$$\begin{array}{c} \text{---}\bigcirc \text{---} \\ \text{---}\bigcirc \text{---} \end{array} = \begin{array}{c} \bigcirc \\ \bigcirc \end{array}, \quad \begin{array}{c} \text{---}\square \text{---} \\ \text{---}\square \text{---} \end{array} = \begin{array}{c} \square \\ \square \end{array}, \quad (37)$$

$$\begin{array}{c} \text{---}\bigcirc \text{---} \\ \text{---}\bigcirc \text{---} \end{array} = \begin{array}{c} \bigcirc \\ \bigcirc \end{array}, \quad \begin{array}{c} \text{---}\square \text{---} \\ \text{---}\square \text{---} \end{array} = \begin{array}{c} \square \\ \square \end{array}, \quad (38)$$

$$\begin{array}{c} \text{---}\bigcirc \text{---} \\ \text{---}\bigcirc \text{---} \end{array} = \begin{array}{c} \bigcirc \\ \bigcirc \end{array}, \quad \begin{array}{c} \text{---}\square \text{---} \\ \text{---}\square \text{---} \end{array} = \begin{array}{c} \square \\ \square \end{array}, \quad (39)$$

while, e.g., the soliton ballistic propagation can be expressed as

$$\begin{array}{c} \text{---}\bigcirc \text{---} \\ \text{---}\bigcirc \text{---} \end{array} = \begin{array}{c} \text{---}\bigcirc \text{---} \\ \text{---}\bigcirc \text{---} \end{array}, \quad \begin{array}{c} \text{---}\square \text{---} \\ \text{---}\square \text{---} \end{array} = \begin{array}{c} \text{---}\square \text{---} \\ \text{---}\square \text{---} \end{array}. \quad (40)$$

IV. CHARGED SOLVABLE STATES

A key concept in the study of the dynamics of dual-unitary circuits is that of *solvable* states [18, 19]. This is a class of non-equilibrium states compatible with the dual unitarity condition and allowing for exact calculations of dynamical properties. In particular, all solvable states can be shown to relax to the infinite temperature state [19]. Here we extend this concept to the case of $U(1)$ symmetric dual-unitary circuits. We show that, because of the block structure of the local gate (cf. Eq. (21)), one can introduce a larger family of solvable states, which we dub *charged solvable* states. In Sec. V we show that charged solvable states generically relax to non-trivial generalised Gibbs ensembles.

We begin by considering states in matrix product state (MPS) form, defined in terms of d^2 , $\chi \times \chi$ matrices $\mathcal{M}^{i,j}$ as

$$|\Psi_0(\mathcal{M})\rangle = \sum_{i_1, i_2, \dots, i_L=1}^d \text{tr} [\mathcal{M}^{i_1, i_2} \mathcal{M}^{i_2, i_3} \dots] |i_1, i_2, \dots, i_L\rangle. \quad (41)$$

The tensor generating the MPS has a convenient graphical representation

$$\text{---}\bigcirc \text{---} = (\mathcal{M} \otimes \mathcal{M}^*)^{\otimes n}, \quad (42)$$

where the thick line represents the replicated auxiliary space. It is useful to reshuffle the indices of $\mathcal{M}^{i,j}$ and view them as matrices $\Gamma_{\mathcal{M}}$ acting on $\mathbb{C}^d \otimes \mathbb{C}^{\chi}$ (whose input/output indices are the right/left legs of the tensor in Eq. (42))

$$\Gamma_{\mathcal{M}} = \sum_{i,j=1}^d |i\rangle\langle j| \otimes \mathcal{M}^{ij}, \quad (43)$$

and to define the transfer matrix of the MPS

$$\tau(\mathcal{M}) = \sum_{i,j} \mathcal{M}^{i,j} \otimes (\mathcal{M}^{i,j})^* = \text{---}\bigcirc \text{---}. \quad (44)$$

Having established the notation we are now in a position to introduce charged solvable states

Definition 1 (Charged Solvable States). *An MPS $|\Psi_0(\mathcal{M})\rangle$ is left charged solvable if the transfer matrix $\tau(\mathcal{M})$ (cf. Eq. (44)) has a unique maximal eigenvalue with absolute value 1 and there exists an operator S acting on the auxiliary space \mathbb{C}^{χ} such that*

$$\Gamma_{\mathcal{M}}^\dagger (\mathbb{1}_d \otimes S) \Gamma_{\mathcal{M}} = \sum_{\alpha} \frac{c_{\alpha}^{(r)}}{d_{\alpha}^{(r)}} \Pi_{\alpha}^{(r)} \otimes S, \quad (45)$$

where $d_{\alpha}^{(r)}$ is defined in Eq. (24) and we introduced the expectation value of a soliton

$$c_{\alpha}^{(r)} = \langle \Psi_0(\mathcal{M}) | (\Pi_{\alpha}^{(r)})_x | \Psi_0(\mathcal{M}) \rangle, \quad x \in \mathbb{Z}. \quad (46)$$

By definition we then have $c_{\alpha}^{(r)} \geq 0$ and $\sum_{\alpha} c_{\alpha}^{(r)} = 1$. Instead, $|\Psi_0(\mathcal{M})\rangle$ is right charged solvable if the transfer matrix has a unique maximal eigenvalue and there exists a S' such that

$$\Gamma_{\mathcal{M}} (\mathbb{1}_d \otimes S') \Gamma_{\mathcal{M}}^\dagger = \sum_{\alpha} \frac{c_{\alpha}^{(\ell)}}{d_{\alpha}^{(\ell)}} \Pi_{\alpha}^{(\ell)} \otimes S', \quad (47)$$

where

$$c_{\alpha}^{(\ell)} = \langle \Psi_0(\mathcal{M}) | (\Pi_{\alpha}^{(\ell)})_{x+1/2} | \Psi_0(\mathcal{M}) \rangle, \quad x \in \mathbb{Z}. \quad (48)$$

Finally, it is charged solvable if it is both left and right charged solvable.

Note that these definitions also imply that for left/right charged solvable states the left/right leading eigenvectors of $\tau(\mathcal{M})$ correspond to the matrices S and S' in Eqs. (45) and (47) upon matrix to vector mapping (cf. Appendix C 1)

$$\langle S| = \sum_{i,j=1}^d (S)_{i,j} \langle i, j|, \quad |S'\rangle = \sum_{i,j=1}^d (S')_{i,j} |i, j\rangle. \quad (49)$$

Recalling that two MPS states $|\Psi_0(\mathcal{M})\rangle, |\Psi_0(\mathcal{M}')\rangle$ are called *equivalent* if, for every local operator O_R (i.e. operator with a finite support)

$$\begin{aligned} & \lim_{L \rightarrow \infty} \langle \Psi_0(\mathcal{M}') | O_R | \Psi_0(\mathcal{M}') \rangle = \\ & = \lim_{L \rightarrow \infty} \langle \Psi_0(\mathcal{M}) | O_R | \Psi_0(\mathcal{M}) \rangle, \end{aligned} \quad (50)$$

we characterise charged solvable states by means of the following theorem (proven in Appendix C 1).

Theorem 2 (Equivalent MPS). *A left charged solvable MPS state is always equivalent, in the thermodynamic limit, to an MPS state \mathcal{M}' with bond dimension χ such that*

$$\Gamma_{\mathcal{M}'}^\dagger \Gamma_{\mathcal{M}'} = \sum_i \frac{c_\alpha^{(r)}}{d_\alpha^{(r)}} \Pi_\alpha^{(r)} \otimes \mathbb{1}_\chi, \quad (51)$$

whose unique maximal right eigenvector of the transfer matrix $\tau(\mathcal{M})$ is

$$|\mathcal{O}_{\chi,1}\rangle = \sum_{i=1}^\chi |i\rangle \otimes |i\rangle. \quad (52)$$

Analogously, a right charged solvable state is equivalent to an MPS such that

$$\Gamma_{\mathcal{M}'} \Gamma_{\mathcal{M}'}^\dagger = \sum_i \frac{c_\alpha^{(\ell)}}{d_\alpha^{(\ell)}} \Pi_\alpha^{(\ell)} \otimes \mathbb{1}_\chi, \quad (53)$$

whose transfer matrix has unique maximal left eigenvector

$$\langle \mathcal{O}_{\chi,1}| = \sum_{i=1}^\chi \langle i| \otimes \langle i|. \quad (54)$$

In essence, Theorem (2) guarantees that one can always replace left/right charged solvable states with equivalent MPS where the matrix S in Definition 1 is the identity.

The equivalent MPS states of Theorem 2 can be further characterised by specialising the local basis of the quantum circuit. To show this we consider the singular value superposition of $\Gamma_{\mathcal{M}}$, i.e. $\Gamma_{\mathcal{M}} = VDW$, and rewrite condition for left charged solvability (51) as

$$\Gamma_{\mathcal{M}}^\dagger \Gamma_{\mathcal{M}} = W D^2 W^\dagger = \sum_i \frac{c_\alpha^{(r)}}{d_\alpha^{(r)}} \Pi_\alpha^{(r)} \otimes \mathbb{1}_\chi. \quad (55)$$

The matrix D^2 is diagonal by construction, and its spectrum needs to match the one of the matrix on the right (the unitary W cannot alter the spectrum). If we choose a basis for each qudit such that all projectors $\Pi_\alpha^{(r)/(\ell)}$ are diagonal (always possible as they commute), we have that the right hand side of Eq. (55) is also diagonal. In this case, upon reordering of the basis, we can take D^2 to be equal to the righthand side. With these choices we find

$$W \sum_\alpha \frac{c_\alpha^{(r)}}{d_\alpha^{(r)}} \Pi_\alpha^{(r)} \otimes \mathbb{1}_\chi W^\dagger = \sum_\alpha \frac{c_\alpha^{(r)}}{d_\alpha^{(r)}} \Pi_\alpha^{(r)} \otimes \mathbb{1}_\chi, \quad (56)$$

so we can move W past D in the SVD of $\Gamma_{\mathcal{M}}$ and include it in the definition of V . This means that most generic $\Gamma_{\mathcal{M}}$ representing a left- solvable state can be written as

$$\Gamma_{\mathcal{M}} = \sum_\alpha \sqrt{\frac{c_\alpha^{(r)}}{d_\alpha^{(r)}}} V \left(\Pi_\alpha^{(r)} \otimes \mathbb{1}_\chi \right), \quad V \in U(\chi \cdot d), \quad (57)$$

and an analogous discussion holds for right charged solvable states. Finally, using this characterisation, in Appendix C 2 we prove the following compatibility condition for charged solvable states

Theorem 3 (Compatibility Condition). *Given the bases for left and right solitons*

$$\mathcal{S}^{(r)} = \{\Pi_\alpha^{(r)}\}_{\alpha=1,\dots,m_r}, \quad \mathcal{S}^{(\ell)} = \{\Pi_\alpha^{(\ell)}\}_{\alpha=1,\dots,m_\ell}, \quad (58)$$

and a charged solvable state fulfilling Eqs. (45)-(47), than there exists a partition $\mathcal{P}^{(r)} = \{\mathcal{P}_1^{(r)}, \dots, \mathcal{P}_{k'}^{(r)}\}$ of $\{1, \dots, m_r\}$ and $\mathcal{P}^{(\ell)} = \{\mathcal{P}_1^{(\ell)}, \dots, \mathcal{P}_{k''}^{(\ell)}\}$ of $\{1, \dots, m_\ell\}$, such that $k' = k'' = k$ and for all $i = 1, \dots, k$ we have

$$\begin{aligned} \sum_{\alpha \in \mathcal{P}_i^{(r)}} d_\alpha^{(r)} &= \sum_{\beta \in \mathcal{P}_i^{(\ell)}} d_\beta^{(\ell)} \equiv d_i \\ \frac{c_\alpha^{(r)}}{d_\alpha^{(r)}} &= \frac{c_\beta^{(\ell)}}{d_\beta^{(\ell)}} \equiv \frac{c_i}{d_i}, \quad \forall \alpha \in \mathcal{P}_i^{(r)}, \beta \in \mathcal{P}_i^{(\ell)}. \end{aligned} \quad (59)$$

Moreover, the left/right fixed points of $\tau(\mathcal{M})$ can be taken to be $|\mathcal{O}_{\chi,1}\rangle, \langle S|$, where S is a strictly positive matrix.

The essence of this theorem is that to have a state that is charged solvable both directions, there must be a compatible blocking structure for solitons moving left and right. Namely, the two matrices

$$\sum_\alpha \frac{c_\alpha^{(r)}}{d_\alpha^{(r)}} \Pi_\alpha^{(r)}, \quad \sum_\alpha \frac{c_\alpha^{(\ell)}}{d_\alpha^{(\ell)}} \Pi_\alpha^{(\ell)}, \quad (60)$$

should have the same spectrum. Moreover, in contrast to what happens for the standard solvability condition (cf. Ref. [19]), it is generically not possible to choose an equivalent MPS such that *both* left and right eigenvectors of $\tau(\mathcal{M})$ are the (vectorised) identity matrix.

Note that the compatibility condition is relatively easy to achieve for gates that have the same dimension for every charge subspace (which also means that they have the same number of left- and right-moving solitons), i.e. $d_\alpha^{(r)} = d_\alpha^{(\ell)} = d/m_r = d/m_\ell$. In this case one just needs to match each right-moving charge with a left-moving one. We also remark that the charged solvable states according to the trivial partitions $\mathcal{P}^{(r)} = \{\{1, \dots, m_r\}\}$ and $\mathcal{P}^{(\ell)} = \{\{1, \dots, m_\ell\}\}$ (i.e. partitions with a single element corresponding to the full set) are those without a charge structure, and correspond to the standard solvable states. In this particular case, it can be shown that the fixed point of the transfer matrix on both sides can be taken to be $|\mathcal{O}_{\chi,1}\rangle$ [19].

V. ENTANGLEMENT DYNAMICS FROM CHARGED SOLVABLE STATES

In this section, we consider the entanglement dynamics after a quantum quench from a charged solvable state. Specifically, we characterise the growth of entanglement between a subsystem A , composed by $2L_A$ contiguous qudits, and the rest of the system by computing the Rényi

entropies

$$S_A^{(n)}(t) = \frac{1}{1-n} \log \text{tr} [\rho_A^n(t)], \quad n \in \mathbb{N}, \quad (61)$$

where $\rho_A^n(t)$ is the state of A at time t . Note that $\lim_{n \rightarrow 1} S_A^{(n)}(t) = S_A(t)$ where $S_A(t)$ is the standard entanglement entropy.

We split the calculation in two steps: In Sec. V A we consider the early time regime $t < L_A/2$ while in Sec. V B the late time regime $t \geq L_A/2$.

A. Early-time Regime

Let us begin considering the early time regime, i.e., we restrict to times $t < L_A/2$. In this regime the two edges of A are causally disconnected (the speed of light is one in our units) and entanglement is generated independently at both edges with equal rate. The contribution of the two edges, however, cannot be completely separated as the initial MPS can encode non-trivial correlations.

Specifically, the diagram giving the n -th moment of the reduced density matrix reads as

$$\begin{aligned} \text{tr} [\rho_A^n(t \leq L_A/2)] &= \text{Diagram 1} \\ &= \text{Diagram 2} \end{aligned} \quad (62)$$

where, in going from the first to the second line, we repeatedly used the unitarity conditions in Eqs. (36) and (38).

To proceed, we note that on the left of this diagram we have $L - 2t - L_A$ powers of the MPS transfer matrix $\tau(\mathcal{M})$ (cf. Eq. (44)) replicated n times, i.e.,

$$(\tau(\mathcal{M})^{\otimes n})^{L-2t-L_A}. \quad (63)$$

As we now show this allows us to compute the thermodynamic limit value of this diagram whenever the initial MPS is charged solvable.

By definition, a charged solvable MPS has a transfer matrix $\tau(\mathcal{M})$ with unique fixed points given by $|S\rangle$ and $\langle \mathcal{O}_{\chi,1}|$ (cf. Definition 1), Eq. (49), and Theorem 2), where we choose the left fixed point to be the identity. This means that

$$\lim_{L \rightarrow \infty} \left(\text{Diagram 3} \right)^{L-2t-L_A} = \text{Diagram 4} \quad (64)$$

where the black circle denotes

$$\text{Diagram 4} = \prod_{a=1}^n \left[\sum_{i,j=1}^d (S)_{i,j} |i\rangle_a |j\rangle_{(a)^*} \right]. \quad (65)$$

It is then immediate to see that, in the thermodynamic limit, the diagram in Eq. (62) is reduced to the following

(66)

This diagram can be fully contracted using the charged solvability conditions (51) and (47). Indeed the latter implies the following diagrammatic relations for the replicated state

(67)

(68)

where the solitons represented in red/blue correspond to the following linear combination of projectors

$$\left(\sum_{\alpha=1}^{m_r/\ell} \frac{c_{\alpha}^{(r)/(\ell)}}{d_{\alpha}^{(r)/(\ell)}} \Pi_{\alpha}^{(r)/(\ell)} \right). \quad (69)$$

We can move each soliton to the top, using (40), obtaining

(70)

and then use dual unitarity 37 to simplify both outer diagonals of gates, and reiterate the procedure until the triangle at both edges are fully simplified. The final result reads as

$$\text{tr} [\rho_A^n(t)] = \left(\sum_{\alpha} \frac{c_{\alpha}^{(r)n}}{d_{\alpha}^{(r)n-1}} \right)^{4t} \Xi_n(L_A - 2t), \quad (71)$$

where the extra contribution $\Xi_n(x)$ comes from the initial MPS entanglement, and $\ln(\Xi_n(x))/(1-n)$ can be thought as the Renyi entropy, on the initial state, of an interval including $2x$ sites. Namely, it is written as

(72)

Noting that this term is $o(t^0)$ we then have

$$S_A^{(n)}(t) = \frac{4t}{1-n} \log \left(\sum_{i=1}^k \frac{c_i^n}{d_i^{n-1}} \right) + o(t), \quad (73)$$

where we used the block matching condition in Eq. (59) to eliminate the labels ℓ/r from c_i and d_i (and k is defined above Eq. (59)). Indeed, using the latter condition one

has

$$\begin{aligned} \sum_{\alpha} \frac{c_{\alpha}^{(r)n}}{d_{\alpha}^{(r)n-1}} &= \sum_{i=1}^k \sum_{\alpha \in P_i^{(r)}} \frac{c_{\alpha}^{(r)n}}{d_{\alpha}^{(r)n-1}} = \sum_{i=1}^k \frac{c_i^n}{d_i^n} \sum_{\alpha \in P_i^{(r)}} d_{\alpha} \\ &= \sum_{i=1}^k \frac{c_i^n}{d_i^{n-1}} = \sum_{\alpha} \frac{c_{\alpha}^{(\ell)n}}{d_{\alpha}^{(\ell)n-1}}. \end{aligned} \quad (74)$$

In particular, in the limit $n \rightarrow 1$ we obtain

$$S_A(t) = 4t(s_{\text{num}} + s_{\text{conf}}) + o(t), \quad (75)$$

where introduced the quantities

$$s_{\text{num}} \equiv - \sum_{i=1}^k c_i \log(c_i), \quad s_{\text{conf}} \equiv \sum_{i=1}^k c_i \log(d_i), \quad (76)$$

whose physical meaning will become clear in the upcoming subsection.

B. Late-time Regime

We now consider times $t \geq L_A/2$. In this regime, after taking the thermodynamic limit, the reduced density

matrix $\rho_A(t)$ has the following graphical representation

$$\rho_A(t) = \text{Diagram} \quad (77)$$

Making now repeated use of the charged solvability conditions in Eqs. (67) and (68), the soliton relation (40) (to move solitons at the top open legs) and dual unitarity in Eq. (37), this diagram can be simplified as follows

$$\rho_A(t) = \text{Diagram} = \text{Diagram} \quad (78)$$

where in the second step we used the unitarity condition in Eq. (40) to fully simplify the diagram. Note that this can only be done if the dashed red line in (78) does not cross the bottom line of initial states, that is for $t \geq L_A/2$. Using the simplified form in Eq. (78), we can write explicit expressions for all Renyi entropies of A . The result reads as

$$S_A^{(n)}(t) = \frac{2L_A}{1-n} \log \left(\sum_{i=1}^k \frac{(c_i)^n}{(d_i)^{n-1}} \right). \quad (79)$$

In the limit $n \rightarrow 1$ the result can be written as

$$S_A(t) = 2L_A(s_{\text{num}} + s_{\text{conf}}), \quad (80)$$

where s_{num} and s_{conf} are defined in Eq. (76). To unveil the physical meaning of these quantities we introduce configurational, $S_{\text{conf}}(t)$, and number, $S_{\text{num}}(t)$, entropies defined as [88–90]

$$\begin{aligned} S_{\text{conf}}(t) &\equiv - \sum_{\alpha, \beta} p_{\alpha, \beta}(t) (\rho_{A, \alpha, \beta}(t) \log \rho_{A, \alpha, \beta}(t)), \\ S_{\text{num}}(t) &\equiv - \sum_{\alpha, \beta} p_{\alpha, \beta}(t) \log p_{\alpha, \beta}(t), \end{aligned} \quad (81)$$

where we introduced the state reduced to a symmetry block

$$\begin{aligned} \rho_{A, \alpha, \beta}(t) &\equiv \frac{\Pi_{\alpha}^{(r)} \Pi_{\beta}^{(\ell)} \rho_A(t) \Pi_{\alpha}^{(r)} \Pi_{\beta}^{(\ell)}}{p_{\alpha, \beta}(t)}, \\ p_{\alpha, \beta}(t) &\equiv \text{tr} \left[\Pi_{\alpha}^{(r)} \Pi_{\beta}^{(\ell)} \rho_A(t) \Pi_{\alpha}^{(r)} \Pi_{\beta}^{(\ell)} \right], \end{aligned} \quad (82)$$

with the projectors in the charge sector with $\alpha = (\alpha_1, \dots, \alpha_{m_r})$ right moving solitons and $\beta = (\beta_1, \dots, \beta_{m_\ell})$ left moving solitons defined as

$$\Pi_{\alpha}^{(r)} = \bigotimes_{i=1}^{L_A} \Pi_{\alpha_i}^{(r)} \otimes \mathbb{1}_d, \quad \Pi_{\beta}^{(\ell)} = \mathbb{1}_d \otimes \bigotimes_{i=1}^{L_A} \Pi_{\beta_i}^{(\ell)}. \quad (83)$$

From their definition, we see that $S_{\text{conf}}(t)$ measures the average of the entanglement in the charge sectors, while $S_{\text{num}}(t)$ the fluctuations of the charge [88–90]. Using Eq. (78) one can readily show

$$S_{\text{conf}}(\infty) = 2L_A s_{\text{conf}}, \quad S_{\text{num}}(\infty) = 2L_A s_{\text{num}}. \quad (84)$$

Therefore we see that s_{num} and s_{conf} are respectively the densities of number and configurational entropy in the stationary state.

Two comments are in order at this point. First, we see that in our case the number entropy is extensive, as opposed to the $\log L_A$ scaling that it displays in the generic situation [52, 90]. This is because in our setting the number of non-trivial charge sectors is exponentially large in L_A , which should be contrasted with the polynomial scaling of the number of charge sectors with L_A that one has in the generic case. Second, even though Eqs. (80) and (84) imply that the entanglement entropy at infinite times is the sum of number and configurational entropy, this does not mean that such a decomposition holds for all times. Indeed, from Eq. (75) one generically has

$$S_A(t) \geq S_{\text{conf}}(t) + S_{\text{num}}(t). \quad (85)$$

The equality holds only if the initial state is an eigenstate of all the charges.

VI. ENTANGLEMENT DYNAMICS FROM NON-CHARGED-SOLVABLE STATES

In this section we look again at the entanglement dynamics after a quench from an MPS state but, crucially, we lift the assumption of full charged solvability. Interestingly, we find that in this case the dynamics of entanglement shows a qualitative change: while it agrees with the charged solvable state result in the early time regime, it does not show immediate saturation for $t \geq L_A/2$. Instead, it continues to grow with a different slope set by the value of the number entropy.

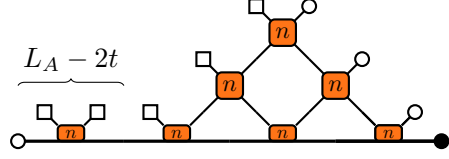
To deal with the great complication of characterising the growth of entanglement without any form of solvability we attack the problem in a gradual fashion. First, we lift charged solvability only on one side. In this case the phenomenology described above can be rigorously shown under a genericity assumption on the blocks $U^{(\alpha, \beta)}$ in Eq. (21). Then, we move to consider fully generic initial states and adapt the entanglement membrane approach [91, 92] to argue that the above features are stable.

A. Entanglement dynamics from left charged solvable states

Here we consider the entanglement dynamics from MPS states (41) that are solvable only on one side: for definiteness we choose left solvability.

In the early time regime, partial solvability means that the diagram in Eq. (66) can be simplified only partially. Specifically, using Eq. (67) and the dual unitarity condi-

tion in Eq. (37) we can simplify the left triangle representing entanglement growth at the left edge of the interval, obtaining


(86)

Although this diagram cannot be further simplified for finite L_A and t , a simplification emerges in the scaling limit

$$L_A, t \rightarrow \infty, \quad \frac{t}{L_A} = \zeta < \frac{1}{2}. \quad (87)$$

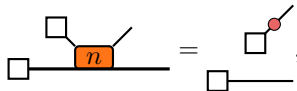
Indeed, in this limit the horizontal line of replicated transfer matrices in (86) (which are $L_A - 2t$) becomes a projector on the fixed points, i.e.,

$$\lim_{L \rightarrow \infty} \left(\text{---} \begin{array}{c} \square \quad \square \\ | \quad | \\ \text{---} \text{---} \\ | \quad | \\ \square \quad \square \end{array} \text{---} \right)^{L_A - 2t} = \text{---} \blacksquare \text{---} \square \text{---}, \quad (88)$$

where we introduced the replicated fixed point

$$\text{---} \blacksquare \text{---} = \prod_{a=1}^n \left[\sum_{i,j=1}^d (S)_{i,j} |i\rangle_a |j\rangle_{(a+1)^*} \right]. \quad (89)$$

Eq. (88) allows us to eliminate the line of transfer matrices and contract the remaining part of the diagram by means of the following multireplica version of the left charged solvability condition


(90)

which involves a different pairing of replicas compared to Eq. (67). The final result reads as

$$\text{tr}[\rho_A^n(t)] \simeq \left(\sum_{\alpha} \frac{(c_{\alpha}^{(r)})^n}{(d_{\alpha}^{(r)})^{n-1}} \right)^{4t} \text{tr}[S^n]^2, \quad (91)$$

where \simeq denotes leading order in the scaling limit and the last term comes from the scalar product of the fixed points of replicated transfer matrices with different pairings, i.e.,

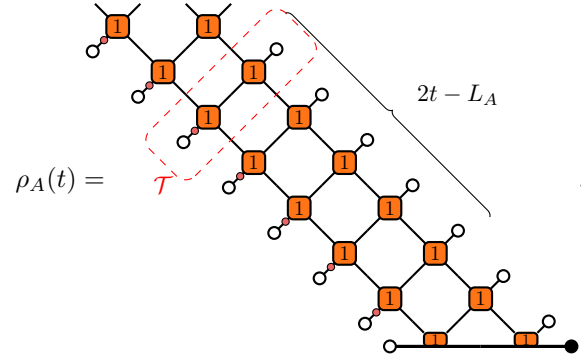
$$\text{---} \circ \text{---} \blacksquare \text{---} = \text{tr}[S^n]. \quad (92)$$

Eq. (91) coincides with the scaling limit of Eq. (73). Therefore, at leading order, lifting solvability on one side

leads to the same entanglement growth in the early time regime, and can be written as

$$S(t \leq L_A/2) = 4t(s_{\text{num}}^{(r)} + s_{\text{conf}}^{(r)}) \equiv 4ts^{(r)}, \quad (93)$$

where $s_{\text{num}/\text{conf}}^{(r)}$ are defined as in (76), using the $c_{\alpha}^{(r)}$ that define left solvability in (45) instead of c_i . As we now show, beyond this regime we instead have qualitative differences. Let us begin considering the infinite time limit. The relevant diagram in this case is the one in Eq. (77). Once again, for left charged solvable states the latter can be simplified only partially and the minimal expression reads as


(94)

We now note that this diagram contains $2t - L_A$ transfer matrices \mathcal{T} as the one circled in red. Therefore, the large time limit can be computed by replacing \mathcal{T} with a projector on its leading eigenvectors, which can be proven to correspond to eigenvalues of unit magnitude (see Appendix D 1). As we discuss in Appendix D 1, these eigenvectors are in one-to-one correspondence with the conserved, ballistic charges in the circuit so, under the assumption of starting with a complete set of solitons, we can find all of them.

From now on we assume this to be the case, namely, we assume that the circuit has no independent conserved-charge densities of support $\ell > 1$: all charges with densities of larger support are written as products of solitons on different sites. In essence, this is a chaoticity assumption for the blocks $U^{(\alpha,\beta)}$ in Eq. (21): for generic blocks there should be no independent conserved charges apart from those enforced by the block structure. Note

that the proof in Ref. [98] guarantees that whenever $d_\alpha^{(r)} = d_\beta^{(\ell)} = 2$ any randomly selected dual unitary block fulfils this assumption with probability one.

Under this assumption, the large time limit is obtained by the following substitution

The diagram shows a unitary block (a square with four legs) being replaced by a sum over strings of solitons. The solitons are represented by circles with legs, some of which are connected to form strings. The equation is:
$$\text{Unitary Block} \rightarrow \sum_{\alpha} \frac{1}{d_{\alpha_1}^{(\ell)} d_{\alpha_2}^{(\ell)} \dots}, \quad (95)$$

where the sum is all over the strings $\{\alpha_1^{(\ell)}, \dots, \alpha_{L_A}^{(\ell)}\}$ with $\alpha_i^{(\ell)} = 1, \dots, m_\ell$, and m_ℓ being the number of left moving solitons. Plugging this form into Eq. (94) we then obtain

The diagram shows a horizontal line representing a system. On the left, there are several solitons (circles with legs) moving towards the right. On the right, there are several solitons moving towards the left. The equation is:
$$\rho_A(\infty) = \sum_{\alpha} \text{Diagram} \quad (96)$$

Note that the sum in this expression is over left-moving solitons and, therefore, this state has correlations only between its odd sites. This means that, unlike the one in Eq. (78), the GGE in Eq. (96) has non-zero chemical potentials also for left moving charges of larger support (which are built using solitons).

In order to handle explicit an expression we focus on the case $\chi = 1$, in order to force these charges of larger support to have 0 expectation value also in this case. Defining $c_\alpha^{(\ell)}/c_\alpha^{(r)}$ as the expectation value of the 1-site left/right moving solitons $\Pi_\alpha^{(\ell)/(r)}$ (notice that this definition agrees with Eq. (51)), we can fully characterize the asymptotic thermal ensemble and write the asymptotic value of the entanglement entropy as

$$S_A(\infty) \simeq L_A(s^{(\ell)} + s^{(r)}), \quad (97)$$

where we introduced

$$s_n^{(\ell/r)} = \frac{1}{1-n} \log \left(\sum_{\alpha=1}^{m_{\ell/r}} \frac{(c_\alpha^{(\ell/r)})^n}{(d_\alpha^{(\ell/r)})^{n-1}} \right), \quad (98)$$

and set $s_1^{(\ell/r)} = s^{(\ell/r)}$. This expression has a very interesting implication: we first note that Eq. (97) does not coincide with the value reached at the end of the early time regime. Indeed, considering Eq. (93) we find

$$S_A(L_A/2) \simeq 2L_A s^{(r)}. \quad (99)$$

Next we note that whenever the state is left charged solvable one has $s_n^{(\ell)} \geq s_n^{(r)}$ (cf. Appendix D 2). This means that Eq. (97) is always *larger* than Eq. (99) and *there must be an additional phase of growth after the early time regime*. This is true also without the $\chi = 1$ assumption

on the MPS: In Appendix D 2 we show that, even though we cannot find an explicit expression for $S^{(\ell)}$ in terms of few parameters we have

$$S^{(\ell)} \geq L_A s^{(r)}, \quad (100)$$

showing the existence of an additional growth phase.

To characterise this second phase we use the following rigorous bound (proven in Appendix D 3 using the data processing inequality)

$$S_A(t > L_A/2) - S_A(L_A/2) \leq (2t - L_A)(2s^{(r)} - s_{\text{num}}^{(r)}). \quad (101)$$

This ensures that, whenever the number entropy density is non-zero, the slope of entanglement growth in the second phase is smaller than the initial one (which is equal to $2s^{(r)}$) and we have a qualitatively different phase of thermalisation. Note that Eq. (101) also gives the following lower bound for the thermalisation time

$$t_{\text{th}} \geq \frac{L_A}{2} \left(\frac{(s^{(\ell)} + s^{(r)} - s_{\text{num}}^{(r)})/2}{s^{(r)} - (s_{\text{num}}^{(r)}/2)} \right), \quad (102)$$

obtained imposing the r.h.s. of the inequality in Eq. (101) to be smaller than $S_A(\infty) - S_A(L_A/2)$.

In the upcoming subsection we use the entanglement membrane picture to argue that the bound in Eq. (101) is in fact saturated at leading order in the scaling limit, justifying our expression for the entanglement velocity at times $t > L_A$ (135).

B. Entanglement dynamics from generic states

Let us now move to initial states with no solvability properties. To treat the problem, we decompose the relevant quantities as sums over the charge sectors and treat each of the sectors using the entanglement membrane picture [91, 92]. This amounts to assuming that the reduced blocks $U^{(\alpha, \beta)}$ (cf. Eq. (21)) are chaotic.

In order for this approach to be valid, we request that the dimension of each charge block is $d_\alpha^{(\ell/r)} \geq 2$ (the membrane picture cannot be applied if the local dimension is one).

For the sake of simplicity, we consider a simple initial state: a normalised pair product state (a special case of the MPS in Eq. (41) with bond dimension 1), defined by a $d \times d$ matrix m

$$|\Psi_0\rangle = \left(\sum_{i,j=1}^d (m)_{i,j} |i, j\rangle \right)^{\otimes L} \quad \text{tr} [mm^\dagger] = 1, \quad (103)$$

where $2L$ is the number of sites of the system (which we always take to be arbitrarily large as to ignore boundary effects).

The graphical representation we use for the matrix m (in the replicated space) is

$$(m \otimes m^*)^{\otimes n} = \text{---} \blacksquare \text{---} . \quad (104)$$

The expectation values $c_\alpha^{(\ell/r)}$ are then given by

$$\begin{aligned} c_\alpha^{(r)} &= \text{tr} \left[m \Pi_\alpha^{(r)} m^\dagger \right] = \text{---} \text{O} \blacksquare \text{---} \text{O} \\ c_\alpha^{(\ell)} &= \text{tr} \left[\Pi_\alpha^{(\ell)} m m^\dagger \right] = \text{---} \text{O} \blacksquare \text{---} \text{O} . \end{aligned} \quad (105)$$

and obey

$$c_\alpha^{(\ell/r)} \geq 0 \quad \sum_\alpha c_\alpha^{(\ell/r)} = 1. \quad (106)$$

The above properties allow us to interpret $\{c_\alpha^{(\ell/r)}\}$ as a classical probability distribution on a single pair of initial state. By defining the probability $p(\alpha, \beta) \equiv c_{\alpha, \beta}$ of measuring simultaneously on a pair of initial state left/right solitons

$$c_{\alpha, \beta} \equiv \text{tr} \left[\Pi_\alpha^{(\ell)} m \Pi_\beta^{(r)} m^\dagger \right] = \text{---} \text{O} \blacksquare \text{---} \text{O} , \quad (107)$$

then $c_\alpha^{(\ell/r)}$ can be interpreted as the marginals of this distribution, i.e.

$$c_\beta^{(r)} = \sum_{\alpha=1}^{m_\ell} c_{\alpha, \beta}, \quad c_\alpha^{(\ell)} = \sum_{\beta=1}^{m_r} c_{\alpha, \beta}. \quad (108)$$

1. Early time growth

The rate of entanglement production at early times ($t < L_A/2$) can be found by evaluating the diagram in Eq. (66). In fact, since we are now focussing on pair product states, the contributions at the two edges factorise and we are left to evaluate

$$\text{tr}_A [\rho_A^n(t)] = \left(\text{---} \begin{array}{c} \text{---} \text{O} \blacksquare \text{---} \text{O} \\ \text{---} \text{O} \blacksquare \text{---} \text{O} \\ \text{---} \text{O} \blacksquare \text{---} \text{O} \\ \text{---} \text{O} \blacksquare \text{---} \text{O} \\ \text{---} \text{O} \blacksquare \text{---} \text{O} \\ \text{---} \text{O} \blacksquare \text{---} \text{O} \end{array} \text{---} \right)^{2t} . \quad (109)$$

We then decompose the $2t$ legs on the left of this diagram using the following resolution of the identity

$$(\mathbb{1}_{n \times d})^{\otimes 2t} = \sum_\alpha \bigotimes_{i=1}^{2t} \left[\bigotimes_{a=1}^n \left(\Pi_{\alpha_{i,a}}^{(\ell)} \otimes \mathbb{1}_d \right) \right]. \quad (110)$$

Analogously, for the $2t$ legs on the right diagonal we have

$$(\mathbb{1}_{n \times d})^{\otimes 2t} = \sum_\alpha \bigotimes_{i=1}^{2t} \left[\bigotimes_{a=1}^n \left(\Pi_{\alpha_{i,a}}^{(r)} \otimes \mathbb{1}_d \right) \right]. \quad (111)$$

The sum is over all possible strings of α s of size $2tn$, since in general we need a different projector on each replica.

In diagrams we then rewrite the square root of Eq. (109) as

$$\sqrt{\text{tr}_A [\rho_A^n(t)]} = \sum_{\alpha, \beta} \text{---} \begin{array}{c} \text{---} \text{O} \blacksquare \text{---} \text{O} \\ \text{---} \text{O} \blacksquare \text{---} \text{O} \\ \text{---} \text{O} \blacksquare \text{---} \text{O} \\ \text{---} \text{O} \blacksquare \text{---} \text{O} \\ \text{---} \text{O} \blacksquare \text{---} \text{O} \\ \text{---} \text{O} \blacksquare \text{---} \text{O} \end{array} \text{---} = \quad (112)$$

$$\sum_{\alpha, \beta} \text{---} \begin{array}{c} \text{---} \text{O} \blacksquare \text{---} \text{O} \\ \text{---} \text{O} \blacksquare \text{---} \text{O} \\ \text{---} \text{O} \blacksquare \text{---} \text{O} \\ \text{---} \text{O} \blacksquare \text{---} \text{O} \\ \text{---} \text{O} \blacksquare \text{---} \text{O} \\ \text{---} \text{O} \blacksquare \text{---} \text{O} \end{array} \text{---} , \quad (113)$$

where, to go from (112) to (113) we used the fact that the solitons in the diagram are projectors, thus they obey

$$\left(\Pi_\alpha^{(\ell/r)} \right)^m = \Pi_\alpha^{(\ell/r)} \quad (114)$$

and then we used the ballistic property (40) to move them around in the diagram showing explicitly that each gate is in a chaotic block. Keeping fixed the values of α, β so that each local gate is now chaotic we are enabled to apply the entanglement membrane theory [91, 92]. The upshot of this approach is to argue that the leading contribution to the diagram is found when the internal legs are divided in two domains; in one domain the internal legs are all set to the state $|\text{O}_{d,n}\rangle$ and in the other to the state $|\text{□}_{d,n}\rangle$.

To find the leading contribution we then consider all possible separations between the two domains that start at the top of the triangle and end at position x , and then sum over the possible values of x . Thanks to dual unitarity, all paths separating the domains that start at the top and end at x , which are causally connected with the top and bottom point are equivalent (indeed the line tension for a dual unitary circuit is constant) and correspond to only one diagram, so the result does not depend on the path chosen. Projecting the internal legs on the two different domains, the diagram becomes the following:

$$\sqrt{\text{tr}_A [\rho_A^n(t)]} = \sum_{\alpha, \beta, x} \frac{1}{\mathcal{N}_{\alpha, \beta}} \quad (115)$$

where the normalisation factor $\mathcal{N}_{\alpha, \beta}$ comes from the fact that the states $|\circ_{d,n}\rangle$ and $|\square_{d,n}\rangle$ are not normalised (cf. Eqs. (34) and (35)).

To evaluate the diagram, we begin by noting that the matrix element of a replicated projector between a bullet and a square state is only non-zero if the components on each replica are the same, i.e.,

$$\begin{aligned} \circ \square &= \text{tr} \left[\Pi_{\alpha_{i,1}}^{(r)} \Pi_{\alpha_{i,2}}^{(r)} \dots \Pi_{\alpha_{i,n}}^{(r)} \right] \\ &= d_{\alpha_i}^{(r)} (\delta_{\alpha_i, \alpha_{i,1}} \dots \delta_{\alpha_i, \alpha_{i,n}}). \end{aligned} \quad (116)$$

Looking at Eq. (115) we see that this observation applies to the first x right moving legs and the last $2t-x$ left moving legs (the ones encircled in respectively red and blue dashed lines). Therefore, it is convenient to write the string $\alpha = \alpha^{(2)} \circ \alpha^{(1)}$, where $\alpha^{(1)}$ and $\alpha^{(2)}$ are respectively of sizes $2t-x$ and x . The first has the same entries on each replica layer. Similarly, we write $\beta = \beta^{(1)} \circ \beta^{(2)}$, where $\beta^{(1)}$ has size x and the same entries on each replica layer. In this language we can write the normalisation factor as

$$\mathcal{N}_{\alpha, \beta} = \left(\prod_{i=1}^x d_{\alpha_i}^{(r)} \prod_{j=1}^{2t-x} d_{\beta_j}^{(\ell)} \right)^n. \quad (117)$$

We now proceed to evaluate the diagram (115) using Eqs. (40), (36), and (38) to simplify all the gates. In particular, using the definitions in Eqs. (107), (108) we

find

$$\begin{aligned} \sqrt{\text{tr}_A [\rho_A^n(t)]} &= \sum_{\substack{x, \\ \alpha^{(1)}, \beta^{(1)} \\ \alpha^{(2)}, \beta^{(2)}}} \prod_{i=1}^x \prod_{a=1}^n \frac{c_{\alpha_{i,a}}^{(2)} \beta_i^{(1)}}{d_{\beta_i}^{(r) n-1}} \prod_{j=1}^{2t-x} \prod_{a=1}^n \frac{c_{\alpha_j}^{(1)} \beta_{j,a}^{(2)}}{d_{\alpha_j}^{(r) n-1}} \\ &= \sum_{\alpha^{(1)}, \beta^{(1)}} \prod_{i=1}^x \frac{c_{\beta_i}^{(r) n}}{d_{\beta_i}^{(r) n-1}} \prod_{j=1}^{2t-x} \frac{c_{\alpha_j}^{(\ell) n}}{d_{\alpha_j}^{(\ell) n-1}} \\ &= \sum_x \left(\sum_{\alpha} \frac{c_{\alpha}^{(r) n}}{d_{\alpha}^{(r) n-1}} \right)^{2t-x} \left(\sum_{\beta} \frac{c_{\beta}^{(\ell) n}}{d_{\beta}^{(\ell) n-1}} \right)^x. \end{aligned} \quad (118)$$

The remaining sum over x is a geometric sum and can be evaluated explicitly. Ignoring $o(1)$ factors, we can write the final result as

$$\sqrt{\text{tr}_A [\rho_A^n(t)]} = \exp \left(t(1-n) \min(s_n^{(r)}, s_n^{(\ell)}) \right), \quad (119)$$

where we introduced

$$s_n^{(\ell/r)} = \frac{1}{1-n} \log \left(\sum_{\alpha} \frac{c_{\alpha}^{(\ell/r) n}}{d_{\alpha}^{(\ell/r) n-1}} \right). \quad (120)$$

Putting all together this finally gives

$$S_A^{(n)}(t < L_A/2) = 4t \min(s_n^{(r)}, s_n^{(\ell)}). \quad (121)$$

This result is consistent with Eq. (91), as one can see recalling that for a left charged solvable state $s_n^{(r)} \leq s_n^{(\ell)}$ (cf. App. D2) and can be analytically continued to all values of n , in particular $n=1$ [103]. In fact, Eq. (121) can also be tested numerically. For instance, in Fig. 3

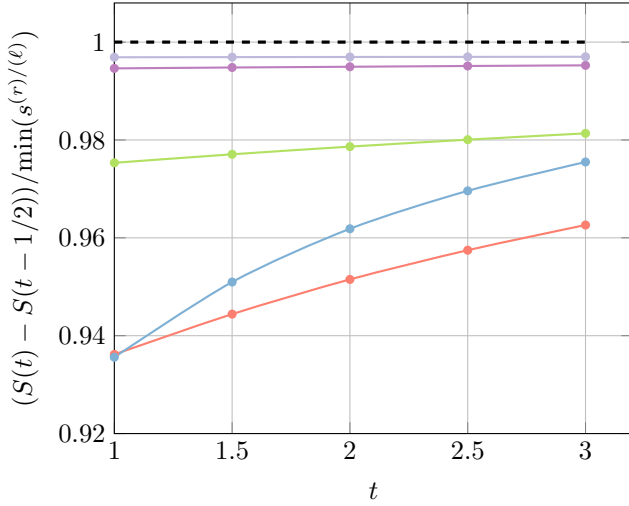


FIG. 3. Entanglement growth at a single edge (meaning that we evaluate $\sqrt{\text{tr}[\rho_A^n(t)]}$ for randomly generated initial states (coloured dots) divided by the analytic prediction (121) obtained measuring the values of $c^{(r)}/c^{(\ell)}$ randomly chosen.

we compare its prediction for the entanglement entropy with exact numerical results obtained for randomly generated initial states with two solitons of dimensions $d_\alpha^{(r)} = d_\alpha^{(\ell)} = 2$ on each leg. The agreement observed is convincing (with corrections of the order of a few percentage points) even for the very short times accessible by the exact numerics.

Note that an interesting prediction of Eq. (121) is the possible occurrence of a non-analyticity in n of the Rényi entropies in the limit $L_A \gg t \gg 1$. The latter takes place, if there exist two $n \neq m$ such that

$$s_n^{(r)} < s_n^{(\ell)}, \quad s_m^{(r)} > s_m^{(\ell)}. \quad (122)$$

2. Asymptotic entanglement value

At asymptotic times $t \gg L_A$, the subsystem A is at equilibrium with the rest and we expect the entanglement entropy to relax to the thermodynamic entropy [99].

In the domain wall language this can be seen by noting that the diagram for the n -th moment of $\rho_A(t)$, i.e.

$$\text{tr}[\rho_A^n] = \text{Diagram}, \quad (123)$$

is dominated by the configuration reported in Fig. 4.

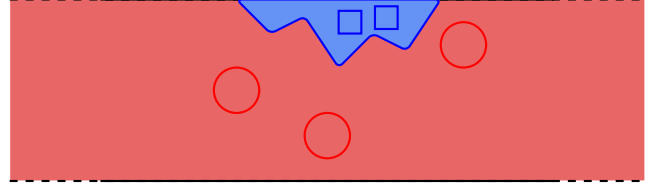


FIG. 4. Pictorial representation of the domain-wall configuration giving the leading contribution to Eq. (123). The domain of square does not reach the bottom part of the diagram (where the initial states are located) as the contribution would otherwise be suppressed as a^t , for some $a < 1$. Instead, if the domain of square is confined to the top part as in this picture, then the suppression does not scale with t . We stress that this domain wall approach works once the gates are projected in a sector where they are “chaotic” and then one looks for the dominant domain configuration in each of these sectors.

To evaluate this contribution, we first decompose the identities along the cuts separating the domain of squares from the rest, proceeding as in Eqs. (110) and (111). This gives

$$\sum_{\alpha, \beta} \text{Diagram}, \quad (124)$$

where

$$\alpha = (\alpha_{i,a})_{i=1, \dots, L_A; a=1, \dots, n}, \quad (125)$$

represents strings of projectors on the right-moving solitons, and β the left-moving ones. Again, we can pin the domain of bullets by projecting the legs across a cut on bullet states (for a fixed value of α and β). Thanks to dual unitarity, all cuts separating the two domains correspond to only one diagram to evaluate (meaning that they can be deformed into one another), so we can just choose the simplest one:

$$\frac{1}{\mathcal{N}_{\alpha, \beta}} \text{Diagram}, \quad (126)$$

where $\mathcal{N}_{\alpha, \beta}$ is a normalization factor. Eq. (116) forces then the solitons β, α to be the same on each replica; dropping the indices of replicas on the string, we can write the normalization factor as

$$\mathcal{N}_{\alpha, \beta} = \prod_{i=1}^{L_A} (d_{\alpha_i}^{(r)} d_{\beta_i}^{(\ell)}). \quad (127)$$

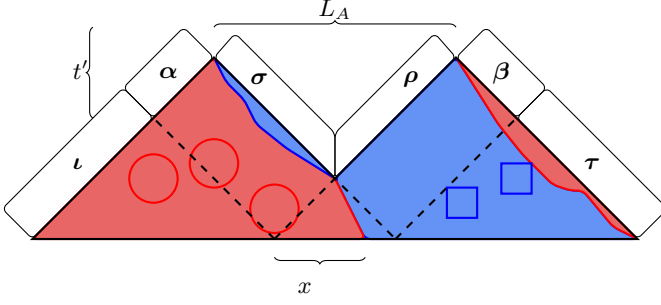


FIG. 5. Pictorial representation of the dominant domain contributions to evaluate Eq. (124) for small values of $t' = t - L_A/2$. We used the fact that, since $s_n^{(r)} < s_n^{(\ell)}$, the dominant domain at the left/right borders is always the one on the left for small values of t' , and we sum over all possible choices of cuts in between the triangles (dashed lines in Fig. 5), which we label as $x = 1, \dots, 2t'$.

Finally, using the charge conservation relations in Eq. (40) to move all the solitons to the bottom part of the diagram, and then the unitarity relation in Eq. (36), we can reduce the diagram to

$$\text{tr} [\rho_A^n(t \gg L_A)] = \sum_{\alpha, \beta} \prod_{i=1}^{L_A} \frac{(c_{\alpha_i}^{(r)} c_{\beta_i}^{(\ell)})^n}{(d_{\alpha_i}^{(r)} d_{\beta_i}^{(\ell)})^{n-1}}. \quad (128)$$

The sum over strings can be carried out by exchanging it with the product, giving again the result obtained in Eq. (97), i.e.,

$$S_A^{(n)} = 2L_A(s_n^{(r)} + s_n^{(\ell)}). \quad (129)$$

3. Second phase of thermalisation

In Sec. VIB 1 we found that, for generic initial states, the Rényi-entropy growth at times $t < L_A/2$ is

$$S_A^{(n)}(t) = 2t \min(s_n^{(r)}, s_n^{(\ell)}) + o(t), \quad (130)$$

while in Sec. VIB 2 we determined its asymptotic value to be

$$S_A^{(n)}(t \gg L_A) = L_A (s_n^{(r)} + s_n^{(\ell)}). \quad (131)$$

These expressions coincide at $t = L_A/2$ only if $s_n^{(r)} = s_n^{(\ell)}$ (e.g. for a solvable state on both sides), where we find a fast thermalisation process, concluded at the minimal possible time allowed by causality. If this is not the case, we expect a second non-trivial phase of thermalisation. Let us now characterise this phase using the entanglement membrane approach: in the rest of the section we set $s_n^{(r)} < s_n^{(\ell)}$ for the calculations.

We again consider the diagram in Eq. (123) but now focus on the case of finite $t > L_A/2$ and set $t' = t - L_A/2$.

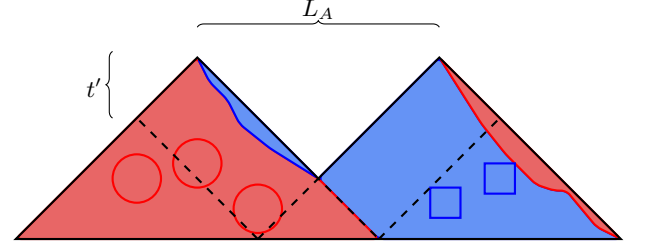


FIG. 6. Dominant domain configuration in the limit $n \rightarrow 1$ assuming $s_n^{(r)} < s_n^{(\ell)}$

We again insert a resolution of the identity in order to decompose the gates into chaotic blocks and then apply the membrane picture (cf. Eq. (124)). Next we sum over several different strings, as indicated in Fig. 5. Referring to the figure we have that only the α and β strings contribute to a growth of entanglement, while the contribution from the others is constant and equal to the entanglement value at the end of the early time regime (cf. Sec. VIB 1). The calculation is similar to those reported in the previous subsections and yields

$$\frac{\text{tr} [\rho_A^n(t' + L_A/2)]}{\text{tr} [\rho_A^n(L_A/2)]} = \sum_x \left[\sum_{\beta=1}^{m(r)} \frac{c_{\beta}^{(r)n}}{d_{\beta}^{(r)2(n-1)}} \right]^x \times \left[\sum_{\alpha=1}^{m(\ell)} \sum_{\beta=1}^{m(r)} \frac{c_{\alpha, \beta}^n}{(d_{\alpha}^{(\ell)} d_{\beta}^{(r)})^{n-1}} \right]^{2t'-x}, \quad (132)$$

the sum in x can be explicitly carried out but, since we are interested in the leading order, we ignore all the factors not scaling exponentially in t' and obtain

$$\frac{\text{tr} [\rho_A^n(t' + L_A/2)]}{\text{tr} [\rho_A^n(L_A/2)]} \quad (133)$$

$$\sim \max \left(\sum_{\alpha=1}^{m(r)} \frac{c_{\alpha}^{(r)n}}{d_{\alpha}^{(r)2(n-1)}}, \sum_{\alpha=1}^{m(r)} \sum_{\beta=1}^{m(\ell)} \frac{c_{\alpha, \beta}^n}{(d_{\alpha}^{(\ell)} d_{\beta}^{(r)})^{n-1}} \right)^{2t'}.$$

As shown in Appendix E, the assumption $s_n^{(r)} < s_n^{(\ell)}$ implies that the first term in Eq. (133) is always dominant in the entanglement entropy limit $n \rightarrow 1$. This means that, in this limit, the dominant domain wall configuration is the one reported in Fig. 6. This gives the following explicit result for the entanglement entropy

$$S_A(L_A/2 + t') = S_A(L_A/2) + 2t' \left(2s_{\text{conf}}^{(r)} + s_{\text{num}}^{(r)} \right) = 4ts^{(r)} - (2t - L_A)s_{\text{num}}^{(r)}. \quad (134)$$

This result implies that the rate of growth decreases by an amount equal to the number entropy density in the sector (left or right) which has the smallest asymptotic entropy density, predicting a saturation of the exact bound in

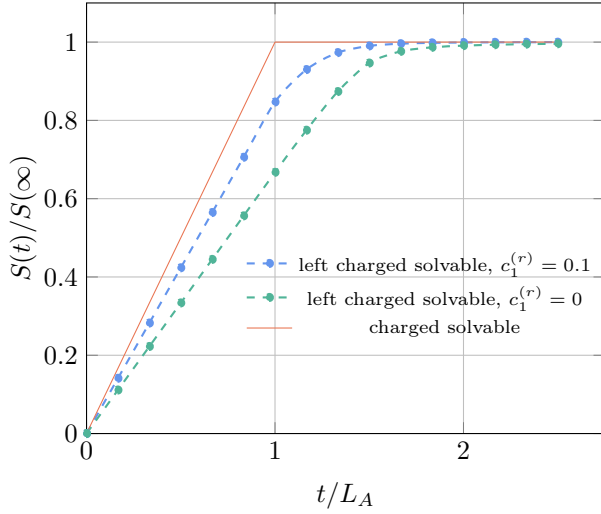


FIG. 7. Entanglement growth for a charged solvable state (red) and a left charged solvable state (blue and green), normalised on the asymptotic entanglement value and on the interval size L_A . In order to reduce the finite size effects, we choose a pair product initial state, i.e. a state as in Eq. (41) with $\chi = 1$.

Eq. (101), in the scaling limit. In other words, we find the following two entanglement velocities

$$v_E(t) \equiv \frac{S(t+1) - S(t)}{S(\infty)/L_A} = \begin{cases} \frac{2s^{(r)}}{s^{(r)} + s^{(\ell)}}, & t \leq L_A \\ \frac{2s^{(r)} - s_{\text{num}}^{(r)}}{s^{(r)} + s^{(\ell)}}, & t > L_A \end{cases}. \quad (135)$$

A numerical check of this equation is reported in Fig. 7 for two examples of left charged solvable states, both chosen such that $c_1^{(\ell)} = c_2^{(\ell)} = 0.5$ (the block structure of the charges is such that $m_{(\ell/r)} = 2$ and $d_{1,2}^{(\ell/r)} = 2$). The data agrees with our prediction on the asymptotic value of the entanglement (cf. Eq. (97)) and is compatible with our results for the behaviour at times $t > L_A$ (which is not fixed by left solvability). Indeed, from Eq. (135) we expect that in the case $c_1^{(r)} = 0, c_2^{(r)} = 1$ (green curve) the slope in the second phase should be the same as the first one (assuming a saturation of the bound (101)). The numerics suggests this to be the case. Instead, the blue dataset has $c_1^{(r)} = 0.1, c_2^{(r)} = 0.9$, which implies $s_{\text{num}}^{(r)} > 0$, displaying a reduction of the slope in accordance with Eq. (135).

VII. ASYMMETRY DYNAMICS AND MPEMBA EFFECT

Further information on the dynamics of \mathcal{G} -symmetric dual-unitary circuits, and on the nature of the second phase of thermalisation, can be obtained by studying symmetry restoration. Namely, preparing the system in

an initial state that is not an eigenstate of the charges and observing how it gradually becomes more symmetric.

This process can be conveniently characterised using the *entanglement asymmetry* [51], which is the relative entropy between $\bar{\rho}_A(t)$ and the symmetrised state

$$\bar{\rho}_A(t) = \sum_{\alpha, \beta} \Pi_{\alpha}^{(r)} \Pi_{\beta}^{(\ell)} \rho_A(t) \Pi_{\alpha}^{(r)} \Pi_{\beta}^{(\ell)}, \quad (136)$$

where $\Pi_{\alpha}^{(r/\ell)}$, introduced in Eq. (83), are the projectors in each charge sector (the latter corresponding to the choice of a soliton α_i on each leg). The entanglement asymmetry is then expressed as

$$\Delta S_A(t) = \rho_A(t) \log \rho_A(t) - \bar{\rho}_A(t) \log \bar{\rho}_A(t). \quad (137)$$

Considering again a quench from the generic pair product states in Eq. (103) we have that the asymmetry at $t = 0$ is given by

$$\Delta S_A(0) = -L_A \sum_{\alpha, \beta} c_{\alpha, \beta} \log(c_{\alpha, \beta}). \quad (138)$$

where $\{c_{\alpha, \beta}\}$ is the probability distribution defined in Eq. (107). Note that this quantity is zero if and only if the initial state is in a single charge sector, i.e., $c_{\alpha, \beta} = \delta_{\alpha, \alpha_0} \delta_{\beta, \beta_0}$. For later convenience we also introduce a symbol to indicate the asymmetry density at time $t = 0$

$$\Delta s_0 \equiv \frac{\Delta S_A(0)}{L_A} = - \sum_{\alpha, \beta} c_{\alpha, \beta} \log(c_{\alpha, \beta}), \quad (139)$$

which is given by the Shannon entropy of $\{c_{\alpha, \beta}\}$.

In order to compute the asymmetry at later times, we use the replica trick. Exploiting the cyclicity of the trace, we can write the n -th moment of the symmetrized density matrix as

$$\text{tr} [(\bar{\rho}_A)^n] = \sum_{\alpha, \beta} \text{tr} \left[\left(\left(\Pi_{\alpha}^{(r)} \Pi_{\beta}^{(\ell)} \right) \rho_A(t) \right)^n \right]. \quad (140)$$

In the early time regime $t < L_A/2$ we have three distinct contributions: one coming from the causally disconnected $2L_A - 4t$ sites in the centre of A , which carry asymmetry $(L_A - 2t)\Delta s_0$, and two separate contributions from the edges taking the form

$$\sum_{\alpha} \left. \begin{array}{c} \text{Diagram of a lattice structure with orange and black nodes and lines, representing a contribution to the entanglement asymmetry. The diagram shows a central region of orange nodes and a surrounding region of black nodes. The total number of sites is labeled as 2t sites.} \end{array} \right\}, \quad (141)$$

$$\sum_{\beta} \left. \begin{array}{c} \text{Diagram of a lattice structure with orange and black nodes and lines, representing a contribution to the entanglement asymmetry. The diagram shows a central region of orange nodes and a surrounding region of black nodes. The total number of sites is labeled as 2t sites.} \end{array} \right\}. \quad (142)$$

Note that the solitons here are chosen to be projectors and must be the same on each replica, as prescribed by Eq. (140).

Assuming, e.g., $s_n^{(r)} < s_n^{(\ell)}$, it is easy to see that the diagram in Eq. (141) gives the same contribution as Eq. (109) at leading order. This follows from the fact that the decomposition used in Sec. VI is essentially the same as in that in Eq. (140): explicitly evaluating (109) in (118) (for a single edge), we get the prescription of choosing the cut to be along the rightmost diagonal, forcing the right-moving charges to be the same in each replica, as in Eq. (140), while the left-moving ones are not, and can be re-summed to be the identity. We get, instead, a non-trivial contribution from the other edge (i.e. Eq. (142))

$$\begin{aligned} & \sum_x \left[\sum_{\alpha, \beta} \frac{c_{\alpha, \beta}^n}{d_{\alpha}^{(r)n-1}} \right]^x \left[\sum_{\beta} \frac{c_{\beta}^{(\ell)n}}{d_{\beta}^{(\ell)n-1}} \right]^{2t-x} = \\ & \sim \left[\max \left(\sum_{\alpha, \beta} \frac{c_{\alpha, \beta}^n}{d_{\alpha}^{(r)n-1}}, \sum_{\beta} \frac{c_{\beta}^{(\ell)n}}{d_{\beta}^{(\ell)n-1}} \right) \right]^{2t}, \end{aligned} \quad (143)$$

without further information one cannot decide which contribution in Eq. (143) is the dominant one, as both cases can be realised.

For example, to produce an example where the first term dominates, one can proceed as follows. Suppose to have gates which chaotic blocks such that $m_{\ell} = m_r$ (i.e. the number of left and right solitons is the same), and choose an initial state such that, for a certain ordering of the soliton labels we have $c_{\alpha, \beta} = c_{\alpha} \delta_{\alpha, \beta}$. Then we have

$$\sum_{\alpha, \beta} \frac{c_{\alpha, \beta}^n}{d_{\alpha}^{(r)n-1}} = \sum_{\alpha} \frac{c_{\alpha}^n}{d_{\alpha}^{(r)n-1}} = \exp\left((1-n)s_n^{(r)}\right). \quad (144)$$

Since by assumption

$$s_n^{(r)} < s_n^{(\ell)}, \quad (145)$$

we find that the first term in (143) is the largest and dominant one. Note that for our choice of the charges $c_{\alpha}^{(\ell)} = c_{\alpha}^{(r)}$ it is still possible to have $s_n^{(r)} \neq s_n^{(\ell)}$ by tuning appropriately the sizes of the charge sectors $d_{\alpha}^{(\ell)} \neq d_{\alpha}^{(r)}$.

From now on, however, we consider an example where the second term dominates. Specifically, we focus on the case where both right and left symmetry sectors have fixed size \mathcal{D} :

$$\begin{aligned} d_{\alpha}^{(\ell)} = d_{\beta}^{(r)} = \mathcal{D} \quad (146) \\ \forall \alpha \in \{1, \dots, m_{\ell}\}, \beta \in \{1, \dots, m_r\} \end{aligned}$$

which immediately implies

$$\sum_{\alpha, \beta} \frac{c_{\alpha, \beta}^n}{\mathcal{D}^n} \leq \sum_{\beta} \frac{(\sum_{\alpha} c_{\alpha, \beta})^n}{\mathcal{D}^n} = \sum_{\beta} \frac{c_{\beta}^{(\ell)n}}{\mathcal{D}^n}, \quad (147)$$

and

$$s_{\text{conf}}^{(\ell/r)} = \log(\mathcal{D}). \quad (148)$$

In this case we can simplify Eq. (143) and, putting all together, find the following expression for the entanglement entropy of the symmetrised state

$$\begin{aligned} -\bar{\rho}_A(t) \log \bar{\rho}_A(t) = \min(2t, L_A) \left(s_{\text{num}}^{(\ell)} + s_{\text{num}}^{(r)} \right) \\ + \max(L_A - 2t, 0) \frac{\Delta S_A(0)}{L_A}, \end{aligned} \quad (149)$$

which we extended also a later times, since the configuration of domain walls at times $t \approx L_A/2$ is the same as the long times one in Fig. 4. Plugging it into Eq. (137) and combining it with the results of the previous section we finally obtain

$$\Delta S_A(t) = \begin{cases} 2t(s_{\text{num}}^{(\ell)} - s_{\text{num}}^{(r)}) + (L_A - 2t)\Delta s_0, & t < L_A/2 \\ |s_{\text{num}}^{(\ell)} - s_{\text{num}}^{(r)}| - (2t - L_A)(s_{\text{num}}^{(r)} + 2\log(\mathcal{D})) & t_{\text{th}} \geq t \geq L_A/2 \\ 0 & t > t_{\text{th}} \end{cases} \quad (150)$$

Note that the slope in the first phase is always negative as one can see by noting (cf. Eq. (138))

$$s_{\text{num}}^{(\ell)} + s_{\text{num}}^{(r)} \geq \Delta s_0 \geq \max(s_{\text{num}}^{(\ell)}, s_{\text{num}}^{(r)}). \quad (151)$$

One can always saturate the first inequality by choosing an initial product state (i.e. a rank 1 matrix m in

Eq. (103)). Indeed, this implies

$$c_{\alpha, \beta} = c_{\alpha}^{(\ell)} c_{\beta}^{(r)} \implies \Delta s_0 = s_{\text{num}}^{(\ell)} + s_{\text{num}}^{(r)}, \quad (152)$$

allowing for a simpler form of (150). In this case, it is easy to find an explicit instance of Mpemba effect, by tuning the initial value of the asymmetry to be high without modifying the thermalisation time, which only depends

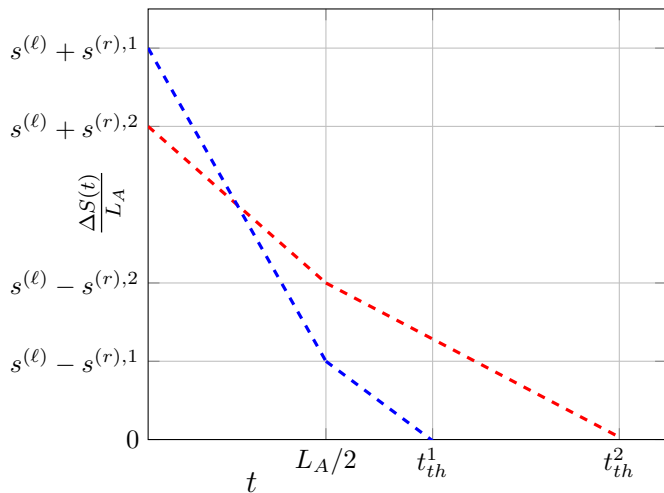


FIG. 8. Example of Mpemba effect choosing two initial product states and tuning them so that they have equal $s^{(\ell)} > s^{(r),1/2}$, and different $s^{(r),1} > s^{(r),2}$. The symbols $t_{th}^{1/2}$ denote the different thermalisation times, computed according to Eq. (10).

on $s_{\text{num}}^{(\ell/r)}$. In particular, recalling the definition of thermalisation time in Eq. (10), we see that we can choose two initial product states that have the same (larger) left number entropy density and different right number entropy densities

$$s_{\text{num}}^{(r),2} < s_{\text{num}}^{(r),1} < s_{\text{num}}^{(\ell),2} = s_{\text{num}}^{(\ell),1}, \quad (153)$$

and trigger a quantum Mpemba effect discussed in Sec. II, see, e.g., Fig. 8.

VIII. DISCUSSION AND OUTLOOK

In this work we introduced and characterised \mathcal{G} -symmetric dual-unitary circuits, a class of quantum circuits where it is possible to investigate exactly the interplay between entanglement and charge fluctuations. These are dual-unitary circuits with an arbitrary number of independent $U(1)$ symmetries that are generically chaotic in each charge sector. We showed that in these circuits one can define a class of low-entangled initial states, the charged solvable states, with exactly solvable entanglement dynamics. This class contains — but is not limited to — the conventional solvable states of dual-unitary circuits described in Ref. [19]. An important difference is that charged solvable states generically relax to non-trivial generalised Gibbs ensembles while conventional solvable states always relax to the infinite temperature state. We then showed that, very surprisingly, if one breaks the solvability condition the entanglement dynamics displays a sharp qualitative change. While after quenches from charged solvable states the entanglement entropy follows the conventional linear-growth-to-relaxation pattern, quenches from states that are not

charged solvable show a two step relaxation with a second phase of entanglement growth characterised by a smaller slope. Interestingly, despite the circuits being dual unitary, non-charged solvable states show a submaximal entanglement velocity even in the early time regime. Moreover, they can also display instances of quantum Mpemba effect. Namely, considering states that break some of the symmetries of the dynamics, one can observe faster restoration in cases where the initial symmetry breaking is larger.

These surprising findings are just starting to unveil the rich structure that conservation laws impose on the non-equilibrium dynamics of \mathcal{G} -symmetric dual-unitary circuits and we expect that future research will help identifying many more such exotic phenomena. An immediate question that can be directly attacked with the techniques introduced here concern, for instance, investigating the operator spreading in these systems, e.g. by computing out-of-time ordered correlators or the operator-space entanglement of local operators. Another interesting set of questions concerns the complexity of computing the time evolution of these circuits with classical computers. Conventional dual unitary circuits are known to be hard to simulate both directly [100] and by exchanging the roles of space and time [101], and it is interesting to ask whether the additional charge structure can help the classical simulation. Finally, it is appealing to wonder whether one can generalise our construction to circuits where the dual unitarity condition has been weakened following the logic of Ref. [102].

ACKNOWLEDGMENTS

We acknowledge financial support from the Royal Society through the University Research Fellowship No. 201101 (A. F. and B. B.). P. C. has been supported by the European Research Council under Consolidator Grant number 771536 “NEMO”. A. F. and B. B. thank SISSA for hospitality during the preparation of this work.

Appendix A: Charge Propagation in Dual-Unitary Circuits

Assume to have a conserved charge Q , which can be written as the sum of one-site charge densities

$$Q = \sum_{x=0}^L q_x + q_{x+1/2}. \quad (A1)$$

Calling \mathbb{U} the time evolution operator (which commutes with Q), we can write the continuity equation for the charge density (assume x is an integer site)

$$\mathbb{U}q_x\mathbb{U}^\dagger = q_x - J_{x+1/2} + J_{x-1/2}, \quad (A2)$$

we make no assumption on J_x , apart from the constraints due to causality and the request that it cancels out once

summing on all sites as in Eq. (A1). In fact, without loss of generality, we can take J_x to be traceless. Indeed, if $\text{tr}[J] \neq 0$ we can always consider $J \mapsto J' = J - \text{tr}[J]\mathbb{1}/d$, which also obeys (A2) and is traceless.

Graphically, we can represent Eq. (A2) using the notation introduced in Sec. IIIB as

$$\begin{aligned} & \text{Diagram with three orange boxes labeled '1' and four white circles} = \\ & = \text{White circle} + \text{White circle with red dot} + \text{White circle} - \text{White circle with black ellipse} + \text{White circle} + \text{White circle with red dot} + \text{White circle} - \text{White circle with black ellipse} + \text{White circle} \end{aligned} \quad (\text{A3})$$

where we represented the J operator with a black ellipse to indicate a generic two-site operator. Tracing out the two rightmost sites (in the replica language this corresponds to the insertion of a bullet) we have

$$\begin{aligned} & \text{Diagram with three orange boxes labeled '1' and four white circles, with a bullet on the rightmost circle} = 0 = \\ & = d^2 (\text{White circle with red dot} - \text{White circle with black ellipse}) + \text{White circle} + \text{White circle} + \text{White circle with black ellipse} \end{aligned} \quad (\text{A4})$$

where we used dual unitarity and unitarity to simplify the left hand side of (A4) obtaining 0 thanks to the traceless condition on $q^{(r)}$. We then immediately have

$$\text{White circle with black ellipse} = \text{White circle with red dot} \quad (\text{A5})$$

meaning that $J_x = -q_{x+1/2}$, which shows to a ballistic transportation of charge at the operatorial level. We will refer from this point on to the one-site charge densities as solitons. Explicitly, they obey

$$\mathbb{U}q_x\mathbb{U}^\dagger = q_{x+1} \quad (\text{A6})$$

or graphically

$$\text{Diagram with three orange boxes labeled '1' and four white circles} = \text{White circle} + \text{White circle} + \text{White circle} + \text{White circle with red dot} \quad (\text{A7})$$

Similarly charges starting on half-integer sites can be shown to move in the left direction: We will use a superscript (ℓ) for left-moving solitons and (r) for right-moving ones.

This immediately implies that conserved charges with support on half integer and integer sites are separately conserved, since, for example

$$\mathbb{U}Q'\mathbb{U} = \mathbb{U} \sum_{x=0}^L q_x^{(r)} \mathbb{U} = \sum_{x=0}^L q_{x+1}^{(r)} = Q'. \quad (\text{A8})$$

Moreover, one can produce exponentially many conserved charges [80]. Noting that the identity operator

$\mathbb{1}_d$ trivially fulfils Eq. (A7) we have that a charge density with support on ℓ sites, having on each integer site either $q^{(r)}$ or $\mathbb{1}_d$, obeys Eq. (A7) too. This gives us 2^ℓ choices for the charge density. Ruling out the identity operator itself (this corresponds to choosing $\mathbb{1}_d$ on each site) one is left with $2^\ell - 1$ independent charge densities with support on integer sites; considering also the ones on half integer sites (left-moving) the total number of conserved charges is $2^{\ell+1} - 2$. More generally, with m_ℓ/m_r solitons (including the identity), the total number of charges with support on at most 2ℓ sites is $(m_\ell)^\ell + (m_r)^\ell - 2$.

Appendix B: Proof of Theorem 1

In this appendix we provide a proof of Theorem 1.

Without loss of generality we work with right-moving solitons. We begin by noting that one can simplify the leftmost gate in the diagram in Eq. (A7) (multiplying both sides by its inverse) obtaining

$$\begin{aligned} & (\mathbb{1}_d \otimes U) (U \otimes \mathbb{1}_d) \left(\sigma^{(r)} \otimes \mathbb{1}_d^{\otimes 2} \right) (U^\dagger \otimes \mathbb{1}_d) (\mathbb{1}_d \otimes U^\dagger) = \\ & = \left(\mathbb{1}_d^{\otimes 2} \otimes \sigma^{(r)} \right). \end{aligned} \quad (\text{B1})$$

Equation (B1) is our starting point. First we note that it implies that the space of right-moving solitons forms an algebra: If $\sigma^{(r)}$ and $\sigma'^{(r)}$ both obey (B1), then their sum and product also do. Note that in general the members of this space are not hermitian (because we allow for linear combination with complex coefficient) but they are normal operators, because by assumption the solitons $\sigma_i^{(r)}$ commute with each other. We call this algebra $Q^{(r)}$.

This observation is enough to prove the first part of the theorem. If $\sigma^{(r)}$ is a soliton we can decompose it in orthogonal subspaces (this can always be done because $\sigma^{(r)}$ normal) as follows

$$\sigma^{(r)} = \sum_{\mu} \Pi_{\mu} \mu, \quad (\text{B2})$$

where we called Π_{μ} the projector in the eigenspace corresponding to the eigenvalue μ . Then, for every eigenvalue μ^* , one can define the polynomial

$$P_{\mu^*}(x) = \prod_{\mu \neq \mu^*} (x - \mu), \quad (\text{B3})$$

such that $P_{\mu^*}(\sigma^{(r)}) \propto \Pi_{\mu^*}$. But since the space of solitons is closed under product and sum also $P_{\mu^*}(\sigma^{(r)})$ must be a soliton. Since these projectors are linearly independent this proves that we can always choose a basis where the solitons are projectors (this is true even if the charge densities do not commute).

To prove the second part of the theorem we rewrite

Eq. (B1) as

$$\begin{aligned} & (U \otimes \mathbb{1}_d) \left(\sigma^{(r)} \otimes \mathbb{1}_d \otimes \mathbb{1}_d \right) (U^\dagger \otimes \mathbb{1}_d) = \\ & = (\mathbb{1}_d \otimes U^\dagger) \left(\mathbb{1}_d \otimes \mathbb{1}_d \otimes \sigma^{(r)} \right) (\mathbb{1}_d \otimes U). \end{aligned} \quad (\text{B4})$$

We now observe that the left hand side of Eq. (B4) is the identity on the last (rightmost) site, while the right hand side is the identity on the first, meaning that both

sides have to be equal to

$$\mathbb{1}_d \otimes \mathcal{L}[\sigma^{(r)}] \otimes \mathbb{1}_d, \quad (\text{B5})$$

where $\mathcal{L}[\bullet]$ is some generic function which is defined from the space of the conserved charge densities $\sigma^{(r)}$ to the space of local operators on one site. More specifically, we can rewrite (B4) as

$$U \left(\sigma^{(r)} \otimes \mathbb{1}_d \right) U^\dagger = \mathbb{1}_d \otimes \mathcal{L}[\sigma^{(r)}]. \quad (\text{B6})$$

We now show that if $\sigma^{(r)}$ obeys Eq. (B1), then also $\mathcal{L}[\sigma^{(r)}]$ does. Starting from Eq. (B6) we expand it on three sites (by attaching an identity on the left) and conjugate both sides with $\mathbb{1}_d \otimes U$ to obtain

$$(\mathbb{1}_d \otimes U) (U \otimes \mathbb{1}_d) \left(\sigma^{(r)} \otimes \mathbb{1}_d \otimes \mathbb{1}_d \right) (U^\dagger \otimes \mathbb{1}_d) (\mathbb{1}_d \otimes U^\dagger) = (\mathbb{1}_d \otimes U) (\mathbb{1}_d \otimes \mathcal{L}[\sigma^{(r)}] \otimes \mathbb{1}) (\mathbb{1}_d \otimes U^\dagger), \quad (\text{B7})$$

which can be simplified using (B1) on the left hand side to obtain

$$\left(\mathbb{1}_d \otimes \mathbb{1}_d \otimes \sigma^{(r)} \right) = (\mathbb{1}_d \otimes U) (\mathbb{1}_d \otimes \mathcal{L}[\sigma^{(r)}] \otimes \mathbb{1}) (\mathbb{1}_d \otimes U^\dagger). \quad (\text{B8})$$

Finally, we can rewrite this equation by multiplying both sides with the same combination of gates, and then substituting Eq. (B6). Specifically

$$\begin{aligned} & (\mathbb{1}_d \otimes \mathbb{1}_d \otimes U) (\mathbb{1}_d \otimes U \otimes \mathbb{1}_d) (\mathbb{1}_d \otimes \mathcal{L}[\sigma^{(r)}] \otimes \mathbb{1}_d \otimes \mathbb{1}_d) (\mathbb{1}_d \otimes U^\dagger \otimes \mathbb{1}_d) (\mathbb{1}_d \otimes \mathbb{1}_d \otimes U^\dagger) = \\ & = (\mathbb{1}_d \otimes \mathbb{1}_d \otimes U) \left(\mathbb{1}_d \otimes \mathbb{1}_d \otimes \sigma^{(r)} \otimes \mathbb{1}_d \right) (\mathbb{1}_d \otimes \mathbb{1}_d \otimes U^\dagger) = \left(\mathbb{1}_d \otimes \mathbb{1}_d \otimes \mathbb{1}_d \otimes \mathcal{L}[\sigma^{(r)}] \right). \end{aligned} \quad (\text{B9})$$

Ignoring all the identities on the leftmost sites, this shows that $\mathcal{L}[\sigma^{(r)}]$ is itself a right-moving soliton, implying that \mathcal{L} is a function that goes from the space of conserved, right-moving solitons to itself. Additionally, notice that $\mathcal{L}[\sigma^{(r)}]$ is an *endomorphism*, meaning that not only it maps the algebra $Q^{(r)}$ to itself, but it is also compatible with its operations, and that

$$(\mathcal{L})^2 [\sigma^{(r)}] = \sigma^{(r)}, \quad (\text{B10})$$

where we used Eq. (B1). Finally, from Eq. (B6), we see that \mathcal{L} is unitary with respect to the Hilbert–Schmidt inner product

$$\langle \sigma_1, \sigma_2 \rangle = \text{tr} \left[\sigma_1^\dagger \sigma_2 \right]. \quad (\text{B11})$$

This means that \mathcal{L} can be diagonalised and its eigenvalues must lie on the unit circle. In fact, Eq. (B10) implies that they can only be ± 1 and we denote the corresponding eigenspaces and their respective dimension as Q^\pm and n_\pm . We consider the subspace of charges with eigenvalue $+1$ and call it Q^+ . It is immediate to see that this is a sub-algebra of Q : if $\sigma_1^{(r)}, \sigma_2^{(r)} \in Q^+$ then

$$\begin{aligned} & \mathcal{L}[\sigma_1^{(r)} \sigma_2^{(r)}] = \mathcal{L}[\sigma_1^{(r)}] \mathcal{L}[\sigma_2^{(r)}] = \sigma_1^{(r)} \sigma_2^{(r)} \\ & \implies \sigma_1^{(r)} \sigma_2^{(r)} \in Q^+, \end{aligned} \quad (\text{B12})$$

and similarly for the sum operation. By the theorem's assumptions all the solitons commute, so we diagonalise all of them simultaneously and find a common decomposition in eigenspaces. We use the projectors on these eigenspaces as a basis of Q^+ and denote its elements by $\sigma_{+,\alpha}^{(r)}$.

Next, we consider solitons in Q^- , the vector space corresponding to the negative eigenvalue of \mathcal{L} . This vector space is not closed under multiplication, since if $\sigma_1^-, \sigma_2^- \in Q^-$, then

$$\begin{aligned} & \mathcal{L}[\sigma_1^- \sigma_2^-] = \mathcal{L}[\sigma_1^-] \mathcal{L}[\sigma_2^-] = (-\sigma_1^-) (-\sigma_2^-) \\ & \implies \sigma_1^- \sigma_2^- \in Q^+. \end{aligned} \quad (\text{B13})$$

Then we decompose the solitons $\sigma_{-,\alpha}^{(r)} \in Q^-$ as follows: first we notice that $\sigma_{-,\alpha}^{(r)2} \in Q^+$ so it can be decomposed into the orthogonal projectors as before

$$\left(\sigma_{-,\alpha}^{(r)} \right)^2 = \bigoplus_{\beta} \mu_{\beta} \sigma_{+,\beta}^{(r)}. \quad (\text{B14})$$

If some $\mu_{\beta} \neq 0$ is degenerate we decompose $\sigma_{-,\alpha}^{(r)}$ further as

$$\sigma_{-,\alpha}^{(r)} = \bigoplus_{\beta | \mu_{\beta} \neq 0} \sigma_{-,\alpha}^{(r)} \sigma_{+,\beta}^{(r)}, \quad (\text{B15})$$

and take each $\sigma_{-, \alpha}^{(r)} \sigma_{+, \beta}^{(r)}$ as a new basis of solitons (being careful of maintaining the linear independence). We iterate this procedure for all the solitons in Q^- in such a way to obtain a new basis, and reorder the indices of the solitons such that

$$\sigma_{+, \alpha}^{(r)} \sigma_{-, \beta}^{(\ell)} = \delta_{\alpha \beta} \sigma_{-, \beta}^{(\ell)} \quad \forall \alpha, \beta \leq n_- \quad (\text{B16})$$

$$\sigma_{+, \alpha}^{(r)} \sigma_{-, \beta}^{(\ell)} = 0 \quad \forall \alpha > n_-, \beta \leq n_- \quad (\text{B17})$$

We then define the projectors belonging to the first group of Theorem 1 as the ones in Q^+ orthogonal to all the solitons $\in Q^-$

$$\sigma_{+, \alpha}^{(r)} = \Pi_{\alpha}^{(r)} \quad \alpha > n_- \quad (\text{B18})$$

To find those in the second group we observe that since $\mathcal{L}[\sigma_{-, \alpha}^{(r)}] = -\sigma_{-, \alpha}^{(r)}$, this means that a similarity transformation (which defined \mathcal{L}) connects $\sigma_{-, \alpha}^{(r)}$ and $-\sigma_{-, \alpha}^{(r)}$. Thus the spectrum of $\sigma_{-, \alpha}^{(r)}$ must be symmetric around the origin. Then, given that $\sigma_{-, \alpha}^{(r)2} \propto \sigma_{+, \alpha}^{(r)}$ has only a nontrivial eigenspace, σ_{α}^- must be written as

$$\sigma_{-, \alpha}^{(r)} = \mu(P_{+, \alpha}^{(r)} - P_{-, \alpha}^{(r)}) \implies \sigma_{\alpha}^+ \propto P_{+, \alpha}^{(r)} + P_{-, \alpha}^{(r)} \quad (\text{B19})$$

for some orthogonal projectors P_{α}^{\pm} . It is then immediate to see that

$$\begin{aligned} \mathcal{L}[P_{+, \alpha}^{(r)}] &= \\ &= \mathcal{L}[P_{+, \alpha}^{(r)} - P_{-, \alpha}^{(r)} + P_{+, \alpha}^{(r)} + P_{-, \alpha}^{(r)}] / 2 = P_{-, \alpha}^{(r)}, \end{aligned} \quad (\text{B20})$$

$$\begin{aligned} \mathcal{L}[P_{-, \alpha}^{(r)}] &= \\ &= \mathcal{L}[P_{-, \alpha}^{(r)} - P_{+, \alpha}^{(r)} + P_{-, \alpha}^{(r)} + P_{+, \alpha}^{(r)}] / 2 = P_{+, \alpha}^{(r)}, \end{aligned} \quad (\text{B21})$$

proving Eq. (19). To prove the completeness relation in Eq. (20), it is sufficient to note that in our notation the identity operator is a conserved charge (although trivial) belonging in Q^+ . Therefore, if the sum of all the mutually orthogonal projectors $\Pi_{\alpha}^{(r)}, P_{\pm, \alpha}^{(r)}$ does not give the identity our set of charges is not a complete basis (note that, since the projectors are mutually orthogonal, their only linear combination that produces the identity is when they are all summed with coefficient 1), and we find a contradiction.

Appendix C: Proof of Theorems 2-3

1. Left solvability

Here we prove Theorem 2 following the proof of Theorem 1 in Ref. [19]. Without loss of generality we consider the case of left charged solvable states. The condition that the transfer matrix $\tau(\mathcal{M})$ has spectrum contained in the disc $|\lambda| < 1$ with only one eigenvalue on its border, corresponds to the request that the initial state $|\Psi(0)\rangle$ is

normalised in the thermodynamical limit, since (assuming a periodic boundary)

$$\langle \Psi_0^L(\mathcal{M}) | \Psi_0^L(\mathcal{M}) \rangle = \text{tr} [\tau(\mathcal{M})^L]. \quad (\text{C1})$$

The left solvability condition (45) implies that the left eigenvector corresponding to this eigenvalue is the (vectorized) operator S , i.e.,

$$\langle S | = \sum_{i,j} \langle i | S | j \rangle \langle i, j |. \quad (\text{C2})$$

To see this explicitly, we trace Eq. (45) on the physical space indices, finding:

$$\sum_{i,j} (\mathcal{M}^{i,j})^{\dagger} S \mathcal{M}^{i,j} = \sum_{\alpha} \frac{c_{\alpha}^{(r)}}{d_{\alpha}} \text{tr} [\Pi_{\alpha}^{(r)}] S = S. \quad (\text{C3})$$

Then, we can use Theorem 3.5 in Ref. [104], which states that a completely positive map \mathcal{E} with a spectral radius r ($r = 1$ in this case), has at least one positive operator X such that $\mathcal{E}[X] = rX$. This theorem can be applied to the matrix τ , which can also be seen as a linear map on the space of operators

$$\tau \leftrightarrow \mathcal{E}_{\tau}[X] = \sum_{i,j} (\mathcal{M}^{i,j})^{\dagger} X \mathcal{M}^{i,j}. \quad (\text{C4})$$

By assumption, the spectrum of τ is nondegenerate at the border of the unit circle, and by virtue of left solvability (45) we know S is a fixed point, from which it follows that S must be a positive operator.

We now show that a solvable MPS is always equivalent, in the thermodynamic limit, to another MPS for which the matrix S (defined as the unique fixed point of the transfer matrix), is not only positive, but strictly positive. This is equivalent to Eq. (51), because if S is strictly positive it is invertible, and we can do a gauge transformation on the MPS

$$\mathcal{M}^{a,b} \rightarrow A \mathcal{M}^{a,b} A^{-1} \implies S \rightarrow (A^{-1})^* S A^{-1}, \quad (\text{C5})$$

which maps S to the identity operator by choosing $A = \sqrt{S}$.

To show the strict positivity of S , suppose by contradiction that S has some zero eigenvalues. Choosing a basis where S is diagonal ($S = \sum_{\alpha} \mu_{\alpha} |\alpha\rangle\langle\alpha|$), we have

$$0 = \sum_{\alpha} \mu_{\alpha} |\alpha\rangle\langle\alpha| - \sum_{i,j} \sum_{\alpha} \mu_{\alpha} (\mathcal{M}^{i,j})^{\dagger} |\alpha\rangle\langle\alpha| \mathcal{M}^{i,j}. \quad (\text{C6})$$

Let P be the projector on the kernel of $S - P = \mathbf{1}_{\chi} - \sum_{\alpha} |\alpha\rangle\langle\alpha|$ — then Eq. (C6) implies

$$\sum_{i,j} \sum_{\alpha} \mu_{\alpha} P (\mathcal{M}^{i,j})^{\dagger} |\alpha\rangle\langle\alpha| \mathcal{M}^{i,j} P = 0. \quad (\text{C7})$$

The matrices inside the sum

$$P (\mathcal{M}^{i,j})^{\dagger} |\alpha\rangle\langle\alpha| \mathcal{M}^{i,j} P, \quad (\text{C8})$$

are all positive and we are requiring their sum to vanish. This can only be true if each of them is 0

$$\forall \alpha, i, j \quad \begin{aligned} P (\mathcal{M}^{i,j})^\dagger |\alpha\rangle \langle \alpha| \mathcal{M}^{i,j} P = 0 &\implies \\ \mathcal{M}^{i,j} P = P \mathcal{M}^{i,j} P, &\end{aligned} \quad (\text{C9})$$

meaning that there is a basis in which the matrices $M^{i,j}$ are all triangular

$$\mathcal{M}^{i,j} = \begin{pmatrix} \mathcal{A}^{i,j} & \mathcal{B}^{i,j} \\ 0 & \mathcal{C}^{i,j} \end{pmatrix}. \quad (\text{C10})$$

Given our periodic boundary conditions on the MPS, the MPS is completely equivalent to one that only has the diagonal part in Eq. (C10) (i.e. $\mathcal{B}^{i,j}$ can be set to 0). Such MPS can be written as $|\Psi\rangle = |\Psi_1\rangle + |\Psi_2\rangle$, where $|\Psi_1\rangle$ is obtained using the matrices $\mathcal{A}^{i,j}$ as MPS and $|\Psi_2\rangle$ with $\mathcal{B}^{i,j}$. Since the leading eigenvalue of τ is nondegenerate by assumption, and has support only on the block corresponding to $\mathcal{A}^{i,j}$ it means that the norm of $|\Psi_2\rangle$ is suppressed in the thermodynamic limit, so that we can reduce the bond dimension using the MPS

$$P \mathcal{M}^{i,j} P, \quad (\text{C11})$$

which is equivalent (in the thermodynamical limit) to the original one. In this reduced space the matrix S is strictly positive, proving the theorem.

2. Charged solvability

Suppose to have a state which obeys both Eqs. (45) and (47). Using the left-solvability we can consider an equivalent MPS which can be written as in (57)

$$\Gamma(\mathcal{M}) = V \left(\sqrt{C^{(r)}} \otimes \mathbb{1}_X \right), \quad (\text{C12})$$

where we defined

$$C^{(r)} \equiv \sum_{\alpha=1}^{m_r} \frac{c_\alpha^{(r)}}{d_\alpha^{(r)}} \Pi_\alpha^{(r)}. \quad (\text{C13})$$

Similarly we can define

$$C^{(\ell)} \equiv \sum_{\alpha=1}^{m_\ell} \frac{c_\alpha^{(\ell)}}{d_\alpha^{(\ell)}} \Pi_\alpha^{(\ell)}. \quad (\text{C14})$$

Then, condition (47) tells us that there is a *unique* matrix S in the auxiliary space such that

$$V \left(C^{(r)} \otimes S \right) V^\dagger = C^{(\ell)} \otimes S. \quad (\text{C15})$$

First of all we note that, since V is a unitary matrix, the operation $V(\bullet)V^\dagger$ is a similarity transformation. This means that the spectra of $C^{(r)} \otimes S$ and $C^{(\ell)} \otimes S$ have to match, implying that there is a matrix $U' \in SU(d)$ such that

$$C^{(r)} = U' C^{(\ell)} U'^\dagger. \quad (\text{C16})$$

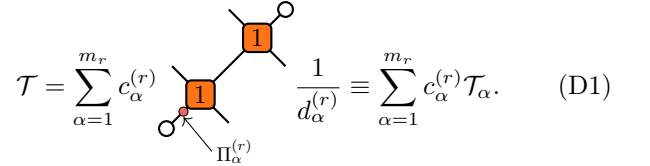
We use U' to change the basis on the odd sites (which generate left moving particles), so that $C^{(r)} = C^{(\ell)} \equiv C$: this proves the blocking condition in Eq. (59).

Repeating the reasoning of App. C1, one can show that S is a strictly positive operator (or that the MPS is equivalent to another MPS with lower bond dimension such that this property holds). In passing we note that there are examples where S cannot be taken to be the identity matrix, differently from the solvable states of Ref. [19].

Appendix D: Late time regime for left charged solvable states

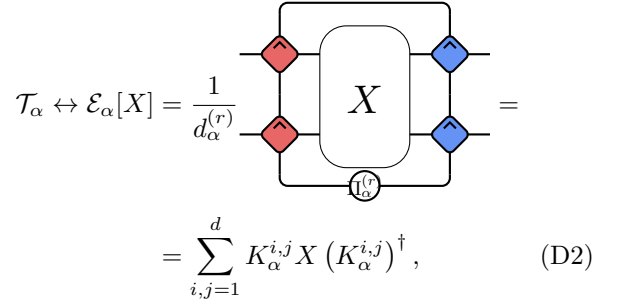
1. Leading eigenvectors of the transfer matrix

We consider transfer matrices as the one in Eq. (95). We start by writing the right-moving soliton on the main diagonal as a linear combination of projectors

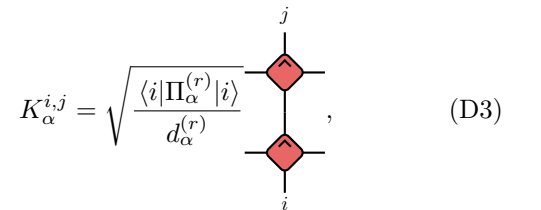
$$\mathcal{T} = \sum_{\alpha=1}^{m_r} c_\alpha^{(r)} \frac{1}{d_\alpha^{(r)}} \equiv \sum_{\alpha=1}^{m_r} c_\alpha^{(r)} \mathcal{T}_\alpha. \quad (\text{D1})$$


In this way, we express the transfer matrix as a convex combination (with coefficients $c_\alpha^{(r)} \geq 0$ that sum to 1) of other transfer matrices \mathcal{T}_α which have the projectors $\Pi_\alpha^{(r)}$ propagating along the main diagonal.

Note that, by unfolding, these transfer matrices can be expressed as quantum channels written in Kraus form, i.e.,

$$\begin{aligned} \mathcal{T}_\alpha \leftrightarrow \mathcal{E}_\alpha[X] &= \frac{1}{d_\alpha^{(r)}} \text{Diagram} = \\ &= \sum_{i,j=1}^d K_\alpha^{i,j} X (K_\alpha^{i,j})^\dagger, \end{aligned} \quad (\text{D2})$$


where we introduced

$$K_\alpha^{i,j} = \sqrt{\frac{\langle i | \Pi_\alpha^{(r)} | i \rangle}{d_\alpha^{(r)}}} \text{Diagram}, \quad (\text{D3})$$


and used i, j as indexes for an orthonormal basis on one site. Unitarity and dual-unitarity imply the channel is

2. Bound between left/right entanglement entropies

In this appendix we compute the Rényi entropies of the state in Eq. (96). We begin by expressing the latter in formulae as follows

$$\rho_A(\infty) = \rho_\ell^{GGE} \otimes \rho_r^{GGE} \quad (\text{D11})$$

where the tensor product is between even and odd sites and we defined

$$\rho_r^{GGE} = \left(\sum_\alpha \frac{c_\alpha^{(r)}}{d_\alpha^{(r)}} \Pi_\alpha^{(r)} \right)^{\otimes L_A}, \quad (\text{D12})$$

$$\rho_\ell^{GGE} = \sum_\alpha \frac{1}{d_\alpha^{(\ell)}} \left[\bigotimes_{i=1}^{L_A} \Pi_{\alpha_i}^{(\ell)} \langle \mathcal{O}_{\chi,1} | N^{\alpha_1} N^{\alpha_2} \dots | S \rangle \right], \quad (\text{D13})$$

and in the second equation we set

$$N^\alpha \equiv \sum_{i,j=1}^d \mathcal{M}^{i,j} \otimes (\mathcal{M}^{i,j})^* \langle i | \Pi_\alpha^{(\ell)} | i \rangle, \quad (\text{D14})$$

$$d_\alpha^{(\ell)} \equiv \prod_i d_{\alpha_i}^{(\ell)}. \quad (\text{D15})$$

Considering traces of powers of $\rho_A(\infty)$ we have

$$\text{tr}[\rho_A(\infty)^n] = \text{tr}[\rho_\ell^{GGE n}] \text{tr}[\rho_r^{GGE n}], \quad (\text{D16})$$

where

$$\text{tr}[\rho_r^{GGE n}] = \left(\sum_\alpha \frac{c_\alpha^{(r)n}}{d_\alpha^{(r)n-1}} \right)^{L_A}, \quad (\text{D17})$$

and

$$\text{tr}[\rho_\ell^{GGE n}] = \sum_\alpha \frac{\langle \mathcal{O}_{\chi,1} | N^{\alpha_1} N^{\alpha_2} \dots | S \rangle^n}{d_\alpha^{(\ell)n-1}}. \quad (\text{D18})$$

The latter expression can be rewritten as

$$\text{tr}[\rho_\ell^{GGE n}] = \langle \mathcal{O}_{\chi,1} | \otimes^n N(n)^{L_A} | S \rangle^{\otimes n}, \quad (\text{D19})$$

where we defined

$$N(n) \equiv \sum_{\alpha=1}^{m_r} \frac{(N^\alpha)^{\otimes n}}{d_\alpha^{(\ell)n-1}}. \quad (\text{D20})$$

This expression can be evaluated efficiently for integer values of n using a transfer matrix approach: the expression is determined by the leading eigenvector of $N(n)$. In this way, however, we are in general unable to provide an efficient analytic continuation for $n \rightarrow 1$.

The entanglement entropy is split in configurational and number entropy contributions: defining

$$p(\alpha) = \langle \mathcal{O}_{\chi,1} | N^{\alpha_1} N^{\alpha_2} \dots | S \rangle, \quad (\text{D21})$$

then it is clear we can write

$$S^{(\ell)} \equiv \lim_{n \rightarrow 1} \frac{\text{tr}[\rho_\ell^{GGE n}]}{1-n} = \sum_\alpha S_{\text{num}}^{(\ell)} + S_{\text{conf}}^{(\ell)} \quad (\text{D22})$$

$$S_{\text{num}}^{(\ell)} = \sum_\alpha -p(\alpha) \log(p(\alpha))$$

$$S_{\text{conf}}^{(\ell)} = \sum_\alpha -p(\alpha) \log(d_\alpha^{(\ell)}) \quad d_\alpha^{(\ell)} = \prod_{i=1}^{L_A} d_{\alpha_i}^{(\ell)}.$$

For a generic MPS the classical probability distribution $p(\alpha)$ is not the product of independent distribution at each site, making its Shannon entropy (which is the number entropy, in our language) hard to evaluate explicitly. In the case of bond dimension one, instead, it simplifies in the product of L_A independent distributions with $p(\alpha) = c_\alpha^{(\ell)}$. The Shannon entropy becomes then additive, and, since we choose a translational invariant states, one has

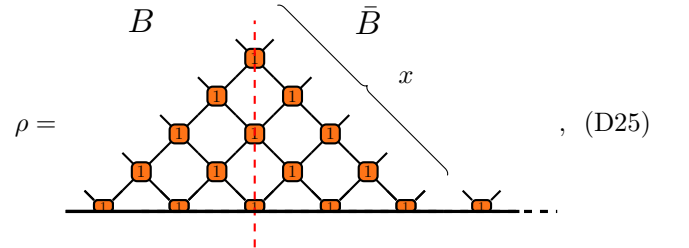
$$S_{\text{num}} = L_A \sum_\alpha c_\alpha^{(\ell)} \log(c_\alpha^{(\ell)}). \quad (\text{D23})$$

We now prove that for a left charged solvable state one has

$$S^{(\ell)} \geq L_A s^{(r)}, \quad (\text{D24})$$

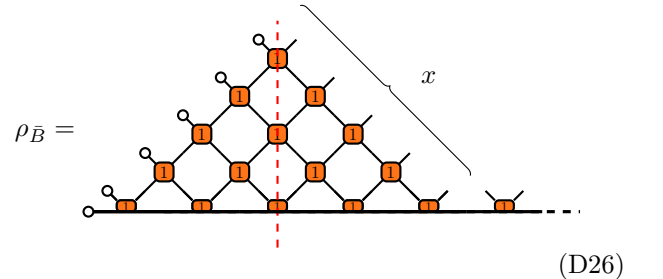
even when $p(\alpha)$ is not factorised.

We start by considering the following pure state



$$\rho = \text{[Diagram]}, \quad (\text{D25})$$

where the bottom line is built with our left-solvable MPS and is understood to be infinite in the right direction. We consider its entanglement across the bipartition $B\bar{B}$ shown with a red dashed line. Tracing out B , and simplifying the transfer matrices with the leading eigenvector, we find



$$\rho_{\bar{B}} = \text{[Diagram]}, \quad (\text{D26})$$

and then, combining solvability, charge conservation and

dual unitarity, we can simplify it as

$$\text{Diagram (D27)} \quad , \quad (D27)$$

so that, apart from a $o(1)$ contribution from the initial MPS, its Rényi entropies are given by

$$S^{(n)}[\rho_B] = x s_n^{(r)}. \quad (D28)$$

Let us now trace Eq. (D25) from the side of \bar{B} . We want to apply on each of the x open leg on the triangle the following quantum channel

$$\mathcal{E}^{(\ell)}[X] = \sum_{\beta=1}^{m_\ell} \frac{\Pi_\beta^{(\ell)}}{d_\beta^{(\ell)}} \text{tr} [X \Pi_\beta^{(\ell)}], \quad (D29)$$

which is unital (preserves the identity) and can be written in Kraus form (it is the same channel considered in the previous subsection, i.e., it corresponds to the transfer matrix in Eq. (D5)).

On the left open leg of the auxiliary MPS space we instead apply the unital quantum channel

$$\mathcal{E}^\chi[X] = \frac{\mathbb{1}_X}{\chi} \text{tr} [X]. \quad (D30)$$

After the application of these channels, the reduced density matrix can be represented as

$$\left(\mathcal{E}^{(\ell) \otimes x} \otimes \mathcal{E}^\chi \right) [\rho_B] = \sum_{\beta} \frac{1}{d_\beta^{(\ell)}} \quad , \quad (D31)$$

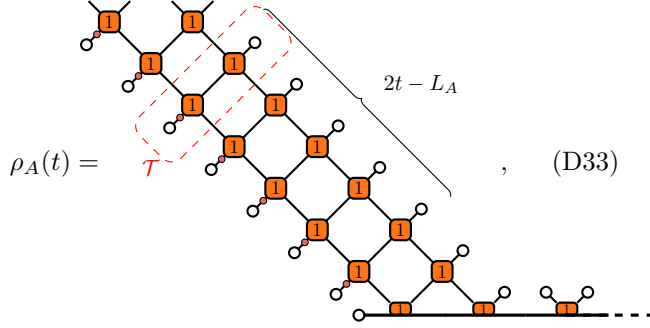
where we substituted the leading eigenvector of the MPS transfer matrix on the right, as per Eq. (64), and the sum is over all strings of left charges β of length x . Moving all the charges to the base of the triangle, it is immediate to see that we recover ρ_ℓ^{GGE} , defined on the x left-sites. Since a unital quantum channel can only increase the Rényi entropies [105], this shows that the Rényi entropies of (D31), and thus those of ρ_ℓ^{GGE} , are always larger than $S^{(n)}[\rho_B] = S^{(n)}[\rho_{\bar{B}}] = x s_n^{(r)}$. This proves Eqs. (D24) and (100) in the main text.

3. Bound on the rate of growth of entanglement in the second phase

To prove the bound in Eq. (101) we begin by observing that

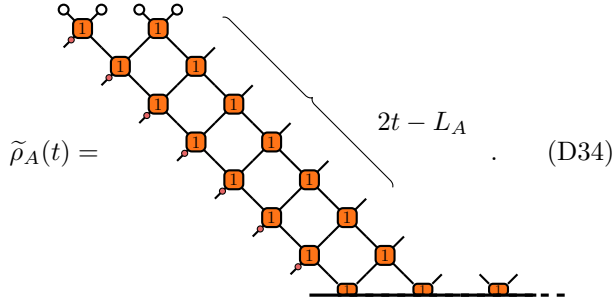
$$\text{tr}[\rho_A(t)^n] = \text{tr}[\tilde{\rho}_A(t)^n], \quad (D32)$$

where we noted that $\rho_A(t)$ in Eq. (94) can be written as



$$\rho_A(t) = \text{[Diagram]} , \quad (\text{D33})$$

and we defined

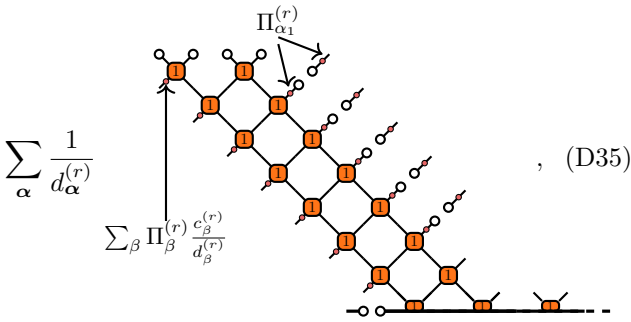


$$\tilde{\rho}_A(t) = \text{[Diagram]} . \quad (\text{D34})$$

The identity follows from the fact that the above diagrams with all legs open corresponds to a pure state and the white bullets correspond to a trace. Therefore, Eq. (D32) is just stating that two reduced density matrices obtained by tracing out two complementary subsystems of a pure state have the same spectrum.

Next, we apply the quantum channel in Eq. (D29), but defined with right-moving solitons, on the open legs on the right of the matrix in Eq. (D34), i.e.,

$$\left(\mathcal{E}^{(r)}\right)^{\otimes 2t-L_A} [\tilde{\rho}_A] =$$



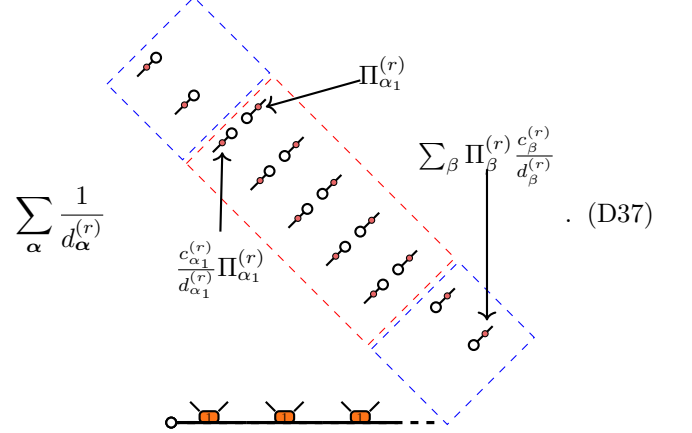
$$\sum_{\alpha} \frac{1}{d_{\alpha}^{(r)}} \text{[Diagram]} , \quad (\text{D35})$$

where we set

$$d_{\alpha}^{(r)} \equiv \prod_i d_{\alpha_i}^{(r)} \quad (\text{D36})$$

and the sum is over strings of $2t - L_A$ projectors on α_i (the charges on right side). In the above equation we also reported the explicit form of the solitons on the leftmost diagonal (which are a linear combination of projectors instead).

The data processing inequality generalised for Rényi entropies, see Ref. [105], implies that a unital quantum channel can only increase the entropies, so the entropies of (D35) will provide an upper bound on the desired ones. We can simplify the diagram using unitarity, dual unitarity and left charged solvability of the initial state to obtain



$$\sum_{\alpha} \frac{1}{d_{\alpha}^{(r)}} \text{[Diagram]} . \quad (\text{D37})$$

From (D37) we can exactly compute the entanglement entropy, finding (we report only the expression for the Von Neumann entropy and neglect the initial entanglement of the state)

$$(2t - L_A) \sum_{\alpha} \left(2c_{\alpha}^{(r)} \log d_{\alpha}^{(r)} - c_{\alpha}^{(r)} \log(c_{\alpha}) \right) + \quad (\text{D38})$$

$$L_A \sum_{\alpha} \left(c_{\alpha}^{(r)} \log d_{\alpha}^{(r)} - c_{\alpha}^{(r)} \log(c_{\alpha}) \right) = S[\mathcal{E}[\tilde{\rho}_A]] \geq S[\rho_A],$$

which proves Eq. (101).

Appendix E: Simplification of Eq. (133)

In the limit $n \rightarrow 1$, the two quantities in Eq. (133) can be written as (taking the log and dividing the result by $1/(1-n)$)

$$s_{\text{num}}^{(r)} + 2s_{\text{conf}}^{(r)},$$

$$\sum_{\alpha, \beta} -c_{\alpha, \beta} \log(c_{\alpha, \beta}) + s_{\text{conf}}^{(\ell)} + s_{\text{conf}}^{(r)}. \quad (\text{E1})$$

We use a chain of inequalities based on the fact that, by assumption,

$$s^{(r)} = s_{\text{num}}^{(r)} + s_{\text{conf}}^{(r)} < s^{(\ell)} = s_{\text{num}}^{(\ell)} + s_{\text{conf}}^{(\ell)}. \quad (\text{E2})$$

The inequalities are as follows

$$s_{\text{num}}^{(r)} + 2s_{\text{conf}}^{(r)} < s_{\text{num}}^{(\ell)} + s_{\text{conf}}^{(\ell)} + s_{\text{conf}}^{(r)} <$$

$$< s_{\text{conf}}^{(\ell)} + s_{\text{conf}}^{(r)} - \sum_{\alpha, \beta} c_{\alpha, \beta} \log(c_{\alpha, \beta}). \quad (\text{E3})$$

Here in the last step, we used the fact that, since

$$c_\alpha^{(r)} = \sum_\beta c_{\alpha,\beta} \implies c_\alpha^{(r)} \succ c_{\alpha,\beta}, \quad (\text{E4})$$

the (classical) distribution of $c_\alpha^{(r)}$ majorises the one $c_{\alpha,\beta}$, meaning that its corresponding entropy has to be strictly less, i.e.

$$\sum_{\alpha,\beta} -c_{\alpha,\beta} \log(c_{\alpha,\beta}) \geq s_{\text{conf}}^{(\ell)}. \quad (\text{E5})$$

The chain in Eq. (E3) proves the desired inequality.

-
- [1] L. Amico, R. Fazio, A. Osterloh, and V. Vedral, Entanglement in many-body systems, *Rev. Mod. Phys.* **80**, 517 (2008).
- [2] P. Calabrese, J. Cardy, and B. Doyon, Entanglement entropy in extended quantum systems, *Journal of Physics A: Mathematical and Theoretical* **42**, 500301 (2009).
- [3] L. F. Santos, A. Polkovnikov, and M. Rigol, Entropy of isolated quantum systems after a quench, *Phys. Rev. Lett.* **107**, 040601 (2011).
- [4] V. Gurarie, Global large time dynamics and the generalized gibbs ensemble, *Journal of Statistical Mechanics: Theory and Experiment* **2013**, P02014 (2013).
- [5] N. Laflorencie, Quantum entanglement in condensed matter systems, *Phys. Rep.* **646**, 1 (2016).
- [6] P. Calabrese, Entanglement and thermodynamics in non-equilibrium isolated quantum systems, *Physica A: Statistical Mechanics and its Applications* **504**, 31 (2018), lecture Notes of the 14th International Summer School on Fundamental Problems in Statistical Physics.
- [7] B. Bertini, K. Klobas, V. Alba, G. Lagnese, and P. Calabrese, Growth of rényi entropies in interacting integrable models and the breakdown of the quasiparticle picture, *Phys. Rev. X* **12**, 031016 (2022).
- [8] P. Calabrese and J. Cardy, Evolution of entanglement entropy in one-dimensional systems, *J. Stat. Mech.: Theory Exp.* **2005** (04), P04010.
- [9] M. Fagotti and P. Calabrese, Evolution of entanglement entropy following a quantum quench: Analytic results for the XY chain in a transverse magnetic field, *Phys. Rev. A* **78**, 010306 (2008).
- [10] V. Alba and P. Calabrese, Entanglement dynamics after quantum quenches in generic integrable systems, *SciPost Phys.* **4**, 17 (2018).
- [11] V. Alba and P. Calabrese, Entanglement and thermodynamics after a quantum quench in integrable systems, *Proc. Natl. Acad. Sci. U.S.A.* **114**, 7947 (2017).
- [12] G. Lagnese, P. Calabrese, and L. Piroli, Entanglement dynamics of thermofield double states in integrable models, 2112.02008 (2021), arXiv:2112.02008.
- [13] H. Liu and S. J. Suh, Entanglement tsunami: Universal scaling in holographic thermalization, *Phys. Rev. Lett.* **112**, 011601 (2014).
- [14] C. T. Asplund, A. Bernamonti, F. Galli, and T. Hartman, Entanglement scrambling in 2d conformal field theory, *J. High Energy Phys.* **2015** (9), 110.
- [15] A. M. Läuchli and C. Kollath, Spreading of correlations and entanglement after a quench in the one-dimensional bose–hubbard model, *J. Stat. Mech.: Theory Exp.* **2008** (05), P05018.
- [16] H. Kim and D. A. Huse, Ballistic spreading of entanglement in a diffusive nonintegrable system, *Phys. Rev. Lett.* **111**, 127205 (2013).
- [17] R. Pal and A. Lakshminarayan, Entangling power of time-evolution operators in integrable and nonintegrable many-body systems, *Phys. Rev. B* **98**, 174304 (2018).
- [18] B. Bertini, P. Kos, and T. Prosen, Entanglement spreading in a minimal model of maximal many-body quantum chaos, *Phys. Rev. X* **9**, 021033 (2019).
- [19] L. Piroli, B. Bertini, J. I. Cirac, and T. Prosen, Exact dynamics in dual-unitary quantum circuits, *Phys. Rev. B* **101**, 094304 (2020).
- [20] S. Gopalakrishnan and A. Lamacraft, Unitary circuits of finite depth and infinite width from quantum channels, *Phys. Rev. B* **100**, 064309 (2019).
- [21] A. Nahum, S. Vijay, and J. Haah, Operator spreading in random unitary circuits, *Phys. Rev. X* **8**, 021014 (2018).
- [22] C. W. von Keyserlingk, T. Rakovszky, F. Pollmann, and S. L. Sondhi, Operator Hydrodynamics, OTOCs, and Entanglement Growth in Systems without Conservation Laws, *Phys. Rev. X* **8**, 021013 (2018).
- [23] C. Jonay, V. Khemani, and M. Ippoliti, Triunitary quantum circuits, *Phys. Rev. Research* **3**, 043046 (2021).
- [24] A. Foligno, P. Kos, and B. Bertini, Quantum information spreading in generalized dual-unitary circuits, *Phys. Rev. Lett.* **132**, 250402 (2024).
- [25] R. Baxter, *Exactly Solved Models in Statistical Mechanics* (Academic Press, 1982).
- [26] P. Hosur, X.-L. Qi, D. A. Roberts, and B. Yoshida, Chaos in quantum channels, *Journal of High Energy Physics* **2016**, 1 (2016).
- [27] A. Nahum, J. Ruhman, S. Vijay, and J. Haah, Quantum entanglement growth under random unitary dynamics, *Phys. Rev. X* **7**, 031016 (2017).
- [28] B. Bertini, P. Kos, and T. Prosen, Exact spectral form factor in a minimal model of many-body quantum chaos, *Phys. Rev. Lett.* **121**, 264101 (2018).
- [29] V. Khemani, A. Vishwanath, and D. A. Huse, Operator spreading and the emergence of dissipative hydrodynamics under unitary evolution with conservation laws, *Phys. Rev. X* **8**, 031057 (2018).
- [30] A. Chan, A. De Luca, and J. T. Chalker, Solution of a minimal model for many-body quantum chaos, *Phys. Rev. X* **8**, 041019 (2018).
- [31] B. Bertini, P. Kos, and T. Prosen, Exact correlation functions for dual-unitary lattice models in 1 + 1 dimensions, *Phys. Rev. Lett.* **123**, 210601 (2019).
- [32] A. J. Friedman, A. Chan, A. De Luca, and J. T. Chalker, Spectral statistics and many-body quantum chaos with conserved charge, *Phys. Rev. Lett.* **123**, 210603 (2019).
- [33] Y. Li, X. Chen, and M. P. A. Fisher, Measurement-driven entanglement transition in hybrid quantum cir-

- cuits, *Phys. Rev. B* **100**, 134306 (2019).
- [34] B. Skinner, J. Ruhman, and A. Nahum, Measurement-induced phase transitions in the dynamics of entanglement, *Phys. Rev. X* **9**, 031009 (2019).
- [35] T. Rakovszky, F. Pollmann, and C. W. von Keyserlingk, Sub-ballistic growth of Rényi entropies due to diffusion, *Phys. Rev. Lett.* **122**, 250602 (2019).
- [36] A. Zabalo, M. J. Gullans, J. H. Wilson, S. Gopalakrishnan, D. A. Huse, and J. H. Pixley, Critical properties of the measurement-induced transition in random quantum circuits, *Phys. Rev. B* **101**, 060301(R) (2020).
- [37] B. Bertini, K. Klobas, P. Kos, and D. Malz, Quantum and classical dynamics with random permutation circuits (2024), arXiv:2407.11960 [cond-mat.stat-mech].
- [38] M. P. A. Fisher, V. Khemani, A. Nahum, and S. Vijay, Random quantum circuits, arXiv:2207.14280 (2022).
- [39] K. Klobas, B. Bertini, and L. Piroli, Exact thermalization dynamics in the “Rule 54” quantum cellular automaton, *Phys. Rev. Lett.* **126**, 160602 (2021).
- [40] T. Prosen, Many-body quantum chaos and dual-unitarity round-a-face, *Chaos: An Interdisciplinary Journal of Nonlinear Science* **31**, 093101 (2021), <https://doi.org/10.1063/5.0056970>.
- [41] P. Kos, B. Bertini, and T. Prosen, Correlations in perturbed dual-unitary circuits: Efficient path-integral formula, *Phys. Rev. X* **11**, 011022 (2021).
- [42] P. W. Claeys, M. Henry, J. Vicary, and A. Lamacraft, Exact dynamics in dual-unitary quantum circuits with projective measurements, *Phys. Rev. Res.* **4**, 043212 (2022).
- [43] B. Bertini, P. Kos, and T. Prosen, Exact spectral statistics in strongly localized circuits, *Phys. Rev. B* **105**, 165142 (2022).
- [44] P. Kos and G. Styliaris, Circuits of space and time quantum channels, *Quantum* **7**, 1020 (2023).
- [45] B. Bertini, C. De Fazio, J. P. Garrahan, and K. Klobas, Exact quench dynamics of the Floquet quantum East model at the deterministic point, arXiv:2310.06128 (2023).
- [46] N. Laflorencie and S. Rachel, Spin-resolved entanglement spectroscopy of critical spin chains and luttinger liquids, *J. Stat. Mech.: Theory Exp.* **2014** (11), P11013.
- [47] M. Goldstein and E. Sela, Symmetry-resolved entanglement in many-body systems, *Phys. Rev. Lett.* **120**, 200602 (2018).
- [48] J. C. Xavier, F. C. Alcaraz, and G. Sierra, Equipartition of the entanglement entropy, *Phys. Rev. B* **98**, 041106 (2018).
- [49] R. Bonsignori, P. Ruggiero, and P. Calabrese, Symmetry resolved entanglement in free fermionic systems, *J. Phys. A: Math. Theor.* **52**, 475302 (2019).
- [50] S. Murciano, G. Di Giulio, and P. Calabrese, Entanglement and symmetry resolution in two dimensional free quantum field theories, *J. High Energy Phys.* **2020** (8), 1.
- [51] F. Ares, S. Murciano, and P. Calabrese, Entanglement asymmetry as a probe of symmetry breaking, *Nat. Commun.* **14**, 2036 (2023).
- [52] B. Bertini, P. Calabrese, M. Collura, K. Klobas, and C. Rylands, Nonequilibrium full counting statistics and symmetry-resolved entanglement from space-time duality, *Phys. Rev. Lett.* **131**, 140401 (2023).
- [53] B. Bertini, K. Klobas, M. Collura, P. Calabrese, and C. Rylands, Dynamics of charge fluctuations from asymmetric initial states, *Phys. Rev. B* **109**, 184312 (2024).
- [54] G. Perez, R. Bonsignori, and P. Calabrese, Quasiparticle dynamics of symmetry-resolved entanglement after a quench: Examples of conformal field theories and free fermions, *Phys. Rev. B* **103**, L041104 (2021).
- [55] S. Murciano, P. Ruggiero, and P. Calabrese, Symmetry resolved entanglement in two-dimensional systems via dimensional reduction, *J. Stat. Mech.: Theory Exp.* **2020** (8), 083102.
- [56] V. Vitale, A. Elben, R. Kueng, A. Neven, J. Carrasco, B. Kraus, P. Zoller, P. Calabrese, B. Vermersch, and M. Dalmonte, Symmetry-resolved dynamical purification in synthetic quantum matter, *SciPost Phys.* **12**, 106 (2022).
- [57] F. Ares, S. Murciano, E. Vernier, and P. Calabrese, Lack of symmetry restoration after a quantum quench: An entanglement asymmetry study, *SciPost Phys.* **15**, 089 (2023).
- [58] S. Murciano, F. Ares, I. Klich, and P. Calabrese, Entanglement asymmetry and quantum Mpemba effect in the XY spin chain, *J. Stat. Mech.: Theory Exp.* **2024** (1), 013103.
- [59] B. J. J. Khor, D. M. Kürkçüoğlu, T. J. Hobbs, G. N. Perdue, and I. Klich, Confinement and kink entanglement asymmetry on a quantum Ising chain, arXiv:2312.08601 (2023).
- [60] F. Ferro, F. Ares, and P. Calabrese, Non-equilibrium entanglement asymmetry for discrete groups: The example of the XY spin chain, *J. Stat. Mech.: Theory Exp.* **2024**, 023101.
- [61] L. Capizzi and M. Mazzoni, Entanglement asymmetry in the ordered phase of many-body systems: The Ising field theory, *JHEP* **2023**, 144 (2023).
- [62] L. Capizzi and V. Vitale, A universal formula for the entanglement asymmetry of matrix product states, arXiv:2310.01962 (2023).
- [63] C. Rylands, K. Klobas, F. Ares, P. Calabrese, S. Murciano, and B. Bertini, Microscopic origin of the quantum Mpemba effect in integrable systems, arXiv:2310.04419 (2023).
- [64] M. Chen and H.-H. Chen, Rényi entanglement asymmetry in (1+1)-dimensional conformal field theories, *Phys. Rev. D* **109**, 065009 (2024).
- [65] M. Fossati, F. Ares, J. Dubail, and P. Calabrese, Entanglement asymmetry in CFT and its relation to non-topological defects, *J. High Energy Phys.* **2024**, 59.
- [66] F. Caceffo, S. Murciano, and V. Alba, arXiv:2402.02918 (2024).
- [67] F. Ares, S. Murciano, L. Piroli, and P. Calabrese, An entanglement asymmetry study of black hole radiation, arXiv:2311.12683 (2023).
- [68] S. Liu, H.-K. Zhang, S. Yin, and S.-X. Zhang, Symmetry restoration and quantum Mpemba effect in symmetric random circuits, arXiv:2403.08459 (2024).
- [69] S. Yamashika, F. Ares, and P. Calabrese, Entanglement asymmetry and quantum Mpemba effect in two-dimensional free-fermion systems, arXiv:2403.04486 (2024).
- [70] F. Ares, V. Vitale, and S. Murciano, The quantum Mpemba effect in free-fermionic mixed states (2024), arXiv:2405.08913.
- [71] K. Chalas, F. Ares, C. Rylands, and P. Calabrese, Multiple crossing during dynamical symmetry restoration and implications for the quantum Mpemba effect (2024),

- arXiv:2405.04436.
- [72] X. Turkeshi, P. Calabrese, and A. D. Luca, Quantum Mpemba effect in random circuits (2024), arXiv:2405.14514.
- [73] K. Klobas, C. Rylands, and B. Bertini, Translation symmetry restoration under random unitary dynamics (2024), arXiv:2406.04296.
- [74] M. Lastres, S. Murciano, F. Ares, and P. Calabrese, Entanglement asymmetry in the critical xxz spin chain (2024), arXiv:2407.06427 [cond-mat.stat-mech].
- [75] F. Benini, V. Godet, and A. H. Singh, Entanglement asymmetry in conformal field theory and holography (2024), arXiv:2407.07969 [hep-th].
- [76] E. B. Mpemba and D. G. Osborne, Cool?, Phys. Educ. **4**, 172 (1969).
- [77] G. Giudice, G. Giudici, M. Sonner, J. Thoenness, A. Lerose, D. A. Abanin, and L. Piroli, Temporal entanglement, quasiparticles, and the role of interactions, Phys. Rev. Lett. **128**, 220401 (2022).
- [78] B. Bertini, P. Kos, and T. Prosen, Operator entanglement in local quantum circuits ii: Solitons in chains of qubits, SciPost Physics **8**, 68 (2020).
- [79] T. Holden-Dye, L. Masanes, and A. Pal, Fundamental charges for dual-unitary circuits (2023), arXiv:2312.14148 [quant-ph].
- [80] B. Bertini, P. Kos, and T. Prosen, Operator Entanglement in Local Quantum Circuits I: Chaotic Dual-Unitary Circuits, SciPost Phys. **8**, 67 (2020).
- [81] T. Farrelly, A review of Quantum Cellular Automata, Quantum **4**, 368 (2020).
- [82] H. C. Po, L. Fidkowski, T. Morimoto, A. C. Potter, and A. Vishwanath, Chiral floquet phases of many-body localized bosons, Phys. Rev. X **6**, 041070 (2016).
- [83] H. C. Po, L. Fidkowski, A. Vishwanath, and A. C. Potter, Radical chiral floquet phases in a periodically driven kitaev model and beyond, Phys. Rev. B **96**, 245116 (2017).
- [84] F. Harper and R. Roy, Floquet topological order in interacting systems of bosons and fermions, Phys. Rev. Lett. **118**, 115301 (2017).
- [85] L. Fidkowski, H. C. Po, A. C. Potter, and A. Vishwanath, Interacting invariants for floquet phases of fermions in two dimensions, Phys. Rev. B **99**, 085115 (2019).
- [86] Z. Gong, A. Nahum, and L. Piroli, Coarse-grained entanglement and operator growth in anomalous dynamics, Phys. Rev. Lett. **128**, 080602 (2022).
- [87] L. Zadnik, M. Ljubotina, Žiga Krajnik, E. Ilievski, and T. Prosen, Quantum many-body spin ratchets (2024), arXiv:2406.01571 [cond-mat.stat-mech].
- [88] A. Lukin, M. Rispoli, R. Schittko, M. E. Tai, A. M. Kaufman, S. Choi, V. Khemani, J. Léonard, and M. Greiner, Probing entanglement in a many-body-localized system, Science **364**, 256 (2019).
- [89] G. Perez, R. Bonsignori, and P. Calabrese, Quasiparticle dynamics of symmetry-resolved entanglement after a quench: Examples of conformal field theories and free fermions, Phys. Rev. B **103**, L041104 (2021).
- [90] G. Perez, R. Bonsignori, and P. Calabrese, Exact quench dynamics of symmetry resolved entanglement in a free fermion chain, J. Stat. Mech.: Theory Exp. **2021** (9), 093102.
- [91] C. Jonay, D. A. Huse, and A. Nahum, Coarse-grained dynamics of operator and state entanglement, arXiv:1803.00089 (2018).
- [92] T. Zhou and A. Nahum, Entanglement membrane in chaotic many-body systems, Phys. Rev. X **10**, 031066 (2020).
- [93] L. K. Joshi, J. Franke, A. Rath, F. Ares, S. Murciano, F. Kranzl, R. Blatt, P. Zoller, B. Vermersch, P. Calabrese, C. F. Roos, and M. K. Joshi, Observing the quantum Mpemba effect in quantum simulations, arXiv:2401.04270 (2024).
- [94] B. Bertini, P. Kos, and T. Prosen, Operator entanglement in local quantum circuits II: Solitons in chains of qubits, SciPost Phys. **8**, 068 (2020).
- [95] M. Borsi and B. Pozsgay, Construction and the ergodicity properties of dual unitary quantum circuits, Phys. Rev. B **106**, 014302 (2022).
- [96] P. W. Claeys and A. Lamacraft, Ergodic and non-ergodic dual-unitary quantum circuits with arbitrary local Hilbert space dimension, Phys. Rev. Lett. **126**, 100603 (2021).
- [97] J. I. Cirac, D. Pérez-García, N. Schuch, and F. Verstraete, Matrix product states and projected entangled pair states: Concepts, symmetries, theorems, Rev. Mod. Phys. **93**, 045003 (2021).
- [98] A. Foligno and B. Bertini, Entanglement of disjoint intervals in dual unitary circuits: Exact results, in preparation.
- [99] P. Calabrese, Entanglement spreading in non-equilibrium integrable systems, SciPost Phys. Lect. Notes, **20** (2020).
- [100] R. Suzuki, K. Mitarai, and K. Fujii, Computational power of one- and two-dimensional dual-unitary quantum circuits, Quantum **6**, 631 (2022).
- [101] A. Foligno, T. Zhou, and B. Bertini, Temporal entanglement in chaotic quantum circuits, Phys. Rev. X **13**, 041008 (2023).
- [102] X.-H. Yu, Z. Wang, and P. Kos, Hierarchical generalization of dual unitarity, arXiv:2307.03138 (2023).
- [103] Note that in general the members of this space are not hermitian (because we allow for linear combination with complex coefficient) but they will be normal operators, because by assumption the solitons $\sigma_i^{(r)}$ commute with each other.
- [104] D. E. Evans and R. Høegh-Krohn, Spectral properties of positive maps on c^* -algebras, Journal of the London Mathematical Society **s2-17**, 345 (1978).
- [105] R. L. Frank and E. H. Lieb, Monotonicity of a relative rényi entropy, Journal of Mathematical Physics **54**, 122201 (2013).

Chapter 6

Entanglement of disjoint intervals in dual unitary circuits: exact results

6.1 Summary

In this work, we consider entanglement growth for a subsystem made of two disjoint intervals, interacting with an infinite environment, evolved with dual unitary gates.

We show that, when the intervals are far enough, the entanglement growth is connected to the leading eigenvector of a suitable transfer matrix built with the local gate.

We pick a specific family of dual unitary gates in arbitrary local dimension (as a generic parametrization is not yet known) and prove that almost certainly the leading eigenvector of the aforementioned transfer matrix is non-degenerate, showing how this implies that the entanglement dynamics follows the membrane picture.

Instead, choosing dual unitary gates with conserved charges, we prove a

rigorous bound showing the dynamics expected for an integrable system. Moreover, our results on the spectrum of this transfer matrix, and in particular how it differs whether the gate has ballistic conserved charges or not, have implications on other properties of the dynamics, such as correlation functions of local operators, shedding light on the difference between chaotic and charge conserving dynamics.

Entanglement of Disjoint Intervals in Dual-Unitary Circuits: Exact Results

Alessandro Foligno^{1,2} and Bruno Bertini³

¹*School of Physics and Astronomy, University of Nottingham, Nottingham, NG7 2RD, UK*

²*Centre for the Mathematics and Theoretical Physics of Quantum Non-Equilibrium Systems, University of Nottingham, Nottingham, NG7 2RD, UK*

³*School of Physics and Astronomy, University of Birmingham, Edgbaston, Birmingham, B15 2TT, UK*

We study the entanglement dynamics for dual unitary circuits for a disjoint subsystem from a simple initial state. We prove rigorously, after an appropriate limit, that the entanglement dynamics for a dual unitary circuit almost certainly behaves according to the prediction from the membrane picture; at the same time we show that the results are qualitatively different if the dual unitary gates are not generic, but possess a charge structure, in which case the entanglement agrees qualitatively with the membrane picture, although in general such gates do not possess quasiparticles.

Under very general conditions, a quantum quench triggers the linear growth of the entanglement entropy between the finite parts of a quantum many-body system [1–16]. This phenomenon can be explained very generally using a duality between space and time [17], which interprets the linear growth as another manifestation of the extensivity of the stationary entropy. The underlying mechanisms driving the growth, however, are believed to depend on the nature of the dynamics, i.e., on whether the system is integrable or chaotic. In the first case the growth is explained in terms of the motion of correlated quasiparticles produced by the quench, while in the second of the expansion of the minimal space-time membranes separating the subsystems. The theories describing these two mechanisms are respectively known as *quasiparticle picture* [1] and *membrane picture* [18, 19].

In one dimension, both theories yield the same qualitative prediction — linear growth followed by saturation — for the entanglement of a single, connected interval. For subsystems with more complicated geometries, however, the predictions of the two theories differ, providing spectacular macroscopic displays of the nature of the microscopic dynamics. For instance, consider a subsystem A made of two intervals of equal size ℓ , separated by a distance $x \gg \ell$. After an initial linear growth phase and saturation, the quasiparticle picture predicts a temporary drop in the entanglement entropy when the two intervals become causally connected, i.e., for times $t \in [x/2v_{\text{qp}}, (x + \ell)/2v_{\text{qp}}]$, where v_{qp} is the quasiparticle speed [20]. Instead, according to the membrane picture, once the entanglement saturates after the initial growth phase, its value remains constant, see Fig. 1.

Currently, however, the only exact results substantiating this picture have been obtained in conformal field theory [7, 21], for non-interacting spin chains [22], and for random unitary circuits in the limit of large local Hilbert space dimension [10]. No exact result exists for clean, microscopic systems in the presence of interactions. In this paper we fill this gap and present a rigorous proof of the occurrence of these different behaviours for dual-unitary circuits [23], a class of quantum circuits that has been extensively studied in recent years [16, 23–28]. These circuits generically exhibit chaotic behaviour,

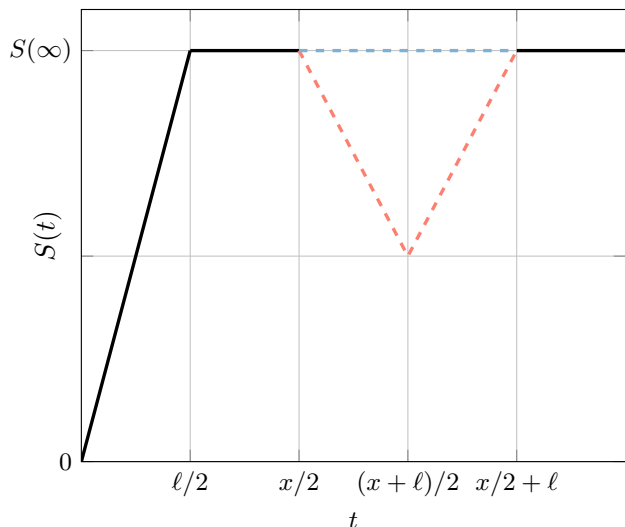


FIG. 1. The entanglement of the disjoint subsystem $A = [0, \ell] \cup [\ell + x, 2\ell + x]$ — composed by two intervals of size ℓ separated by a distance $x > \ell$ — according to the membrane picture (dashed blue) and the quasiparticle one (dashed red). The continuous black line refers to the points on which both predictions agree. The quasiparticles are taken to move at speed $v_{\text{qp}} = 1$.

and we will indeed prove that they generically follow the membrane picture in Fig. 1, however, they can also be equipped with a charge structure [29–31], which can drastically affect their entanglement dynamics [32]. We will show that, although they are generically non-integrable, charged dual unitary circuits follow the quasiparticle prediction in Fig. 1.

More specifically we consider locally interacting quantum many-body systems of qudits in discrete space time. A step of time evolution is implemented by the many-body unitary operator \mathbb{U} constructed in terms of a two-qudit gate U through the following brickwork pattern

$$\mathbb{U} = \mathbb{U}_e \mathbb{U}_o, \quad \mathbb{U}_e = \bigotimes_{x=0}^L U_{x,x+1/2}, \quad \mathbb{U}_o = \bigotimes_{x=0}^L U_{x+1/2,x}. \quad (1)$$

Here the qubits sit at half integer positions, the operator

$U_{a,b}$ acts as U on the qudits located at a and b , and we denote by $2L$ number of qudits, which we take to be much larger than all other quantities at play. Moreover, we take periodic boundary conditions, so that sites 0 and L coincide, and indicate by d the number of states of each qudit (local Hilbert space dimension).

Our local gate U is *dual-unitary* (DU) [23], meaning that also the matrix \tilde{U} obtained as

$$\langle ij|\tilde{U}|kl\rangle \equiv \langle jl|U|ik\rangle, \quad (2)$$

is a unitary matrix. Physically, this reshuffling corresponds to an exchange of space and time in the quantum circuit [15, 23, 33], therefore DU gates can be defined as those generating unitary dynamics in *both* space and time.

A complete parameterisation of DU gates is only known for $d = 2$ [23], however, families of DU gates are known for any $d \geq 2$ [28, 34–37]. Here we will be interested in the following one

$$\mathcal{S}_L = \{S \cdot U^{[\rho]^L} \cdot (\mathbb{1}_d \otimes v) \quad v, \rho^{(1)}, \dots, \rho^{(d)} \in U(d)\}, \quad (3)$$

where S is the SWAP gate and $U^{[\rho]^L}$ is a control gate defined in terms of d unitary matrices $\rho^{(i)}$ as

$$U^{[\rho]^L}(|i\rangle \otimes |j\rangle) = |i\rangle \otimes \rho^{(i)}|j\rangle. \quad (4)$$

When seen as a manifold, the set \mathcal{S}_L has a number of parameters scaling as d^3 for large d . This is the largest known scaling observed in the known families of DU gates [36, 37]. This set, however, is not the only known one with this property. For instance, one can construct a different family, \mathcal{S}_R , by applying a spatial reflection on the elements of \mathcal{S}_L . Namely, $\mathcal{S}_R = S \cdot \mathcal{S}_L \cdot S$. Note that for $d = 2$, both \mathcal{S}_L and \mathcal{S}_R coincide with the set of all DU gates [23].

We now consider a quantum quench from an initial state made of maximally entangled Bell pairs among nearest neighbour, i.e.,

$$|\Psi_0\rangle = \bigotimes_{x=1}^L \sum_{i=1}^d \frac{|i\rangle_x |i\rangle_{x+1/2}}{\sqrt{d}}, \quad (5)$$

and compute the entanglement between a region A and its complement by measuring the entanglement entropy $S_A(t) \equiv -\text{tr}[\rho_A(t) \log \rho_A(t)]$, where $\rho_A(t)$ is the density matrix of A . As anticipated before, we consider the case in which A is composed of two intervals of length ℓ (meaning they contain 2ℓ qudits in our units) separated by a region of length $x > \ell$.

The evolution of quantum circuits is conveniently represented graphically. Specifically, we introduce the following diagrammatic notation for gate and initial state, in a one-replica, or *folded* space

$$U \otimes U^* = \begin{array}{c} \circ \\ \diagdown \quad \diagup \\ \boxed{1} \\ \diagup \quad \diagdown \\ \circ \end{array}, \quad (6)$$

$$|\Psi_0\rangle\langle\Psi_0| = \frac{1}{d^L} \underbrace{\quad} \quad \underbrace{\quad} \quad \underbrace{\quad} \quad \underbrace{\quad}. \quad (7)$$

The local trace operation becomes a state which we represent with a white circle:

$$|\circ\rangle = \left(\sum_{i=1}^d |i, i\rangle \right) \equiv \text{---}\circ. \quad (8)$$

In this notation, the dual-unitarity property is expressed by the graphical rules

$$\begin{array}{c} \circ \\ \diagdown \quad \diagup \\ \boxed{1} \\ \diagup \quad \diagdown \\ \circ \end{array} = \begin{array}{c} \circ \\ \diagdown \\ \diagup \\ \circ \end{array}, \quad \begin{array}{c} \diagdown \quad \diagup \\ \boxed{1} \\ \diagdown \quad \diagup \\ \circ \quad \circ \end{array} = \begin{array}{c} \circ \\ \diagdown \\ \diagup \\ \circ \end{array}, \quad (9)$$

$$\begin{array}{c} \diagdown \quad \diagup \\ \boxed{1} \\ \diagdown \quad \diagup \\ \circ \quad \circ \end{array} = \begin{array}{c} \circ \\ \diagdown \\ \diagup \\ \circ \end{array}, \quad \begin{array}{c} \circ \\ \diagdown \quad \diagup \\ \boxed{1} \\ \diagup \quad \diagdown \\ \circ \end{array} = \begin{array}{c} \circ \\ \diagdown \\ \diagup \\ \circ \end{array}, \quad (10)$$

and $\rho_A(t)$ as in Fig. 2. For all the times where the two intervals remain causally disconnected, $t \leq x/2$, the entanglement of $\rho_A(t)$ can be characterised exactly. Indeed, using the rules in Eq. 10, we can simplify the top diagram in Fig. 2 to

$$\rho_A \propto \left(\begin{array}{c} \text{---} \circ \quad \circ \quad \text{---} \\ \diagdown \quad \diagup \\ \boxed{A} \\ \diagup \quad \diagdown \\ \circ \quad \circ \end{array} \right)^{\otimes 2} \simeq \begin{array}{c} \circ \quad \circ \\ \diagdown \quad \diagup \\ \circ \quad \circ \end{array} \quad (11)$$

where in the second step we performed a similarity transformation within A , which does not change the entanglement, in order to remove the gates. This gives the following exact expression for entanglement entropy for $t \leq x/2$ which is the one obtained for a single interval in [15], with an extra factor of 2:

$$S_A(t) = 4 \min(2t, \ell) \log(d). \quad (12)$$

With a completely analogous reasoning, using the relations in Eq. (9)-(10), one can also show that at times $t \geq x/2 + \ell$ the state of the region A relaxes to the infinite temperature state: $\rho_A(t \geq x/2 + \ell) \propto \mathbb{1}_{4\ell}$, where $\mathbb{1}_x$ represents the identity operator in \mathbb{C}^{d^x} . Therefore, we have $S_A(t \geq x/2 + \ell) = 4\ell \log(d)$.

The only time interval whose behaviour is not fixed by the combination of unitarity and dual unitarity is thus $x/2 < t < x/2 + \ell$ and, as we shall see, it depends on the specific choice of local gate U . In this regime, the reduced density matrix can be simplified as the one depicted in Fig. 2 (bottom panel). Its expression involves x applications of the following two transfer matrices

$$T_z^L = \begin{array}{c} \diagdown \quad \diagup \\ \circ \quad \circ \\ \diagdown \quad \diagup \\ \boxed{1} \\ \diagup \quad \diagdown \\ \circ \quad \circ \end{array}, \quad T_z^R = \begin{array}{c} \diagup \quad \diagdown \\ \circ \quad \circ \\ \diagup \quad \diagdown \\ \boxed{1} \\ \diagdown \quad \diagup \\ \circ \quad \circ \end{array}, \quad (13)$$

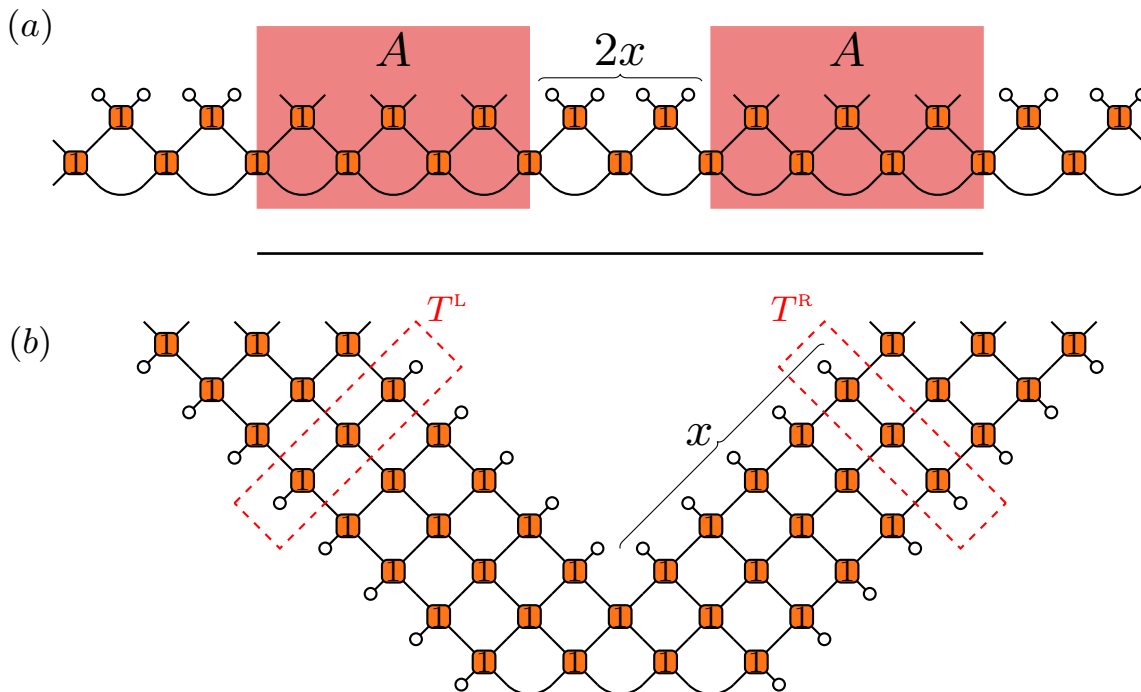


FIG. 2. Top panel: reduced density matrix at initial times $t \leq x$ when the two intervals are not causally connected, and their contribution to the entanglement factorizes. Bottom panel: reduced density matrix at the times where the two intervals are connected by some light-cones, i.e. at times $x/2 < t < \ell + x/2$, which cannot be simplified using only dual unitarity.

circled in red in Fig. 2. This suggests that, for large enough x , the diagram can be simplified by truncating the transfer matrices to their leading eigenspaces. A characterisation of the leading eigenspaces of T_z^L and T_z^R for generic DU gates is provided by the following theorem, which is the first main result of this letter.

Theorem 1. *Randomly drawing U from \mathcal{S}_L produces almost surely a transfer matrix T_z^L with a unique maximal eigenvalue d and both left and right eigenvectors fixed to be $|\mathcal{O}\rangle^{\otimes z}$.*

An analogous result holds when replacing L with R.

Theorem 1 guarantees that, if one draws U at random from, say, \mathcal{S}_L , and then constructs the time evolution operator according to Eq. (1), the diagram in Fig. 2 will be constructed in terms of the matrix T_z^L fulfilling

$$(T_z^L)^x \mapsto (d|\mathcal{O}\rangle\langle\mathcal{O}|)^{\otimes z}, \quad (14)$$

for large enough x . Making this replacement allows one to fully contract the diagram using Eq. 10 to obtain $\rho_A(t) \propto \mathbb{1}_{4\ell}$, showing that also in the regime $x/2 < t < x/2 + \ell$ the reduced state is proportional to the infinite temperature state. This gives an expression for the entanglement entropy at all times

$$S_A(t) = \min(8t, 4\ell) \log(d), \quad x \gg \ell, \quad (15)$$

which agrees with the membrane-picture prediction [10]. We stress that there is no noise in this system: once the

evolution gate U is chosen from \mathcal{S}_L , it is kept constant in both time and space.

Let us now present a proof of Theorem 1. We start by fixing $v = \mathbb{1}_d$ in Eq. (3), and choose a set of d ρ -matrices from $SU(d)$. Then, we can fully characterize the spectrum of T_z^L , since its open legs correspond to the control qudits of the underlying gate, and thus the matrix is diagonal in the computational basis. More precisely, the eigenvectors are in one to one correspondence with pairs of strings of length z , which we represent as $|\mathbf{j}, \mathbf{k}\rangle$, taking values $j_a, k_a = 1, \dots, d$

$$|\mathbf{j}, \mathbf{k}\rangle = \bigotimes_{a=1}^z |j_a\rangle \otimes |k_a\rangle, \quad (16)$$

where the string \mathbf{j} acts on the forward layer of U , and \mathbf{k} on the backward one of U^* ; their corresponding eigenvalue is

$$\lambda_{\mathbf{j}, \mathbf{k}} = e^{i \sum_{a=1}^z \phi_{j_a} - \phi_{k_a}} \text{tr} \left[\rho^{[j_1]} \dots \rho^{[j_z]} \left(\rho^{[k_1]} \dots \rho^{[k_z]} \right)^\dagger \right] \quad (17)$$

Since the product of matrices in the trace is also in $SU(d)$, it is clear that $|\lambda| \leq d$; in order to saturate this bound, the product of ρ s has to be proportional to the identity, with a proportionality factor which has to be a d -root of unity, given the constraint of having determinant = 1.

Now we use a powerful theorem proven in Ref.[38] which

states that any Haar-random choice of a z -tuple of matrices from $SU(d)$ forms a free group with probability 1 (that is, neglecting events with measure 0). This can be rephrased to state that the only product of matrices of arbitrary size built using $\rho^{[i]}, \rho^{[j]^\dagger}$ that is equal to the identity, has to be able to be simplified using unitarity. Since by assumption we must have

$$\rho^{j,k} \equiv \rho^{[j_1]} \dots \rho^{[j_z]} \left(\rho^{[k_1]} \dots \rho^{[k_z]} \right)^\dagger = e^{i\frac{2\pi n}{d}} \mathbf{1}_d, \quad (18)$$

for some integer n , then

$$(\rho^{j,k})^d = \mathbf{1}_d, \quad (19)$$

but given the free group property, this would imply that the left-hand side of (19) has to be simplified to be the identity using only unitarity, which is only possible if $\alpha = \beta$. This shows that the largest eigenvectors of this transfer matrix are of the form $|\alpha, \alpha\rangle$ and their corresponding eigenvalue is exactly d . We now choose a generic value of v in the parametrization (3): the transfer matrix is modified as

$$T_z^L \rightarrow T_z^{L,v} = T_z^L (v \otimes v^*)^{\otimes z}. \quad (20)$$

The matrix T_z^L (built with $v = \mathbf{1}$) is a normal matrix (its eigenvectors (16) are orthonormal) and can be decomposed as

$$T_z^L = (P_{\max} + T_{\text{rem}}), \quad (21)$$

where P_{\max} is the projector on the block with eigenvalue d , while $\|T_{\text{rem}}\|_2 = \sup_{|v\rangle} \frac{\|T_{\text{rem}}|v\rangle\|}{\|v\rangle} < d$ (since the matrix is normal, its singular values are the square norm of eigenvalues); P_{\max} can be written as

$$P_{\max} = \sum_{j \in \mathbb{Z}_d^z} |j, j\rangle\langle j, j| = \left(\sum_{j=1}^d |j, j\rangle\langle j, j| \right)^{\otimes z} \equiv p_{\max}^{\otimes z}. \quad (22)$$

The matrix $T_z^{L,v}$ can have eigenvector with eigenvalue $|\lambda| = d$ if and only if there is a maximal eigenvector of T_z^L which is also an eigenvector of the unitary matrix $(v \otimes v^*)^{\otimes z}$. To see this, let us call $|\psi\rangle$ such eigenvector, then one has

$$d^2 = \langle \psi | T_z^{L,v} (T_z^{L,v})^\dagger | \psi \rangle = \langle \psi | T_z^L (T_z^L)^\dagger | \psi \rangle \implies P_{\max} |\psi\rangle = |\psi\rangle, \quad (23)$$

where we used the fact that, since the matrix T_z^L is normal, the P_{\max} is also the eigenspace corresponding to the maximal singular value of $T_z^L (T_z^L)^\dagger$. This is equivalent to searching for eigenvectors with eigenvalues of largest magnitude of

$$p_{\max}^{\otimes z} (v \otimes v^*)^{\otimes z} p_{\max}^{\otimes z} \equiv w^{\otimes z}; \quad (24)$$

in the orthonormal basis of p_{\max} , the matrix w has matrix elements

$$w_{ij} = \langle i, i | v \otimes v^* | j, j \rangle = |v_{ij}|^2, \quad (25)$$

but, since v is Haar random, with probability 1 one has

$$v_{ij} \neq 0 \quad \forall i, j = 1, \dots, d \implies |v_{ij}|^2 > 0 \quad (26)$$

thus, in this basis, the matrix w will almost certainly have strictly positive entries and, by Perron Frobenius theorem [39], it must have a simple eigenvalue with strictly larger modulus than all the others, with strictly positive entries, which is indeed the bullet state, with eigenvalue 1 and with entries all equal to 1 in this basis, proving thus that $T_z^{L,v}$ will almost certainly have only one eigenvector with largest eigenvalue in modulus.

One can repeat the proof for the right transfer matrix using gates obtained by spatial reflection of Eq. (3), showing that almost certainly they have a strictly larger simple eigenvalue; this implies that the intersection between the two sets, assuming it has a nonzero measure, has this property simultaneously for both left and right transfer matrices with probability 1. Since for $d = 2$ these sets coincide, this shows the statement for almost all such DU gates, simultaneously for left and transfer matrices.

As an application of this, we note that the left-right transfer matrices correspond to the quantum channels

$$\mathcal{M}_z^\pm \Leftrightarrow T_z^{\text{R/L}}, \quad (27)$$

considered for example in Refs. [15]-[28] to study correlation functions of local operators; a gap in the spectrum corresponds to an ergodic behaviour the gate, which thus holds, almost certainly, *for any multisite local operator*. Let us now consider DU with left/right moving solitons as in Ref [40]; in this case, one can always choose a convenient linear combination of these such that they are mutually orthogonal projectors (independently for left and right moving charges) $\Pi_\alpha^{\text{L/R}}$, each acting on a space of dimension $d_\alpha^{\text{L/R}}$ and satisfying a completeness relation:

$$d_\alpha^{\text{L/R}} \equiv \text{tr} \left[\Pi_\alpha^{\text{L/R}} \right] \sum_{\alpha=1}^{m_{\text{L/R}}} \Pi_\alpha^{\text{L/R}} = \mathbf{1}_d. \quad (28)$$

These solitons move ballistically and obey

$$U(\Pi_\alpha^{\text{R}} \otimes \Pi_\beta^{\text{L}}) = (\Pi_\beta^{\text{L}} \otimes \Pi_\alpha^{\text{R}})U. \quad (29)$$

The original DU gate can be *decomposed* into smaller dual unitary blocks, acting on qudits of dimensions $d_\alpha^{\text{R}}, d_\beta^{\text{L}}$

$$U^{\alpha,\beta} = (\Pi_\beta^{\text{L}} \otimes \Pi_\alpha^{\text{R}}) U (\Pi_\alpha^{\text{R}} \otimes \Pi_\beta^{\text{L}}). \quad (30)$$

The expectation value of these charges on the initial state defines a classical probability of being in the sectors α, β in the initial Bell state

$$c_{\alpha,\beta} = \frac{1}{d} \text{tr} \left[\Pi_\alpha^{\text{L}} \Pi_\beta^{\text{R}} \right] \geq 0; \quad (31)$$

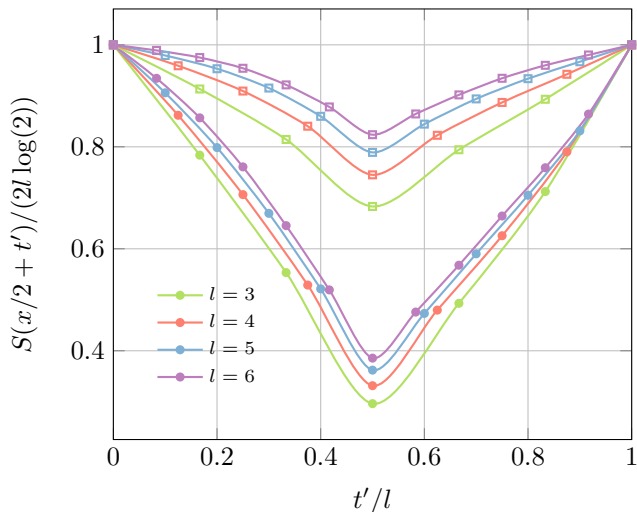


FIG. 3. Numerical simulation for the entanglement entropy in the time interval not fixed by dual unitarity and solvability $t \in [x/2, l+x/2]$ for chaotic gates with different values of l and $x = kl$. In particular the circle marks correspond to the choice $l/x = 1$, while the squares correspond to the choice $l/x = 4$. Notice that, keeping the ratio constant, larger values of x, l tend to flatten and we conjecture that in the scaling limit the plot becomes exactly flat, as predicted by the membrane picture (cf. Fig 1, blue dotted plot)

the marginal distributions give the probability of finding a left/right moving site in the sector α :

$$c_{\beta}^L = \sum_{\alpha=1}^{m_R} c_{\alpha,\beta} \quad c_{\alpha}^R = \sum_{\beta=1}^{m_L} c_{\alpha,\beta} \quad c_{\alpha}^{L/R} = \frac{d^{L/R}}{d}. \quad (32)$$

Our starting point is again the density matrix ρ_A in Fig. 2, since simplifications outside the time interval $x/2 < t < l+x/2$ only require dual unitarity, which holds also in this case. We apply the following quantum channel on each of the l left moving legs of the left part of A in 2:

$$\mathcal{E}^L[X] = \sum_{\alpha=1}^{m_L} \Pi_{\alpha}^L \frac{1}{d_{\alpha}^L} \text{tr} [\Pi_{\alpha}^L X]. \quad (33)$$

and similarly

$$\mathcal{E}^R[X] = \sum_{\alpha=1}^{m_R} \Pi_{\alpha}^R \frac{1}{d_{\alpha}^R} \text{tr} [\Pi_{\alpha}^R X] \quad (34)$$

on the rightmoving legs on the right interval of A .

Now we note that, because of the monotonicity of quantum relative entropy [41], a unital quantum channel can only increase the entanglement entropy, so we have

$$S[\rho_A] \leq S[(\mathcal{E}^R)^{\otimes l} (\mathcal{E}^L)^{\otimes l} [\rho_A]]. \quad (35)$$

Moreover, as we show in the Supplemental Material, the soliton conservation property implies

$$S[(\mathcal{E}^R)^{\otimes l} (\mathcal{E}^L)^{\otimes l} [\rho_A]] = 4l \log(d) - (l - |2t - (x+l)|) I_{L,R}, \quad (36)$$

where $I_{L,R}$ is the classical mutual information between left and right-moving charges, computed using the probability distribution (31)

$$I_{L,R} = \sum_{\alpha,\beta} c_{\alpha,\beta} \log(c_{\alpha,\beta}) - \sum_{\alpha=1}^{m_L} c_{\alpha}^L \log(c_{\alpha}^L) - \sum_{\alpha=1}^{m_R} c_{\alpha}^R \log(c_{\alpha}^R). \quad (37)$$

This shows that, for a DU circuit with conserved charges one has a drop in the value of the entanglement entropy when the two intervals become causally connected (*without* any large distance assumption $x \gg l$ as for the chaotic case), exactly as predicted by the quasiparticle picture, considering that the velocity of the solitons is 1 in this case (although this system does not have, in general, quasiparticles):

$$S\left(\frac{x}{2} < t < \frac{x+l}{2}\right) \leq 4l \log(d) - (l - |2t - (x+l)|) I_{L,R}. \quad (38)$$

This bound holds for any dual unitary gate with one-site conserved charges, including, for example, those studied in [42], although we do not expect the bound to be saturated in that case. In the Supplemental Material, we prove that this bound is saturated if the intervals are far enough apart and each DU block $U^{\alpha,\beta}$ (cf. Eq (30)) has local dimension $d_{\alpha/\beta}^{L/R} = 2$ and is chosen randomly and independently from the others. In this case, large powers of the left/right transfer matrices reduce to the channels used for the bound (33)-(34).

As a final note, we conjecture that our results for the entanglement of chaotic DU gates hold for any $l > x$ in a scaling limit, i.e. choosing $x = k \cdot x_0$, $l = k \cdot l_0$ and taking $k \rightarrow \infty$. We show some numerical evidence for this claim in Fig. 3.

In this work we rigorously showed the occurrence of a qualitatively different entanglement dynamics for a disjoint subsystem evolved using dual unitary gates, depending on whether the gate have conserved charges. This elaborates on the work in [40] which showed a qualitatively different behaviour for the entanglement dynamics of a single connected interval. The free group approach that we employed here is a rather general idea which can be used to investigate other probes of the non-equilibrium dynamics like OTOCs or operator entanglement or spectral statistics, like spectral form factors or the eigenstate thermalization hypothesis.

Acknowledgements — We thank Paolo Tognini for very fruitful discussions and insights on some technical aspects of this work. This research has been supported by the

Royal Society through the University Research Fellowship No. 201101. We warmly acknowledge the hospitality of the Simons Center for Geometry and Physics during the program “Fluctuations, Entanglements, and

Chaos: Exact Results” and the International School for Advanced Studies (SISSA) where part of this work has been performed.

-
- [1] P. Calabrese and J. Cardy, Evolution of entanglement entropy in one-dimensional systems, *J. Stat. Mech.: Theory Exp.* **2005** (04), P04010.
- [2] M. Fagotti and P. Calabrese, Evolution of entanglement entropy following a quantum quench: Analytic results for the XY chain in a transverse magnetic field, *Phys. Rev. A* **78**, 010306 (2008).
- [3] V. Alba and P. Calabrese, Entanglement dynamics after quantum quenches in generic integrable systems, *SciPost Phys.* **4**, 17 (2018).
- [4] V. Alba and P. Calabrese, Entanglement and thermodynamics after a quantum quench in integrable systems, *Proc. Natl. Acad. Sci. U.S.A.* **114**, 7947 (2017).
- [5] G. Lagnese, P. Calabrese, and L. Piroli, Entanglement dynamics of thermofield double states in integrable models, 2112.02008 (2021), arXiv:2112.02008.
- [6] H. Liu and S. J. Suh, Entanglement tsunami: Universal scaling in holographic thermalization, *Phys. Rev. Lett.* **112**, 011601 (2014).
- [7] C. T. Asplund, A. Bernamonti, F. Galli, and T. Hartman, Entanglement scrambling in 2d conformal field theory, *J. High Energy Phys.* **2015** (9), 110.
- [8] A. M. Läuchli and C. Kollath, Spreading of correlations and entanglement after a quench in the one-dimensional bose–hubbard model, *J. Stat. Mech.: Theory Exp.* **2008** (05), P05018.
- [9] H. Kim and D. A. Huse, Ballistic spreading of entanglement in a diffusive nonintegrable system, *Phys. Rev. Lett.* **111**, 127205 (2013).
- [10] A. Nahum, J. Ruhman, S. Vijay, and J. Haah, Quantum entanglement growth under random unitary dynamics, *Phys. Rev. X* **7**, 031016 (2017).
- [11] A. Nahum, S. Vijay, and J. Haah, Operator spreading in random unitary circuits, *Phys. Rev. X* **8**, 021014 (2018).
- [12] C. W. von Keyserlingk, T. Rakovszky, F. Pollmann, and S. L. Sondhi, Operator Hydrodynamics, OTOCs, and Entanglement Growth in Systems without Conservation Laws, *Phys. Rev. X* **8**, 021013 (2018).
- [13] R. Pal and A. Lakshminarayanan, Entangling power of time-evolution operators in integrable and nonintegrable many-body systems, *Phys. Rev. B* **98**, 174304 (2018).
- [14] B. Bertini, P. Kos, and T. Prosen, Entanglement spreading in a minimal model of maximal many-body quantum chaos, *Phys. Rev. X* **9**, 021033 (2019).
- [15] L. Piroli, B. Bertini, J. I. Cirac, and T. Prosen, Exact dynamics in dual-unitary quantum circuits, *Phys. Rev. B* **101**, 094304 (2020).
- [16] S. Gopalakrishnan and A. Lamacraft, Unitary circuits of finite depth and infinite width from quantum channels, *Phys. Rev. B* **100**, 064309 (2019).
- [17] B. Bertini, K. Klobas, V. Alba, G. Lagnese, and P. Calabrese, Growth of rényi entropies in interacting integrable models and the breakdown of the quasiparticle picture, *Phys. Rev. X* **12**, 031016 (2022).
- [18] C. Jonay, D. A. Huse, and A. Nahum, Coarse-grained dynamics of operator and state entanglement, arXiv:1803.00089 (2018).
- [19] T. Zhou and A. Nahum, Entanglement membrane in chaotic many-body systems, *Phys. Rev. X* **10**, 031066 (2020).
- [20] Note that in integrable models one generally has several species of quasiparticles with different velocities. This results in a smoothening of the curve in Fig. 1, see, e.g., Ref. [43]. Here, for simplicity, we focus on the case with a single species of quasiparticles.
- [21] P. Calabrese, J. Cardy, and E. Tonni, Entanglement entropy of two disjoint intervals in conformal field theory, *Journal of Statistical Mechanics: Theory and Experiment* **2009**, P11001 (2009).
- [22] M. Fagotti and P. Calabrese, Entanglement entropy of two disjoint blocks in xy chains, *Journal of Statistical Mechanics: Theory and Experiment* **2010**, P04016 (2010).
- [23] B. Bertini, P. Kos, and T. Prosen, Exact correlation functions for dual-unitary lattice models in 1 + 1 dimensions, *Phys. Rev. Lett.* **123**, 210601 (2019).
- [24] T. Prosen, Many-body quantum chaos and dual-unitarity round-a-face, *Chaos: An Interdisciplinary Journal of Nonlinear Science* **31**, 093101 (2021), <https://doi.org/10.1063/5.0056970>.
- [25] P. Kos, B. Bertini, and T. Prosen, Correlations in perturbed dual-unitary circuits: Efficient path-integral formula, *Phys. Rev. X* **11**, 011022 (2021).
- [26] B. Bertini, P. Kos, and T. Prosen, Exact spectral statistics in strongly localized circuits, *Phys. Rev. B* **105**, 165142 (2022).
- [27] P. Kos and G. Styliaris, Circuits of space and time quantum channels, *Quantum* **7**, 1020 (2023).
- [28] P. W. Claeys and A. Lamacraft, Ergodic and non-ergodic dual-unitary quantum circuits with arbitrary local Hilbert space dimension, *Phys. Rev. Lett.* **126**, 100603 (2021).
- [29] B. Bertini, P. Kos, and T. Prosen, Operator Entanglement in Local Quantum Circuits I: Chaotic Dual-Unitary Circuits, *SciPost Phys.* **8**, 67 (2020).
- [30] B. Bertini, P. Kos, and T. Prosen, Operator entanglement in local quantum circuits ii: Solitons in chains of qubits, *SciPost Physics* **8**, 68 (2020).
- [31] T. Holden-Dye, L. Masanes, and A. Pal, Fundamental charges for dual-unitary circuits (2023), arXiv:2312.14148 [quant-ph].
- [32] A. Foligno, P. Calabrese, and B. Bertini, Non-equilibrium dynamics of charged dual-unitary circuits (2024), arXiv:2407.21786 [cond-mat.stat-mech].
- [33] B. Bertini, P. Kos, and T. Prosen, Random matrix spectral form factor of dual-unitary quantum circuits, *Commun. Math. Phys.* , 1 (2021).
- [34] S. Aravinda, S. A. Rather, and A. Lakshminarayanan, From dual-unitary to quantum bernoulli circuits: Role of the entangling power in constructing a quantum ergodic hierarchy, *Phys. Rev. Res.* **3**, 043034 (2021).

- [35] S. A. Rather, S. Aravinda, and A. Lakshminarayan, Creating ensembles of dual unitary and maximally entangling quantum evolutions, *Phys. Rev. Lett.* **125**, 070501 (2020).
- [36] T. Prosen, Many-body quantum chaos and dual-unitarity round-a-face, *Chaos: An Interdisciplinary Journal of Nonlinear Science* **31**, 093101 (2021).
- [37] M. Borsi and B. Pozsgay, Construction and the ergodicity properties of dual unitary quantum circuits, *Phys. Rev. B* **106**, 014302 (2022).
- [38] D. B. A. Epstein, Almost all subgroups of a lie group are free, *Journal of Algebra* **19**, 261 (1971).
- [39] F. Gantmacher, *The Theory of Matrices, Vol II* (Chelsea Publishing Company, 1980).
- [40] A. Foligno, P. Calabrese, and B. Bertini, Non-equilibrium dynamics of charged dual-unitary circuits (2024), arXiv:2407.21786 [cond-mat.stat-mech].
- [41] A. Wehrl, General properties of entropy, *Rev. Mod. Phys.* **50**, 221 (1978).
- [42] G. Giudice, G. Giudici, M. Sonner, J. Thoenniss, A. Lerose, D. A. Abanin, and L. Piroli, Temporal entanglement, quasiparticles, and the role of interactions, *Phys. Rev. Lett.* **128**, 220401 (2022).
- [43] V. Alba and P. Calabrese, Quantum information scrambling after a quantum quench, *Phys. Rev. B* **100**, 115150 (2019).

In this Supplemental Material, we report some complementary results from the main text. In particular

- In Sec A we explicitly show the application of the quantum channels $\mathcal{E}^{L/R}$ to the reduced density matrix representing the state at the times of interest, working out the expression for the corresponding entanglement entropy.
- In Sec B we show how the presence of conserved charges on the gates changes the spectrum of the transfer matrix, which we characterize exactly under certain assumptions, and show that large powers of the transfer matrix correspond to the application of the quantum channels studied in Sec. A

Appendix A: Entanglement entropy after the quantum channel

In this section, we show more in details how dual unitarity and charge conservation allow us to find the entanglement entropy of the reduced density matrix after applying the quantum channel in the main text.

find the entanglement entropy for the reduced density matrix ρ_A at times $x/2 + l \leq t \leq x/2 + l$ after applying the quantum channel

$$\mathcal{E}^L[X] = \sum_{\alpha=1}^{m^L} \Pi_{\alpha}^L \frac{\text{tr}[\Pi_{\alpha}^L X]}{d_{\alpha}^L} \quad (\text{A1})$$

on its left-moving legs on the left interval and

$$\mathcal{E}^R[X] = \sum_{\alpha=1}^{m^L} \Pi_{\alpha}^R \frac{\text{tr}[\Pi_{\alpha}^R X]}{d_{\alpha}^L} \quad (\text{A2})$$

on the right-moving legs on its right interval. First, we show that $\mathcal{E}^{L/R}[X]$ is indeed a quantum channel. We can choose an orthonormal basis for the local Hilbert space on each leg which is compatible with the projectors Π_{α}^L :

$$|i, \alpha\rangle_{i=1, \dots, d_{\alpha}^L} \quad \sum_{i=1}^{d_{\alpha}^L} |i, \alpha\rangle\langle i, \alpha| = \Pi_{\alpha}^L. \quad (\text{A3})$$

Then, we can write (A1) in Kraus form:

$$\mathcal{E}^L[X] = \sum_{\alpha=1}^{m^L} \sum_{i,j=1}^{d_{\alpha}^L} |i, \alpha\rangle\langle j, \beta| X |i, \alpha\rangle\langle j, \beta| \frac{1}{d_{\alpha}^L}, \quad (\text{A4})$$

proving that (A1) is indeed a CPT map.

This channel is also *unital*, meaning it preserves the identity:

$$\mathcal{E}^L[\mathbb{1}_d] = \sum_{\alpha=1}^{m^L} \Pi_{\alpha}^L \frac{\text{tr}[\Pi_{\alpha}^L]}{d_{\alpha}^L} = \sum_{\alpha=1}^{m^L} \Pi_{\alpha}^L = \mathbb{1}_d, \quad (\text{A5})$$

where we used the completeness relation (28). We now introduce a graphical notation for the solitons $\Pi_{\alpha}^{R/L}$ in order to make the calculations more transparent:

$$\Pi_{\alpha}^R \otimes \mathbb{1}_d = \text{---} \bullet \text{---}, \quad \Pi_{\alpha}^L \otimes \mathbb{1}_d = \text{---} \bullet \text{---}. \quad (\text{A6})$$

The soliton property (29) can be written as

$$\text{---} \bullet \text{---} = \text{---} \bullet \text{---}, \quad \text{---} \bullet \text{---} = \text{---} \bullet \text{---}. \quad (\text{A7})$$

If we represent an operator X in the replica space as

$$\text{---} \circ \text{---}, \quad (\text{A8})$$

then the action of the quantum channel (A1) acting on it, can be represented as

$$\mathcal{E}^L[X] = \sum_{\alpha} \frac{1}{d_{\alpha}^L} \cdot \text{Diagram} \quad (\text{A9})$$

In this notation, we can represent the quantum channel acting on the reduced density matrix in Eq. (35) as

$$(\mathcal{E}^R)^{\otimes l} (\mathcal{E}^L)^{\otimes l} [\rho_A] \propto \sum_{\alpha, \beta} \frac{1}{d_{\alpha}^L d_{\beta}^R} \cdot \text{Diagram} \quad (\text{A10})$$

where we dropped an overall normalization factor for the reduced density matrix for simplicity (which can be found at the end by imposing that the trace of the resulting matrix is 1) and we summed over strings α, β of l projectors: $\alpha = (\alpha_1, \dots, \alpha_l)$, and similarly for β . The factors $d_{\alpha}^L, d_{\beta}^R$ are a shorthand notation for the product of all the factors coming from the channels:

$$d_{\alpha}^L = \prod_{i=1}^l d_{\alpha_i}^L \quad d_{\beta}^R = \prod_{i=1}^l d_{\beta_i}^R. \quad (\text{A11})$$

Using the relation (A7), combined with unitarity and dual unitarity (9)-(10), we can simplify the diagram (A10) to obtain (ignoring global normalization factors):

$$\sum_{\alpha, \beta} \frac{1}{d_{\alpha}^L d_{\beta}^R} \cdot \text{Diagram} \quad (\text{A12})$$

The number of pairs of charges connected via an initial state is $l - |2t - (x + l)|$ (as the one circled in blue in (A10)-(A12)); the remaining charges, which are not connected, (see e.g. the ones circled in orange in Eq. (A12)) can be resummed to show they are equal to the infinite temperature state; to see this notice that the factor $\frac{1}{d_{\alpha}^{L/R}}$ gets cancelled by the scalar product at the bottom, which is just $\text{tr} [\Pi_{\alpha}^{L/R}] = d_{\alpha}^{L/R}$. Then we use the fact that

$$\sum_{\alpha} \Pi_{\alpha}^{L/R} = \mathbf{1}_d. \quad (\text{A13})$$

Putting everything together, after the channel, the (normalized) density matrix can be written as

$$\rho = \left(\frac{\mathbf{1}_d}{d} \right)^{\otimes 2l + |4t - 2(x+l)|} \otimes \left(\sum_{\alpha, \beta} \Pi_{\alpha}^L \otimes \Pi_{\beta}^R \frac{\text{tr} [\Pi_{\alpha}^L \Pi_{\beta}^R]}{d d_{\alpha}^L d_{\beta}^R} \right)^{\otimes l - |2t - (x+l)|}, \quad (\text{A14})$$

whose entanglement entropy is

$$S^{(1)} = (2l + |4t - 2(x + l)|) \log(d) + (l - |2t - (x + l)|) \sum_{\alpha, \beta} c_{\alpha, \beta} (\log(d_\alpha d_\beta) - \log(c_{\alpha, \beta})), \quad (\text{A15})$$

where we used Eq. (31). This expression can be rewritten by noting that

$$c_\alpha^L = \sum_\beta c_{\alpha, \beta} = \frac{\text{tr}[\Pi_\alpha^L]}{d} = \frac{d_\alpha^L}{d} \quad c_\beta^R = \sum_\alpha c_{\alpha, \beta} = \frac{d_\beta^R}{d}, \quad (\text{A16})$$

allowing to rewrite Eq. (A15) as:

$$S^{(1)} = 4l \log(d) - (l - |2t - (x + l)|) \left[\sum_{\alpha, \beta} c_{\alpha, \beta} \log(c_{\alpha, \beta}) - \sum_\alpha c_\alpha^L \log(c_\alpha^L) - \sum_\beta c_\beta^R \log(c_\beta^R) \right]. \quad (\text{A17})$$

The quantity in parenthesis in (A17) corresponds to the classical mutual information of the probability distribution $c_{\alpha, \beta}$, implying that it is strictly positive. Expression (A17), which only depends on the expectation value of the solitons $c_\alpha^{L/R}$ and $c_{\alpha, \beta}$, generalizes to any charged solvable state, as defined in [40]; here we considered the simplest case to make the calculations more transparent.

Appendix B: Eigenvalues of the transfer matrix built with charge conserving gates

We consider a transfer matrix built with m^2 blocked dual unitary gates acting on qudits of local dimension $d = 2m$

$$U = \bigoplus_{\alpha=1}^m \bigoplus_{\beta=1}^m U^{\alpha, \beta}; \quad (\text{B1})$$

$$U^{\alpha, \beta} = U^{\alpha, \beta} (\Pi_\alpha^R \otimes \Pi_\beta^L) = (\Pi_\beta^L \otimes \Pi_\alpha^R) U^{\alpha, \beta} \quad (\text{B2})$$

where the blocks act on qubits (i.e. on a local dimension $d_{loc} = \frac{d}{m} = 2$)

$$d_\alpha^{L/R} = \text{tr}[\Pi_\alpha^{L/R}] = 2 \quad d = 2m^R = 2m^L. \quad (\text{B3})$$

The blocks are assumed to be chaotic dual unitaries extracted independently for each α, β . Since both the parametrization in Eq (3) and the one obtained by spatial reflection are complete and coincide in $d = 2$, we can use either depending on our convenience. We start by using a parametrization (3) and consider left-transfer matrices. The gate in a charge block $U^{\alpha, \beta}$ can be written as

$$U^{\alpha, \beta} = S \cdot U^{[\rho], \alpha, \beta, L} \cdot (v^{\alpha, \beta} \otimes \mathbf{1}_2) \quad v^{\alpha, \beta} \in SU(d) \quad (\text{B4})$$

where the matrices $\rho_{\alpha, \beta}^{(i)}$ and phases $\phi_{i, \alpha, \beta}$, which define a control gate as in (4), are extracted randomly and independently for each i, α, β . Given the block structure, the left transfer matrix can be written as a sum of other transfer matrices $T_{z, \alpha}^L$ which have their main diagonal projected on the right-moving soliton Π_α^R :

$$T_z^L = \sum_{\alpha=1}^{m_R} T_{z, \alpha}^L; \quad (\text{B5})$$

the transfer matrices T_α^L can be represent using the notation introduced the previous section for the solitons:

$$T_{z, \alpha}^L = \begin{array}{c} \alpha \\ \circ \\ \diagdown \\ \text{---} \\ \diagup \\ \circ \end{array} \begin{array}{c} \text{---} \\ \text{---} \\ \text{---} \\ \text{---} \end{array} \begin{array}{c} \circ \\ \alpha \\ \text{---} \\ \text{---} \\ \text{---} \\ \text{---} \\ \text{---} \\ \text{---} \\ \text{---} \\ \text{---} \\ \circ \end{array} \quad (\text{B6})$$

Due to the unitarity of the folded gate, it is immediate to see that each transfer matrix T_α^L has eigenvalues of modulus $\leq d_\alpha^R = 2$. We now show that *each* $T_{z,\alpha}^L$ has the same set of largest eigenvectors, all with eigenvalue 2, thus implying that these are the largest eigenvectors of the sum $T_z^L = \sum_\alpha T_{z,\alpha}^L$.

Thanks to the soliton conservation condition (29), the transfer matrices commute with all the strings of left-moving projectors:

$$\Pi_{\beta,\gamma}^L = \bigotimes_{i=1}^z \Pi_{\beta_i}^L \otimes \Pi_{\gamma_i}^L \quad (\text{B7})$$

$$[T_{z,\alpha}^L, \Pi_{\beta,\gamma}^L] = 0, \quad (\text{B8})$$

so we can just look at the spectrum of the transfer matrix projected on one string

$$\Pi_{\beta,\gamma}^L T_{z,\alpha}^L \Pi_{\beta,\gamma}^L. \quad (\text{B9})$$

In each block, the transfer matrix is now built with random DU gates of local dimension $d = 2$. By using the reasoning of the main text, first setting $v^{\alpha,\beta} = \mathbb{1}_2$ shows that the eigenvalues of a transfer matrix can be written as strings of bits $|(\mathbf{j}, \boldsymbol{\beta}), (\mathbf{k}, \boldsymbol{\gamma})\rangle$, where

$$|(\mathbf{j}, \boldsymbol{\beta}), (\mathbf{k}, \boldsymbol{\gamma})\rangle \equiv \prod_{a=1}^z |(j_a, \beta_a)\rangle \otimes |(k_a, \gamma_a)\rangle \quad j_a, k_a = 1, 2, \quad (\text{B10})$$

where it is understood that $\{|(1, \beta)\rangle, |(2, \beta)\rangle\}$ is an orthonormal basis of the Hilbert space projected by Π_β^L . The corresponding eigenvalue of $|(\mathbf{j}, \boldsymbol{\beta}), (\mathbf{k}, \boldsymbol{\gamma})\rangle$ is

$$\lambda_{\mathbf{j}, \boldsymbol{\beta}, \mathbf{k}, \boldsymbol{\gamma}} = \exp\left(\sum_{a=1}^z \phi_{j_a, \alpha, \beta_a} - \phi_{k_a, \alpha, \gamma_a}\right) \text{tr} \left[\left(\prod_{a=1}^z \rho_{\beta_a, \alpha}^{(j_a)} \right) \left(\prod_{a=1}^z \rho_{\gamma_a, \alpha}^{(k_a)} \right)^\dagger \right]; \quad (\text{B11})$$

as per the reasoning of the main text, in order to have a maximal eigenvalue the matrix inside the trace must be the identity; but by the theorem in [38], since the matrix are randomly chosen, almost surely this can happen only if

$$j_a = k_a \quad \beta_a = \gamma_a, \quad (\text{B12})$$

showing that the only charge blocks of the transfer matrix B9 with maximal eigenvalue must have the same charges on both the forward and backward layer of the gates (i.e. $\boldsymbol{\beta} = \boldsymbol{\gamma}$). Once we restrict to one such reduced space, we choose randomly the matrices $v_{\alpha,\beta}$, independently in each block. As per the reasoning of the main text, we can use Perron Frobenius theorem to show that in each of these block there can only be a simple largest eigenvalue, which is the bullet state (defined with the states in that block). This shows that the eigenvectors can be written as

$$|\psi_{\boldsymbol{\beta}}^{\text{max}}\rangle = \bigotimes_a \sum_{j=1}^2 |(j, \beta_a), (j, \beta_a)\rangle \quad j_a = 1, 2, \beta_a = 1, \dots, m^L. \quad (\text{B13})$$

In the quantum channel language: $T_z^L \rightleftharpoons \mathcal{M}_z^L$ (cf. Eq. (27)), the largest eigenvectors, which are now operators, can also be written as (we insist that in this picture the vectors are operator on the original space, hence the change in notation)

$$O_{\boldsymbol{\beta}}^{\text{max}} \equiv \Pi_{\boldsymbol{\beta}}^L = \bigotimes_{a=1}^z \Pi_{\beta_a}^L. \quad (\text{B14})$$

This implies that, in the limit where the channel projects on its largest eigenvectors, we can write

$$\lim_{n \rightarrow \infty} (\mathcal{M}_z^L)^n [\bullet] = \sum_{\boldsymbol{\beta}} \Pi_{\boldsymbol{\beta}}^L \text{tr} [\Pi_{\boldsymbol{\beta}}^L \bullet] = (\mathcal{E}^L)^{\otimes z}, \quad (\text{B15})$$

showing saturation of the bound obtained in Sec. A.

Chapter 7

Conclusions

In this Thesis, I studied analytically the dynamics of several classes of interacting quantum circuits. In order to find these results, I used some constraints on the dynamics (mostly revolving around variations of Dual Unitarity).

While one of the most compelling questions at the moment is to understand how much the class of solvable circuits can be extended, these results show that already dual unitary circuits can offer a rather diverse landscape of quantum dynamics. For instance, I have shown in [110] that there are examples of dual unitary circuits that have conserved charges and thermalize to non-trivial Gibbs Ensembles, and have a different entanglement dynamics to the chaotic ones, analogous to the one of integrable systems [111].

Future works might focus on calculations of different markers of the dynamics, which have already been computed for chaotic dual unitaries, and see how the charge structure changes the result, such as the temporal entanglement or the spectral form factor, to try underpin some universal features in the dynamics.

Another fertile direction of research is the study of the effect of feedback and measurements on the dynamics; the recent results on the measurement induced phase transition [48], and the advancement in quantum computers,

especially regarding quantum error correction algorithms, show that there is much still to be uncovered about the interplay of unitary dynamics with unitary-breaking operations. In the context of Dual Unitary circuits, there are already several protocols which implement measurements on the system without destroying the solvability [112, 101, 113, 114], showing the great versatility of this model.

Finally, there are many interesting open problems regarding dual unitary gates yet to be solved: for example the full parametrization of dual unitary gates in arbitrary dimension, which then might be combined with some of the ideas in [111] to show ergodicity almost certainly for the full set of such gates.

7.1 Acknowledgements

First and foremost, I am deeply grateful to my supervisor, Bruno Bertini, who trusted and assisted me during my PhD. Without his constant help and guidance this PhD would certainly not have been successful; I also want to thank Katja Klobas for always being present for an advice or a discussion, when needed.

A special thanks to Pasquale Calabrese for hosting and welcoming me in SISSA for several weeks; I will always carry fond memories of my stay and work there, which I have been crucial for my academic development.

I would also like to thank all my friends and my family, whose support, while not always directly related to academic matters, has been precious to me in these years.

Bibliography

- [1] Tim Langen, Sebastian Erne, Remi Geiger, Bernhard Rauer, Thomas Schweigler, Maximilian Kuhnert, Wolfgang Rohringer, Igor Mazets, T. Gasenzer, and Jörg Schmiedmayer. Experimental observation of a generalized gibbs ensemble. *Science (New York, N.Y.)*, 348, 11 2014.
- [2] Robert M. Wald. The thermodynamics of black holes. *Living Rev. Rel.*, 4:6, 2001.
- [3] P. C. W. Davies. Thermodynamics of Black Holes. *Proc. Roy. Soc. Lond. A*, 353:499–521, 1977.
- [4] Sai Vinjanampathy and Janet Anders. Quantum thermodynamics. *Contemporary Physics*, 57:545 – 579, 2015.
- [5] Charles H. Bennett. Notes on landauer’s principle, reversible computation, and maxwell’s demon. *Studies in History and Philosophy of Science Part B: Studies in History and Philosophy of Modern Physics*, 34(3):501–510, 2003. Quantum Information and Computation.
- [6] Stuart Freedman and John Clauser. Experimental test of local hidden-variable theories. *Physical Review Letters*, 28, 04 1972.
- [7] Alain Aspect, Philippe Grangier, and Gérard Roger. Experimental realization of einstein-podolsky-rosen-bohm gedankenexperiment: A new violation of bell’s inequalities. *Phys. Rev. Lett.*, 49:91–94, Jul 1982.

- [8] Pasquale Calabrese and John Cardy. Entanglement entropy and conformal field theory. *Journal of Physics A: Mathematical and Theoretical*, 42(50):504005, dec 2009.
- [9] I. Bengtsson and K. Zyczkowski. *Geometry of Quantum States: An Introduction to Quantum Entanglement*. Cambridge University Press, 2007.
- [10] Tibor Rakovszky, Frank Pollmann, and C. W. von Keyserlingk. Sub-ballistic growth of rényi entropies due to diffusion. *Phys. Rev. Lett.*, 122:250602, Jun 2019.
- [11] Yichen Huang. Dynamics of Rényi entanglement entropy in diffusive qudit systems. *IOP SciNotes*, 1(3):035205, dec 2020.
- [12] Alessandro Foligno, Tianci Zhou, and Bruno Bertini. Temporal entanglement in chaotic quantum circuits. *Phys. Rev. X*, 13:041008, Oct 2023.
- [13] Vincenzo Alba and Pasquale Calabrese. Entanglement and thermodynamics after a quantum quench in integrable systems. *Proc. Natl. Acad. Sci. U.S.A.*, 114(30):7947–7951, 2017.
- [14] Marcos Rigol, Vanja Dunjko, and Maxim Olshanii. Thermalization and its mechanism for generic isolated quantum systems. *Nature*, 452(7189):854–858, 2008.
- [15] J. M. Deutsch. Quantum statistical mechanics in a closed system. *Phys. Rev. A*, 43:2046–2049, Feb 1991.
- [16] P. Bocchieri and A. Loinger. Quantum recurrence theorem. *Phys. Rev.*, 107:337–338, Jul 1957.
- [17] J. M. Deutsch, Haibin Li, and Auditya Sharma. Microscopic origin of thermodynamic entropy in isolated systems. *Phys. Rev. E*, 87:042135, Apr 2013.

- [18] W Beugeling, A Andreanov, and Masudul Haque. Global characteristics of all eigenstates of local many-body hamiltonians: participation ratio and entanglement entropy. *J. Stat. Mech.: Theory and Exp.*, 2015(2):P02002, feb 2015.
- [19] V Gurarie. Global large time dynamics and the generalized gibbs ensemble. *J. Stat. Mech.: Theory and Exp.*, 2013(02):P02014, feb 2013.
- [20] Pasquale Calabrese and John Cardy. Evolution of entanglement entropy in one-dimensional systems. *J. Stat. Mech.: Theory Exp.*, 2005(04):P04010, apr 2005.
- [21] Benjamin Doyon. Thermalization and pseudolocality in extended quantum systems. *Commun. Math. Phys.*, 351(1):155–200, 2017.
- [22] Fabian H L Essler and Maurizio Fagotti. Quench dynamics and relaxation in isolated integrable quantum spin chains. *J. Stat. Mech.: Theory Exp.*, 2016(6):064002, Jun 2016.
- [23] Pavel Kos, Tomaž Prosen, and Bruno Bertini. Thermalization dynamics and spectral statistics of extended systems with thermalizing boundaries. *Phys. Rev. B*, 104:214303, Dec 2021.
- [24] Tomaž Prosen. Open xxz spin chain: Nonequilibrium steady state and a strict bound on ballistic transport. *Phys. Rev. Lett.*, 106:217206, May 2011.
- [25] E. Ilievski, J. De Nardis, B. Wouters, J.-S. Caux, F. H. L. Essler, and T. Prosen. Complete generalized gibbs ensembles in an interacting theory. *Phys. Rev. Lett.*, 115:157201, Oct 2015.
- [26] M B Hastings. An area law for one-dimensional quantum systems. *Journal of Statistical Mechanics: Theory and Experiment*, 2007(08):P08024, aug 2007.

- [27] Itai Arad, Alexei Y. Kitaev, Zeph Landau, and Umesh V. Vazirani. An area law and sub-exponential algorithm for 1d systems. *arXiv: Quantum Physics*, 2013.
- [28] Yichen Huang. Area law in one dimension: Degenerate ground states and renyi entanglement entropy, 2015.
- [29] U. Schollwöck. The density-matrix renormalization group. *Rev. Mod. Phys.*, 77:259–315, Apr 2005.
- [30] Karen A. Hallberg. New trends in density matrix renormalization. *Advances in Physics*, 55(5-6):477–526, 2006.
- [31] Pasquale Calabrese and John Cardy. Entanglement entropy and quantum field theory. *Journal of Statistical Mechanics: Theory and Experiment*, 2004(06):P06002, jun 2004.
- [32] R.L. Hagemans. *Dynamics of Heisenberg spin chains*. PhD thesis, 2007.
- [33] Minoru Takahashi. *Thermodynamics of One-Dimensional Solvable Models*. Cambridge University Press, 1999.
- [34] Subir Sachdev and Jinwu Ye. Gapless spin-fluid ground state in a random quantum heisenberg magnet. *Phys. Rev. Lett.*, 70:3339–3342, May 1993.
- [35] Vladimir Rosenhaus. An introduction to the syk model. *Journal of Physics A: Mathematical and Theoretical*, 52(32):323001, July 2019.
- [36] Maksym Serbyn, Dmitry A. Abanin, and Zlatko Papić. Quantum many-body scars and weak breaking of ergodicity. *Nature Physics*, 17(6):675–685, June 2021.
- [37] Sanjay Moudgalya, B Andrei Bernevig, and Nicolas Regnault. Quantum many-body scars and hilbert space fragmentation: a review of exact results. *Reports on Progress in Physics*, 85(8):086501, jul 2022.

- [38] Anushya Chandran, Thomas Iadecola, Vedika Khemani, and Roderich Moessner. Quantum Many-Body Scars: A Quasiparticle Perspective. *Ann. Rev. Condensed Matter Phys.*, 14:443–469, 2023.
- [39] Rahul Nandkishore and David A. Huse. Many body localization and thermalization in quantum statistical mechanics. *Ann. Rev. Condensed Matter Phys.*, 6:15–38, 2015.
- [40] Luca Dalessio, Yariv Kafri, A. Polkovnikov, and Marcos Rigol. From quantum chaos and eigenstate thermalization to statistical mechanics and thermodynamics. *Advances in Physics*, 65, 09 2015.
- [41] Matthew P. A. Fisher, Vedika Khemani, Adam Nahum, and Sagar Vijay. Random quantum circuits. 2022.
- [42] Adam Nahum, Jonathan Ruhman, Sagar Vijay, and Jeongwan Haah. Quantum entanglement growth under random unitary dynamics. *Phys. Rev. X*, 7:031016, Jul 2017.
- [43] Adam Nahum, Sagar Vijay, and Jeongwan Haah. Operator spreading in random unitary circuits. *Phys. Rev. X*, 8:021014, Apr 2018.
- [44] C. W. von Keyserlingk, Tibor Rakovszky, Frank Pollmann, and S. L. Sondhi. Operator Hydrodynamics, OTOCs, and Entanglement Growth in Systems without Conservation Laws. *Phys. Rev. X*, 8:021013, Apr 2018.
- [45] Yichen Huang. Dynamics of rényi entanglement entropy in diffusive qudit systems. *IOP SciNotes*, 1(3):035205, December 2020.
- [46] Vedika Khemani, Ashvin Vishwanath, and David A. Huse. Operator spreading and the emergence of dissipative hydrodynamics under unitary evolution with conservation laws. *Phys. Rev. X*, 8:031057, Sep 2018.

- [47] Aaron J. Friedman, Amos Chan, Andrea De Luca, and J. T. Chalker. Spectral statistics and many-body quantum chaos with conserved charge. *Phys. Rev. Lett.*, 123:210603, Nov 2019.
- [48] Brian Skinner, Jonathan Ruhman, and Adam Nahum. Measurement-induced phase transitions in the dynamics of entanglement. *Phys. Rev. X*, 9:031009, Jul 2019.
- [49] Elliott H. Lieb and Derek W. Robinson. The finite group velocity of quantum spin systems. *Communications in Mathematical Physics*, 28(3):251 – 257, 1972.
- [50] Chi-Fang (Anthony) Chen, Andrew Lucas, and Chao Yin. Speed limits and locality in many-body quantum dynamics. *Reports on Progress in Physics*, 86(11):116001, sep 2023.
- [51] Guifré Vidal. Efficient simulation of one-dimensional quantum many-body systems. *Phys. Rev. Lett.*, 93:040502, Jul 2004.
- [52] K Satzinger, Y.-J Liu, A Smith, C Knapp, M Newman, C Jones, Zhaoshi Chen, Céline Quintana, Xiaohua Mi, A Dunsworth, C Gidney, I. Aleiner, F Arute, K Arya, J Atalaya, R Babbush, Joseph Bardin, R Barends, J Basso, and P Roushan. Realizing topologically ordered states on a quantum processor. *Science (New York, N.Y.)*, 374:1237–1241, 12 2021.
- [53] Xiao Mi, Matteo Ippoliti, Chris Quintana, Ami Greene, Zijun Chen, Jonathan Gross, Frank Arute, Kunal Arya, Juan Atalaya, Ryan Babbush, Joseph Bardin, Joao Basso, Andreas Bengtsson, Alexander Bilmes, Alexandre Bourassa, Leon Brill, Michael Broughton, Bob Buckley, David Buell, and Pedram Roushan. Time-crystalline eigenstate order on a quantum processor. *Nature*, 601:1–1, 01 2022.
- [54] Jin Ming Koh, Shi-Ning Sun, Mario Motta, and Austin J. Minnich. Measurement-induced entanglement phase transition on a supercon-

- ducting quantum processor with mid-circuit readout. *Nature Phys.*, 19(9):1314–1319, 2023.
- [55] Yaodong Li, Xiao Chen, and Matthew P. A. Fisher. Quantum zeno effect and the many-body entanglement transition. *Phys. Rev. B*, 98:205136, Nov 2018.
- [56] Bruno Bertini, Pavel Kos, and Tomaž Prosen. Exact spectral form factor in a minimal model of many-body quantum chaos. *Phys. Rev. Lett.*, 121:264101, Dec 2018.
- [57] Amos Chan, Andrea De Luca, and J. T. Chalker. Solution of a minimal model for many-body quantum chaos. *Phys. Rev. X*, 8(4):041019, Nov 2018.
- [58] Bruno Bertini, Pavel Kos, and Tomaž Prosen. Exact correlation functions for dual-unitary lattice models in $1 + 1$ dimensions. *Phys. Rev. Lett.*, 123:210601, Nov 2019.
- [59] Katja Klobas, Bruno Bertini, and Lorenzo Piroli. Exact thermalization dynamics in the “Rule 54” quantum cellular automaton. *Phys. Rev. Lett.*, 126:160602, Apr 2021.
- [60] Tomaž Prosen. Many-body quantum chaos and dual-unitarity round-a-face. *Chaos: An Interdisciplinary Journal of Nonlinear Science*, 31(9):093101, 2021.
- [61] Pavel Kos, Bruno Bertini, and Tomaž Prosen. Correlations in perturbed dual-unitary circuits: Efficient path-integral formula. *Phys. Rev. X*, 11:011022, Feb 2021.
- [62] Bruno Bertini, Pavel Kos, and Tomaž Prosen. Exact spectral statistics in strongly localized circuits. *Phys. Rev. B*, 105:165142, Apr 2022.
- [63] Pavel Kos and Georgios Styliaris. Circuits of space and time quantum channels. *Quantum*, 7:1020, May 2023.

- [64] Bruno Bertini, Cecilia De Fazio, Juan P. Garrahan, and Katja Klobas. Exact quench dynamics of the Floquet quantum East model at the deterministic point. 2023.
- [65] Sarang Gopalakrishnan and Austen Lamacraft. Unitary circuits of finite depth and infinite width from quantum channels. *Phys. Rev. B*, 100:064309, Aug 2019.
- [66] Xie-Hang Yu, Zhiyuan Wang, and Pavel Kos. Hierarchical generalization of dual unitarity. 2023.
- [67] Grace M. Sommers, Sarang Gopalakrishnan, Michael J. Gullans, and David A. Huse. Zero-temperature entanglement membranes in quantum circuits, 2024.
- [68] Alessandro Foligno, Pavel Kos, and Bruno Bertini. Quantum information spreading in generalized dual-unitary circuits. *Physical Review Letters*, 132(25), June 2024.
- [69] Alexander Bobenko, Martin Bordemann, Charlie Gunn, and Ulrich Pinkall. On two integrable cellular automata. *Communications in Mathematical Physics*, 158(1):127 – 134, 1993.
- [70] Katja Klobas and Bruno Bertini. Exact relaxation to Gibbs and non-equilibrium steady states in the quantum cellular automaton Rule 54. *SciPost Phys.*, 11:106, 2021.
- [71] Bruno Bertini, Pavel Kos, and Tomaž Prosen. Localized dynamics in the floquet quantum east model. *Phys. Rev. Lett.*, 132:080401, Feb 2024.
- [72] Tianci Zhou and Adam Nahum. Emergent statistical mechanics of entanglement in random unitary circuits. *Phys. Rev. B*, 99:174205, May 2019.
- [73] Tianci Zhou and Adam Nahum. Entanglement membrane in chaotic many-body systems. *Phys. Rev. X*, 10:031066, Sep 2020.

- [74] Cheryne Jonay, David A. Huse, and Adam Nahum. Coarse-grained dynamics of operator and state entanglement. 2018.
- [75] Bruno Bertini, Elena Tartaglia, and Pasquale Calabrese. Entanglement and diagonal entropies after a quench with no pair structure. *Journal of Statistical Mechanics: Theory and Experiment*, 2018(6):063104, jun 2018.
- [76] Bruno Bertini, Katja Klobas, Vincenzo Alba, Gianluca Lagnese, and Pasquale Calabrese. Growth of rényi entropies in interacting integrable models and the breakdown of the quasiparticle picture. *Phys. Rev. X*, 12:031016, Jul 2022.
- [77] Subir Ghoshal and Alexander B. Zamolodchikov. Boundary S matrix and boundary state in two-dimensional integrable quantum field theory. *Int. J. Mod. Phys. A*, 9:3841–3886, 1994. [Erratum: *Int.J.Mod.Phys.A* 9, 4353 (1994)].
- [78] Lorenzo Piroli, Balázs Pozsgay, and Eric Vernier. What is an integrable quench? *Nuclear Physics B*, 925:362–402, 2017.
- [79] Márk Mezei. Membrane theory of entanglement dynamics from holography. *Phys. Rev. D*, 98:106025, Nov 2018.
- [80] Márk Mezei and Julio Virrueta. Exploring the membrane theory of entanglement dynamics. *Journal of High Energy Physics*, 2020(2):1–35, 2020.
- [81] Pasquale Calabrese and John Cardy. Evolution of entanglement entropy in one-dimensional systems. *Journal of Statistical Mechanics: Theory and Experiment*, 2005(04):P04010, apr 2005.
- [82] Vincenzo Alba and Pasquale Calabrese. Entanglement dynamics after quantum quenches in generic integrable systems. *SciPost Phys.*, 4:17, 2018.

- [83] Jonah Kudler-Flam, Yuya Kusuki, and Shinsei Ryu. The quasi-particle picture and its breakdown after local quenches: mutual information, negativity, and reflected entropy. *Journal of High Energy Physics*, 2021, 2020.
- [84] Yuya Kusuki and Masamichi Miyaji. Entanglement Entropy, OTOC and Bootstrap in 2D CFTs from Regge and Light Cone Limits of Multi-point Conformal Block. *JHEP*, 08:063, 2019.
- [85] Curtis T. Asplund, Alice Bernamonti, Federico Galli, and Thomas Hartman. Entanglement Scrambling in 2d Conformal Field Theory. *JHEP*, 09:110, 2015.
- [86] Jonah Kudler-Flam, Laimei Nie, and Shinsei Ryu. Conformal field theory and the web of quantum chaos diagnostics. *JHEP*, 01:175, 2020.
- [87] Pavan Hosur, Xiao-Liang Qi, Daniel A Roberts, and Beni Yoshida. Chaos in quantum channels. *Journal of High Energy Physics*, 2016(2):1–49, 2016.
- [88] Yusuf Kasim and Tomaž Prosen. Dual unitary circuits in random geometries. *Journal of Physics A: Mathematical and Theoretical*, 56(2):025003, jan 2023.
- [89] M Akila, D Waltner, B Gutkin, and T Guhr. Particle-time duality in the kicked Ising spin chain. *J. Phys. A: Math. Theor.*, 49(37):375101, Aug 2016.
- [90] Bruno Bertini, Pavel Kos, and Tomaž Prosen. Entanglement spreading in a minimal model of maximal many-body quantum chaos. *Phys. Rev. X*, 9(2):021033, May 2019.
- [91] Pieter W Claeys and Austen Lamacraft. Ergodic and non-ergodic dual-unitary quantum circuits with arbitrary local Hilbert space dimension. *Phys. Rev. Lett.*, 126:100603, Mar 2021.

- [92] S. Aravinda, Suhail Ahmad Rather, and Arul Lakshminarayan. From dual-unitary to quantum bernoulli circuits: Role of the entangling power in constructing a quantum ergodic hierarchy. *Phys. Rev. Res.*, 3:043034, Oct 2021.
- [93] Suhail Ahmad Rather, S. Aravinda, and Arul Lakshminarayan. Creating ensembles of dual unitary and maximally entangling quantum evolutions. *Phys. Rev. Lett.*, 125:070501, Aug 2020.
- [94] Tomaž Prosen. Many-body quantum chaos and dual-unitarity round-a-face. *Chaos: An Interdisciplinary Journal of Nonlinear Science*, 31:093101, 09 2021.
- [95] Márton Borsi and Balázs Pozsgay. Construction and the ergodicity properties of dual unitary quantum circuits. *Phys. Rev. B*, 106:014302, Jul 2022.
- [96] Lorenzo Piroli, Bruno Bertini, J. Ignacio Cirac, and Tomaž Prosen. Exact dynamics in dual-unitary quantum circuits. *Phys. Rev. B*, 101:094304, Mar 2020.
- [97] Tianci Zhou and Aram W. Harrow. Maximal entanglement velocity implies dual unitarity. *Phys. Rev. B*, 106(20):L201104, November 2022.
- [98] Bruno Bertini, Pavel Kos, and Tomaž Prosen. Random matrix spectral form factor of dual-unitary quantum circuits. *Commun. Math. Phys.*, pages 1–24, 2021.
- [99] Pieter W. Claeys and Austen Lamacraft. Maximum velocity quantum circuits. *Phys. Rev. Research*, 2:033032, Jul 2020.
- [100] Wen Wei Ho and Soonwon Choi. Exact emergent quantum state designs from quantum chaotic dynamics. *Phys. Rev. Lett.*, 128:060601, Feb 2022.

- [101] Pieter W. Claeys and Austen Lamacraft. Emergent quantum state designs and biunitarity in dual-unitary circuit dynamics. *Quantum*, 6:738, June 2022.
- [102] Leonard Logarić, Shane Dooley, Silvia Pappalardi, and John Goold. Quantum Many-Body Scars in Dual-Unitary Circuits. *Phys. Rev. Lett.*, 132(1):010401, 2024.
- [103] Giacomo Giudice, Giuliano Giudici, Michael Sonner, Julian Thoeniss, Alessio Lerose, Dmitry A. Abanin, and Lorenzo Piroli. Temporal entanglement, quasiparticles, and the role of interactions. *Phys. Rev. Lett.*, 128:220401, Jun 2022.
- [104] Bruno Bertini and Lorenzo Piroli. Scrambling in random unitary circuits: Exact results. *Phys. Rev. B*, 102:064305, Aug 2020.
- [105] Eli Chertkov et al. Holographic dynamics simulations with a trapped-ion quantum computer. *Nature Phys.*, 18(9):1074–1079, 2022.
- [106] Xiao Mi et al. Information scrambling in quantum circuits. *Science*, 374(6574):abg5029, 2021.
- [107] M. C. Bañuls, M. B. Hastings, F. Verstraete, and J. I. Cirac. Matrix product states for dynamical simulation of infinite chains. *Phys. Rev. Lett.*, 102:240603, Jun 2009.
- [108] Alessio Lerose, Michael Sonner, and Dmitry A. Abanin. Influence matrix approach to many-body floquet dynamics. *Phys. Rev. X*, 11:021040, May 2021.
- [109] Lorenzo Piroli, Eric Vernier, and Pasquale Calabrese. Exact steady states for quantum quenches in integrable Heisenberg spin chains. *Phys. Rev. B*, 94:054313, Aug 2016.
- [110] Alessandro Foligno, Pasquale Calabrese, and Bruno Bertini. Non-equilibrium dynamics of charged dual-unitary circuits. *arXiv: Quantum Physics*, 2024.

- [111] Alessandro Foligno and Bruno Bertini. Entanglement of disjoint intervals in dual unitary circuits: Exact results. 2024.
- [112] Matteo Ippoliti and Wen Wei Ho. Dynamical purification and the emergence of quantum state designs from the projected ensemble. *PRX Quantum*, 4:030322, Aug 2023.
- [113] Wen Wei Ho and Soonwon Choi. Exact emergent quantum state designs from quantum chaotic dynamics. *Phys. Rev. Lett.*, 128:060601, Feb 2022.
- [114] Pieter W. Claeys, Marius Henry, Jamie Vicary, and Austen Lamacraft. Exact dynamics in dual-unitary quantum circuits with projective measurements. *Phys. Rev. Res.*, 4:043212, Dec 2022.